Variations of lithospheric strength in different tectonic settings

Ershad Gholamrezaie
M. Sc. Geophysik

Kumulative Dissertation
zur Erlangung des akademischen Grades
"doctor rerum naturalium"
(Dr. rer. nat.)
in der Wissenschaftsdisziplin " Geologie"

eingereicht an der
Mathematisch-Naturwissenschaftlichen Fakultät
Institut für Geowissenschaften
der Universität Potsdam
und
4.5 Sedimentbeckenanalyse
Deutsches GeoForschungsZentrum Potsdam

Ort und Tag der Disputation:
Online – 29. April 2021

Hauptbetreuer*in:	Prof. Manfred R. Strecker, PhD
Betreuer*innen:	Dr. Gerold Zeilinger Prof. Dr. Magdalena Scheck-Wenderoth
Gutachter*innen:	Prof. Manfred R. Strecker, PhD Prof. Dr. Fabrice Cotton Prof. Dr. Hans-Jürgen Götze

Published online on the
Publication Server of the University of Potsdam:
https://doi.org/10.25932/publishup-51146
https://nbn-resolving.org/urn:nbn:de:kobv:517-opus4-511467

Abstract

Rheology describes the flow of matter under the influence of stress, and - related to solids- it investigates how solids subjected to stresses deform. As the deformation of the Earth's outer layers, the lithosphere and the crust, is a major focus of rheological studies, rheology in the geosciences describes how strain evolves in rocks of variable composition and temperature under tectonic stresses. It is here where deformation processes shape the form of ocean basins and mountain belts that ultimately result from the complex interplay between lithospheric plate motion and the susceptibility of rocks to the influence of plate-tectonic forces. A rigorous study of the strength of the lithosphere and deformation phenomena thus requires in-depth studies of the rheological characteristics of the involved materials and the temporal framework of deformation processes.

This dissertation aims at analyzing the influence of the physical configuration of the lithosphere on the present-day thermal field and the overall rheological characteristics of the lithosphere to better understand variable expressions in the formation of passive continental margins and the behavior of strike-slip fault zones. The main methodological approach chosen is to estimate the present-day thermal field and the strength of the lithosphere by 3-D numerical modeling. The distribution of rock properties is provided by 3-D structural models, which are used as the basis for the thermal and rheological modeling. The structural models are based on geophysical and geological data integration, additionally constrained by 3-D density modeling. More specifically, to decipher the thermal and rheological characteristics of the lithosphere in both oceanic and continental domains, sedimentary basins in the Sea of Marmara (continental transform setting), the SW African passive margin (old oceanic crust), and the Norwegian passive margin (young oceanic crust) were selected for this study.

The Sea of Marmara, in northwestern Turkey, is located where the dextral North Anatolian Fault zone (NAFZ) accommodates the westward escape of the Anatolian Plate toward the Aegean. Geophysical observations indicate that the crust is heterogeneous beneath the Marmara basin, but a detailed characterization of the lateral crustal heterogeneities is presented for the first time in this study. Here, I use different gravity datasets and the general non-uniqueness in potential field modeling, to propose three possible end-member scenarios of crustal configuration. The models suggest that pronounced gravitational anomalies in the basin originate from significant density heterogeneities within the crust. The rheological modeling

reveals that associated variations in lithospheric strength control the mechanical segmentation of the NAFZ. Importantly, a strong crust that is mechanically coupled to the upper mantle spatially correlates with aseismic patches where the fault bends and changes its strike in response to the presence of high-density lower crustal bodies. Between the bends, mechanically weaker crustal domains that are decoupled from the mantle are characterized by creep.

For the passive margins of SW Africa and Norway, two previously published 3-D conductive and lithospheric-scale thermal models were analyzed. These 3-D models differentiate various sedimentary, crustal, and mantle units and integrate different geophysical data, such as seismic observations and the gravity field. Here, the rheological modeling suggests that the present-day lithospheric strength across the oceanic domain is ultimately affected by the age and past thermal and tectonic processes as well as the depth of the thermal lithosphere-asthenosphere boundary, while the configuration of the crystalline crust dominantly controls the rheological behavior of the lithosphere beneath the continental domains of both passive margins.

The thermal and rheological models show that the variations of lithospheric strength are fundamentally influenced by the temperature distribution within the lithosphere. Moreover, as the composition of the lithosphere significantly influences the present-day thermal field, it therefore also affects the rheological characteristics of the lithosphere. Overall my studies add to our understanding of regional tectonic deformation processes and the long-term behavior of sedimentary basins; they confirm other analyses that have pointed out that crustal heterogeneities in the continents result in diverse lithospheric thermal characteristics, which in turn results in higher complexity and variations of rheological behavior compared to oceanic domains with a thinner, more homogeneous crust.

Kurzfassung

Die Rheologie ist die Wissenschaft, die sich mit dem Fließ- und Verformungsverhalten von Materie beschäftigt. Hierzu gehören neben Gasen und Flüssigkeiten vor allem auch Feststoffe, die einer Spannung ausgesetzt sind und einem daraus resultierenden Verformungsprozess unterliegen - entweder unter bruchhaften oder plastischen Bedingungen. In den Geowissenschaften umfasst die Rheologie die kombinierte Analyse tektonischer Spannungen und resultierender Deformationsphänomene in Gesteinen unter unterschiedlichen Temperatur- und Druckbedingungen sowie im Zusammenhang mit physikalischen Eigenschaften der Krusten- und Mantelgesteine. Die Verformung des lithosphärischen Mantels und der Kruste ist ein Schwerpunkt rheologischer Untersuchungen, denn in diesem Zusammenhang bilden sich Ozeanbecken und Gebirgsgürtel, die letztendlich aus dem komplexen Zusammenspiel der Bewegungen lithosphärischer Platten und der unterschiedlichen Deformierbarkeit von Krusten- und Mantelgesteinen unter dem Einfluss plattentektonischer Kräfte resultieren. Eine genaue Untersuchung der Festigkeit der Lithosphäre und der Deformationssphänomene erfordert daher eingehende Studien der rheologischen Eigenschaften der beteiligten Materialien.

Vor diesem Hintergrund ist es das Ziel dieser Dissertation, die allgemeinen rheologischen Charakteristika der Lithosphäre in drei verschiedenen geodynamischen Bereichen zu analysieren, um unterschiedlich geprägte passive Kontinentalränder sowie das Verhalten von Transformstörungen innerhalb der Kontinente besser zu verstehen. Der wichtigste methodische Ansatz, der hierfür gewählt wurde, ist die numerische 3D-Modellierung, um eine Abschätzung des gegenwärtigen thermischen Feldes und der Festigkeit der Lithosphäre zu ermöglichen. Die räumliche Verteilung der Gesteinseigenschaften in Kruste und Mantel wird dabei durch 3-D-Strukturmodelle bereitgestellt, die als Grundlage für die thermische und rheologische Modellierung verwendet werden. Die Strukturmodelle basieren auf der Integration geophysikalischer und geologischer Daten, die zusätzlich durch eine 3D-Dichtemodellierung validiert werden. Um die thermischen und rheologischen Eigenschaften der Lithosphäre sowohl im ozeanischen als auch im kontinentalen Bereich zu entschlüsseln, wurden für diese Studie Sedimentbecken im Marmarameer im Bereich der kontinentalen Nordanatolischen Transformstörung sowie im Bereich der passiven Plattenränder von SW-Afrika (alte ozeanische Kruste) und vor Norwegen (junge ozeanische Kruste) ausgewählt.

Das Marmarameer im Nordwesten der Türkei befindet sich in einer Region, wo die dextrale Nordanatolische Störung (NAFZ) die westwärts gerichtete Ausweichbewegung der Anatolischen Platte in Richtung Ägäis ermöglicht. Geophysikalische Beobachtungen deuten darauf hin, dass die kontinentale Kruste unter dem Marmara-Becken heterogen ist, allerdings stellt diese Arbeit zum ersten Mal eine detaillierte Charakterisierung dieser lateralen Krustenheterogenitäten vor. Hierzu verwende ich verschiedene Schweredaten und die Potenzialfeldmodellierung, um drei mögliche Szenarien zur Erklärung der Unterschiede im Charakter der Kruste vorzuschlagen. Die Modelle legen nahe, dass ausgeprägte Schwereanomalien im Becken von signifikanten Dichte-Heterogenitäten innerhalb der Kruste hervorgerufen werden. Die rheologische Modellierung zeigt, dass damit verbundene Unterschiede in der Festigkeit der Lithosphäre die mechanische Segmentierung der NAFZ steuern und sich auf seismogene Prozesse auswirken. Demnach korrelieren Krustenbereiche hoher Festigkeit, die mechanisch an den oberen Mantel gekoppelt sind, räumlich mit aseismischen Sektoren in der Region um die Störungszone, in denen sich das Streichen der NAFZ ändert. Zwischen den Bereichen mit den veränderten Streichrichtungen der Störung existieren dagegen mechanisch schwächere Krustenbereiche, die vom Mantel entkoppelt und durch Kriechbewegungen gekennzeichnet sind.

Für die passiven Kontinentalränder von SW-Afrika und Norwegen wurden zwei veröffentlichte thermische 3-D-Modelle hinsichtlich des Einflusses der Temperaturverteilung auf die Festigkeit der Lithosphäre analysiert. Diese 3-D-Modelle differenzieren verschiedene Sediment-, Krusten- und Mantelbereiche und integrieren unterschiedliche geophysikalische Daten, wie zum Beispiel seismische Beobachtungen und Schwerefeldmessungen. Hier legt die rheologische Modellierung nahe, dass die derzeitige Lithosphärenfestigkeit im ozeanischen Bereich letztlich durch das Alter und vergangene thermische und tektonische Prozesse sowie die Tiefe der thermischen Grenze zwischen Lithosphäre und Asthenosphäre beeinflusst wird, während die Konfiguration der kristallinen Kruste das rheologische Verhalten der Lithosphäre in den kontinentalen Bereichen der beiden passiven Ränder dominiert.

Die thermischen und rheologischen Modelle zeigen, dass die Variationen in der Festigkeit der Lithosphäre grundlegend von der Temperaturverteilung innerhalb der Lithosphäre selbst beeinflusst werden. Dabei steuert die Zusammensetzung der Lithosphäre das heutige thermische Feld entscheidend mit und darüber auch die rheologischen Eigenschaften der Lithosphäre. Diese Ergebnisse tragen somit zu einem besseren Verständnis regionaler

tektonischer Deformationsprozesse und der dynamischen Langzeitentwicklung von Sedimentbecken bei; sie bestätigen außerdem frühere Analysen, die bereits darauf hingewiesen haben, dass die Heterogenität der Kruste in den Kontinenten mit unterschiedlichen thermischen Eigenschaften der Lithosphäre einhergeht, welches wiederum zu einer höheren Komplexität und Variabilität des rheologischen Verhaltens im Vergleich zu ozeanischen Gebieten mit einer geringer mächtigen, homogeneren Kruste führt.

Declaration of author contributions

I hereby declare that the work presented in this thesis was composed by me as the author of this dissertation and as the first author of the publications involved. These publications are referenced through the related chapters and sections. Accordingly, the numbering of the figures tables and equations were adjusted to the style of this thesis. The related bibliography and the supplementary figures for these publication are also presented at the end of the dissertation. The involved publications are listed in chronological order as follow:

I. In Section 1.4.2 and Chapter 4: "Variability of the geothermal gradient across two differently aged magma-rich continental rifted margins of the Atlantic Ocean: The Southwest African and the Norwegian margins, Solid Earth, 9, 139–158, https://doi.org/10.5194/se-9-139-2018, 2018" co-authored by Ershad Gholamrezaie, Magdalena Scheck-Wenderoth, Judith Sippel, and Manfred R. Strecker.

   - ***Author contributions.*** *EG and MSW designed the study. EG did the study of the geothermal variations and discussed the results with all co-authors. EG produced the figures and wrote the paper supported by all co-authors. All co-authors contributed to the reviewing and editing of the paper.*

II. In Section 1.4.1 and Chapter 2: "3-D crustal density model of the Sea of Marmara, Solid Earth, 10, 785–807, https://doi.org/10.5194/se-9-139-2018, 2019" co-authored by Ershad Gholamrezaie, Magdalena Scheck-Wenderoth, Judith Bott, Oliver Heidbach, and Manfred R. Strecker.

   - ***Author contributions.*** *EG, MSW, and OH designed the study. OH provided the initial model. EG did the density modeling and discussed the results with all co-authors. EG produced the figures and wrote the paper supported by all co-authors. All co-authors contributed to the reviewing and editing of the paper.*

III. In Chapter 3: "Lithospheric strength variations and seismotectonic segmentation below the Sea of Marmara, Turkey" submitted to Tectonophysics (2021) and co-authored by Ershad Gholamrezaie, Magdalena Scheck-Wenderoth, Mauro Cacace, Judith Bott, Oliver Heidbach, Marco Bohnhoff, and Manfred R. Strecker.

   - ***Author contributions.*** *EG and MSW designed the study. EG did the thermal and rheological modeling and discussed the results with all co-authors. EG produced the figures and wrote the paper supported by all co-authors. All co-authors contributed to the reviewing and editing of the paper.*

Table of Contents

Abstract i

Kurzfassung iii

Declaration of author contributions vi

Table of Contents vii

List of Figures xi

List of Tables xiii

Chapter 1: Introduction 1

1.1. State-of-the-art 2

1.2. Motivation 3

1.3. Objectives 3

1.4. Model areas 4

1.4.1. The intracontinental transform fault setting in the Sea of Marmara 5

1.4.2. The passive continental margin setting in the Atlantic 8

Chapter 2: 3-D crustal density model of the Sea of Marmara 12

2.1. Introduction 13

2.2. Method and model setup 15

2.3. Input data 18

2.3.1. Topography and bathymetry 18

2.3.2. Initial model 19

2.3.3. Geophysical data 21

2.4. Results 24

2.4.1. Initial model 25

2.4.2. Differentiated crust....28
2.4.2.1. Pre-kinematic sediments....28
2.4.2.2. Crystalline crust....29
2.4.2.3. Best-fit models....30
2.5. Interpretation and discussion of the best-fit models....34
2.5.1. High-density bodies of 3150 kg m^{-3} (Model I and Model II)....36
2.5.2. High-density bodies of 2890 kg m^{-3} (Model III)....38
2.5.3. Comparison with published 3-D density model....39
2.5.4. Model limitations....40
2.5.5. Implications....41
2.6. Conclusions....42
Chapter 3: Thermal and Rheological models of the Sea of Marmara....44
3.1. Introduction....45
3.2. 3-D geological models....47
3.3. Methods....49
3.3.1. Thermal modeling....49
3.3.2. Rheological modeling....50
3.4. Results of the thermal modeling....54
3.5. Results of the rheological modeling....57
3.6. Discussion....60
3.7. Conclusions....67
Chapter 4: Present-day thermal field of the SW African and the Norwegian passive margins....69
4.1. Introduction....70

4.2. Method 72
4.2.1. 3-D conductive thermal model 72
4.2.2. Geothermal gradient 74
4.3. Exploited models 75
4.3.1. Southwest African passive margin 75
4.3.2. Norwegian passive margin 78
4.4. Results 81
4.4.1. The onshore domain 82
4.4.2. The continental margin domain 82
4.4.2.1 The SW African passive margin 82
4.4.2.2 The Norwegian margin 83
4.4.3. The oceanic crustal domain 86
4.5. Interpretation and discussion 87
4.5.1. The onshore domain 88
4.5.2. The continental margin domain 89
4.5.2.1. The SW African passive margin 89
4.5.2.2. The Norwegian margin 90
4.5.3. The oceanic crustal domain 91
4.5.4. Implications 94
4.6. Conclusions 95
Chapter 5: Rheological models of the magma-rich continental rifted passive margins 97
5.1. Introduction 98
5.2. Results 98
5.3. Discussion 102
5.4. Conclusions 108

Chapter 6: Discussion 109

6.1. Impact of the lithospheric thermal field on lithospheric strength 110

6.1.1. The passive Atlantic continental margin setting 110

6.1.2. The intracontinental transform fault setting in the Sea of Marmara 111

6.2. Factors that control temperature distribution in the lithosphere 112

6.3. Fundamental assumptions, model sensitivities 113

6.3. Outlook 114

Chapter 7: Conclusions 115

References 117

Supplementary Figures 133

Acknowledgments 146

List of Figures

1.1: Tectonic setting of the North Anatolian Fault and the Sea of Marmara. 6
1.2: Location of the model areas of the passive margins 9
2.1: The topography and bathymetry of the Marmara model area 14
2.2: Intial strucutural model of the Sea of Marmara 16
2.3: Thickness distribution map of the initial strucutural model of the Sea of Marmara 17
2.4: Seismic data across the Sea of Marmara 20
2.5: Considered gravity datasets across the Sea of Marmara 24
2.6: Differentiated crustal structural model of the Sea of Marmara 25
2.7: Gravity responses of the structural models of the Sea of Marmara 26
2.8: Residual gravity anomaly maps for different models of the Sea of Marmara 27
2.9: Thickness of the high-density bodies 32
2.10: Cross-sections for alternative best-fit density models 33
2.11: The high-density bodies in 3-D 36
3.1: Cross-sections along the Main Marmara Fault 48
3.2: Shallow crustal geometry and results of thermal modeling of the Sea of Marmara 55
3.3: Deep crustal geometry and results of thermal modeling of the Sea of Marmara 56
3.4: Modeled lithospheric strength of the Sea of Marmara 59
3.5: Cross-sections along the Main Marmara Fault for Model I 61
3.6: Cross-sections along the Main Marmara Fault for Model II 62
3.7: Integrated crustal viscosity below the Sea of Marmara 64
4.1: The geothermal gradient calculation 72
4.2: SW African margin: cumulative thickness map and depth to top basement. 76
4.3: SW African margin: thickness of the crystalline crust and the lithospheric mantle 77
4.4: Thermal boundary conditions for the SW African thermal model 79
4.5: Norwegian margin: cumulative sediment thickness and depth to top basement 79
4.6: Norwegian margin: thickness of the crystalline crust and the lithospheric mantle 80
4.7: Thermal boundary conditions for the Norwegian thermal model 81
4.8: Geothermal gradient maps at the SW African margin 84
4.9: Geothermal gradient maps at the Norwegian margin 85
4.10: The thermal gradient variations with depth 88
4.11: Structural and thermal cross sections at the passive margins 92
5.1: Modeled lithospheric strength of the SW African passive margin 100

5.2: Modeled lithospheric strength of the Norwegian passive margin 101
5.3: Structural, thermal and rheological cross-sections of the SW African passive margin.. 105
5.4: Structural, thermal and rheological cross-sections of the Norwegian passive margin ... 106
S2.1: High resolution bathymetry within the Marmara Trough 133
S2.2: Polynomial regression to the Nafe–Drake Curve 133
S2.3: Crustal thickness based on best-fit gravity models of the Sea of Marmara 134
S2.4: Density-structural model of the Sea of Marmara from Kende et al. (2017)..... 135
S2.5: Gravity response and corresponding misfit model of Kende et al. (2017) 136
S3.1: 3-D structural input of the Sea of Marmara for thermal and rheological modeling. 137
S3.2: 3-D conductive thermal model for Model I..... 138
S3.3: 3-D conductive thermal model for Model II 139
S3.4: Observed and calculated surface heat flow and tempreture at Marmara Region 140
S3.5: Observed seismicity across the Sea of Marmara 141
S4.1: Temperature-depth distributions at the SW African margin 142
S4.2: Temperature-depth distributions at the Norwegian margin 143
S4.3: Geothermal gradient at the SW African margin 144
S4.4: Geothermal gradient at the Norwegian margin 145

List of Tables

2.1: Structural units of the Sea of Marmara and interpreted lithology 37
3.1: Thermo-mechanical properties of the geological units of the Sea of Marmara.....53
4.1: Structural units of the Atlantinc passive margins and their thermal properties 73
5.1: Mechanical properties of the geological units of the Atlantinc passive margins.....99

Chapter 1
Introduction

1.1. State-of-the-art

The publication of the predecessor of the plate-tectonic paradigm, the theory of continental drift by Alfred Wegener in 1912, triggered questions regarding the mechanical state of the lithosphere and its relation to geological phenomena. Since these early discussions and controversial ideas, topics such as lithospheric strength and the rheological behavior of the lithosphere have been subject to ongoing debate. For instance, early debates focused on the possible existence of a fluid asthenosphere underlying a strong lithosphere (Barrell, 1914) and the movement of the continents with high velocities (Wegener, 2003), while in the context of plate tectonics subsequent discussions (Le Pichon et al., 1973; Watts, 2001; Turcotte and Schubert, 2014) centered on spatiotemporal lithospheric strength variations in the context of mountain building and the formation of rifts and ocean basins (Cochran, 1980; Jackson, 2002; Burov and Watts, 2006; Burov, 2010, 2011).

Various studies of the flexural behavior of the lithosphere suggest that the rheology of the lithosphere is more complex in the continents compared to the oceanic realm (Burov and Diament, 1992; Watts, 2001; Burov and Watts, 2006; Burov, 2010, 2011). Across the oceanic domains, lithospheric strength largely resides in the mantle, and the crust is mechanically coupled with the mantle (Burov and Watts, 2006; Burov, 2010, 2011). In contrast, three major scenarios are considered to best describe the rheological behavior of the continental lithosphere (Burov and Watts, 2006). Two of these scenarios are categorized under the analogous concept of "jelly sandwich", in which a strong continental crust is mechanically coupled to or decoupled from a strong lithospheric mantle. Here, the presence of a relatively weak lower crust is key for the mechanical interactions above and beneath the Moho. In the third suggested scenario, which has been informally named the "crème-brûlée" model (Burov and Watts, 2006), the lithospheric strength resides mainly in the upper continental crust, and the lithospheric mantle is excessively weak.

Overall, considering the rheology of the lithosphere and long-wavelength deformation processes on timescales in excess of 1 Ma, jelly sandwich models are suggested to provide a better description of lithospheric strength characteristics across continental domains than the "crème-brûlée" model (Burov, 2010).

1.2. Motivation

Parameters that control lithospheric strength are of key importance in order to characterize the long-term rheological behavior of the lithosphere and its relationship with deformation processes. The lithospheric brittle strength is essentially a temperature-independent function of density and depth (Byerlee, 1978; Goetze and Evans, 1979; Ranalli, 1995; Burov, 2011). At greater depths, however, the dominant rheological behavior of rocks is characterized by non-linear viscous flow (i.e. ductile), which is mainly dependent on temperature (Goetze and Evans, 1979; Karato and Wu, 1993; Burov, 2011), but also on strain rate. Therefore, the rheological behavior of the lithosphere strongly depends on the structural configuration, the physical properties of the rocks, and temperature variations within the lithosphere. In this context one important question has been as to how the interaction of these different factors mentioned above and which parameters ultimately lead to a mechanically complex lithosphere in the continents compared to oceanic regions.

Against the background of this ongoing discussion, this dissertation aims at analyzing the influences of the physical configuration of the lithosphere in the context of the present-day thermal field and the long-term rheological conditions in sedimentary basin environments of in different tectonic settings and age of their formation. Accordingly, two principal scientific questions constitute the basis for this study:

1. Which first-order factors determine the thermal field and the strength of the lithosphere?
2. How do these factors translate into the long-term rheological behavior of the lithosphere?

1.3. Objectives

In order to answer the two principal research questions, I set out to study the thermal and rheological characteristics of the lithosphere in both oceanic and continental domains and associated with sedimentary basins in two different tectonic settings. These include (1) a basin related to an intracontinental transform fault, and (2) basins related to passive continental margins. In an attempt to include the effects of the age of the lithosphere in these considerations, the passive margin settings in the North and South Atlantic were selected for this study. Accordingly, and based on the available datasets, three distinct sedimentary basins are analyzed: The Sea of Marmara (continental transform setting), the SW African passive

margin next to an old oceanic crust, and the Norwegian passive margin, which borders young oceanic crust.

Consequently, four main objectives have guided the work during the course of this dissertation:

1. Developing a 3-D structural modeling of the Sea of Marmara (Chapter 2)
2. Calculating the 3-D thermal and rheological configuration of the lithosphere below the Sea of Marmara (Chapter 3)
3. Comparing the 3-D lithospheric thermal field models of two differently aged passive margins (Chapter 4)
4. Assessing the 3-D rheological characteristics of these two different passive margins (Chapter 5).

The principal workflow to reach the above objectives of this dissertation consisted of three main steps. First, a 3-D density model was built based on the integration of geophysical and geological data, which was subsequently constrained by 3-D forward gravity modeling. In this thesis, milligal (mGal) is used as a unit of acceleration to discuss and visualize the acceleration of Erath's gravity. In relation to the International System of Units (SI), 1 mGal (10^{-3} Gal) equals to 1×10^{-5} meters per second squared (m s^{-2}). The related methodology is explained in detail in Section 2.2. Secondly, an assessment of the 3-D conductive thermal field was carried out based on numerical thermal simulations for the structural models resulting from the previous step. Finally, the strength of the lithosphere was evaluated based on the results of thermal modeling. Both the thermal and rheological numerical modeling approaches are comprehensively described in Section 3.2.

1.4. Model areas

The initial database for this study consists of regional 3-D lithospheric-scale structural and thermal models for the SW African (Maystrenko et al., 2013) and the Norwegian passive margins (Scheck-Wenderoth et al., 2007; Scheck-Wenderoth and Maystrenko, 2008), as well as the depth to the Moho beneath the Sea of Marmara (Hergert and Heidbach, 2010). To keep the consistency with the previous studies and to build on previous results, the model areas have been kept identical to their earlier counterparts.

1.4.1. The intracontinental transform fault setting in the Sea of Marmara*

In the large-scale plate-tectonic framework of Asia Minor (Fig. 1.1a), the North Anatolian Fault Zone (NAFZ) accommodates the westward escape of the Anatolian Plate in response to the northward motion and indentation of the Arabian Plate into Eurasia and the breakoff of the slab beneath the Bitlis–Hellenic subduction zone (McKenzie, 1972; Şengör et al., 2005; Faccenna et al., 2006; Jolivet et al., 2013). This process of continental escape has resulted in numerous deformation features along the well-defined trace of the fault and along the northern flanks of the Anatolian plateau (Barka and Hancock, 1984; Barka and Reilinger, 1997; Pucci et al., 2006; Yildirim et al., 2011, 2013).

The NAFZ is a right-lateral continental transform fault that extends from the Karliova triple junction in eastern Anatolia to the northern Aegean. In its westernmost sector, the NAFZ bifurcates into three strands of locally variable strikes (Armijo et al., 1999, 2002): the northern, middle, and southern branches (Fig. 1.1b). The northern branch traverses the Sea of Marmara and forms the N70°E striking Main Marmara Fault (MMF; Le Pichon *et al.*, 2001, 2003). The approximately E–W-striking middle branch passes through the Armutlu Peninsula and continues westward along the southern coast of the Sea of Marmara; this branch changes strike to NE–SW in the southern part of the Kapıdag Peninsula (Yaltirak and Alpar, 2002; Kurtuluş and Canbay, 2007). The southern branch traverses to the south of the southern margin of the Sea of Marmara.

The region of the Sea of Marmara is an integral part of the NAFZ, which began its activity in the east approximately 13 to 11 Ma ago (Şengör et al., 2005). Although different models and timing constraints for the onset of basin formation in the Sea of Marmara have been presented in the context of the evolution of the NAFZ and the Aegean region (Armijo et al., 1999; Ünay et al., 2001; Yaltirak, 2002; Şengör et al., 2005; Le Pichon et al., 2014, 2016), offset geological marker horizons, displaced structures, and paleontological data point to a transtensional origin during the propagation and sustained movement of the NAFZ. These movements were

*This section largely corresponds to a paper published as "*3-D crustal density model of the Sea of Marmara, Solid Earth, 10, 785–807, https://doi.org/10.5194/se-10-785-2019, 2019"* and co-authored by Ershad Gholamrezaie, Magdalena Scheck-Wenderoth, Judith Bott, Oliver Heidbach, and Manfred R. Strecker.

associated with the displacement and rotations of crustal blocks after the Zanclean transgression in the Early Pliocene. Such a geodynamic scenario of transtensional dextral strike-slip faulting is compatible with space-geodetic data, the pattern of seismicity, and geomorphic indicators in the landscape (Barka and Kadinsky-Cade, 1988; Reilinger et al., 1997, 2006; Bürgmann et al., 2002; Pucci et al., 2006; Akbayram et al., 2016; Yildirim and Tüysüz, 2017).

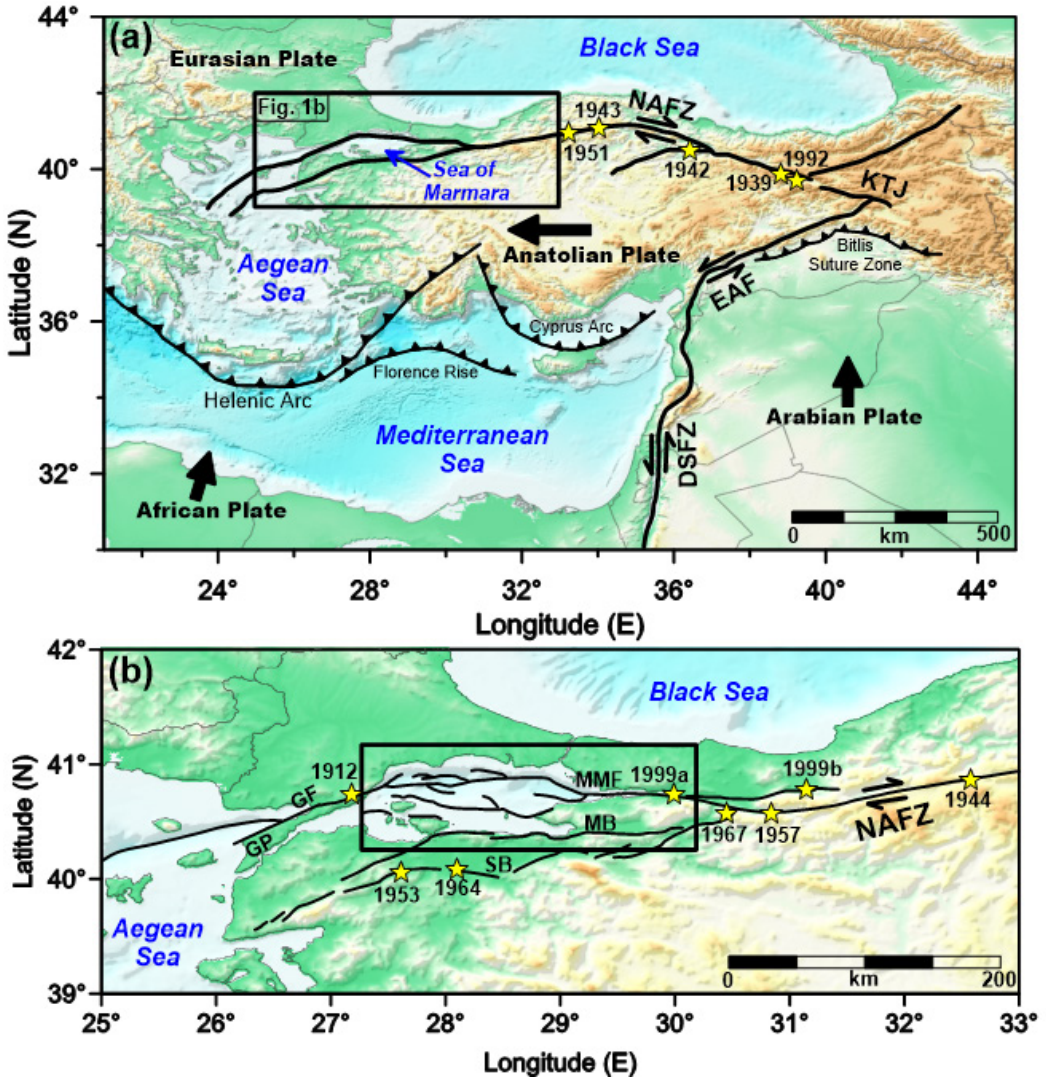

Figure 1.1: Tectonic setting of the North Anatolian Fault and the Sea of Marmara (after Hergert et al., 2011 and Gholamrezaie et al., 2019). (a) Tectonic map covering the contacts between the Arabian, African, Anatolian and Eurasian plates. Yellow stars show the epicenters of major earthquakes (Mw>6.5) during the last century (Stein et al., 1997; Barka et al., 2002). (b) The westernmost sector of the NAFZ (Armijo et al., 2002, 2005). The black box shows the model area of the Sea of Marmara. Abbreviations: North Anatolian Fault Zone (NAFZ), East Anatolian Fault (EAF), Dead Sea Fault Zone (DSFZ), Karliova triple junction (KTJ), Main Marmara Fault (MMF), middle branch (MB), southern branch (SB), Ganos Fault (GF), Gallipoli Peninsula (GP).

The NAFZ is a right-lateral continental transform fault that extends from the Karliova triple junction in eastern Anatolia to the northern Aegean. In its westernmost sector, the NAFZ bifurcates into three strands of locally variable strikes (Armijo et al., 1999, 2002): the northern, middle, and southern branches (Fig. 1.1b). The northern branch traverses the Sea of Marmara and forms the N70°E striking Main Marmara Fault (MMF; Le Pichon *et al.*, 2001, 2003). The approximately E–W-striking middle branch passes through the Armutlu Peninsula and continues westward along the southern coast of the Sea of Marmara; this branch changes strike to NE–SW in the southern part of the Kapıdag Peninsula (Yaltirak and Alpar, 2002; Kurtuluş and Canbay, 2007). The southern branch traverses to the south of the southern margin of the Sea of Marmara.

The region of the Sea of Marmara is an integral part of the NAFZ, which began its activity in the east approximately 13 to 11 Ma ago (Şengör et al., 2005). Although different models and timing constraints for the onset of basin formation in the Sea of Marmara have been presented in the context of the evolution of the NAFZ and the Aegean region (Armijo et al., 1999; Ünay et al., 2001; Yaltirak, 2002; Şengör et al., 2005; Le Pichon et al., 2014, 2016), offset geological marker horizons, displaced structures, and paleontological data point to a transtensional origin during the propagation and sustained movement of the NAFZ. These movements were associated with the displacement and rotations of crustal blocks after the Zanclean transgression in the Early Pliocene. Such a geodynamic scenario of transtensional dextral strike-slip faulting is compatible with space-geodetic data, the pattern of seismicity, and geomorphic indicators in the landscape (Barka and Kadinsky-Cade, 1988; Reilinger et al., 1997, 2006; Bürgmann et al., 2002; Pucci et al., 2006; Akbayram et al., 2016; Yildirim and Tüysüz, 2017).

In contrast, based on GPS velocity data and surface geological observations, arguments have also been put forward that the kinematics of the MMF corresponds to a pure right-lateral strike-slip fault, with the exception of the Çınarcık basin area, where the bend of the Princes' Islands segment causes a transtensional setting (Le Pichon et al., 2003, 2016).

No matter which of the two settings are valid, geophysical observations and structural models for both scenarios indicate that the present-day Sea of Marmara is underlain by two major sedimentary units: a pre-kinematic unit that predates the opening of the basin, and a second unit that is syn-kinematic with the opening of the basin (Laigle et al., 2008; Bécel et al., 2009, 2010; Bayrakci et al., 2013; Kende et al., 2017; Gholamrezaie et al., 2019). These sedimentary

units document that the regional tectonic setting has changed since the opening of the Sea of Marmara.

1.4.2. The passive continental margin setting in the Atlantic*

The locations of the modeled areas of the Norwegian passive margin and of the SW African passive margins are shown as Box A and Box B in Figure 1.2, respectively.

Passive continental margins evolve in consequence to continental rifting and breakup with the formation of new oceanic crust (White et al., 1987; Huismans and Beaumont, 2008). Rifted margins, according to the level of magmatic processes that have influenced them, are divided into two general categories: (a) magma-poor rifted margins, and (b) magma-rich (volcanic) rifted margins (Boillot et al., 1980; Sibuet et al., 1987, Whitmarsh et al., 2001; Franke, 2013). One of the typical characteristics of magma-rich passive continental margins and a major contrast to magma-poor margins, is only moderate thinning at the proximal margin, whereas crustal thinning at the distal margin is significant. As parts of the continental crust are replaced by lower crustal bodies associated with emplacement of intrusives and underplated material, the remaining ordinary crystalline crust is thinned to a few kilometers. After the rifting process has stopped, the lower crustal bodies are usually characterized by high p-wave velocities of more than 7.3 km s^{-1} (White et al., 1987; Talwani and Abreu, 2000; Lavier and Manatschal, 2006; Huismans and Beaumont, 2008; Franke, 2013). Two more characteristic features of volcanic passive margins are seaward-dipping reflectors (SDRs), interpreted as the expression of basalt flows (Hinz, 1981; Mutter et al., 1982; White et al., 1987; White and McKenzie, 1989) and usually more than 10-km-thick syn- and post-rift sediments as a result of accommodation space that has formed as a result of the combination of tectonic and thermal subsidence (White and McKenzie, 1989; Huismans and Beaumont, 2008; Franke, 2013).

The volcanic passive margin of Norway is the result of the last phase of the break-up of Pangea (55 Ma bp) during the early Cenozoic. The Norwegian margin evolved in response to the North Atlantic breakup, which is inferred to have been initiated by abnormally hot mantle, updoming and faulting associated with the Iceland plume (White, 1989; Skogseid et al., 1992; Ren et al.,

*This section largely corresponds to a paper published as "*Variability of the geothermal gradient across two differently aged magma-rich continental rifted margins of the Atlantic Ocean: The Southwest African and the Norwegian margins, Solid Earth, 9, 139–158, https://doi.org/10.5194/se-9-139-2018, 2018"* and co-authored by Ershad Gholamrezaie, Magdalena Scheck-Wenderoth, Judith Sippel, and Manfred R. Strecker.

1998). The Norwegian continental margin records several rifting phases prior to breakup that played a major role in initiating the formation of deep sedimentary basins (Skogseid, 1994; Blystad et al., 1995; Swiecicki et al., 1998; Doré et al., 1999, 2002). For instance, the deep Vøring and Møre basins in the Norwegian Sea were formed due to an earlier rifting phase at approximately 150 Ma that did not lead to continental breakup, but to the accumulation of more than 10 km of late Mesozoic deposits (Scheck-Wenderoth et al., 2007).

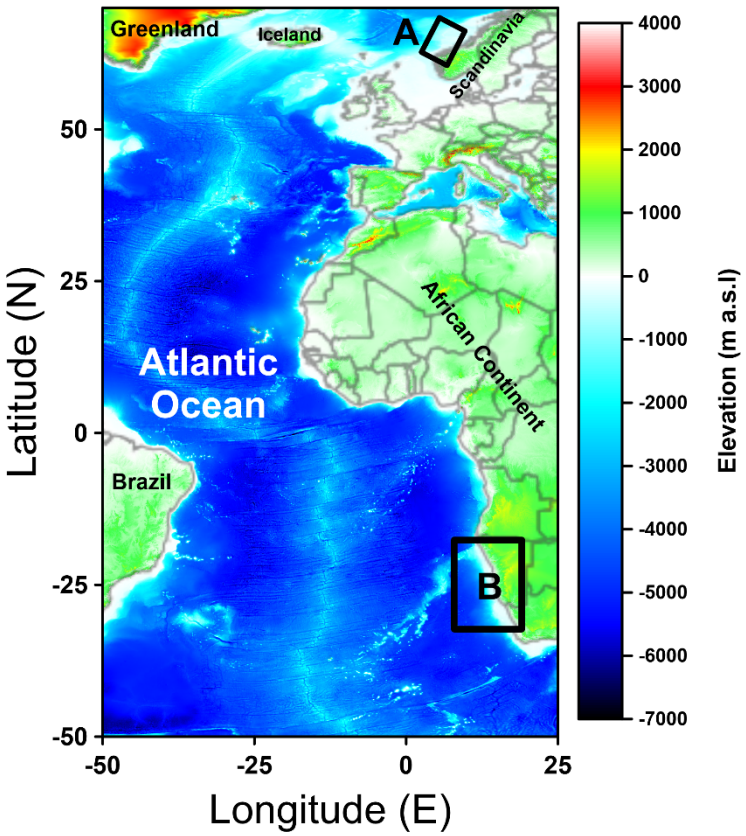

Figure 1.2: Location of the model areas of the passive margins. Box A and box B represent the model area across the Norwegian passive margin and the SW African passive margin, respectively.

In contrast, the breakup event leading to the creation of the South Atlantic and the formation of the SW African margin occurred significantly earlier than the breakup leading to the Norwegian margin formation. At about 130 Ma the continental lithosphere began rifting apart and generated the South Atlantic Ocean (Larson and Ladd, 1973; Rabinowitz and LaBrecque, 1979; Unternehr et al., 1988; O'Connor and Duncan, 1990; Nürnberg and Müller, 1991; Brown et al., 1995; Talwani and Abreu, 2000; Blaich et al., 2009). These processes were followed by post-breakup cooling, resulting in the formation of several sedimentary basins along the

margins of the South Atlantic (Stewart et al., 2000; Macdonald et al., 2003; Séranne and Anka, 2005; Dressel et al., 2016).

Both passive margin settings have similar crustal configurations: crystalline crustal rocks are exposed onshore, thick sedimentary sequences along the rifted margins are underlain by a severely thinned upper crust and are associated with high-velocity high-density lower crustal bodies and pronounced seaward dipping reflections (SDRs) that approach the continent-ocean boundary. The sedimentary units in both settings are predominantly composed of siliciclastic rocks with varying degrees of compaction (Stewart et al., 2000; Brekke, 2000; Scheck-Wenderoth et al., 2007; Scheck-Wenderoth and Maystrenko, 2008; Maystrenko et al., 2013). The crustal configuration of these sedimentary basins and their evolution during different tectonic phases has been discussed controversially (Stewart et al., 2000; Macdonald et al., 2003; Fernandez et al., 2005; Lundin and Doré, 2011; Koopmann et al., 2014; Nirrengarten et al., 2014; Gernigon et al., 2015; Dressel et al., 2016; Mjelde et al., 2016; Maystrenko et al., 2017). However, the different published concepts agree with respect to the presence of SDRs near the continent–ocean transition, the existence of a thick sedimentary succession above thin crystalline crust beneath the margins, and the presence of a high-velocity/high-density lower crustal body below the distal margins. All studies furthermore agree that the North and South Atlantic oceans are of significantly different age regarding the onset of ocean spreading processes. However, controversies emerged with respect to geodynamic concepts explaining the observed variations in subsidence rate and uplift phases during the post-rift evolution and with respect to the origin of the lower crustal high-velocity/high-density bodies. In this context, the role of mantle dynamics for post-breakup vertical movements have been especially debated. For the margins along the South Atlantic the lower crustal bodies are predominantly interpreted as the relicts of breakup-related mafic underplating (gabbros), whereas in the North Atlantic the process of underplating is just one of the different concepts that have been discussed. The bodies have been alternatively discussed in that they either represent serpentinized mantle in response to water-mantle interaction, or eclogites that are may represent remnants of earlier orogenic processes (White and McKenzie, 1989; Eldholm et al., 2000; Gernigon et al., 2004; Ebbing et al., 2006). Autin et al. (2016) have examined the thermal implications of these different hypotheses for the Argentine continental margin and concluded that a serpentinite composition would require a significantly colder thermal field, whereas eclogites and gabbros would have similar, but higher-temperature effects.

There are also some major differences between the two margins, which are related to the different times of breakup and the different post-breakup histories. The younger North Atlantic margin is bordered by a younger and thinner oceanic lithosphere and shows a thickened oceanic crust near the continent–ocean transition compared to the South Atlantic margin.

Chapter 2

3-D crustal density model of the Sea of Marmara*

*This chapter largely corresponds to a paper published as "*3-D crustal density model of the Sea of Marmara, Solid Earth, 10, 785–807, https://doi.org/10.5194/se-10-785-2019, 2019"* and co-authored by Ershad Gholamrezaie, Magdalena Scheck-Wenderoth, Judith Bott, Oliver Heidbach, and Manfred R. Strecker.

2.1. Introduction

As one of the most active plate-bounding strike-slip faults in the world (Fig. 1.1), and being located in the Istanbul metropolitan area with a population of approximately 15 million, the NAFZ has been the focus of numerous geoscientific investigations over the past decades (e.g. Ambraseys, 1970; Barka, 1996; Stein et al., 1997; Armijo et al., 1999; Şengör et al., 2005; Le Pichon et al., 2016). Several recent research programs (e.g. SEISMARMARA – Hirn and Singh, 2001: https://doi.org/10.17600/1080050; GONAF – Bohnhoff et al., 2017a: https://www.gonaf-network.org, last access: 14 May 2019; MARsite: http://marsite.eu, last access: 14 May 2019) have been embarked on to improve the observational basis for the seismic hazard assessment in the Sea of Marmara region.

The Marmara section of the NAFZ is considered to be a 150 km long seismic gap along the MMF between the ruptures of two strong events in 1912 (Mw7.3) and 1999 (Mw7.4) and is a zone of strong earthquakes (Mw7.4) with a recurrence time of approximately 250 years (Fig. 2.1); this section experienced the last earthquake in 1509 and 1766, suggesting that the fault is mature and that the potential for a large seismic event is regarded as high (Ambraseys, 2002; Barka et al., 2002; Parsons, 2004; Janssen et al., 2009; Murru et al., 2016; Bohnhoff et al., 2013, 2016a, b, 2017b). A key question is if this 150 km long seismic gap will rupture in the future in one event or in several separate events due to segmentation of the MMF, an issue that will depend a lot on the stress evolution along the strike among other forcing factors. In this regard, three-dimensional (3-D) geological models are the fundament of geomechanical models, and the distribution of density is of key importance, as density controls body forces. Density modeling is generally done by integrating geological information, seismic observations, and gravity data. Furthermore, gravity models can also help to assess the density distribution at greater depths where borehole observations and/or seismic surveys have limitations.

Our study aims to evaluate the deep crustal configuration of the Sea of Marmara and surrounding areas. To address the question of whether there is a spatial relationship between fault activity and the distribution of certain physical properties in the crust, we develop 3-D density models that integrate available seismological observations and that are consistent with observed gravity measurements. In a previous gravity modeling effort (Kende et al., 2017), an inversion method was applied to calculate the Moho depth below the Marmara region. Building on an earlier 3-D structural model developed to evaluate the stress–strain state in this region

(Hergert and Heidbach, 2010, 2011; Hergert et al., 2011), we use crustal- and regional-scale forward 3-D gravity modeling and seismic data as additional constraints. In addition, we compare and discuss our results with the previously published results of Kende et al. (2017). This comparison confirms that significant density heterogeneities are laterally present within the crust below the Sea of Marmara. In particular, we find indications for lateral density heterogeneities within the crust in the form of two local high-density bodies that may influence the kinematics of the NAFZ below the Sea of Marmara.

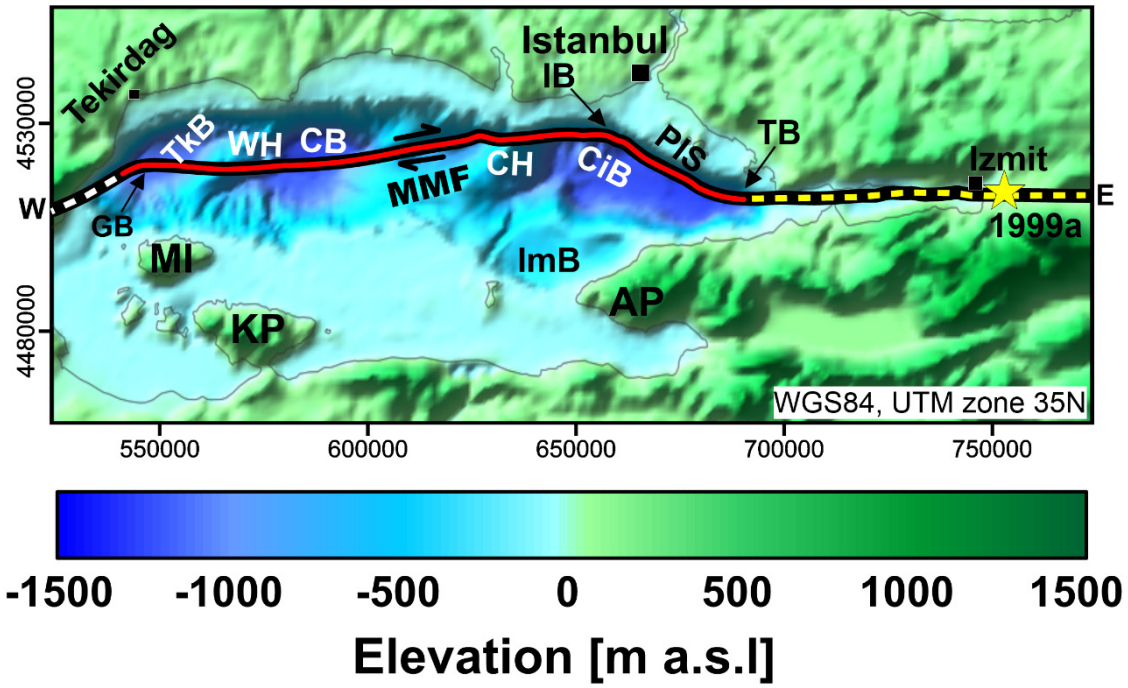

Figure 2.1: The topography and bathymetry of the model area (Le Pichon et al., 2001; Amante and Eakins, 2009). The seismic gap (red line) that has existed since 1766 (Bohnhoff et al., 2013, 2017), and the approximate ruptures (Barka et al., 2002; Bohnhoff et al., 2017) related to the major events of 1912 Ganos (pink line) and 1999 Izmit (yellow line). The yellow star represents the epicenter of the 1999 Izmit earthquake. Abbreviations: Main Marmara Fault (MMF), Princes' Islands segment (PIS), Tuzla Bend (TB), Istanbul Bend (IB), Ganos Bend (GB), Çınarcık Basin (CiB), Central Basin (CB), Tekirdağ Basin (TkB), Imralı Basin (ImB), central high (CH), western high (WH), Marmara Island (MI), Kapidağ Peninsula (KP), and Armutlu Peninsula (AP).

2.2. Method and model setup

Like for the earlier 3-D model (Hergert and Heidbach, 2010), our study area extends from 40.25° N–27.25° E to 41.15° N–30.20° E and is projected as a rectangular shape in WGS84, UTM zone 35° N, with a dimension of 250 km×100 km (Fig. 2.1). It covers the Sea of Marmara and the adjacent onshore areas as well as the city of Istanbul and the Bosporus.

The principal approach used for this study is crustal-scale 3-D gravity forward modeling to assess the density configuration of different structural units. In this methodology, the gravity response of a model is calculated and compared with gravity anomaly datasets. The model is iteratively modified to find the best fit with the data. Since the solution is not unique in gravity modeling, reducing the number of free parameters by integrating other available geophysical and/or geological data as additional constraints is required. In the spirit of this philosophy, the workflow adopted in this study consists of the following: (1) setting up an initial density model (Figs. 2.2 and 2.3) – in our case, based on the previous studies (Hergert and Heidbach, 2010, 2011; Hergert et al., 2011), (2) calculating the gravity response of this initial model and analyzing the misfit (gravity residual) between the gravity model and the input gravity data, and (3) modifying the initial model by introducing additional density variations while integrating additional constraining data to obtain the density–geometry configuration that reproduces the gravity anomaly data grid best. In general, positive residual anomalies indicate that a greater mass is required in the model to fit the gravity anomaly data, whereas negative residuals imply that the mass in the model is too large in the domain of the misfit.

3-D forward gravity modeling has been performed using the Interactive Gravity and Magnetic Application System – IGMAS+ (https://igmas.git-pages.gfz-potsdam.de/igmas-pages; Götze and Lahmeyer, 1988; Götze et al., 2015; Schmidt et al., 2011, 2020; Anikiev et al., 2021). In IGMAS+, the gravity response of a 3-D structural and density model is calculated and compared with the input gravity data over the model area. Therefore, the model has to be defined in terms of the geometric configuration of its individual structural units. In addition to geometry, information on the densities needs to be assigned to the different units of the model to calculate the gravity response. The chosen parameter combinations for the different models studied are detailed in Section 2.4. IGMAS+ provides the density–geometry configuration in the form of triangulated polyhedrons over the 3-D model domain. These polyhedrons span between 2-D vertical working sections where the model can be interactively modified (Schmidt et al., 2011). For this study, a lateral resolution of 2500m is considered, which results in 100

north–south-oriented working sections. The models extend downward to a constant depth of 50 km b.s.l., and the unit comprised between the Moho and the lower model boundary is considered to be the uniform lithospheric mantle. To avoid lateral boundary effects, the models extend, on all sides, 370 km further than the study area.

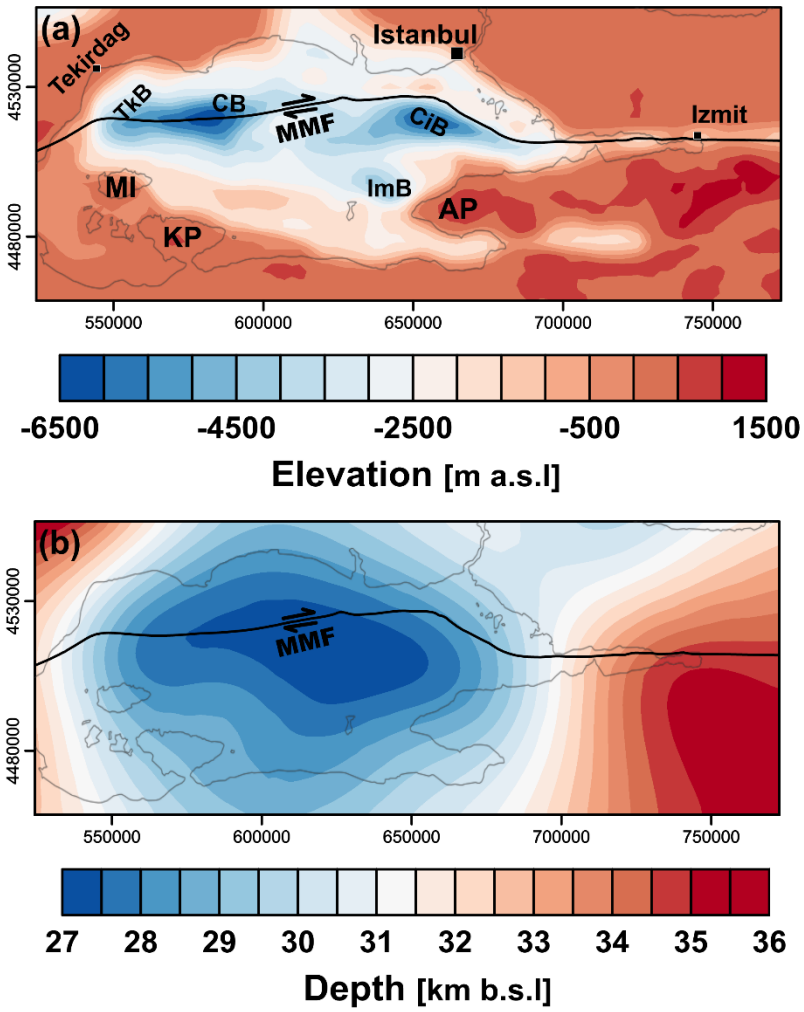

Figure 2.2: Main horizons within the initial mode; (a) depth to top basement, and (b) depth to Moho. The corresponding thickness maps are illustrated in Fig. 2.3.

Key horizons where major contrasts in density are expected are the air–water interface, the sediment–water interface, the interface separating sediments and the crystalline crust, and the crust–mantle boundary (Moho). These interfaces also are well imaged with seismic methods and can therefore easily be integrated. Internal heterogeneities within the crust may not be identified by seismic methods or may only be identified locally along individual profiles. This is where 3-D gravity modeling can be used in addition to translate velocities to densities first along the seismic section and use density modeling to close the gaps in between. This strategy together with the three-dimensionality of the calculation strongly reduces model uncertainties imposed by the general non-uniqueness of gravity modeling, as densities need to be in certain

ranges for different rock types and density anomalies at different depths produce gravity effects of different wavelengths (e.g. Schmidt et al., 2011; Maystrenko et al., 2013; Sippel et al., 2013; Maystrenko and Scheck-Wenderoth, 2013).

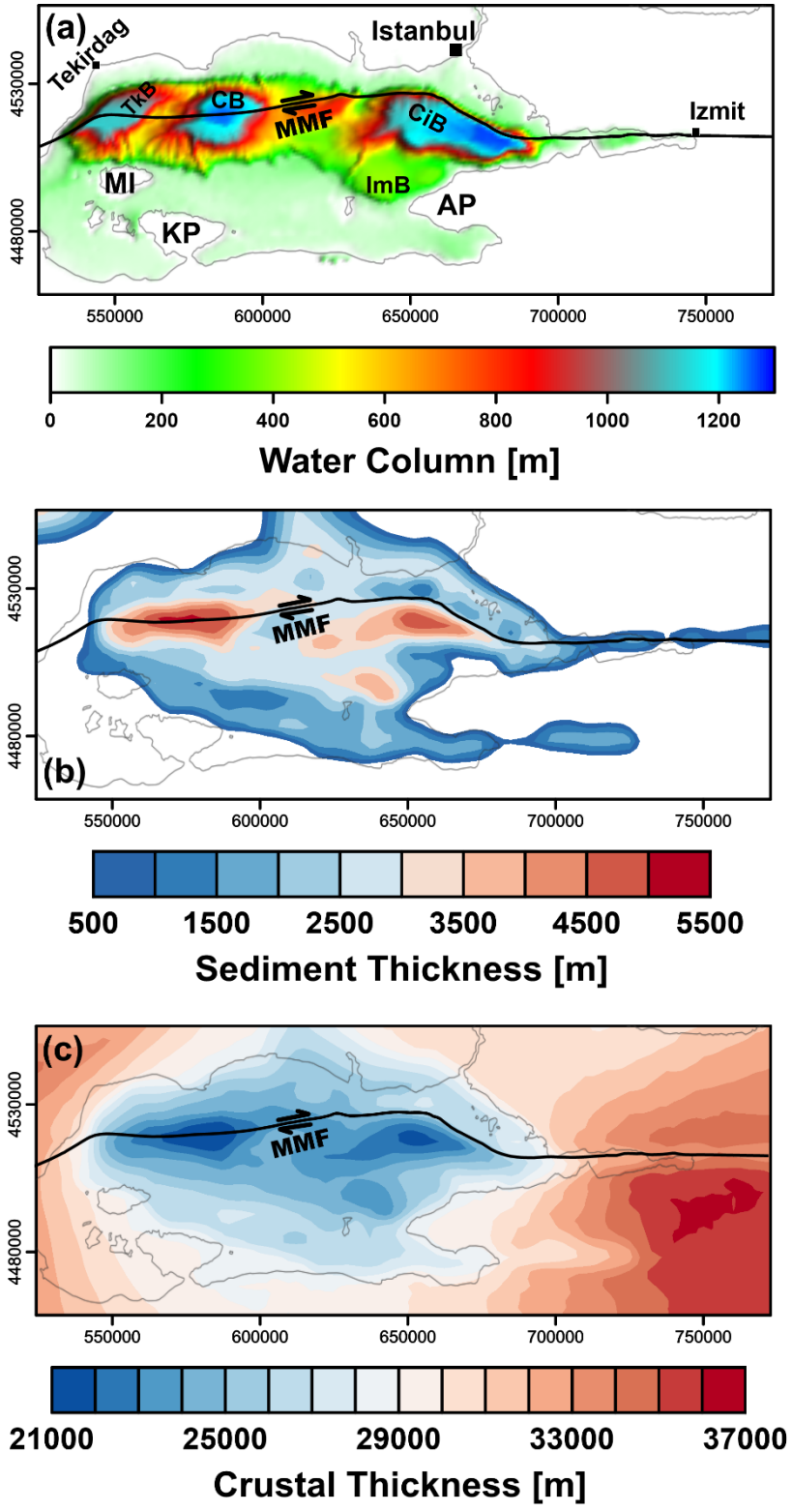

Figure 2.3: Thickness distribution map of the initial structural model; (a) seawater column, (b) syn-kinematic sediment thickness, and (c) homogeneous crustal thickness.

To assess the density variations in the deeper crust of the Sea of Marmara region, we calculate the gravity response for models of increasing complexity concerning their 3-D structural and density configuration: (1) the initial model with homogeneous crust below the sediments, (2) a more differentiated model integrating additional seismic observations for the different crustal levels below the sediments, and (3) a series of final best-fit models in which the remaining residual anomaly is minimized by implementing additional density–geometry changes in the crust but respecting the seismic data. As two different gravity datasets are available, we calculate the difference between model response and gravity anomaly data grid for both datasets.

Throughout the modeling procedure, the uppermost surface, the bathymetry (Fig. 2.1), the top-basement depth (Fig. 2.2a), and the depth to the Moho discontinuity (Fig. 2.2b) are kept fixed as defined in the initial model, since the geometries of these interfaces are well-constrained by geological and geophysical data. In all tested models, an average density of 1025 kg m^{-3} was assumed for seawater, and a homogeneous density of 3300 kg m^{-3} is assigned to the mantle below the Moho. For all gravity models presented, we define the uppermost surface of the model as the onshore topography and as the sea level offshore. Accordingly, the thickness between the sea level and bathymetry (Fig. 2.1) corresponds to the column of seawater (Fig. 2.3a) which attains the largest values in the Tekirdağ, Central, and Çınarcık basins.

2.3. Input data

The database for this study includes topography–bathymetry data, geometrical and density information from a previous 3-D structural model, seismic observations, and different sets of published free-air gravity data including the shipboard gravity dataset.

2.3.1. Topography and bathymetry

The topography–bathymetry (Fig. 2.1) was exported from the 1 arcmin global relief model (ETOPO1; Amante and Eakins, 2009). This dataset, over the study area, integrates the 30 arcsec grid obtained from NASA's Shuttle Radar Topography Mission (SRTM) and a bathymetry dataset (MediMap Group, 2005) with 1 km resolution. In addition, to increase the bathymetry resolution within the northern Marmara Trough, high-resolution multibeam (EM300) acquired bathymetry (Le Pichon et al., 2001) is integrated into the model (Fig. S2.1 in the Supplement).

Figure 2.1 shows that the present-day Sea of Marmara is surrounded by regions that are up to 1500m high. The configuration of the present-day seafloor shows that the Sea of Marmara is structured into the three main depocentres of the Tekirdağ basin, the Central basin, and the Çınarcık basin, where the water depth reaches up to 1300 m. While the axis of the Central basin is aligned along the MMF, the Çınarcık basin and the Tekirdağ basin extend only south and mostly north of the MMF, respectively. The MMF bends along the northern boundary of the Çınarcık basin, at the Tuzla bend, from an E–W-directed strike (east of the Sea of Marmara) to an ESE–WNW strike direction at the northwestern margin of the Çınarcık basin before it resumes the E–W strike direction at the Istanbul bend. The segment of the MMF between the two bends is the Princes' Islands segment. Farther to the west of the Sea of Marmara, at the Ganos bend, the MMF once more changes strike direction from E–W to ENE–WSW. There, the MMF exits the Sea of Marmara and creates the Ganos Fault segment of the NAFZ.

2.3.2. Initial model

The 3-D structural model (Fig. 2.3: Hergert and Heidbach, 2010; Hergert et al., 2011), considered to be the initial model for our study, differentiates three main horizons: (1) the topography–bathymetry (Fig. 2.1), (2) a top-basement surface (Fig. 2.2a), and (3) the Moho discontinuity (Fig. 2.2b). In their study, Hergert and Heidbach (2010), modeled the top basement geometry based on seismic observations (Parke et al., 2002; Carton et al., 2007; Laigle et al., 2008; Bécel et al., 2009, 2010) and other geophysical and geological data such as 3-D seismic tomography (Bayrakci, 2009), well data (Ergün and Özel, 1995; Elmas, 2003), and geological maps (Elmas and Yigitbas, 2001). This surface, however, has been interpreted by others as the top of Cretaceous limestone that is pre-kinematic with respect to the opening of the Sea of Marmara (Ergün and Özel, 1995; Parke et al., 2002; Le Pichon et al., 2014). Hergert and Heidbach (2010) derived the thickness of the sediments of the Sea of Marmara as the difference between bathymetry–topography and the top basement. Accordingly, their "basement" delineates the base of the sediments and not the crystalline basement. First, deep seismic surveys in the Sea of Marmara (Fig. 2.4: Laigle et al., 2008; Bécel et al., 2009) indicate that this basement is a pre-kinematic basement with respect to the opening of the Sea of Marmara. Accordingly, Laigle et al. (2008), suggests the term of "syn-kinematic" infill for the sediments above the pre-kinematic basement. We, therefore, regard these sediments as the syn-kinematic sediments and refer to the top basement of the initial model as the base syn-kinematic sediments in the following.

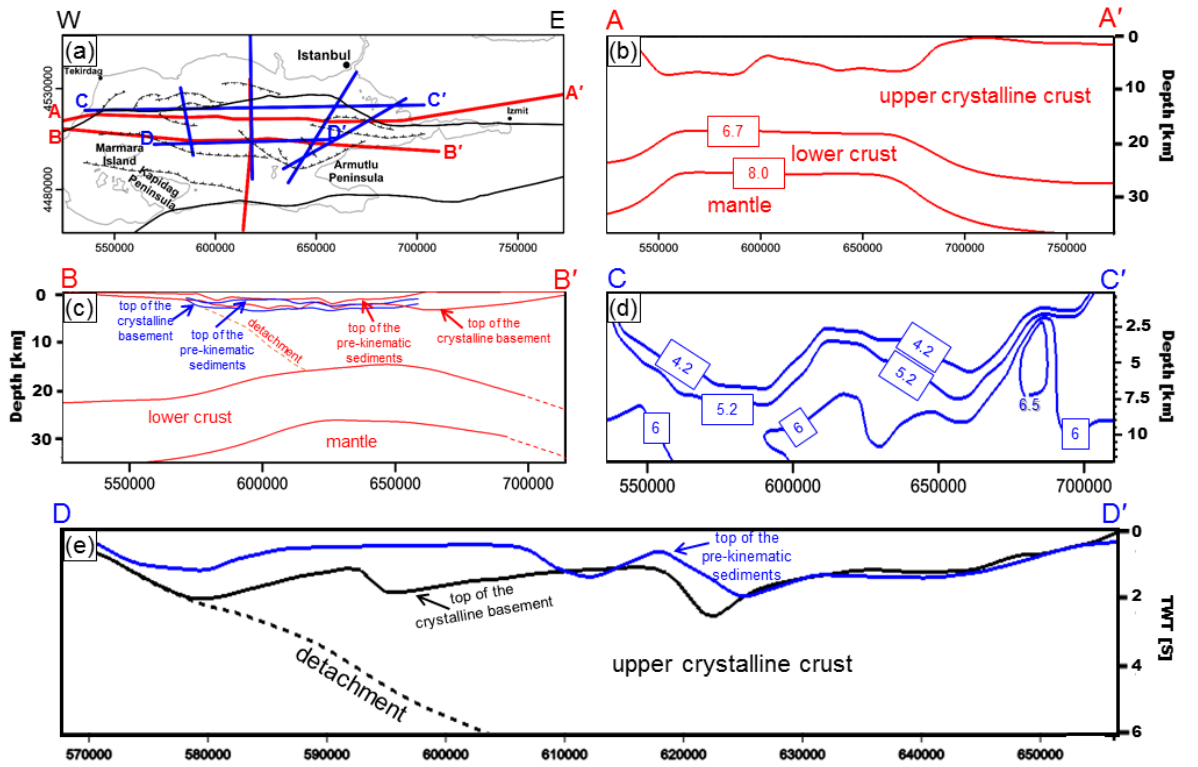

Figure 2.4: Location of seismic profiles considered in this study and corresponding P-wave velocities and interpretations (modified after Laigle et al., 2008; Bécel et al., 2009; Bayrakci et al., 2013). (a) Location of the seismic profiles. Red lines are from reflection–refraction survey (Bécel et al., 2009), and blue lines are from sediment–basement tomography (Bayrakci et al., 2013). (b) Crustal structure and depth to Moho along the AA′ cross-section. Numbers are modeled P-wave velocities for top of the lower crust (6.7 km s^{-1}) and the Moho discontinuity (8 km s^{-1}). (c) Crustal structure and depth to Moho along the BB′ cross-section, including interpretations of the tomographic results along the DD′ profile. (d) P-wave velocity contours form the tomographic modeling along the CC′ profile. Modeled P-wave velocities of 4.2 km s^{-1} and 5.2 km s^{-1} respectively represent base syn-kinematic sediments and base pre-kinematic-sediments. (e) Tomographic modeled iso-velocity of 4.2 km s^{-1} (blue line) representing top of the pre-kinematic sediments in two-way travel time along the DD′ profile, and multichannel reflection seismic interpretation form Laigle et al. (2008) on the same profile.

The syn-kinematic sediments in our model represent the deposits related to the opening of the Sea of Marmara and are interpreted to be mainly Pliocene–Quaternary infill (Laigle et al., 2008; Bécel et al., 2010; Bayrakci et al., 2013; Le Pichon et al., 2016). Accordingly, they are mostly missing in the domains outside the Sea of Marmara in response to their syn-kinematic origin. They are characterized by normal fault-bounded initial synrift graben fills overlain by postrift deposits overstepping the initial graben-like sub-basins. The full nature of the mechanical conditions for the Sea of Marmara initiation are less clear. It is even partly still debated if the initiation of the Sea of Marmara and the propagation of the MMF coincide in time. There are two competing hypotheses: (1) the Sea of Marmara opened in extension, which weakened the lithosphere such that the North Anatolian Fault propagated along the weakened domains (e.g.

Le Pichon et al., 2001, 2015), and (2) the releasing bend of the already-propagated North Anatolian Fault or a dextral step-over between the MMF and the southern fault favored local transtension, resulting in the formation of the Sea of Marmara as a pull-apart basin (e.g. Armijo et al., 2002, 2005). However, seismic information proves that there is a clear change in the tectonic regime with the opening of the Sea of Marmara (Fig. 2.4: Laigle et al., 2008; Bécel et al., 2009, 2010; Bayrakci et al., 2013). The thickness between the topography–bathymetry and the base syn-kinematic sediments represents the syn-kinematic sediment fill (Fig. 2.3b). This thickness is on average about 2.5 km over the Sea of Marmara area. Two thickness maxima indicate localized subsidence and sediment accumulation, the first maximum being aligned along the MMF where the syn-kinematic sediments are more than 5.2 km thick below the present-day Central basin and the southeastern part of the Tekirdağ basin and the second maximum being up to 5 km below the Çınarcık basin, limited to the northward direction by the MMF.

The depth to the Moho interface in the initial model (Fig. 2b) has been obtained by interpolating between various seismic data covering a larger area than the model area (Hergert et al., 2011). To constrain the Moho depth to the model area, Hergert et al. (2011) applied a Gaussian filter to adjust the local variation of the Moho depth. The Moho is distinctly shallower below the Sea of Marmara than below the surrounding onshore areas and shows doming to a depth of 27 km below the basin. Along the basin margins, the Moho is about 30 km deep and descends eastward to more than 35 km depth beneath Anatolia.

2.3.3. Geophysical data

The seismic observations considered for this study, in addition to those taken into account in the initial model, include P-wave velocity profiles from an offshore–onshore reflection–refraction survey (Bécel et al., 2009) and from a 3-D seismic tomography study focused on the sediment–basement configuration of the northern Marmara Trough (Bayrakci et al., 2013). Both studies are based on the SEISMARMARA Leg 1 seismic survey (Hirn and Singh, 2001), and the locations of the related profiles in the model area are shown in Fig. 2.4a. Three-dimensional seismic tomography modeling in the northern Marmara Trough (Bayrakci et al., 2013) indicates that the P-wave velocities vary between 1.8 and 4.2 km s^{-1} within the syn-kinematic sediments. Bayrakci et al. (2013) derive the top of the crystalline basement as an iso-velocity surface with a P-wave velocity of 5.2 km s^{-1}. In addition, relying on wide-angle reflection–refraction modeling, Bécel et al. (2009) interpreted a refractor below the base syn-

kinematic sediments with a P-wave velocity close to 5.7 km s^{-1} as the top of the crystalline basement. These seismic studies suggest that the crust beneath the syn-kinematic sediments is not homogeneous as assumed in the initial model but that there is a unit of pre-kinematic sediments beneath the syn-kinematic sediments with an average P-wave velocity of 4.7 km s^{-1} above the crystalline crust (Fig. 2.4). The pre-kinematic sediments encompass all deposits that have accumulated before the Sea of Marmara opening. In the realm of the Sea of Marmara, based on borehole observations, these deposits are separated from the syn-kinematic sediments by a diachronous unconformity that cuts units of variable age, reaching from early Cenozoic in the upper Miocene to uppermost Cretaceous (Le Pichon et al., 2014). The pre-kinematic sediments are thinned in response to the extension–transtension related to the Sea of Marmara opening that is most pronounced in the northern Marmara Trough. Onshore, surface geological observations (Ergün and Özel, 1995; Genç, 1998; Turgut and Eseller, 2000; Yaltırak, 2002; Le Pichon et al., 2014) mapped Eocene–Oligocene sediments at the northwestern and southern margins of the Sea of Marmara that might be related to the missing units below the observed unconformity within the basin.

Furthermore, Bécel et al. (2009) interpreted a reflective horizon with a P-wave velocity of 6.7 km s^{-1} and that was largely parallel to the Moho topography as the top lower crystalline crust (Fig. 2.4b and c). Moreover, multichannel seismic reflection data collected in the southwestern part of the Central basin and in the northeastern part of Marmara Island documented a 43 km long low-angle dipping reflector interpreted as a normal detachment fault cutting through the upper crystalline crust down to the lower crust (Fig. 2.4c and e; Laigle et al., 2008; Bécel et al., 2009). In brief, within the upper crystalline crust, the P-wave velocity varies from 5.7 km s^{-1} at the top of the crystalline basement to 6.3 km s^{-1} above the top of the lower crystalline crust. Lateral velocity variations (~0.3 km s^{-1}) are also observed surrounding the detachment fault in the upper crystalline crust.

The first set of gravity anomaly data grid considered in this study are based on EIGEN-6C4 (Förste et al., 2014). This dataset is a combined global gravity field model up to the degree and order of 2190, correlating satellite observations (LAGEOS, GRACE, and GOCE) and surface data (DTU 2′×2′ global gravity anomaly grid). We used the free-air gravity anomaly, downloaded with the resolution of ETOPO1 (1 arcmin), from the International Centre for Global Earth Models (ICGEM; Barthelmes et al., 2016; Ince et al., 2019). The free-air anomaly map of the study area (Fig. 2.5a) displays generally low gravity values (±20 mGal) over the

basin area, indicating that the basin is largely isostatically compensated. An exception is a pronounced negative anomaly with values as low as –80 mGal in the northwestern area of the Sea of Marmara around the MMF. Comparing the bathymetry (Fig. 2.1) with the free-air gravity anomaly map, it is evident that this negative anomaly is not related to a larger basin depth, as bathymetry is rather uniform along the entire axial part of the basin. Likewise, the basement of the syn-kinematic sediments (Fig. 2.2a) is in the same range in both sub-basins. Accordingly, the negative anomaly is not due to thickness variations of the young sediments or water depth. Apart from the onshore area next to this negative anomaly, the Sea of Marmara basin is surrounded by a chain of positive free-air gravity anomalies in a range of +70 to +120 mGal that largely correlate with high topographic elevations.

The second gravity dataset used in this study is a combined satellite (TOPEX) and marine ship gravity measurements (Fig. 2.5b; data from Kende et al., 2017). We refer to this dataset as Improved-TOPEX. The satellite dataset is based on a marine gravity model from CryoSat-2 and Jason-1, with the horizontal resolution of 2500m and ~1.7 mGal of gravity accuracy over the Sea of Marmara and the Earth Gravitational Model 2008 over the onshore areas (EGM 2008; Pavlis et al., 2012; Sandwell et al., 2013, 2014). The shipboard gravity is from the Marsite cruise survey in 2014 with a ~1m horizontal resolution. Like the gravity anomaly data from EIGEN-6C4, this combined gravity dataset shows mostly low gravity values (±20 mGal) over the Sea of Marmara and a chain of large gravity values (+70 to +120 mGal) over the onshore domain apart from the northwestern part of the model. Along the MMF, there are local negative gravity values as low as –80, –70, and –50, spatially correlating with the Central, Çınarcık, and Tekirdağ sub-basins, respectively.

The overall difference between these two datasets is a few milligals (±10 mGal); however, EIGEN-6C4 shows higher local gravity values up to 65 mGal at the southern part of the Princes' Islands segment and up to 50 mGals at the southern part of the Ganos bend (Fig. 2.5c). As shown by Kende et al. (2017), the satellite gravity dataset of TOPEX has good consistency with the processed Marsite shipboard gravity data; therefore, this discrepancy is due to the different satellite gravity datasets of TOPEX and EIGEN-6C4. In summary, and considering the discrepancy between the two datasets, it can be stated that apart from the local negative anomaly domains, the syn-kinematic sediments need to be isostatically balanced in the crust, given that the Moho topography varies on a far longer wavelength below the basin.

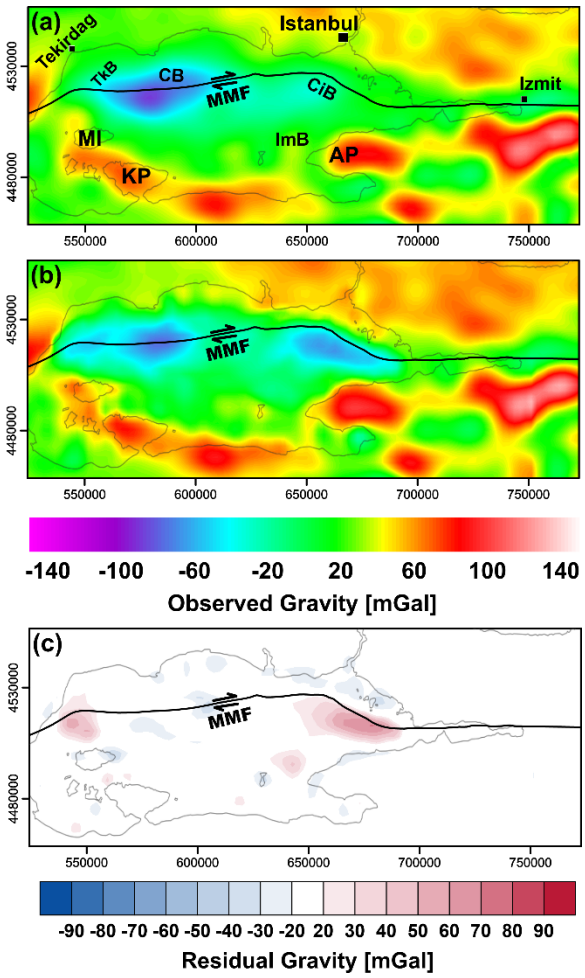

Figure 2.5: Considered gravity datasets in this study. (a) Free-air gravity anomaly map from EIGEN-6C4, a combined global gravity field model including GOCE satellite data (Förste et al., 2014). (b) Free-air anomaly map of Improved-TOPEX from Kende et al. (2017), combining the Jason-1 and CryoSat-2 satellite data (Sandwell et al., 2014) and the Marsite cruise gravity measurements over the Sea of Marmara. Onshore gravity of this dataset is based on EGM 2008 (Pavlis et al., 2012). (c) The difference between the two gravity datasets (a – b).

2.4. Results

In addition to the initial structural model with a homogeneous crustal layer below the syn-kinematic sediments (Fig. 2.3), relying on seismic profiles (Fig. 2.4), we modified the structural model differentiating three crustal layers (Fig. 2.6). Considering the two different datasets (EIGEN-6C4 and Improved-TOPEX) and the non-uniqueness in potential field modeling, a range of possible configurations were tested, and of these, we present three possible best-fit models obtained from the 3-D forward gravity modeling. These results are summarized in Table 2.1. The gravity response of these 3-D structural density models and their corresponding residual gravity anomaly for each of the two gravity datasets are shown in Figs. 2.7 and 2.8, respectively.

2.4.1. Initial model

The initial model (Hergert and Heidbach, 2010; Hergert et al., 2011) resolves only the three structural units: water, syn-kinematic sediments, and a homogeneous crust (Fig. 2.3). Hergert et al. (2011) considered a depth-dependent density gradient based on seismic velocities for the sediments and crust. The gradient profile varies from 1700 to 2300 kg m^{-3} within the syn-kinematic sediments, from 2500 to 2700 kg m^{-3} for the first 20% of the crust, and from 2700 to 3000 kg m^{-3} for the lower parts of the crust. According to this profile, we derived thickness-weighted average densities of 2000 and 2800 kg m^{-3} for the syn-kinematic sediments and the crust, respectively.

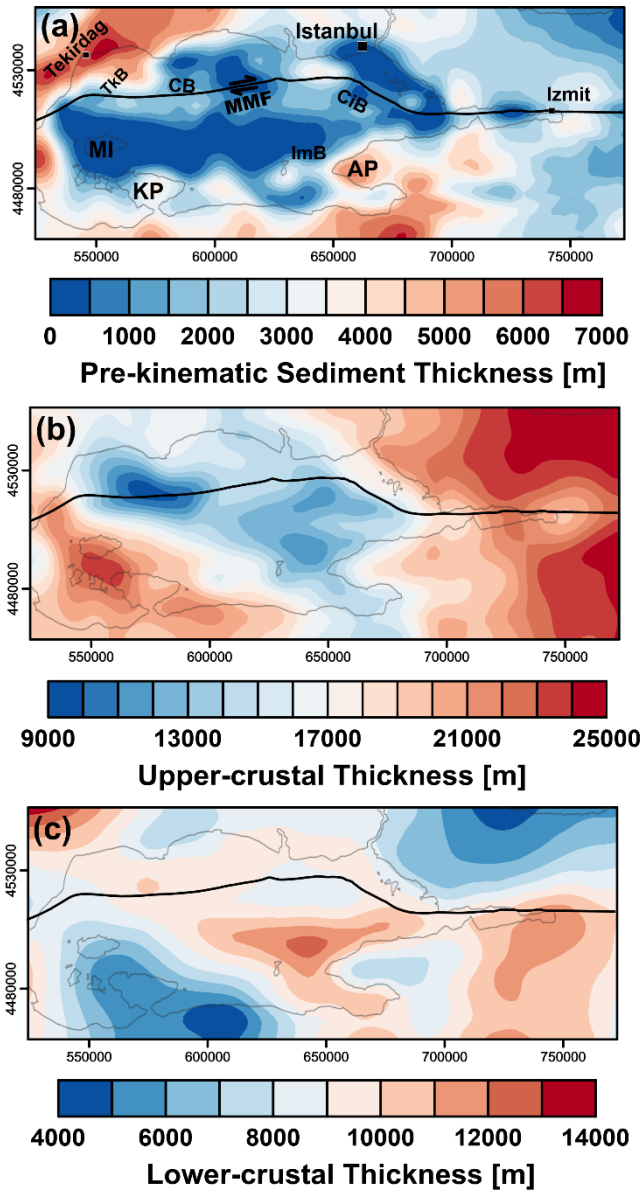

Figure 2.6: Differentiated crustal structural model integrating seismic observations along the profiles in Fig. 4. (a) Pre-kinematic sediment thickness. (b) Upper crystalline crustal thickness. (c) Lower crystalline crustal thickness.

The calculated gravity response of the initial model (Fig. 2.7a) indicates a significant misfit with respect to the gravity anomaly map of EIGEN-6C4 (Fig. 2.5a). In the eastern part of the model, the misfit between EIGEN-6C4and modeled gravity is rather small and is in the range of ±20 mGal (Fig. 2.8a). Furthermore, within the offshore domain, along the MMF, there are two local positive residual gravity anomalies with more than +90 mGal (A and B in Fig. 2.8a). These positive anomalies indicate mass deficits in the model and spatially correlate with the bends along the MMF: one occurs in the southern part of the Princes' Islands segment, between the Tuzla bend and the Istanbul bend, and the other one is present south of the Ganos bend. There is also a local short-wavelength positive residual anomaly, reaching values higher than +60 mGal at the location of the Imralı basin (C in Fig. 2.8a). In addition, a pronounced west–east-oriented continuous negative residual anomaly of around –50 mGal is detected adjacent to the southern coastline.

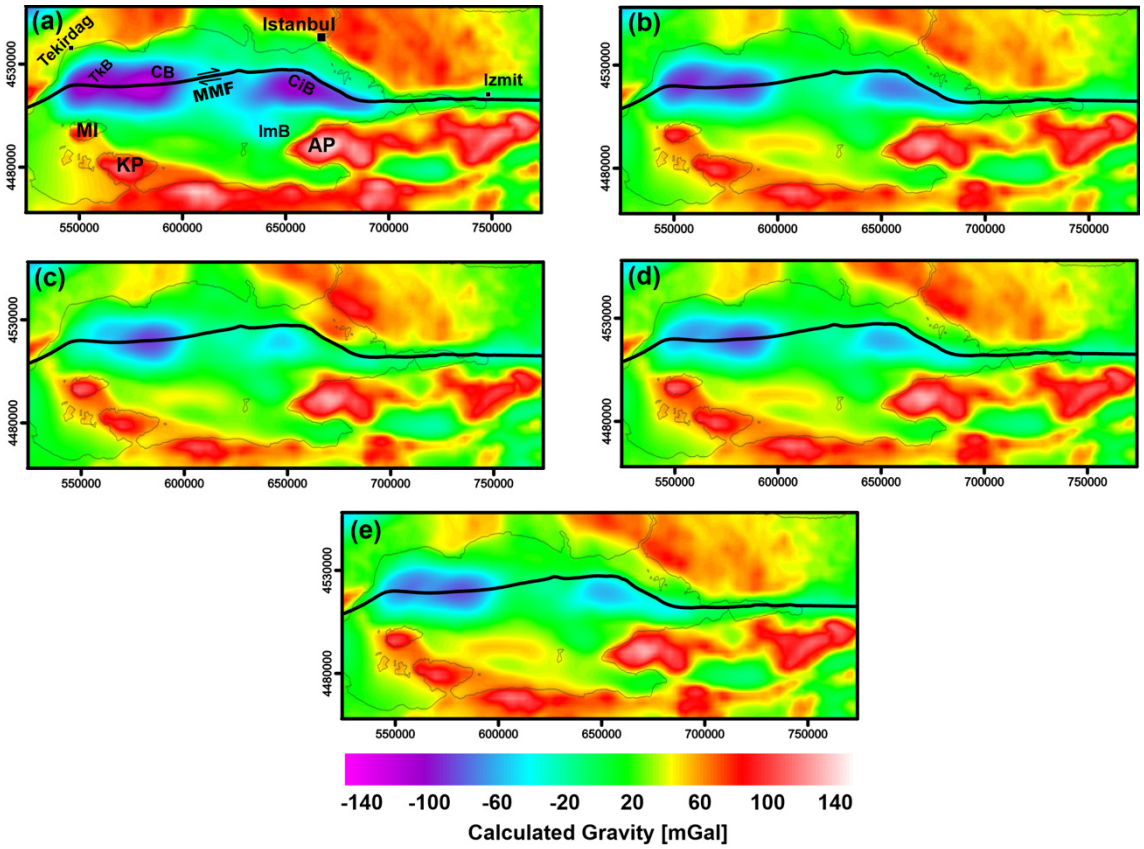

Figure 2.7: Calculated gravity over the model area. (a) Initial model gravity response. (b) Gravity response of a model with differentiated crust based on the seismic observations (Fig. 4); (c) Gravity response of Model I, the best-fit model based on the forward gravity modeling on EIGEN-6C4 (Förste et al., 2014). (d) Gravity response of Model II, the best-fit model based on the forward gravity modeling in Improved-TOPEX (Kende et al., 2017). (e) Gravity response of Model III, the alternative best-fit model based on the forward gravity modeling in Improved-TOPEX (Kende et al., 2017). The average density for the modeled high-density bodies is 3150 kg m^{-3} in Model I and Model II and 2890 kg m^{-3} in Model III. The corresponding residual gravity anomaly of each model is shown in Fig. 8.

The gravity response of the initial model shows a better fit with the gravity anomaly data of Improved-TOPEX compared to EIGEN-6C4 (Fig. 2.8b). In the onshore domain, the residual anomalies are very similar to the residual anomalies for the EIGEN-6C4 dataset. Offshore, a distinct west–east-oriented continuous positive residual anomaly of around +40 mGal is noticeable along the MMF for the Improved-TOPEX dataset. In addition, two local positive residual gravity anomalies of A and B (Fig. 2.8a) are evident up to +60 mGal for the Improved-TOPEX dataset. The short-wavelength positive residual anomaly of C previously observed across the Imralı basin (Fig. 2.8a) is also evident for the Improved-TOPEX dataset, but with a lower value of residual gravity up to +40 mGal.

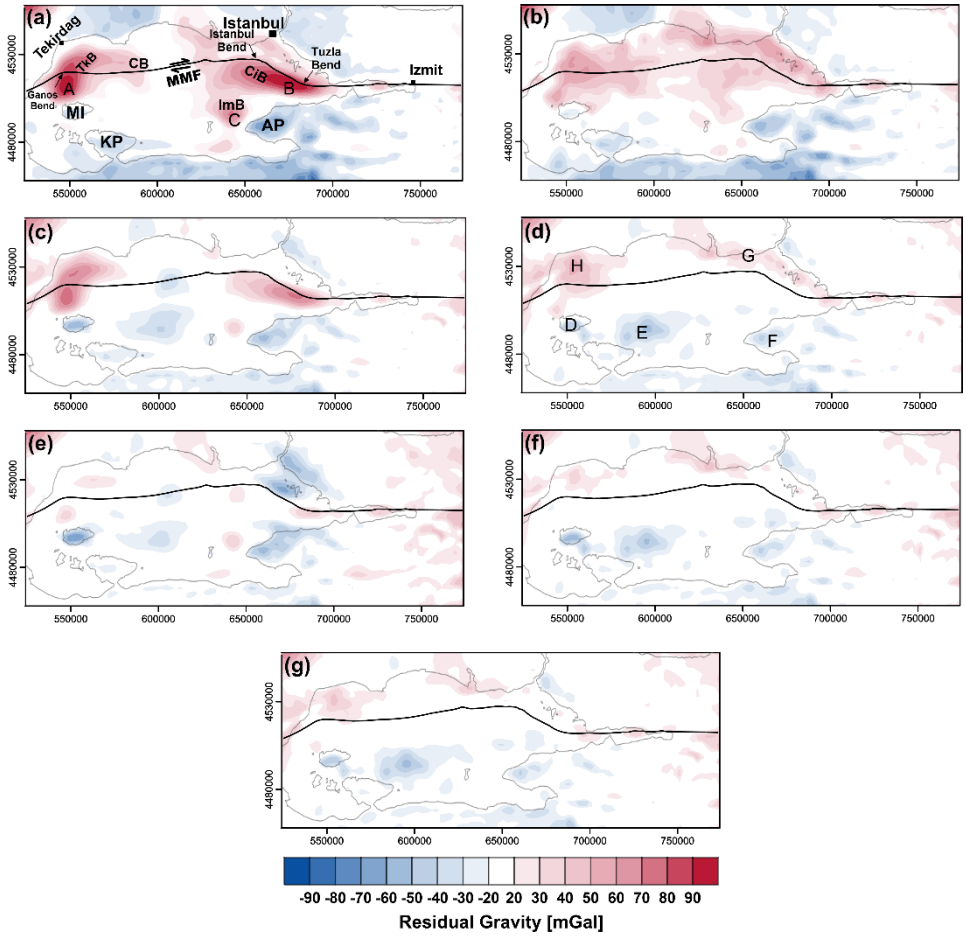

Figure 2.8: Residual gravity anomaly maps show the misfit between the gravity anomaly data (Fig. 2.5) and calculated gravity (Fig. 2.7) of different structural models across the study area. (a) Initial model to EIGEN-6C4 (Förste et al., 2014). (b) Initial model to Improved-TOPEX (Kende et al., 2017). (c) Model with a differentiated crustal unit to EIGEN-6C4. (d) Model with a differentiated crustal unit to Improved-TOPEX. (e) Model I, the best-fit model based on the forward gravity modeling in EIGEN-6C4. (f) Model II, the best-fit model based on the forward gravity modeling on Improved-TOPEX. (g) Model III, the alternative best-fit model based on the forward gravity modeling in Improved-TOPEX. The average density for the modeled high-density bodies is 3150 kg m^{-3} in Model I and Model II and 2890 kg m^{-3} in Model III.

Overall, these residuals for both gravity datasets indicate that the long-wavelength gravity field is reproduced by the initial model and that the Moho topography (Fig. 2.2b) is consistent with gravity anomaly data grid. However, the large residual anomalies of a few tens of kilometers in diameter indicate the presence of crustal density heterogeneities causing gravity anomalies of smaller wavelengths, i.e. shallower depth.

2.4.2. Differentiated crust

In addition to this indication of density heterogeneities in the crust from gravity, seismic observations (e.g. Laigle et al., 2008; Bécel et al., 2009, 2010; Bayrakci, 2009; Bayrakci et al., 2013) also point to crustal heterogeneity, expressed as distinct lateral and vertical variations in seismic velocity (Fig. 2.4). To integrate the outcomes of the seismic studies, we differentiate the crust in the next step into three units: (1) a unit of pre-kinematic sediments, (2) a unit of upper crystalline crust, and (3) a lower crystalline crustal unit.

2.4.2.1. Pre-kinematic sediments

In the initial model (Hergert and Heidbach, 2010; Hergert et al., 2011), the upper limit of the crust below the syn-kinematic sediments (their top basement) was mainly defined as pre-kinematic Cretaceous limestone (Ergün and Özel, 1995; Parke et al., 2002; Le Pichon et al., 2014): a surface corresponding to an increase in P-wave velocity to values larger than 4.5 km s^{-1}. Furthermore, Bécel et al. (2009) interpreted a top crystalline basement as a surface where P-wave velocity increases to values above 5.7 km s^{-1} based on seismic imaging. In addition, Bayrakci et al. (2013) derived the top of the crystalline crust at an iso-velocity surface of 5.2 km s^{-1} based on a 3-D P-wave tomography model beneath the northern Marmara Trough. These seismic observations justify the differentiation of an additional unit of pre-kinematic sediments. Accordingly, we implement a unit whose upper limit corresponds to the top of the pre-kinematic Cretaceous limestone (the base syn-kinematic sediments in the initial model) and whose base corresponds to the top crystalline basement (Fig. 2.6).

The top crystalline crust topography proposed by Bécel et al. (2009) and by Bayrakci et al. (2013) is similar, and the depth difference between the surfaces presented in the two studies is mostly less than 2 km (Fig. 2.4c). Therefore, we derive the geometry of the top crystalline basement for the gravity test, applying a convergent interpolation between the seismic profiles (Fig. 2.4) of Bayrakci et al. (2013) and of Bécel et al. (2009).

As the newly implemented pre-kinematic sedimentary unit represents the pre-Sea of Marmara deposits, it is mostly absent in the realm of the present-day Sea of Marmara (Fig. 2.6a). Its thickness displays maxima of up to 7.2 km along the northwestern and southern margins of the present-day Sea of Marmara and significantly decreases eastwards to less than 1.5 km.

Bayrakci et al. (2013) showed that the average velocity of the pre-kinematic sediments is around 4.7 km s^{-1}. To convert the velocity information for this unit into density, we use an empirical equation (Eq. 2.1) which is a polynomial regression to the Nafe–Drake curve valid for P-wave velocities between 1.5 to 8.5 km s^{-1} (Fig. S2.2 in the Supplement; Brocher, 2005; after Ludwig et al., 1970). Correspondingly, an average density of 2490 kg m^{-3} has been assigned to the pre-kinematic sediments, considering an average P-wave velocity of 4.7 km s^{-1}:

$$\rho\ (kg\ m^{-3}) = 1661.2V_p - 472.1V_p^2 + 67.1V_p^3 - 4.3V_p^4 + 0.106V_p^5. \quad \text{(Eq. 2.1)}$$

2.4.2.2. Crystalline crust

Apart from the unit of pre-kinematic sediments, the P-wave velocity model of Bécel et al. (2009) differentiates an additional crustal interface across which P-wave velocities increase from values of around 6.2 km s^{-1} above the interface to values higher than 6.7 km s^{-1} below the interface. They interpreted this interface as the top of the lower crystalline crust. Consequently, we applied a convergent interpolation between the seismic profiles (Fig. 2.4) of Bécel et al. (2009) to derive the top lower crystalline crust implemented into the next model. Eventually, we considered the thickness between the top crystalline basement and the top of the lower crystalline crust to be the upper crystalline crustal unit. Its thickness distribution (Fig. 2.6b) shows pronounced thickness minima below the thickness maxima of the syn-kinematic sediments, where the upper crystalline crust is less than 12 km thick. In contrast, the upper crystalline crust is up to 23 km thick below the southwestern margin of the present-day Sea of Marmara and reaches more than 25 km in thickness along the eastern margin.

Below the upper crystalline crust, a lower crystalline crustal unit is modeled, bounded to its base by the Moho discontinuity. It is characterized by an almost-uniform thickness distribution (Fig. 2.6c) of around 10 km across the Sea of Marmara. In the northwestern corner of the model area, where the Moho surface (Fig. 2.2b) descends, the thickness of the modeled lower crystalline crust reaches its maximum of up to 14 km. In contrast, this unit thins to less than 5 km below the southwestern and northeastern margins of the present-day Sea of Marmara,

where the upper crystalline crust thickens to 23 and 25 km, respectively. Offshore, adjacent to the Armutlu Peninsula, the lower crystalline crust has an increased thickness (up to 13 km) correlating with the upper crustal thinning to around 12 km.

Throughout the upper crystalline crustal unit, seismic velocities increase with depth from 5.7 to 6.3 km s^{-1} (Bécel et al., 2009). Therefore, we considered 6 km s^{-1} to be the average P-wave velocity of the upper crystalline crust. P-wave velocities for the lower crystalline crust show less variation; thus, 6.7 km s^{-1} has been adopted as the average P-wave velocity within the lower crystalline crust. The density for both crystalline crustal layers is calculated respecting the P-wave velocities (Eq. 2.1): 2720 and 2890 kg m^{-3} for the upper and lower crystalline crust, respectively.

The gravity calculated for this refined model shows a better fit with the free-air gravity datasets in comparison to the initial model (Fig. 2.8). Nevertheless, regarding the EIGEN-6C4 dataset, the three local large positive residual gravity anomalies observed for the initial model (A, B, and C in Fig. 2.8a) are still evident, indicating that the implemented subdivision of the crust alone is insufficient (Fig. 2.8c). The wavelength of the two other positive residual anomalies at A and B is too large to be caused by a high-density feature at the sedimentary fill level but too small to be a result of density heterogeneities in the mantle. Thus, we concluded that these misfits are most likely related to high-density bodies within the crystalline crust. The short-wavelength positive anomaly at location C could be interpreted as a local lack of mass within the modeled sedimentary fill of the Imralı basin.

In contrast, considering the Improved-TOPEX dataset, implementing the pre-kinematic sediments and two crystalline crustal units instead of a uniform crustal unit successfully compensate the local positive residuals of C over the Imralı basin as well as the west–east-oriented continuous positive residual anomaly along the MMF (Fig. 2.8d). However, the residual map still shows values of negative anomalies down to –60 mGal across Marmara Island, in the northeast of the Kapidağ Peninsula (offshore), and over the Armutlu Peninsula (D, E, and F in Fig. 2.8d). In addition, up to C50 mGal of positive residual anomalies are detected in the northeastern margin of the Sea of Marmara and across the Tekirdağ basin (G and H in Fig. 2.8d).

2.4.2.3. Best-fit models

To overcome the remaining misfits between the gravity response of the structural models and the gravity anomaly datasets, we incorporated additional crustal density heterogeneities during

forward gravity modeling that we tested with respect to both gravity datasets. The gravity response of the best-fit models and their corresponding residuals are shown in Figures 2.7c–e and 2.8e–g, respectively. Over most of the model area, the residual gravity anomaly (Fig. 2.8e–g) shows differences between modeled and input gravity datasets of ±20 mGal. Achieving this fit required the implementation of two dome-shaped high-density bodies of considerable dimension in the crystalline crust. Considering the differences between the two alternative gravity datasets (Fig. 2.5) and non-uniqueness of the gravity method, several configurations of these high-density bodies are plausible that differ in size or density. Here, we present three possible end-members of the high-density bodies respecting both gravity datasets: one model for EIGEN-6C4 (Model I) and two models for Improved-TOPEX (Model II and Model III).

In Model I, high-density bodies have an average density of 3150 kg m^{-3}, thus being denser than the lower crystalline crust (average density 2890 kg m^{-3}) but less dense than the mantle (3300 kg m^{-3}). They extend from the Moho upward, cutting through the lower crystalline crust and reaching into the upper crystalline crust as shallow as ~5 km depth. Accordingly, the high-density bodies attain thicknesses of up to 25 km (Figs. 2.9 and 2.10).

The position of these high-density bodies spatially correlates with the domains where the MMF bends (Figs. 2.9 and 2.11). At the western margin of the Sea of Marmara and below the Ganos bend, the high-density body cuts the lower crystalline crust at a depth of around 22 km b.s.l. and continues through the upper crystalline crust. The shallower part of this body (less than 6 km b.s.l.) is located directly to the east of the Ganos bend, where the MMF changes its strike direction from E–W to ENE–WSW. Likewise, the second high-density body is modeled beneath the Princes' Islands segment at the eastern margin of the Sea of Marmara, and the top of the body is located at a depth of around 5 km b.s.l. (Figs. 2.9 and 2.11).

By introducing the two high-density bodies into the structural model, eventually the thickness distribution of the upper and lower crystalline crust has changed below the Çınarcık and Tekirdağ basins, where the high-density bodies largely replace the crystalline crustal units (Fig. S2.3 in the Supplement). Over the rest of the model area, the thickness distribution of the crystalline crustal units is similar to the one in the model explained in Section 2.4.2.2. Remarkably, the long axis of the eastern high-density body follows the strike direction of the Princes' Islands segment (Figs. 2.9 and 2.11). In addition, a spatial correlation is evident between the location of the two high-density bodies with the position of the young depocentres

of the Çınarcık and Tekirdağ basins, as indicated by the deepest present-day bathymetry and by thickness maxima of the syn-kinematic sediments (Figs. 2.1 and 2.3).

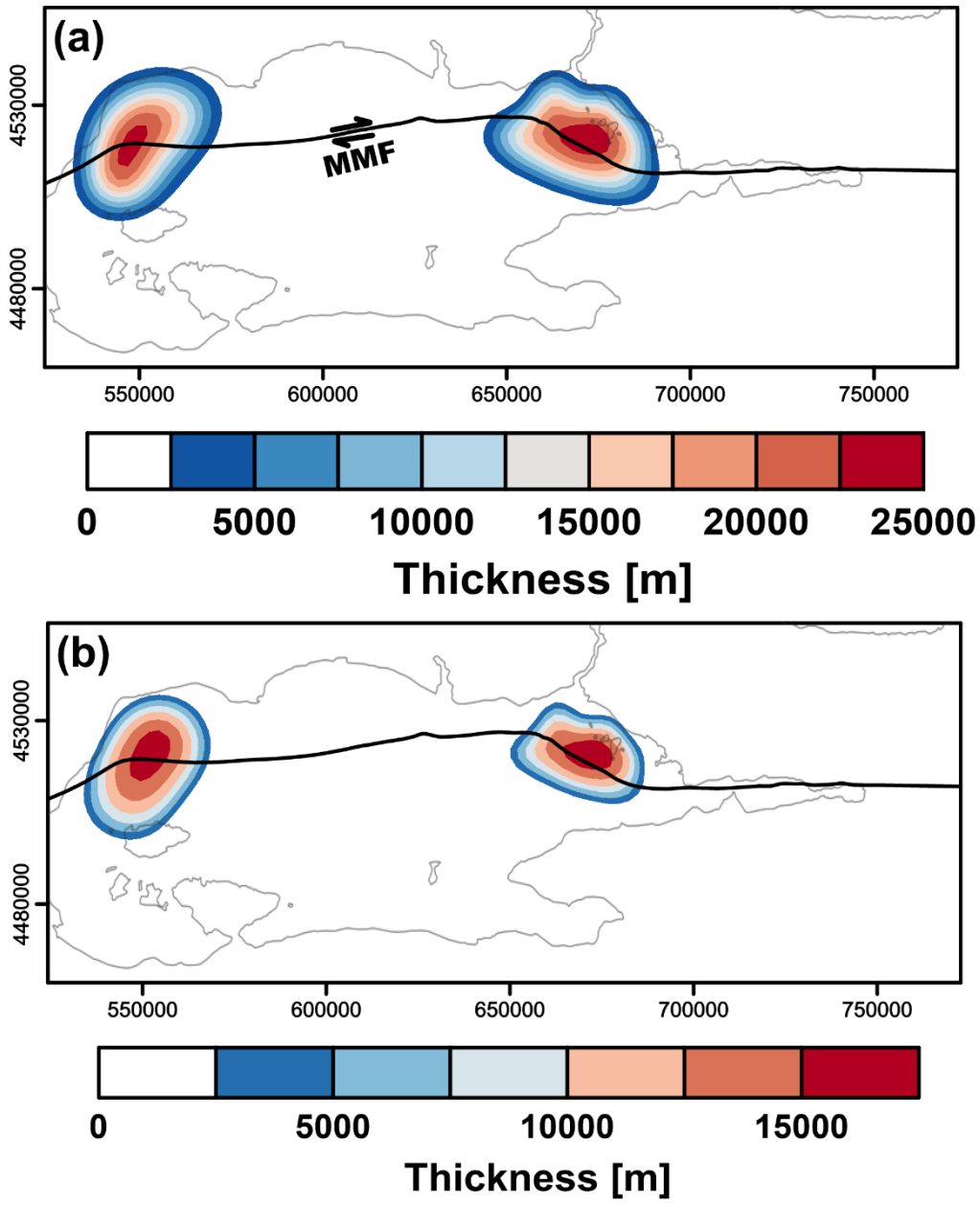

Figure 2.9: Thickness of the high-density bodies achieved from the forward gravity modeling. (a) This thickness map represents the high-density bodies that present the best fit with an average density of 3150 kg m^{-3} to EIGEN-6C4 (Model I) and of 2890 kg m^{-3} to Improved-TOPEX (Model III). (b) Thickness of high-density bodies with an average density of 3150 kg m^{-3} that shows the best-fit to Improved-TOPEX (Model II).

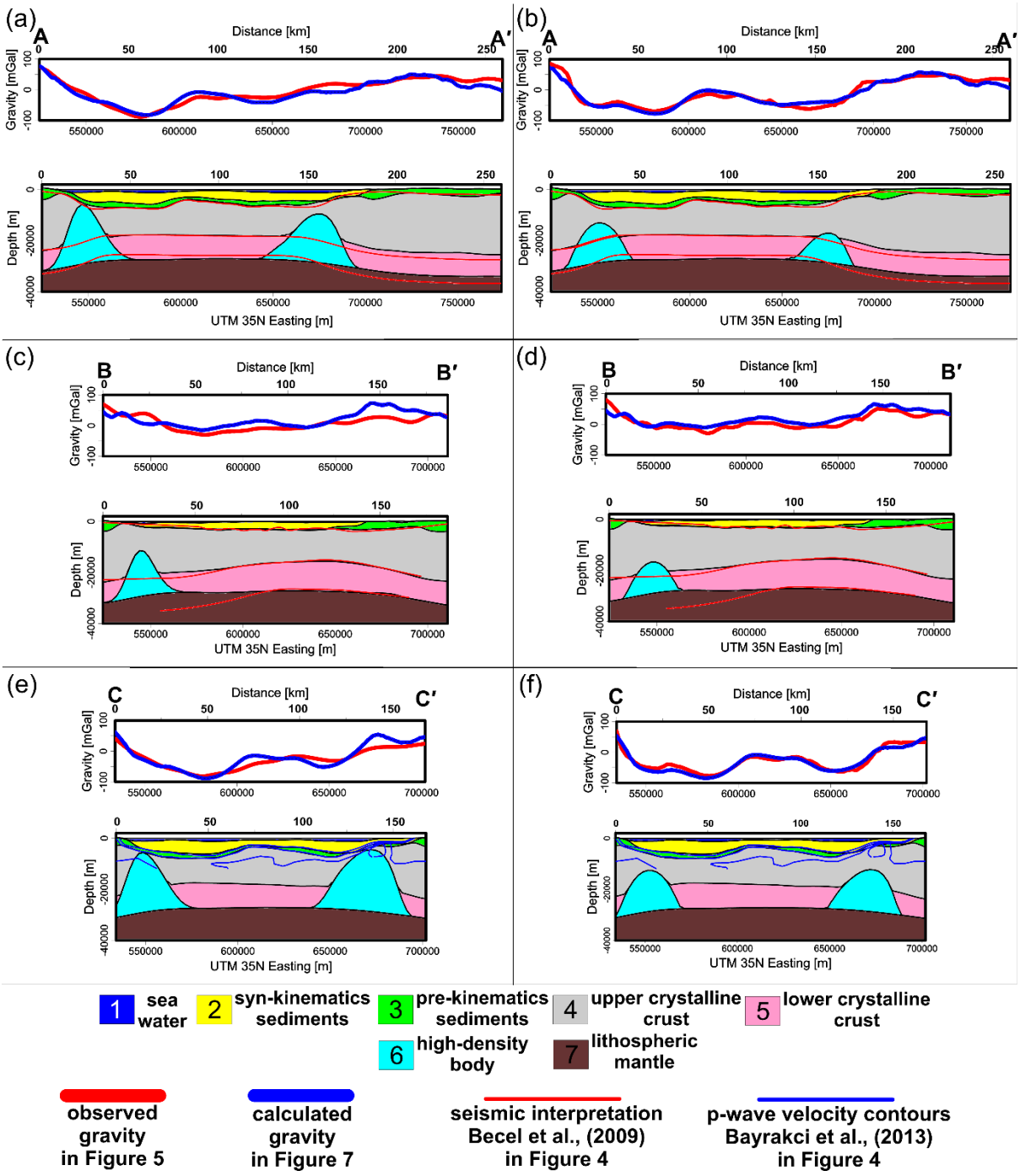

Figure 2.10: Cross-sections for alternative best-fit density models to the two different gravity datasets including high-density bodies, with an average density of 3150 kg m^{-3} (Model I and Model II) with the gravity anomaly data, the calculated gravity, and the seismic information along the AA′, BB′, and CC′ profiles in Fig. 2.4. Model I shows the best-fit gravity model to EIGEN-6C4 dataset (Förste et al., 2014) and Model II represents the best-fit gravity model to Improved-TOPEX dataset (Kende at al., 2017): (a) Model I, (b) Model II, (c) Model I, (d) Model II, (e) Model I, and (f) Model II.

Based on the Improved-TOPEX gravity dataset, however, the forward gravity modeling output (Model II) indicates that the high-density bodies need to be smaller in size for the same average density value of 3150 kg m^{-3}. The corresponding misfit between Model II and gravity data of Improved-TOPEX shows that the positive residuals of G and H are considerably reduced as well as the continuous negative residuals at the southern margin of the Sea of Marmara (Fig. 2.8f). Comparing with Model I (the best-fit model to EIGEN-6C4), these high-density bodies can be modeled for the same location, but with a smaller maximum thickness of ~16 km (Figs. 2.9, 2.10, and 2.11).

As the second end-member solution for a best-fit model to Improved-TOPEX (Model III), we test a configuration in which the geometry of the high-density bodies is identical to Model I (the best-fit model to EIGEN-6C4). Therefore, Model III has a similar structural setting to Model I. The results show that an average density of 2890 kg m^{-3}, equivalent to the value assigned for the lower crust average density, would fit the gravity response of Model III to the Improved-TOPEX dataset best (Fig. 2.8g).

In summary, all three best-fit models indicate significant lateral density variation within the crystalline crust and require the presence of two dome-shaped high-density bodies that spatially correlate with the bends of the MMF with the density ranges of ~2890 to ~3150 kg m^{-3}.

2.5. Interpretation and discussion of the best-fit models

The response of the best-fit gravity models (Fig. 2.7c–e) and their corresponding misfit (Fig. 2.8e–g) confirmed that the crust below the Sea of Marmara is characterized by significant density heterogeneities. In summary, these models resolve six crustal units with different densities that indicate different lithological settings within the crust (Fig. 2.10 and Table 2.1).

The uppermost and youngest layer is the present-day water column (Fig. 2.3a) that is largest in the present-day sub-basins of the Sea of Marmara and underlain by the unit of syn-kinematic sediments of the Sea of Marmara (Fig. 2.3b). These syn-kinematic sediments are present mainly inside the Sea of Marmara domain, and their thickness distribution indicates a subsidence regime similar to the present-day one. The relationship between the individual sub-basins of the Sea of Marmara and the course of the MMF are, however, different: the shape of the present-day Tekirdağ basin is not evident in the thickness distribution of the syn-kinematic sediments, whereas the Central basin along the MMF and the Çınarcık basin largely follow their present-day counterparts. This indicates that the differentiation in the present-day Central

and Çınarcık basins postdates the syn-kinematic phase of the Sea of Marmara. The average density of 2000 kg m^{-3} and the observed seismic velocities of 1800 to 4200 m s^{-1} (Bayrakci et al., 2013) indicate that this unit is mainly composed of poorly consolidated clastic deposits. There is, however, little information on their precise ages; suggested time intervals for the deposition of this unit range from the Late Miocene to Holocene, with a longer deposition portion of the unit assigned to the interval between Pliocene and Holocene times (Le Pichon et al., 2014, 2015).

The third modeled unit is characterized by an average density of 2490 kg m^{-3} and by observed seismic velocities of 4200–5200 m s^{-1} (Fig. 2.4d and e; Laigle et al., 2008; Bayrakci et al., 2013) representative of sediments. At the same time, the unit is largely missing below the present-day Sea of Marmara. We therefore interpret this unit as a pre-Sea of Marmara sedimentary unit above the top crystalline basement. The areas where the maximum thickness is more than 6 km are modeled for the pre-kinematic sediments (NW and S of the Sea of Marmara) coincide spatially with the location where pre-Neogene rocks are present according to surface geology (Yaltırak, 2002). Other surface geological observations (Ergün and Özel, 1995; Genç, 1998; Turgut and Eseller, 2000; Le Pichon et al., 2014) also report the presence of Eocene–Oligocene sediments at the location where the maximum thickness of the pre-kinematic sediment unit is modeled.

The sedimentary units are underlain by the upper crystalline crust, which is thinned below both the Sea of Marmara and the pre-kinematic sediments. This indicates that upper crustal thinning accompanied both phases of basin evolution. Both the modeled average density and observed seismic velocities for the upper crystalline crust indicate that this unit is dominantly composed of felsic crystalline rocks. A comparison of the average density of 2720 kg m^{-3} and average P-wave velocity of 6000 m s^{-1} (Bécel et al., 2009) of the upper crystalline crust with velocity–density pairs derived from laboratory measurements (Christensen and Mooney, 1995) indicates a composition corresponding to phyllite and/or biotite gneiss.

Below the upper crystalline crust, the lower crystalline crust follows; the top of which is largely parallel to the Moho topography. The thickness of this unit (Fig. 2.6c) indicates no clear spatial relationship with the formation of both generations of pre- and syn-kinematic basins. Here, the modeled average density and observed seismic velocities are indicative of an intermediate to mafic composition. Combining the physical properties of the lower crystalline crust (ρ = 2890

kg m^{-3} and V_p = 6700 m s^{-1}) and the property compilations of Christensen and Mooney (1995), the lithology of the lower crustal unit could be interpreted as diorite and/or granulite.

The sixth unit is the one with the largest differences in density–geometry configuration based on the forward gravity modeling to the two alternative gravity datasets. For this unit, we predict three alternative lateral density configurations that all entail two dome-shaped high-density bodies within the crystalline crust: two models with an average density of 3150 kg m^{-3} (Model I and Model II) and one model with an average density of 2890 kg m^{-3} (Model III).

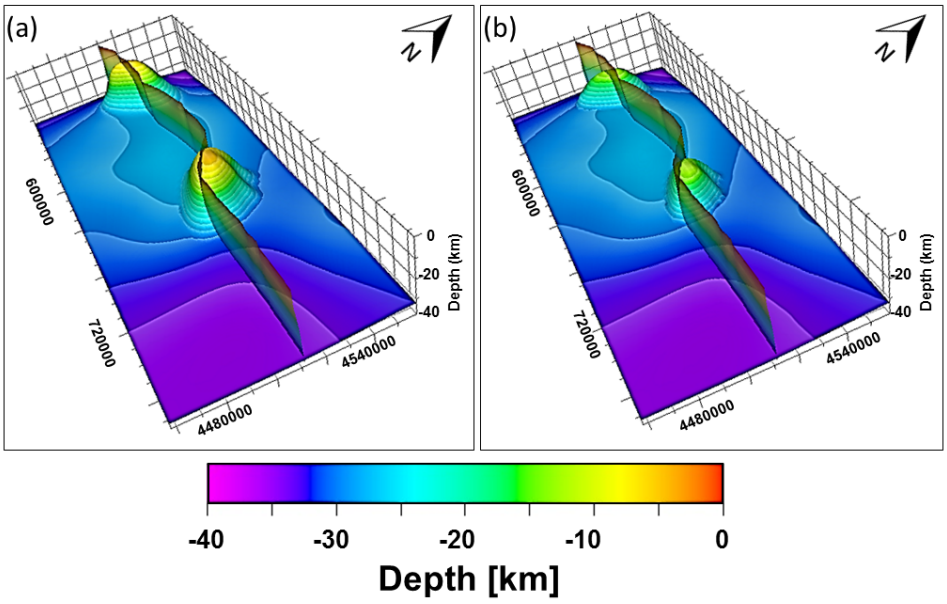

Figure 2.11: The high-density bodies' location spatially correlates with the bent segments of the MMF. (a) High-density bodies according to Model I and Model III with an average density of 3150 and 2890 kg m^{-3}, respectively; (b) high-density bodies according to Model II with an average density of 3150 kg m^{-3}. The Moho depth and the 3-D fault plane from Hergert and Heidbach (2010).

2.5.1. High-density bodies of 3150 kg m^{-3} (Model I and Model II)

In the best-fit gravity model with respect to EIGEN-6C4 (Model I), the sixth unit encompasses two high-density bodies rising from the Moho in a dome-shaped manner through both crystalline crustal layers (Fig. 2.9a). For these bodies, a rather high-density (3150 kg m^{-3}) has to be assumed, which indicates that they are of mafic composition. Considering the seismic velocity and density relationship (Eq. 2.1), a corresponding average P-wave velocity for such a high-density body with an average density would be around 7.5–7.6 km s^{-1}.

In contrast, the forward gravity modeling with respect to Improved-TOPEX (Model II) predicts that the sixth unit with the same average density value of 3150 kg m^{-3} is smaller in size (Fig. 2.9b). In both solutions, the locations of the high-density bodies correlate spatially with the location of two major bends of the MMF (Figs. 2.9 and 2.11), indicating that such a mafic composition in concert with their considerable thickness could result in greater strength compared to the surrounding felsic upper crust or the intermediate–mafic lower crust.

Table 2.1: Structural units of the Sea of Marmara and corresponding physical properties and interpreted lithology. The seismic velocity and density relationship is based on the Eq. 2.1 (Brocher, 2005). Note that the high-density bodies have not been (yet) imaged by seismic observations, and their physical properties are according to the density modelling.

Structural Units	Average P-wave Velocity (m s^{-1})	Average Density (kg m^{-3})	Lithological Interpretation
Seawater	–	1025	–
Syn-kinematic Sediments	2250 (1800 to 4200)[a]	2000 (1700 to 2300)[b]	Clastic sediments (poorly consolidated)
Pre-kinematic Sediments	4700 (4200 to 5200)[a]	2490	Sediments (consolidated)
Upper crystalline crust	6000 (5700 to 6300)[a, c]	2720	Felsic metamorphic (biotite gneiss, phyllite)[d]
Lower crystalline crust	6700[c]	2890	Intermediate to Mafic (diorite, granulite)[d]
High-density bodies	–	2890	Intermediate to Mafic (diorite, granulite)[d]
		3150	Mafic (gabbroic intrusive)[d]
Mantle	8000[c]	3300	–

[a] Bayrakci et al., 2013; [b] Hergert et al., 2011; [c] Bécel et al., 2009; [d] Christensen and Mooney, 1995

The mechanisms and timing of the emplacement of the high-density bodies are, however, difficult to determine. The modeled density indicates that the high-density bodies represent magmatic additions to the Marmara crust, potentially originating from larger depths that rose buoyantly into domains of local extension. Magnetic anomalies across the Sea of Marmara indicate positive anomalies along the MMF that may be interpreted as magnetic bodies along the fault (Ates et al., 1999, 2003, 2008). In particular, the locations of the high-density bodies beneath the Çınarcık basin correlate spatially with the maximum positive magnetic anomaly

(Ates et al., 2008), which indicates that some mafic lithology is present there below the non-magnetic sediments.

The spatial correlation between the position of the high-density bodies and the position of the eastern thickness maxima in the syn-kinematic sediments indicates that subsidence in the syn-kinematic basins at least partly took place in response to cooling of previously emplaced (magmatic) high-density bodies. This would imply that the emplacement of the high-density bodies predates the formation of the Sea of Marmara sub-basins and the propagation of the MMF. To assess the possible contribution of thermal cooling to the subsidence history of the Sea of Marmara, a detailed subsidence analysis with determination of the tectonic subsidence would be required.

As we do not have further evidence for a magmatic origin of the high-density bodies, other possible interpretations of these domains may be considered. For example, these high-density bodies could represent inherited structures of former deformation phases such as ophiolites along the Intra-Pontide suture that has been mapped on land but have not yet been explored offshore (Okay and Tüysüz, 1999; Robertson and Ustaömer, 2004; Le Pichon et al., 2014; Akbayram et al., 2017). The two different emplacement mechanisms would have opposing consequences for the propagation of the North Anatolian Fault. The magmatic origin would be consistent with crustal weakening in these domains, whereas the ophiolite origin would imply the opposite. In both cases, however, a local strength anomaly in these domains would be the consequence that could be related to the bending of the fault. Whatever the origin of these bodies, their mafic composition would imply that they represent domains of higher strength in the present-day setting.

2.5.2. High-density bodies of 2890 kg m^{-3} (Model III)

In Model III, as the alternative best-fit model for the Improved-TOPEX gravity dataset, the sixth unit has been calculated identical to the geometry of Model I (Fig. 2.9a), but with the average density of 2890 kg m^{-3}, being similar to the average density of the lower crust. This density value is consistent with the average density value of intermediate to mafic metamorphic rocks such as granulite (Christensen and Mooney, 1995). In this case, these two dome-shaped bodies may be interpreted as trapped metamorphic rocks along the Intra-Pontide suture zone that spatially correlates with the North Anatolian Fault propagation (Şengör et al., 2005; Le Pichon et al., 2014; Akbayram et al., 2017).

Several studies of exhumed orogen-related strike-slip faults indicate that dome-shaped metamorphic bodies of lower crust are a common phenomenon below transtensional pull-apart basins (Leloup et al., 1995; West and Hubbard, 1997; Jolivet et al., 2001; Labrousse et al., 2004; Corsini and Rolland, 2009). Thus the high-density bodies could represent metamorphic core complexes exhumed in response to strike-slip deformation. Such exhumation has also been proposed from numerical modeling studies across strike-slip basins such as the Sea of Marmara or the Dead Sea (Sobolev et al., 2005; Le Pourhiet et al., 2012, 2014).

2.5.3. Comparison with published 3-D density model

In a previous density modeling study, Kende et al. (2017) inverted the long-wavelength gravity signals to derive the Moho topography below the Marmara region using the same Improved-TOPEX gravity dataset that we used in our study. We also consider the same bathymetry and the same seismic dataset within the Sea of Marmara as Kende et al. (2017). The main difference between their density modeling and ours consists of the applied gravity methods. In our approach, we applied forward gravity modeling method, while Kende et al. (2017) mainly used an inversion method to compensate for the misfit between modeled and gravity anomaly data. The second principal difference is that Kende at al. (2017) considered the Moho depth to be the primary reason for the misfit. As mentioned earlier (initial model in Section 2.4.1), the depth to the Moho in our model (Fig. 2.2b) has been obtained based on various seismic data covering a larger area than the Marmara region (Hergert et al., 2011) and was kept fixed during the forward gravity modeling. In contrast, the Moho topography in Kende et al. (2017) was obtained by gravity inversion.

We have tested the full density model of Kende et al. (2017), and the results are presented as supplementary information (Figs. S2.4 and S2.5). The misfit between the previous model (Kende et al., 2017) and the gravity anomaly data of EIGEN-6C4 (Fig. S2.5) generally has the same characteristics as the misfit between our differentiated crust model (two sediment units, upper crust, and lower crust) and EIGEN-6C4 gravity dataset (Fig. 2.8c). This indicates that the two positive residual anomalies of A and B (Fig. 2.8) are not related to the sediment thickness. Specifically, it means that the local Moho uplifts in the model of Kende et al. (2017) would need to be much larger than 5 km to fit the calculated gravity if one considered the gravity dataset of EIGEN-6C4.

Comparing our results with the ones from Kende et al. (2017), we see consistent features. In particular, there is a need in both studies for a deep compensation of the sedimentary fill, and

Kende et al. (2017) propose solving this with an uplift of the Moho in the domains of our lower crustal high-density bodies. In detail, assuming a laterally uniform density of the crystalline crust, they propose ~5 km local shallowing of the Moho. In other words, Moho uplifts in their model are also high-density bodies that are 5 km thick, with a density of 3330 kg m^{-3}, which is comparable to ~16 km thick high-density bodies with an average density of 3150 kg m^{-3} or ~25 km thick high-density bodies with an average density of 2890 kg m^{-3} in our models.

2.5.4. Model limitations

The modeled upper and lower crystalline crustal units are consistent with seismic observations and velocity modeling (Figs. 2.4 and 2.10; Laigle et al., 2008; Bécel et al., 2009, 2010; Bayrakci et al., 2013). In contrast, seismic studies did not report the presence of large high-velocity bodies that would coincide spatially with the modeled high-density bodies. There are only a few indications from seismic tomography (Bayrakci et al., 2013) discriminating a zone of high P-wave velocity (V_p > 6.5 km s^{-1}) below the top crystalline basement beneath the Çınarcık basin (Fig. 2.4). This high-velocity zone approximately correlates with the top of the high-density body in this area (Fig. 2.10). In addition, other tomography results (Yamamoto et al., 2017) indicate a zone of higher S-wave velocity and slightly higher P-wave velocity at about 20 km depth b.s.l., in the area where the western high-density body cuts the boundary between the upper and the lower crystalline crust.

While the aeromagnetic maps (Ates et al., 2003, 2008) indicate a clear positive anomaly (indicative for a mafic body at depth) beneath the Çınarcık basin that spatially correlates with the eastern high-density bodies, there are no such indications for the western high-density body beneath the Ganos bend. Considering the non-uniqueness of solutions in potential field modeling, other possible solutions based on different initial models should also be contemplated beneath the Ganos bend (e.g. Kende et al., 2017; see Figs. S2.4 and S2.5 in the Supplement).

The gravity responses of the best-fit models present a good fit (±20 mGal) over most of the model area. Nevertheless, there are still some negative residual gravity anomalies across Marmara Island, in the northeast of the Kapidağ Peninsula (offshore), and over the Armutlu Peninsula (D, E, and F in Fig. 2.8). The short wavelengths of these negative residual anomalies indicate that shallow low-density features remain unresolved in the model. Regarding the negative residuals anomaly at location E, an interpretation remains difficult due to the offshore location of the anomaly. In contrast, considering the surface geological observations might help

to reveal the negative residual at the location of Marmara Island and the Armutlu Peninsula. The thickness distribution maps (Figs. 2.3 and 2.6) show that Marmara Island dominantly exposes rocks of the upper crystalline crust. More precisely, geological surface observations in this area (Aksoy 1995, 1996; Attanasio et al., 2008; Karacık et al., 2008; Ustaömer et al., 2009) differentiate three main rock types in outcrops: a Permian marble unit in the north, an Eocene granodiorite unit in the center, and a Permian metabasite in the south of Marmara Island. Considering the residual anomalies (Fig. 2.8), these three units have densities that are different from the average density assumed for the upper crystalline crust (2720 kg m^{-3}). Our result of obtaining a negative residual indicates that the subsurface extent of rocks with densities lower than the assumed average for the upper crystalline crust is larger than that of the units with higher densities. In other words, the marble would make up a larger portion of the island's subsurface than the metabasites or granodiorites.

The negative residual anomaly at Armutlu Peninsula (F in Fig. 2.8) is found where the syn-kinematic sedimentary unit is absent (Fig. 2.3b), whereas a thickening of the pre-kinematic sediments is modeled there (Fig. 2.6a). Geological maps (Genç, 1998; Yaltırak, 2002; Akbayram et al., 2016a) show that this area is mainly covered by pre-Neogene basement, Miocene acid-intermediate volcanic rocks, and some Pliocene–Holocene clastic sediments. However, the model does not account for these locally documented occurrences of syn-kinematic sediments (Pliocene–Holocene clastics) and of Miocene volcanic rocks in this domain, which, overall, could explain the negative residual anomaly.

2.5.5. Implications

The gravity modeling demonstrates that considering a homogenous crystalline crust beneath the Sea of Marmara is not a valid assumption but rather that a two-layered crystalline crust cross-cut by two large local high-density (3150 kg m^{-3}) bodies is plausible.

An interesting finding is the spatial correlation between the position of the high-density bodies and the two major bends of the MMF. If the high-density bodies represent high-strength domains of the Sea of Marmara crust, it would cause local stress deviations influencing the fault propagation direction. The 3-D view of the MMF in relation to the position of the high-density bodies illustrates how the MMF bends in these high-strength domains (Fig. 2.11). This would imply that the emplacement of the high-density bodies also predates the propagation of the North Anatolian Fault into the Sea of Marmara. Such an interpretation would support the previously proposed hypothesis that the NAFZ reached the eastern part of the present-day Sea

of Marmara (Izmit) around 4 Ma before present, when the area was a domain of distributed transtensional and/or tensional deformation, and started to propagate beneath the present-day Sea of Marmara as the MMF about 2.5 Ma ago (Le Pichon et al., 2014, 2015).

Another implication from density modeling is that the compositional and therefore also rheological heterogeneity of the Marmara crust may result in a differential response of the area to present-day far-field stresses. Accordingly, conclusions drawn from earlier studies investigating the stress–strain state in the region of the Sea of Marmara with a geomechanical–numerical model (Hergert and Heidbach, 2010, 2011; Hergert et al., 2011) need to be revised.

One of the important discussions in the area of the Marmara region is on aspects that govern the dynamics of the MMF, where a 250-year seismic gap 15 km south of Istanbul is observed. The western segment of the MMF is considered to be a partially creeping segment (Schmittbuhl et al., 2016; Bohnhoff et al., 2017b; Yamamoto et al., 2019), whereas the eastern–central segment of the MMF is thought to be locked down to 10 km depth (Bohnhoff et al., 2013, 2017b; Ergintav et al., 2014; Sakic et al., 2016). The reasons why this seismic gap of the MMF has not ruptured over the past 250 years are debated. The felsic to intermediate crustal composition deduced from our gravity model would favor creep between the two crustal high-density bodies, whereas the two domains of the high-density bodies could represent locked segments that would require high-stress levels to fail. In case of failure, however, the energy would probably be released in a strong earthquake. These high-density bodies are interpreted as mafic and therefore represent stronger material than the surrounding felsic to intermediate crustal material of the same depth. Such rheological heterogeneities would explain the distribution of different deformation modes with creeping segments in the felsic to intermediate crustal domains and locked to critically stressed segments in the mafic domains. This hypothesis could have implications for hazard and risk assessment in this area but need to be tested by geodynamic models considering thermo-mechanical principles.

2.6. Conclusions

In this study, 3-D crustal density configurations are presented for the Sea of Marmara that integrate available seismological observations and are consistent with gravity datasets. Testing successively models of increasing complexity, three best-fit models are derived that resolve six crustal units with different densities (Table 2.1). From our results, we conclude the following:

1. The present-day seafloor of the Sea of Marmara has a more complex structure than during the phase of its initiation and is divided into the three main depocentres of the Tekirdağ basin, the Central basin, and the Çınarcık basin.

2. Below the present-day seafloor, the unit of syn-kinematic sediments of the Sea of Marmara indicates that two main depocentres were subsiding during the early phase of basin formation. A lower sedimentary unit is interpreted as pre-kinematic sediments of the Sea of Marmara. The sedimentary units are underlain by a felsic upper crystalline crust that is significantly thinned below the basin. The lowest crustal layer of regional extent is an intermediate to mafic lower crystalline crust. Both crystalline crustal layers are cut by two up-doming high-density bodies that rise from the Moho to relatively shallow depths.

3. The emplacement of the high-density bodies within the crystalline crust could have a causal relationship with the basin-forming mechanism.

4. The spatial correlation between the high-density bodies with two major bends of the MMF indicates that rheological contrasts in the crust may control the propagation and movement of the MMF; these high-density bodies are a possible explanation for the bends of the MMF and support the hypothesis that the MMF is geomechanically segmented.

5. The configurations of the high-density bodies are exclusively based on 3-D forward gravity modeling, a method characterized by inherent non-uniqueness of the solutions. Only for the eastern bend, seismic and magnetic data support the presence of a deep high-density body, whereas for the western bend, such indications are missing. Therefore, further geophysical observations are required to further constrain the detailed density–geometry configuration of these bodies.

6. The high-density bodies may have an impact on the stress variability along the MMF. Thus, geomechanical models of the area should account for lateral variations in crustal density.

Chapter 3

Thermal and Rheological models of the Sea of Marmara*

* This chapter largely corresponds to an under review paper submitted as "Lithospheric strength variations and seismotectonic segmentation below the Sea of Marmara, Turkey" to Tectonophysics and co-authored by Ershad Gholamrezaie, Magdalena Scheck-Wenderoth, Mauro Cacace, Judith Bott, Oliver Heidbach, Marco Bohnhoff, and Manfred R. Strecker.

3.1. Introduction

The Marmara Region has experienced a number of strong earthquakes during the last few hundred years, indicating that the westernmost portion of the NAFZ is a mature active fault with a potential for seismic hazard that presents a high level of risk to the greater Istanbul metropolitan region (Figs. 1.1 and 2.1). The 1999 Izmit (Mw7.4) and Düzce (Mw7.1) earthquakes were the most recent strong (Mw>6.9) earthquakes in the Marmara Region (Bohnhoff et al., 2016b). The last event occurred at the easternmost tip of the Sea of Marmara and was the most recent in a sequence of strong, westward migrating earthquakes that have occurred along the NAFZ since 1939 (Stein et al., 1997; Armijo et al., 2002; Lorenzo-Martín et al., 2006) (Fig. 1.1). The MMF (Le Pichon et al., 2001, 2003) runs beneath the Sea of Marmara and represents a seismic gap (Figs. 2.1 and 3.1), with a possible recurrence interval of 250 years (Ambraseys, 2002; Barka et al., 2002; Parsons, 2004; Janssen et al., 2009; Bohnhoff et al., 2013, 2016a, 2017; Murru et al., 2016) that has not ruptured since 1766. The western limit of this seismic gap is marked by the rupture of the 1912 Mw7.4 Ganos earthquake (Figs. 1.1 and 2.1).

A key question for seismic hazard and risk assessment in this region is whether the next rupture of the MMF will result in a single large earthquake, or in a number of smaller ones due to geomechanical segmentation (Armijo et al., 2002, 2005; Yaltirak, 2002; Le Pichon et al., 2003; Hergert and Heidbach, 2011; Hergert et al., 2011; Şengör et al., 2014; Bulut et al., 2019; Gholamrezaie et al., 2019, 2020). Hergert and Heidbach (2010) reported that changes in the strike and dip of the MMF result in along-strike variations in stress loading, which would support the likelihood of geomechanically controlled segmentation. These authors assumed a homogenous rheology along the fault, which was locked to 15 km depth. However, segmentation could also be associated with variations in rock strength, and hence with the rheology of the MMF. For example, it remains uncertain which parts of the MMF are creeping and which parts are locked to a particular depth (Bohnhoff et al., 2013, 2017; Ergintav et al., 2014; Schmittbuhl et al., 2016). This question cannot be conclusively resolved using GPS data as all measuring stations are located on land and therefore too far away from the MMF along most of its length. Results from seafloor strain observations (Lange et al., 2019; Yamamoto et al., 2019) suggest that the seismic gap may include a complex system of locked and partially creeping fault segments with an accumulated slip deficit that has the potential to translate into an earthquake of Mw>7.1. Following this idea, we hypothesize that the observed segmentation

could be associated with variations in crustal rock strength, and hence with the background long-term rheology of the lithosphere along the MMF.

Understanding the structural setting of the Sea of Marmara and the interactions between the kinematics and geomechanics of the MMF is of key importance for seismic hazard and risk assessment. Geophysical observations and 3-D structural models both suggest the presence of crustal heterogeneities beneath the Sea of Marmara (Laigle et al., 2008; Bécel et al., 2009, 2010; Bayrakci et al., 2013; Kende et al., 2017; Gholamrezaie et al., 2019). Gholamrezaie et al. (2019) identified the possible existence of lateral density heterogeneities within the crust on the basis of geophysical data integration and 3-D forward gravity modeling. Their results indicate that lateral stress variability along the MMF may be due to the presence of two dome-shaped, high-density crustal bodies (see Chapter 2). The question that then arises is what effect such lithological heterogeneities beneath the Sea of Marmara have on the lithospheric strength? To answer this question, we used 3-D numerical modeling of the lithospheric thermal field and lithospheric strength for analyzing the rheology of the lithosphere beneath the Sea of Marmara and its influence on the MMF.

The main objective therefore is to estimate the yield strength of the lithosphere beneath the Marmara Region by developing static thermal and rheological models for the “end-member” structural settings from Chapter 2. To derive the YSE, the 3-D distribution of rock properties is described on the basis of structural geological models and then 3-D lithospheric-scale thermal modeling is carried out for these geological models. Then, the results from the geological and thermal modeling are used to calculate the 3-D distribution of lithospheric strength in the Marmara Region. This methodology has been used previously on both global and regional scales to investigate the static rheology of the lithosphere (Tesauro et al., 2013; Cacace and Scheck-Wenderoth, 2016).

It is therefore presented herein first-order 3-D lithospheric thermal and rheological models to discuss the implications of two different structural settings. It is shown that the lithological heterogeneities beneath the Sea of Marmara deduced from density and velocity models could account for significant thermal and rheological variations along the MMF, thus supporting the hypothesis that the segmentation of this structure is mechanically controlled. These results indicate a spatial correlation between the mechanically strongest crustal zones and the aseismic zones observed along the MMF (Wollin et al., 2018), suggesting that lateral crustal heterogeneities may in turn correlate with locked segments of the MMF.

3.2. 3-D geological models

It was shown in Chapter 2 that despite the fact of the non-uniqueness of solutions in potential field modeling, density modeling based on the two different gravity datasets indicate crustal heterogeneities beneath the Sea of Marmara. However, since the Improved-TOPEX dataset is a combined dataset of satellite and shipboard gravity observation, it may provide better resolution of the gravity anomalies across the Sea of Marmara. Therefore, the geological units that are considered for the thermal and rheological modeling are two "end-member" models based on the Improved-TOPEX gravity dataset (Model II & Model III in Chapter 2). In the following and for simplicity reasons, these models will be dubbed as Model I and Model II. Accordingly, the high-density bodies in Model I are larger in size and smaller in the average density value than their counterparts in Model II (Fig. 3.1). Consistent with the modeled densities the high-density bodies in Model I have been interpreted as intermediate to mafic gabbroic intrusive rocks and the ones in Model II as mafic granulite rocks (Table 3.1).

Both models indicate the presence of two sedimentary units beneath the Sea of Marmara, separated by a regional unconformity; the lower unit is pre-kinematic and the upper unit syn-kinematic with respect to the opening of the Marmara basin (Laigle et al., 2008; Bécel et al., 2009, 2010; Bayrakci et al., 2013; Le Pichon et al., 2014; Gholamrezaie et al., 2019). The seismic velocities (Laigle et al., 2008; Bécel et al., 2009, 2010; Bayrakci et al., 2013) and modeled densities (Kende et al., 2017; Gholamrezaie et al., 2019) beneath these sedimentary units indicate the presence of a felsic upper crystalline crust that has been significantly thinned beneath the Sea of Marmara. This felsic unit is in turn underlain by a lower, intermediate to mafic crystalline crust. Both the upper and lower crustal layers are cut by two dome-shaped, high-density bodies rising from the Moho the topography of which is imaged by various seismological data (Hergert and Heidbach, 2010). The two structural models considered differ only in the density-geometry configuration of the crystalline crust; they are identical in their sediment and mantle configurations (Fig. 3.1). Below the Moho a unit of homogeneous lithospheric mantle follows the crustal base. Accordingly, the model ends at the thermal lithosphere-asthenosphere boundary (LAB, see Section 3.3. Methods and Fig. 3.2).

The lithological interpretations (Table 3.1) are based on the observed P-wave velocities (Laigle et al., 2008; Bécel et al., 2009, 2010; Bayrakci et al., 2013) and the densities modeled for each unit (Chapter 2), together with compilations of laboratory measurements (Christensen and

Mooney, 1995). However, the lithological interpretations for the high-density bodies are based only on their modeled densities as no deep seismic velocities are available to date.

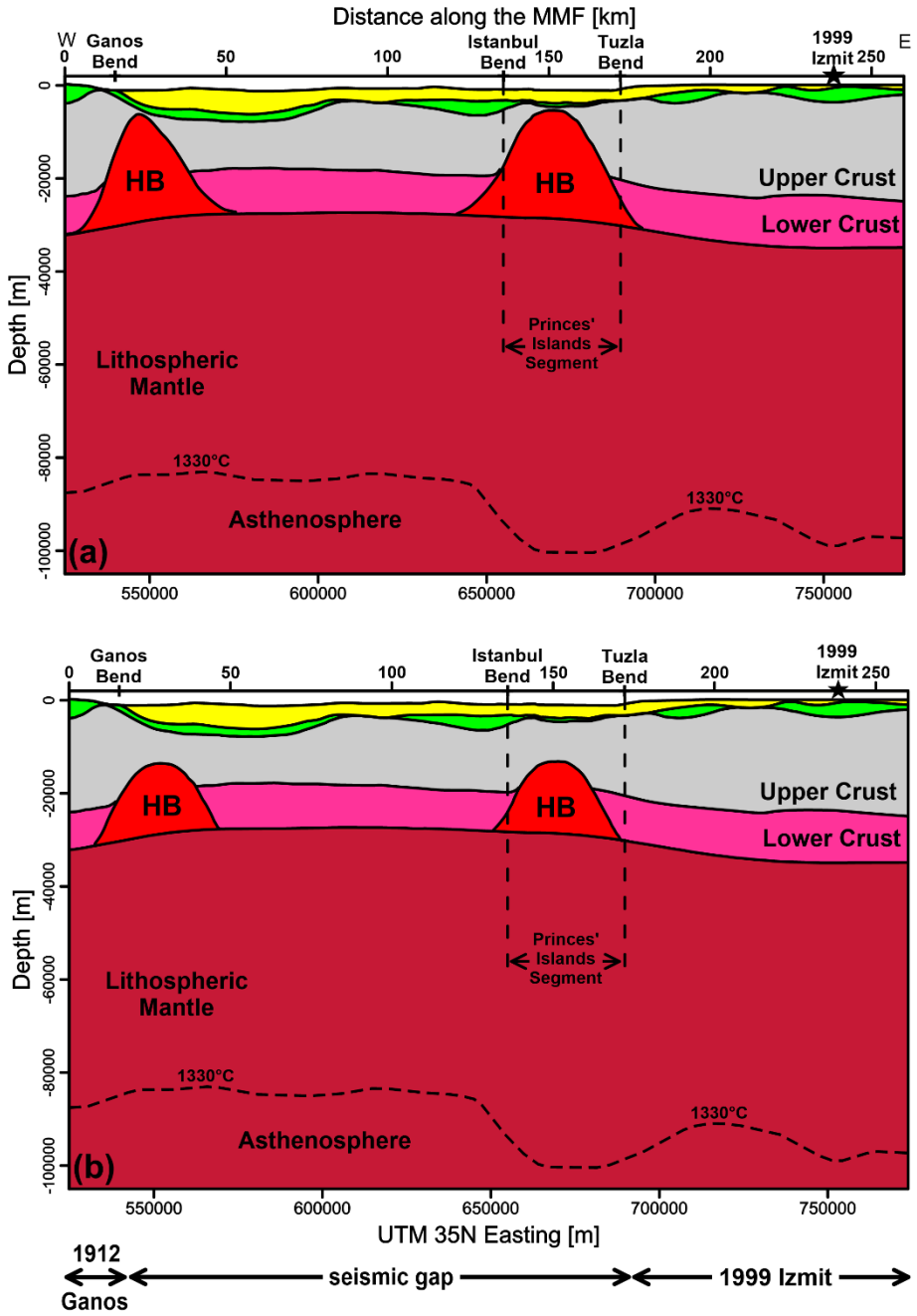

Figure 3.1: Cross-sections along the MMF from the two "end-member" structural models. (a) Model I, which includes two high-density bodies (HB) with an average density of 2890 kg m^{-3}, and (b) Model II, which also includes two high-density bodies but with an average density of 3150 kg m^{-3}. Yellow and green units represent syn-kinematic and pre-kinematic sediments, respectively. The black dashed line is the 1330°C isotherm, assumed as the thermal LAB and representing the position of the lower thermal boundary. The black star shows the epicenter of the 1999 Izmit earthquake (Barka et al., 2002).

3.3. Methods

3.3.1. Thermal modeling

The thermal modeling was based on the general assumption that conduction is the main mechanism for heat transfer within the thermally equilibrated lithosphere. According to Fourier's law, the heat transfer equation in a steady-state system is

$$\nabla.(\lambda\nabla T) + S = 0, \qquad \text{(Eq. 3.1)}$$

where S is the radiogenic heat production, λ is the thermal conductivity, and ∇T is the temperature gradient.

For the thermal modeling parametrization, constant values of average radiogenic heat production and average bulk (solid plus fluid) thermal conductivity were assigned to each geological unit (Table 3.1). These thermal properties were assigned taking into account the lithological interpretations from the 3-D density models and corresponded to published values based on laboratory measurements (Cermak and Rybach, 1982; Seipold, 1992; McKenzie et al., 2005; Vilà et al., 2010).

Thermal boundary conditions were required to finalize the thermal model setup. The lateral boundaries were set to be closed to heat flow. For the upper thermal boundary condition, a constant value of 15°C was assigned to the topography-bathymetry surface (Fig. 2.1). This value represents an average annual surface temperature in the Marmara Region and is in agreement with the measured seafloor temperature in the Sea of Marmara (Henry et al., 2007).

The lower thermal boundary condition was defined as the depth of the 1330°C isotherm (Fig. 3.2) derived from modeled S-wave velocities (Fichtner et al., 2013) using the *VeloDT* program (Meeßen, 2018), which is an implementation of the empirical approach of Priestley and McKenzie (Priestley and McKenzie, 2006). To define a lithospheric-scale model, the lower boundary condition was assumed to represent the thermal lithosphere-asthenosphere boundary (LAB). The material between the Moho and the lower boundary condition was therefore treated as homogeneous lithospheric mantle.

Finally, the steady-state conductive thermal field (Eq. 3.1) was numerically solved in 3-D by using the Finite Element Method as implemented in the software Golem (Cacace and Jacquey, 2017; Jacquey and Cacace, 2017). The resolution of the model is 2,500 meter horizontally, that

is identical to the input structural models. The vertical resolution, however, depends to the variable thickness (Fig. 3.1) of the modeled structural units.

3.3.2. Rheological modeling

The rheological modeling was based on three main equations, these being for Byerlee's law (Equation 3.2), for power-law creep (Equation 3.3), and for Dorn's law creep (Equation 3.4):

$$\Delta\sigma_b = f_f\, \rho_b g z\left(1 - f_p\right) \qquad \text{(Eq. 3.2)}$$

$$\Delta\sigma_d = \left(\frac{\dot{\varepsilon}}{A}\right)^{\frac{1}{n}} \exp\left(\frac{Q}{nRT}\right)$$

$$\Delta\sigma_d = \sigma_0 \left(1 - \left[-\frac{RT}{Q_D} \ln \frac{\dot{\varepsilon}}{\dot{\varepsilon}_0}\right]^{\frac{1}{2}}\right)$$

In the Byerlee's law equation (Eq. 3.2), $\Delta\sigma_b$ is the brittle yield strength, f_f is the Byerlee's friction coefficient, ρ_b is the bulk density, g is the gravitational acceleration, z is the depth (below the ground surface) and f_p is the pore factor, which was considered to have a constant value of 0.37. In the creep equations (Eqs. 3.3 and 3.4), $\Delta\sigma_d$ is the ductile strength, $\dot{\varepsilon}$ is the reference strain rate, A is the power-law strain rate, n is the power-law exponent, Q is the activation enthalpy, R is the gas constant (8.314 $JK^{-1}mol^{-1}$), T is the absolute temperature, σ_0 is Peierls' critical stress, Q_D is the Dorn's law activation energy, and $\dot{\varepsilon}_0$ is the Dorn's law critical strain rate.

According to Byerlee's law (Eq. 3.2), the lithospheric brittle strength is essentially a temperature-independent function of density and depth (Byerlee, 1978; Ranalli, 1995; Burov, 2011). At greater lithospheric depths, however, the dominant rheological behavior of rocks is non-linear viscous flow, which is mainly temperature-dependent (Karato and Wu, 1993; Burov, 2011). Dorn's law has been shown to provide a better estimate of the solid-state creep in the lithospheric mantle (Goetze, 1978; Goetze and Evans, 1979). Dislocation creep in the crustal layers was therefore defined on the basis of the power-law (Eq. 3.3) while creep in the lithospheric mantle was considered to be based on Dorn's law (Eq. 3.4). The temperature variable for the strength calculations was derived from the modeled temperature distributions. We calculated the brittle strength with Byerlee's law, using the bulk densities from the 3-D density models (Table 3.1). The load of the seawater column (ρ = 1025 kg m^{-3}) was also taken

into account as an initial pressure on the seabed. The Byerlee friction coefficient ranges between 0.6 to 0.85 for an extensional environment (Byerlee, 1978) and a constant average value of 0.75 was therefore used to model the brittle strength.

The reference strain rate ($\dot{\varepsilon}$ in Eqs. 3.3 and 3.4) is the derivative of the strain function over the time:

$$\dot{\varepsilon} = \frac{d}{dt}\,\varepsilon(t) = \frac{v(t)}{L_0} \qquad \text{(Eq. 3.5)}$$

where $\varepsilon(t)$ is the strain change over the time, $v(t)$ is the speed (slip rate), and L_0 is the original length (i.e., the width of the modeled area). By considering the entire 100 km width of the modeled area and using a slip rate for the MMF(Le Pichon et al., 2003; Flerit et al., 2004; Reilinger et al., 2006; Hergert and Heidbach, 2010) of 12.8 to 24.8 mm yr^{-1}, the average reference strain rate calculated for the modeled area was about 10^{-14} s^{-1}.

The mechanical parameters assigned to the structural units were chosen on the basis of the interpreted physical properties of the modeled units and laboratory measurements on their reference rheological equivalents (Table 3.1). For the calculation of glide creep in the lithospheric mantle, the values of the Dorn's law rheological parameters were considered to be constant values (8.5×10^9 Pa for the Peierls' critical stress, 5.7×10^{11} s^{-1} for the critical strain rate, and 535 kJ mol^{-1} for the activation energy (Burov, 2011).

In order to visualize the rheological modeling results, the YSE was calculated as a minimum function of the brittle and ductile strengths (Eq. 3.6). We also vertically integrated the modeled strength over the entire thickness of the lithosphere and crust (Eq. 3.7), and calculated the ratio between the integrated crustal strength and the total lithospheric strength.

$$\mathrm{YSE} = \min(\Delta\sigma_b, \Delta\sigma_d). \qquad \text{(Eq. 3.6)}$$

$$\sigma(z) = \int_{z_0}^{z_l} \min(\Delta\sigma_b, \Delta\sigma_d)\, dz. \qquad \text{(Eq. 3.7)}$$

Within the crustal domain, the effective viscosity (η_{eff}) can be parameterized based on the thermally activated power-law dislocation creep (Eq. 3.3). Accordingly, the efficiency of viscous creep in Figure 3.7 was calculated based on the following equation:

$$\eta_{eff} = \frac{2^{\frac{1-n}{n}}}{3^{\frac{1+n}{2n}}} A^{(-\frac{1}{n})} \dot{\varepsilon}^{(\frac{1}{n}-1)} exp\left(\frac{Q}{nRT}\right) \quad \text{(Eq. 3.8)}$$

We used a C++ script, based on the previous work of Cacace and Scheck-Wenderoth (2016), to numerically calculate the lithospheric strength and to obtain the related results.

Table 3.1: Thermo-mechanical properties of the modeled geological units based on the interpreted lithologies and compilations of corresponding laboratory measurements.

Modeled geological unit	Syn-kinematic sediments	Pre-kinematic sediments	Upper crystalline crust	Lower crystalline crust	High-density bodies (Model I)	High-density bodies (Model II)	Mantle (lithospheric)
Dominate lithology [a]	Clastic (poorly consolidated)	Clastic & chemical (consolidated)	Felsic (granite, gneiss)	Intermediate to mafic (gabbroic rocks)	Intermediate to mafic (gabbroic intrusive)	Mafic (mafic granulite)	-
Average bulk density (ρ)[kg m^{-3}] [b]	2000	2490	2720	2890	2890	3150	3300
Bulk thermal conductivity (λ) [W m^{-1} K^{-1}]	2.00 [c]	2.80 [c]	3.00 [d]	2.50 [c]	2.50 [c]	2.00 [d]	3.50 [e]
Radiogenic heat production [(f)] (S) [μW m^{-3}]	1.00	0.50	3.10	0.25	0.25	0.15	0.01
Reference rheological type	Brittle rocks	Brittle rocks	Granite dry [g]	Diabase dry [g]	Diabase dry [g]	Mafic granulite [h]	Olivine dry [i]
Activation enthalpy (Q)[kJ]	–	–	186	276	276	445	510
Power-law exponent (n)	–	–	3.30	3.05	3.05	4.20	3.00
Power-law strain rate (A) [Pa^{-n} s^{-1}]	–	–	3.16E-26	6.31E-20	6.31E-20	8.83E-22	7.00E-14

[a] Christensen and Mooney (1995), [b] 3-D density modeling (Chapter 2), [c] Čermák and Rybach (1982), [d] Seipold (1992), [e] McKenzie et al. (2005), [f] Vilà et al. (2010), [g] Carter and Tsenn (1987), [h] Wilks and Carter (1990), [i] Goetze and Evans (1979).

3.4. Results of the thermal modeling

Figures 3.3 and 3.4 illustrate the main features of the modeled thermal field; additional temperature-depth maps can be found in the Supplementary Information (Figs. S3.2 and S3.3).

The characteristics of the shallow conductive thermal field (Fig. 3.3) are presented using the depth of the 100°C isotherm (Fig. 3c and d), and by the lateral temperature variations on the upper surface of the pre-kinematic sediments (Fig. 3.3e and f) as well as on the top of the crystalline basement (Fig. 3.3g and h). The depth of the 100°C isotherm generally correlates spatially with the topographic–bathymetric surface (Fig. 2.1). For both models, the isotherm is deepest beneath the Çınarcık, Central and Tekirdağ basins, and is shallowest beneath the topographic highs in the eastern part of the modeled area (Fig. 3c and d). Overall, the isotherm depth is very similar in the two thermal models with slight differences detected beneath the Çınarcık and Tekirdağ basins, below which the high-density bodies are located.

The upper surface of the pre-kinematic sediments is deepest (~6 km b.s.l.) beneath the Sea of Marmara (Fig. 3.3a), where the syn-kinematic sediments are thickest (Fig. S3.1a). Due to its low thermal conductivity the syn-kinematic sedimentary unit will store heat, both within and beneath the unit, with the amount of heat stored being directly related to the thickness of the unit. This thermal blanketing effect of the syn-kinematic sedimentary unit is evident at its base, with the highest temperatures (up to 215°C) occurring beneath the Marmara basin (Fig. 3.3e and f). The low thermal conductivity of the pre-kinematic sediments also results in a similar thermal blanketing effect. Comparing the lateral variations in temperature at the top crystalline basement (Fig. 3.3g and h) with variations in the depth to this surface (Fig. 3.3b) and with the thickness of the pre-kinematic sediments (Fig. S3.1b) reveals that this thermal blanketing effect is largest where the pre-kinematic sediments are thickest, leading to maximum modeled temperatures of 265°C at the top crystalline basement.

The characteristics of the deep thermal field are illustrated in Figure 3.4 using the depth to the 450°C isotherm and the lateral temperature variations at the Moho. The 450°C isotherm is often used as a proxy for the brittle-ductile transition zone since this is the temperature at which felsic crustal rocks start to creep (Braun et al., 2013). To facilitate the interpretation of the thermal field derived for the two structural models, the depth to the top of the high-density bodies in Model I and Model II are shown in Figures 3.4a and 3.4b, respectively. The Moho topography is shown in Figure 3.4c and the depth to the base of the models in Figure 3.4d.

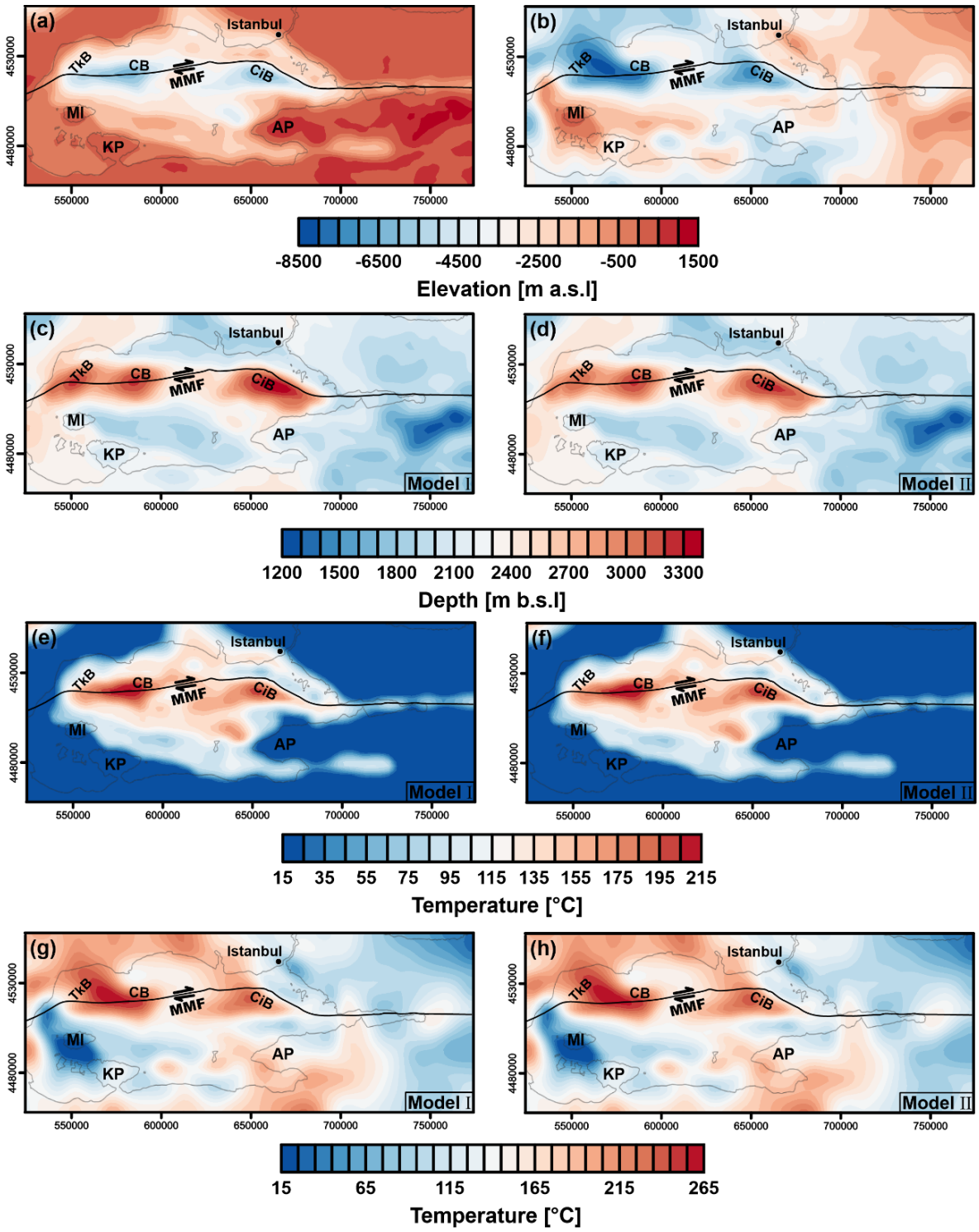

Figure 3.2: Shallow crustal geometry and results of thermal modeling for Model I and Model II. (a) Depth to the upper boundary of the pre-kinematic sediments. (b) Depth to the upper boundary of the crystalline basement. (c) Depth of the 100°C isotherm for Model I. (d) Depth of the 100°C isotherm for Model II. (e) Temperature distribution on the upper surface of the pre-kinematic sediments (Model I). (f) Temperature distribution on the upper surface of the pre-kinematic sediments (Model II). (g) Temperature distribution on the upper surface of the crystalline basement for Model I. (h) Temperature distribution on the upper surface of the crystalline basement for Model II. Abbreviations: Main Marmara Fault (MMF), Çınarcık Basin (CiB), Central Basin (CB), Tekirdağ Basin (TkB), Marmara Island (MI), Kapidağ Peninsula (KP), and Armutlu Peninsula (AP).

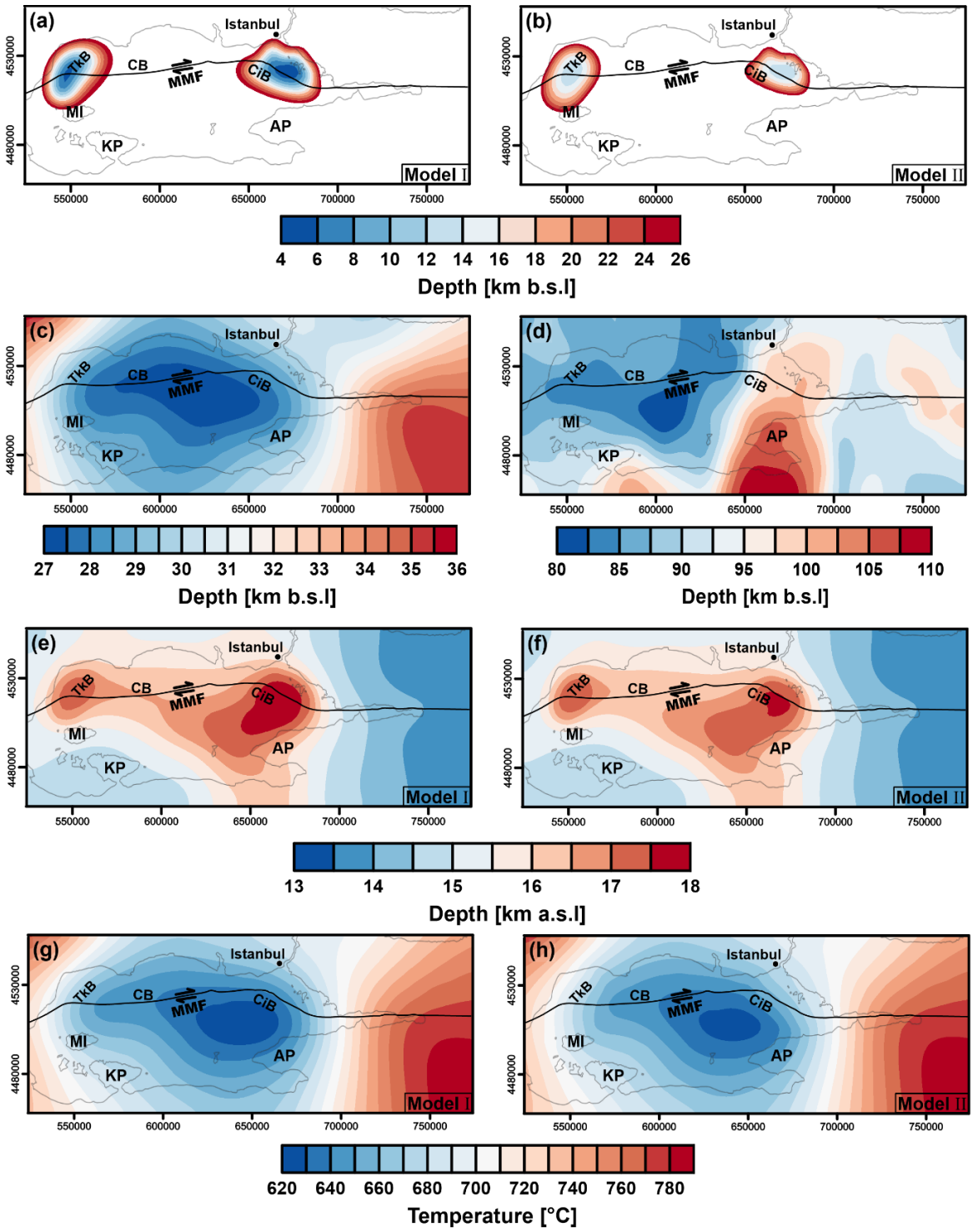

Figure 3.3: Deep crustal geometry and results of thermal modeling for Model I and Model II. (a) Depth to the high-density bodies for Model I. (b) Depth to the high-density bodies for Model II. (c) Depth to the Moho. (d) Depth to the lower thermal boundary (1330 °C). (e) Depth to the 450°C isotherm for Model I. (f) Depth to the 450°C isotherm for Model II. (g) Temperature distribution map on the Moho for Model I. (h) Temperature distribution map on the Moho for Model II. Abbreviations: Main Marmara Fault (MMF), Çınarcık Basin (CiB), Central Basin (CB), Tekirdağ Basin (TkB), Marmara Island (MI), Kapidağ Peninsula (KP), and Armutlu Peninsula (AP).

The 450°C isotherm (Fig. 3.4e and f) is shallowest in the eastern part of the modeled area (~13 km b.s.l.) and deepest beneath the Sea of Marmara: the deepest parts of the isotherm (~18 km b.s.l.) are beneath the Çınarcık and Tekirdağ basins, which correlate spatially with the high-density bodies. Comparing the depth variation of the 450°C isotherm with that of the Moho reveals that the crustal thickness is a major factor controlling the deep crustal thermal field. Specifically, the thickness of the upper crystalline crust (Fig. S3.1c and d) and the associated high radiogenic heat production contributing to the heat budget strongly influences the deep crustal thermal field. This is also expressed in the modeled lateral temperature distribution at the Moho (Fig. 3.4g and h). The maximum modeled temperatures at the Moho (up to 790°C) are in the eastern part of the modeled area, where the Moho is deepest and the upper crystalline crust is thickest. In contrast, the lowest temperatures (~620°C) were modeled beneath the Sea of Marmara, where the crust has been thinned. The lack of any clear spatial correlation between the depth of the lower model boundary (Fig. 3.4d) and the deep crustal thermal field indicates that the crustal setting beneath the Marmara Region dominates the thermal configuration. At lithospheric depths in excess of 60 km b.s.l, however, the depth of the thermal lithosphere-asthenosphere boundary (LAB), imposed as the lower thermal boundary condition (see Methods), controls the lateral variations in temperature (Figs. S3.2 and S3.3).

By comparison, the deep thermal field in Model II is slightly hotter than in Model I, as was the case for the shallow thermal field. This thermal difference between the two models is particularly evident directly above the high-density bodies. The smaller size of the high-density bodies in Model II translates into a thicker felsic and radiogenic upper crystalline crust, which makes a significant contribution to the heat budget.

3.5. Results of the rheological modeling

The results of the rheological modeling reveal variations in the integrated lithospheric and crustal strengths (Fig. 3.5). The modeled integrated lithospheric strength across the model area ranges between 14.9 and 15.55 Log_{10} Pa m (Fig. 3.5a and b). The greatest difference between the two models is found in the domains of the high-density bodies beneath the Çınarcık and Tekirdağ basins, with higher lithospheric strengths (~0.05 Log_{10} Pa m) derived in Model II than in Model I.

The strength of the lithosphere is generally low towards the Anatolian Plateau, in the eastern part of the modeled area, and tends to be higher beneath the Sea of Marmara. This pattern of

variation in lithospheric strength shows no spatial correlation with the thermal LAB (Fig. 3.4d), but it does show a spatial correlation with the temperature distribution at the Moho (Fig. 3.4c, g, and h): where the Moho surface is relatively shallow and cool the lithospheric strength tends to be high, and vice versa. The highest strengths are attained at the locations of the two high-density bodies. Local high lithospheric strengths are also obtained beneath the Imralı Basin, where the lower crust is thicker and the upper crust is thin (Fig. S3.1). Such variations in crustal thickness can produce cool thermal anomalies that result in greater strength, mainly due to the lower radiogenic heat production of lower crystalline crustal unit (Table 3.1; Fig. S3.2d and e, and Fig. S3.3d and e).

The integrated crustal strength (Fig. 3.5c and d) reaches its highest values for the locations of the high-density bodies. These values reach 14.65 Log_{10} Pa m for Model I and 14.95 Log_{10} Pa m for Model II. Local high integrated crustal strengths are also evident beneath the Imralı Basin. Once again, the distribution of the integrated crustal strength generally correlates with the thickness of the crystalline crustal units. The crustal strength is low where the upper crystalline crust is thick (Fig. S3.1) as a thicker felsic crust produces more radiogenic heat. This in turn results in a hotter and mechanically weaker crust than where the upper crust is thin (Figs. S3.2 and S3.3). Below the Sea of Marmara, however, the ratio of the integrated crustal strength to the total lithospheric strength is largest at the locations of the high-density bodies (Fig. 3.5e and f). This indicates that the high-density bodies are the main crustal contributors to the integrated lithospheric strength across the offshore area and along the MMF.

The thermal and rheological results along the MMF are illustrated in Figures 3.6 and 3.7 for Model I and Model II, respectively. These profiles show the structural models and observed seismicity (Figs. 3.6a and 3.7a), the depth of the 450°C and 750°C isotherms as well as the calculated YSEs for four different points (Figs. 3.6b and 3.7b), the integrated lithospheric and crustal strengths (Figs. 3.6c and 3.7c) and the corresponding ratios (Figs. 3.6d and 3.7d).

In both models the high-density bodies have higher strengths than the surrounding crystalline crust (Figs. 3.5, 3.6 and 3.7). The high-density bodies in Model II have distinctly higher strengths than their counterparts in Model I (Figs. 3.5, 3.6, and 3.7). Indeed, this rheological contrast was predictable due to the lithological differences between the two models and the corresponding mechanical parametrization (Table 3.1). For both models the high-density bodies are thermally cooler and mechanically stronger than the surrounding upper crustal rocks (see 450°C isotherm in Figs. 3.6b and 3.7b), and therefore characterizing stronger crustal units.

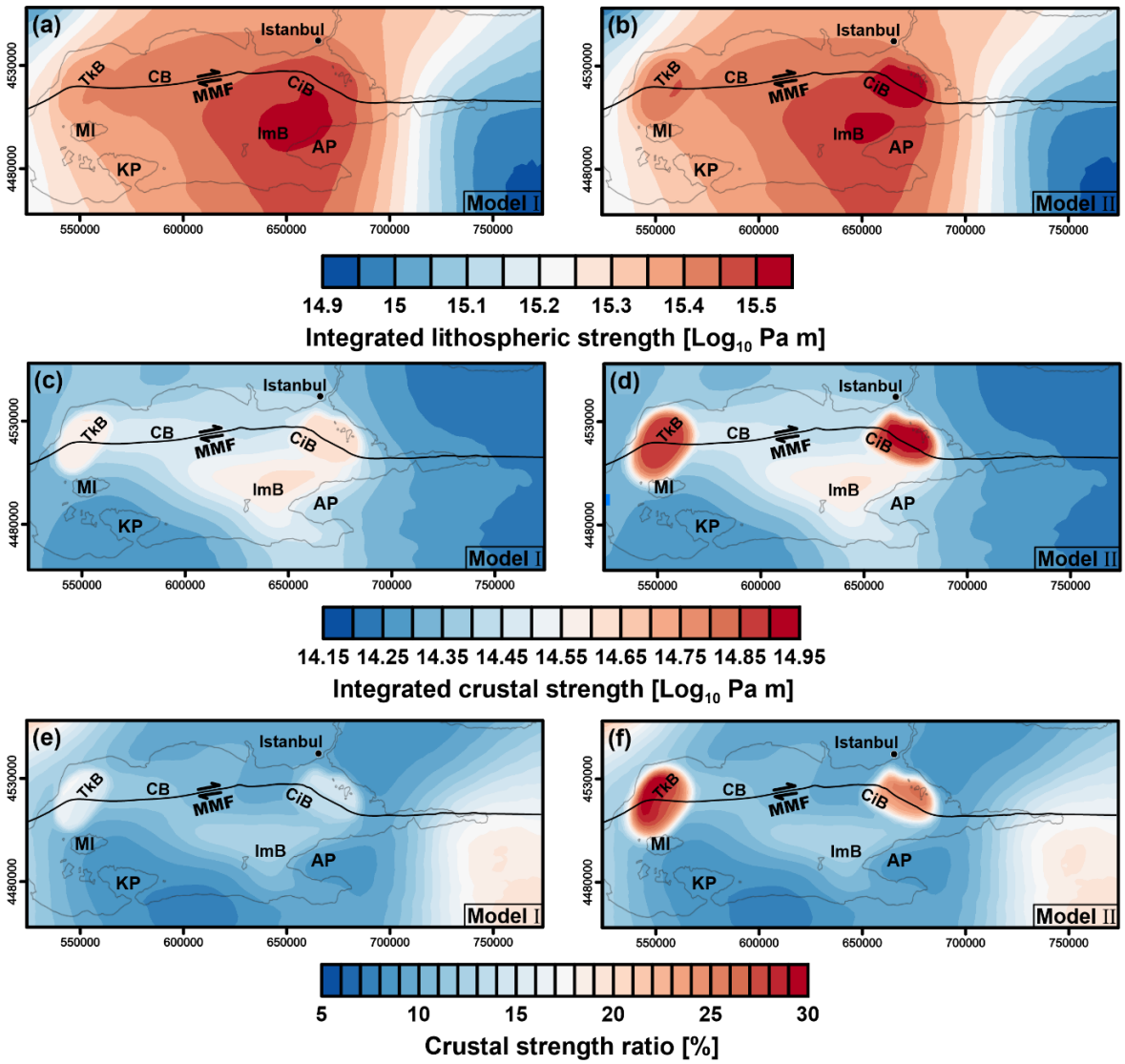

Figure 3.4: Modeled lithospheric strength. (a) Integrated lithospheric strength for Model I. (b) Integrated lithospheric strength for Model II. (c) Integrated crustal strength for Model I. (d) Integrated crustal strength for Model II. (e) Ratio of the integrated crustal strength to the total integrated lithospheric strength for Model I. (f) Ratio of the integrated crustal strength to the total integrated lithospheric strength for Model II. Abbreviations: Main Marmara Fault (MMF), Çınarcık Basin (CiB), Central Basin (CB), Tekirdağ Basin (TkB), Imralı Basin (ImB), Marmara Island (MI), Kapidağ Peninsula (KP), and Armutlu Peninsula (AP).

Both models indicate that the lower crust is mainly a relatively weak, ductile unit, while the upper few kilometers of the lithospheric mantle beneath the Sea of Marmara are relatively strong and brittle (Figs. 3.6b and 3.7b). Since in our models the lithospheric mantle is considered to be homogeneous, these rheological characteristics are only temperature and pressure dependent. The upper part of the lithospheric mantle along the MMF is cooler (and consequently stronger) beneath the Sea of Marmara than in the adjacent land area (see 750°C isotherm in Figs. 3.6b, 3.7b, S3.2, and S3.3). Apart from the domains of the high-density bodies, the thermal and rheological modeling results suggest a “jelly sandwich” rheological

configuration (Bürgmann and Dresen, 2008) along the MMF, characterized by a strong upper crystalline crust separated from a strong lithospheric mantle by a relatively weak lower crystalline crust.

3.6. Discussion

Our results indicate that modeled lateral variations in lithospheric strength in the Marmara Region correlate with crustal compositional heterogeneities rather than with thermal anomalies within the mantle. In addition, the spatial correlation between the mechanically strong, high-density bodies and bends in the MMF suggests that these crustal rheological contrasts may have affected the kinematics of the fault. Accordingly, our findings support the hypothesis that the observed segmentation along the MMF is controlled by the presence of a mechanically heterogeneous off-fault crustal configuration.

Our aim is to quantify the long-term strength configuration and to obtain information on its mechanical stability, and, by default to the seismic activity in the area. Therefore, we consider the lithosphere as an overall conductive system in thermodynamic equilibrium with its present-day geological setting. We are nevertheless aware that this assumption has two major implications, that computed temperatures (1) are conservative upper bound estimates of the temperature distribution at shallower depths as transient thermal effects due to sedimentation have been neglected; and (2) they are not representative of secondary, transient effects due to fluid circulation within permeable sedimentary units and along major fracture zones. From point 1 above, we would expect generally colder temperatures than those modeled within the syn-kinematic sediments as these relative young sediments have been deposited over the past 4.5 Ma (Le Pichon et al., 2014, 2016) within a shallow system that may not yet have reached thermal equilibrium. However, we have neglected this effect in our study on the base of a previous study (Ehlers, 2005) that have demonstrated a range of variations of 2-5°C Ma^{-1} being limited to the first 4 km depth below the surface. This effect would not impact our conclusions, and we remain positive that our principal findings concerning the first-order characteristics of the thermal field remain robust. The influence of active fluid circulation has far reaching implications as indicated by the mapping of episodic mantle degassing events along major fault segments and overpressure generation observed in the Sea of Marmara (Géli et al., 2018) which can influence the local mechanical state and stability. However, a proper assessment of such effects would require observations on local temperature, heat flow and, possibly, pore-pressure variations, which are so far overly limited across the Marmara Region or not publicly available.

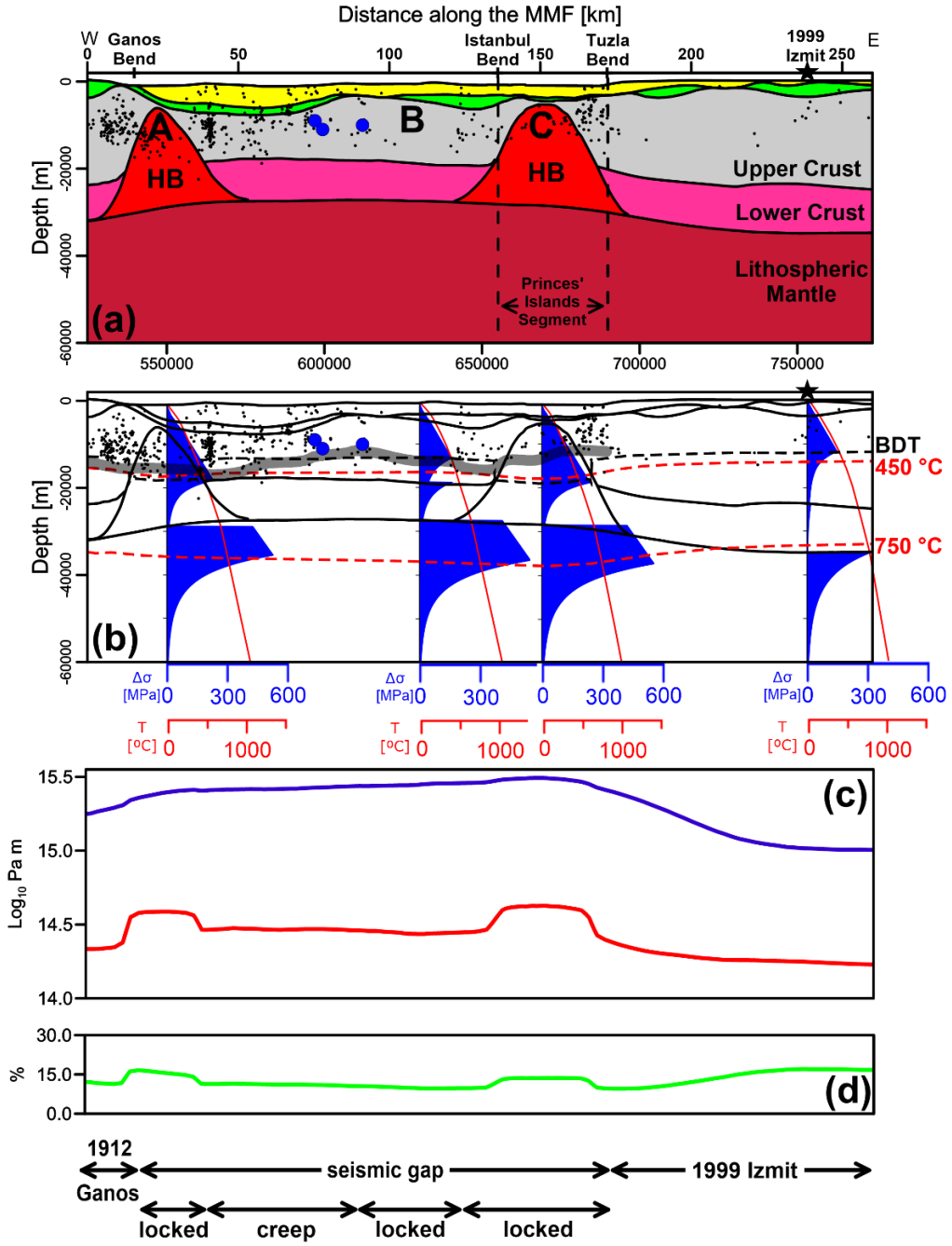

Figure 3.5: Cross-sections along the MMF represents results and interpretation from thermal and rheological models for Model I. (a) The structural mode (for details see Fig. 3.1a). The small black dots represent observed seismicity (Mw>2.1; Wollin et al., 2018) in a window of ±5 km around the MMF, and the small blue circles represent recent seismic activity in September 2019 (Mw4.4, Mw5.7, Mw 4.1 in west-east direction, data from GEOFON Data Center, see also Fig. S3.5). Locations of the observed (Wollin et al., 2018) aseismic patches are also shown as A, B, and C. (b) Calculated YSE for four different points correlating with the locations of the observed aseismic patches, and the epicenter of the 1999 Izmit earthquake. The tick gray line represents the base of the observed (Wollin et al., 2018) seismogenic layer (based on P-wave and S-wave travel-time inversions), while the black dash line is the modeled crustal brittle-ductile transition (BDT). The modeled 450°C and 750°C isotherms are indicated as red dashed lines. (c) Integrated lithospheric strength in blue and integrated crustal strength in red. (d) Ratio of the integrated crustal strength to the total integrated lithospheric strength, following with the interpretation of fault segmentations along the seismic gap.

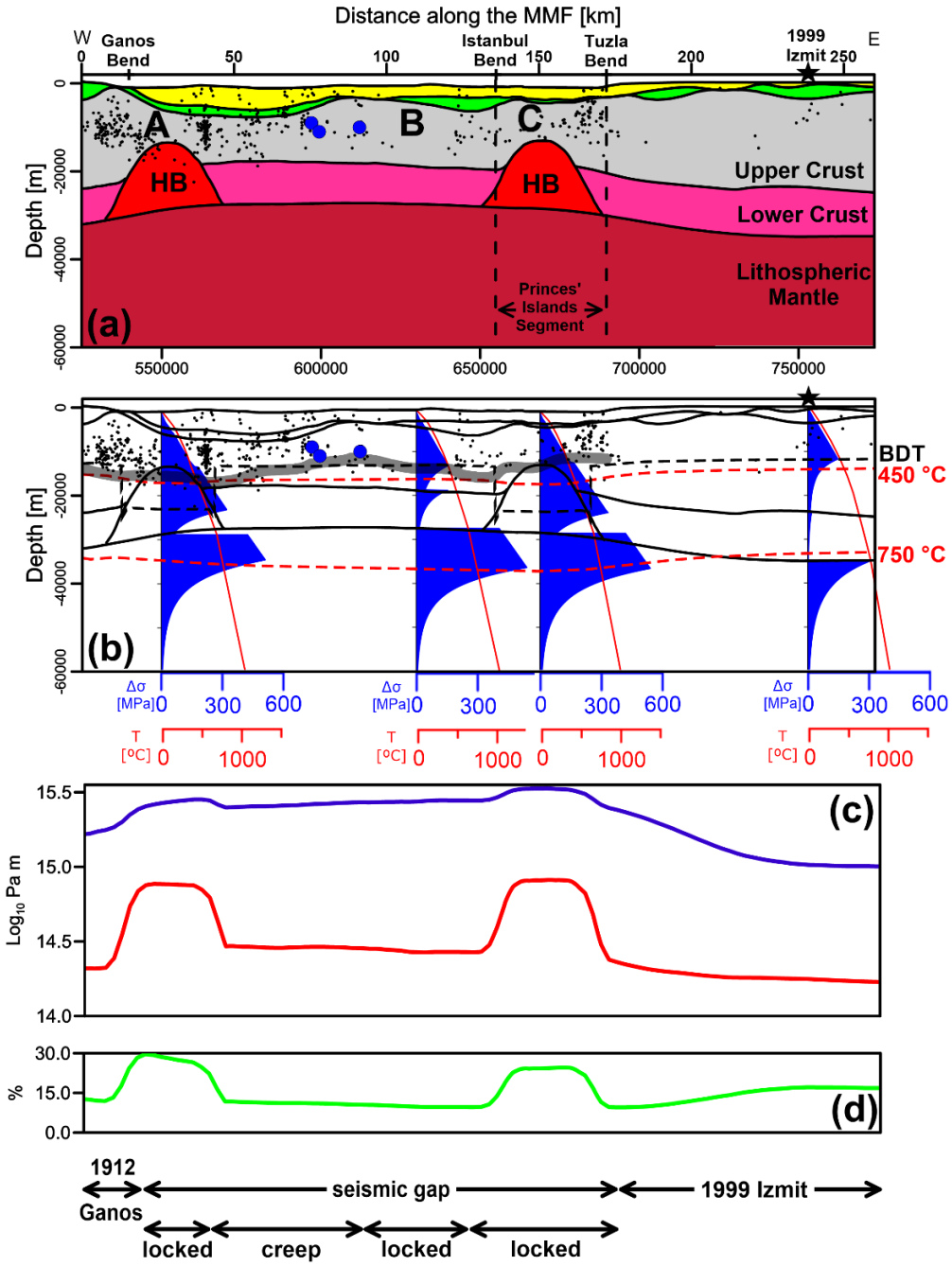

Figure 3.6: Cross-sections along the MMF represents results and interpretation from thermal and rheological models for Model II. (a) The structural model (for details see Fig. 3.1b). The small black dots represent observed seismicity (Mw>2.1; Wollin et al., 2018) in a window of ±5 km around the MMF, and the small blue circles represent recent seismic activity in September 2019 (Mw4.4, Mw5.7, Mw 4.1 in west-east direction, data from GEOFON Data Center, see also Fig. S3.5). Locations of the observed (Wollin et al., 2018) aseismic patches are also shown as A, B, and C. (b) Calculated YSE for four different points correlating with the locations of the observed aseismic patches, and the epicenter of the 1999 Izmit earthquake. The tick gray line represents the base of the observed (Wollin et al., 2018) seismogenic layer (based on P-wave and S-wave travel-time inversions), while the black dash line is the modeled crustal brittle-ductile transition (BDT). The modeled 450°C and 750°C isotherms are indicated as red dashed lines. (c) Integrated lithospheric strength in blue and integrated crustal strength in red. (d) Ratio of the integrated crustal strength to the total integrated lithospheric strength, following with the interpretation of fault segmentations along the seismic gap.

For the model area, two sets of onshore measured surface heat flow data from shallow boreholes (~100 m) exist as well as temperature measurements from a 2500 m onshore deep well (Pfister et al., 1998; Erkan, 2015). The measured surface heat flow varies in a range of 60±25 mW m^{-2} across the Marmara Region (Fig. S3.4). As expected, the modeled shallow thermal gradients and surface heat flux slightly overestimate the observations. Yet, the modeled surface heat flow around the Sea of Marmara is around 70±10 mW m^{-2} and thus in the range of the measurements (mean value of 60 mW m^{-2}, Fig. S3.4). Moreover, a good fit between observed and modeled temperature is found within the deeper parts of the well (Fig. S3.4).

As we are interested in quantifying the long-term rheological configuration of the lithosphere against which the MMF evolves we consider secondary creep as the only active dissipation mechanism. This requires a priori knowledge of the background strain rate, which could be representative of the whole plate. Due to ongoing activity of the NAFZ, the actual surface strain rate is likely to vary spatially over the Marmara Region, with a major concentration along the MMF, as reported by recent studies (Le Pichon et al., 2003; Flerit et al., 2004; Reilinger et al., 2006; Hergert and Heidbach, 2010). However how representative those measurements are at greater depths is a matter of debate. Given the current lack of knowledge of the state of stress in the crust, in our study we therefore decided to rely on a constant strain rate value ($\dot{\varepsilon} = 10^{-14}$ s^{-1}) over the entire modeled area. Our choice stems from the results of geodetic measurements(Hussain et al., 2018), which provided indications of an invariance strain rate (~0.5 microstrain yr^{-1}) during the whole inter-seismic period for the NAFZ. Accordingly, for the entire 250-year inter-seismic period, strain rate values can be considered as constant, with the exception of the first 10 years following a major earthquake. Given the time interval since the last earthquake along the MMF (1766), our assumption of constant strain rate remains valid. Moreover, the estimated surface strain value of ~0.5 microstrain yr^{-1} along the NAFZ leads to a strain rate estimate in the range of 10^{-14} to 10^{-15} s^{-1}.

Another parameter that plays an important role in our rheological modeling is the coefficient of friction, which we used to describe crystal plasticity following Byerlee's law. In our study, we did not attempt to model any variations in such coefficient, but rather imposed a unique value of 0.75 (see Methods) and we do not consider a reduction in the friction along the MMF. Hergert and Heidbach (2011) showed that a value of 0.05 for the coefficient of friction for the MMF is compatible with the measured slip-rate along the fault. This supports our interpretation of the MMF as a weak fault cutting through a variably strong lithosphere. In addition, Hussain

et al. (2018) showed that for an inter-time event of 250 years (as an approximate for the recurrence time of the Marmara seismic gap), average viscosities of the lower crust must be greater than 10^{20} Pa s to match the constant strain rate during the whole inter-seismic period for the NAFZ. This is in the range of magnitudes for crustal viscosities as derived from our rheological modeling (10^{20}–10^{21} Pa s, Fig. 3.7). Accordingly, a weak fault zone embedded within a strong lower crust is required to reconcile the geodetic observation. Our study provides a geologically consistent explanation for such off-fault rheological configuration that is required to match the observed strain rate data and the recorded seismicity. It is the presence of the strong high-density bodies in our model, which provide the strong substratum around the weak MMF fault thus limiting seismic activities within the fault proper. In addition, postseismic strain rate might not be representative to characterize the rheological crustal configuration at all spatial scales. Thus evaluating the deep crustal structure with the type of a model as presented in this study can be the key to assess the geomechanical behavior of large fault zones.

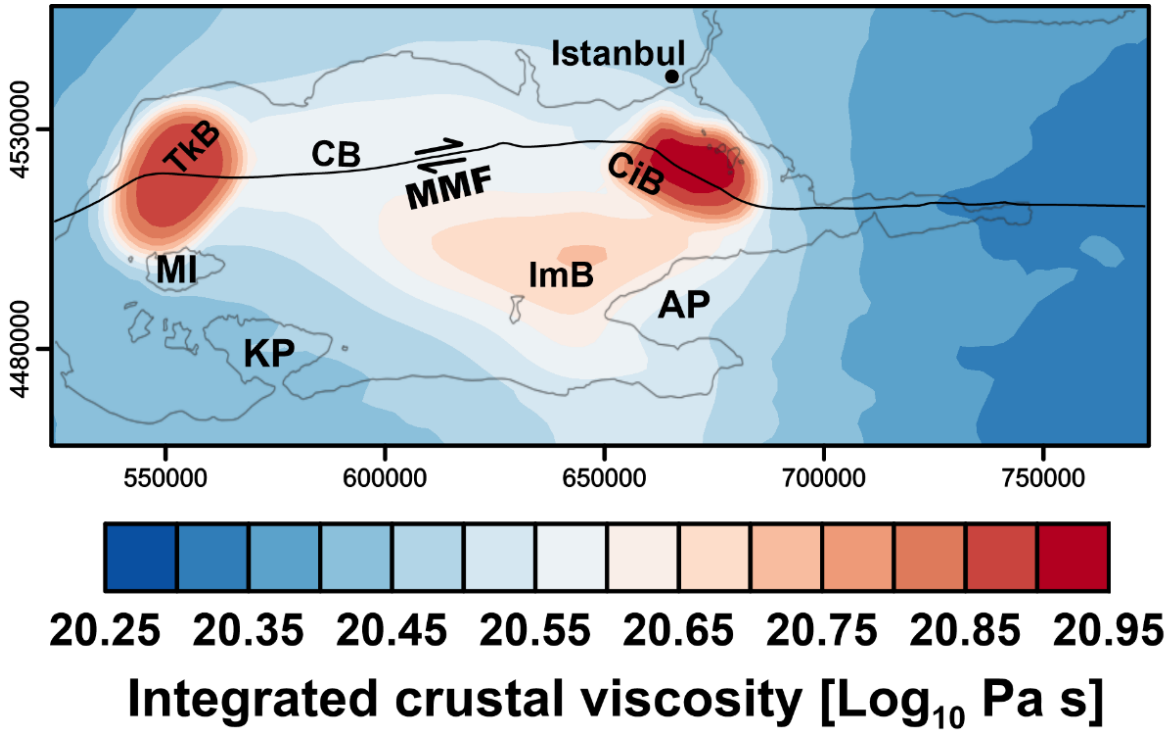

Figure 3.7: Integrated crustal viscosity based on the calculated average effective viscosity (see Methods, Eq. 3.8) for upper crystalline crust, lower crystalline crust and high-density bodies. Abbreviations: Main Marmara Fault (MMF), Çınarcık Basin (CiB), Central Basin (CB), Tekirdağ Basin (TkB), Imralı Basin (ImB), Marmara Island (MI), Kapidağ Peninsula (KP), and Armutlu Peninsula (AP).

Since the last two large earthquakes along the MMF were in September 1509 and May 1766, the recurrence time would appear to be approximately 250 years (Ambraseys, 2002; Barka et al., 2002; Parsons, 2004; Janssen et al., 2009; Bohnhoff et al., 2013, 2016a, 2017; Murru et al., 2016). While the extent and exact location of the ruptures that caused these two historical events remains uncertain, there is general agreement that their magnitudes were comparable to those of recent events to the east and west, on adjacent sections of the NAFZ (~Mw7.4). The recently published unified earthquake catalogue for the Sea of Marmara (Wollin et al., 2018) covering the period between 2006 and 2016 lists 6812 events and identifies the MMF as the most seismically active segment of the NAFZ in the Marmara Region. The majority of the listed events are 1.5<Mw<3 and occurred at depths between 5 and 15 km (Fig. S3.6). Most of the seismicity occurred above the modeled depth of the 450°C isotherm. Furthermore, the seismicity distribution displays three main aseismic patches (labeled A, B and C in Figs. 3.6 and 3.7), which are considered as locked segments along the MMF and potential nucleation points for the next Mw>7 Marmara earthquake(Bohnhoff et al., 2013, 2017; Wollin et al., 2018; Bulut et al., 2019; Lange et al., 2019).

Relating these observations on the MMF to the thermal and rheological results (Figs. 3.6 and 3.7), we can consider the weak crystalline crustal units (i.e. the lower parts of the felsic upper crust and the ductile intermediate to mafic lower crust) extending between the two high-density bodies as the domains prone to creeping. The section between the two high-density bodies is characterized by a relatively shallow brittle-ductile transitional domain (Figs. 3.6b and 3.7b) in response to a more felsic and radiogenic composition than in the domains of the high-density bodies. Consequently, we propose that deeper crust along this segment of the seismic gap represents a domain where seismic energy dissipation by creep is dominant. Our conclusion is consistent with the interpretation by Yamamoto et al. (2019) based on seafloor strain-rate observations in the western high that showed a steady-rate right-lateral deformation of 10.7±4.7 mm yr^{-1}. Accordingly earthquakes between the two strong lower crustal high-density bodies are likely to be relatively shallow and of low magnitude, as observed recently in September 2019 (GEOFON Data Centre, 1993), with creep occurring at greater depths.

Following a similar reasoning, we conclude that the presence of a strong crust (high-density bodies) provides the explanation of why the MMF is locked at these locations over long time scales. Two of the observed aseismic fault patches (A and C in Figs. 6a and 7a) correlate spatially with the locations of the modeled high-density bodies, whereas dense seismic activity

is evident along their boundaries. Therefore we can interpret these areas as limiting the extent of aseismic patches of the fault, thus representing the locked-creeping transition (Bohnhoff et al., 2013, 2017; Wollin et al., 2018). We therefore identify the overly stiff high-density bodies as exerting the main control on the state of stress along the MMF, being the reason behind the locked state of the fault segments to levels below the seismogenic layer.

There is however also an aseismic zone ("B", Figs. 6a and 7a) between the two crustal high-density bodies and beneath the central high. The sparse seismicity documented beneath this region indicates that assuming a shallow-locked segment characterized by creep at deeper crustal levels (Wollin et al., 2018; Lange et al., 2019) is insufficient to explain the mechanical behavior of this segment of the fault. This then implies that either aseismic creep occurs, or that the fault is fully locked as interpreted by Lange et al. (2019) based on seafloor strain-meter measurements. Although the modeled rheology does not provide a clear indication for a fully locked segment in this area at a crustal scale, the high strength of the lithospheric mantle (Figs. 6b and 7b) in this domain could result in the fault being locked at a lithospheric scale.

Bohnhoff et al. (2016a) investigated the temporally and spatially distributed crustal response framing the two major seismic events in 1999, one on 17 August at Izmit (Mw7.4, 1999a in Fig. 1.1b) and the second on 12 November at Düzce (Mw7.1, 1999b in Fig. 1.1b). They identified aseismic fault patches along the rupture zones of the Izmit and Düzce events and found a spatial correlation between the location of these aseismic patches and the maximum postseismic creep deformation in the ductile lower crust.

The Mw7.4 Izmit earthquake (Barka et al., 2002) on 17 August 1999 has been thoroughly investigated and can probably serve as a reference event for evaluating the potential seismic hazard within the modeled area. This earthquake, which had a hypocentral depth between 10-16 km (Barka et al., 2002), was the last major event in the Marmara Region. The results from our modeling shows that the hypocenter coincides with the resolved the brittle-ductile transition at a depth of about 11 km (Figs. 6b and 7b) and that the lower crustal unit beneath the hypocenter is a rather weak ductile layer. If we compare the rheological profile beneath the Izmit earthquake epicenter (Figs. 6 and 7) with the one beneath the aseismic patch "B", it becomes clear that these two domains share a similar rheological crustal configuration. However, the lithospheric mantle is considerably colder and rheologically stronger beneath the aseismic patch "B" under the central high than beneath the Izmit area, which could result in a different deformation behavior in the two areas.

Due to the presence of the two high-density bodies, the modeled lithospheric strength beneath the Princes' Island segment (Çınarcık Basin) and the Tekirdağ Basin is noticeably higher than beneath the epicenter of the 1999 Izmit event (Figs. 6b and 7b). In particular, a strong crust mechanically coupled with the underlying mantle in Model II (Fig. 7b), which in turn would imply am overly stiffer lithosphere requiring significantly higher differential stresses than for the Izmit earthquake to fail. However, under such a configuration a seismic failure beneath the Princes' Islands segment (or Tekirdağ Basin) would have a higher energy potential. In addition, the observed seismogenic depth along the MMF (Wollin et al., 2018) ties in remarkably well with the tops of the high-density bodies in model II (Fig. 7b), again supporting the hypothesis that the MMF is locked at these locations.

It remains an open question how exactly variable surface strain rates propagate to deeper crustal and lithosphere levels along the weak fault and beyond and how rheological heterogeneities in the lithosphere interact with the fault itself. Our rheological model, despite its assumptions, clearly indicate the presence of variations in the lithosphere strength that correlate spatially with on-fault seismotectonic segments. We therefore suggest that the rheology of the crust away from the fault (high-density bodies) has the primary control on the long-term, inter-event strain within the Marmara Region. This differs to the dynamics driving the deformation within the fault domain proper, where the fault rheology (inherently weak) controls the temporal decay of deformation on the shorter, postseismic time scale.

3.7. Conclusions

In this study, static thermo- rheological results are presented for two different structural models of the Sea of Marmara. Based on these results, we conclude the following:

1. There are rheological heterogeneities in the lithosphere beneath the Marmara region. These contrasts are principally related to the crustal heterogeneities rather than the thermal anomalies within the deeper mantle.

2. Along the main Marmara fault (MMF), the lithospheric rheological variations are mainly associated with the crustal high-density bodies that spatially correlate with the two major bent segments of the fault. These bodies are mechanically stronger than the surrounding crystalline crust, and they may affect the dynamics of the MMF.

3. The rheological discontinuities along the MMF support the hypothesis that the MMF is mechanically segmented.

4. The realms of the two high-density bodies may exemplify the MMF locked segments while the fault partially creeps between the two crustal high-density bodies.

5. Comparing the two different structural settings (Model I and II) with the observed seismogenic depth along the MMF, Model II with the smaller-sized but denser (mafic) high-density bodies shows a better fit to the observed seismogenic depth below the MMF.

6. The static thermal and rheological model can be used as input data for mechanical modeling of the stress field along the MMF to further investigate the segmentation hypothesis.

Chapter 4

Present-day thermal field of the SW African and the Norwegian passive margins*

* This chapter largely corresponds to a paper published as "*Variability of the geothermal gradient across two differently aged magma-rich continental rifted margins of the Atlantic Ocean: The Southwest African and the Norwegian margins, Solid Earth, 9, 139–158, https://doi.org/10.5194/se-9-139-2018, 2018"* and co-authored by Ershad Gholamrezaie, Magdalena Scheck-Wenderoth, Judith Sippel, and Manfred R. Strecker.

4.1. Introduction

Comprehension of the lithosphere-scale thermal state is a key to unraveling the evolution, strength, and physical and chemical processes of the lithosphere (e.g., Davies, 1980; Chapman, 1986; Artemieva and Mooney, 2001; Scheck-Wenderoth and Lamarche, 2005; McKenzie et al., 2005; Ebbing et al., 2009). Furthermore, analyzing the thermal field of the lithosphere has important applications in industrial sectors such as geo-resources exploration (e.g., Muffler and Cataldi, 1978; Tissot et al., 1987; Grevemeyer and Villinger, 2001; Wallmann et al., 2012).

The lithospheric thermal field generally depends on the thermal thickness and the thermal properties of the lithosphere. This has been deduced from continental crustal geotherms (Pollack, 1986; McKenzie and Bickle, 1988; Rudnick and Nyblade, 1999; Kaminski and Jaupart, 2000; Artemieva and Mooney, 2001; Artemieva, 2006; Jaupart and Mareschal, 2007; Mareschal and Jaupart, 2013) and from plate cooling models explaining oceanic heat flow patterns and seafloor depth evolution (Parsons and Sclater, 1977; Johnson and Carlson, 1992; Stein and Stein, 1992; Goodwillie and Watts, 1993; DeLaughter et al., 1999; Watts and Zhong, 2000; Crosby et al., 2006; Crosby and McKenzie, 2009). There is consensus that conduction is the main heat transfer mechanism in the lithosphere and generally controlled by (1) the heat input from larger mantle depths, (2) the heat internally produced in the lithosphere by the decay of radioactive elements, and (3) the thermal conductivity of different lithospheric layers (summary in Allen and Allen, 2005; Turcotte and Schubert, 2014). The interaction of these controlling factors complicates predictions of temperature increase with depth. This difficulty largely arises from the variability of the lithosphere in terms of structure and composition, parameters that are a product of the tectonic setting and evolution of the location of interest. One well-established strategy to investigate the present-day thermal field of a certain area is to integrate existing geophysical and geological data into 3-D structural models that provide the basis for numerical modeling, which simulates heat transport processes after setting boundary conditions and thermal properties according to the geological structure (e.g., Scheck-Wenderoth and Lamarche, 2005; Noack et al., 2013; Scheck-Wenderoth et al., 2014; Sippel et al., 2015; Balling et al., 2016).

Although there is already a large number of such 3-D models for different settings worldwide, none of these studies has focused on the variability of geothermal gradients with respect to geological structure. It is self-evident that the geothermal gradient is a function of local

temperature, which depends on the thermal state. This is an important issue because geothermal gradient variations in the shallow parts of the subsurface (measured or modeled) may be indicative of the thermal field and temperature-controlled processes at greater depths. Moreover, methods used to assess the thermal history of specific tectonic settings generally apply strongly simplified assumptions concerning the geothermal gradient and its changes in space and time (e.g., Burnham and Sweeney, 1989; Barker, 1996; Allen and Allen, 2005; Naeser and McCulloh, 2012). Accordingly, a better understanding of variations in the geothermal gradient could also improve the quality of thermochronological results of thermal history models. In this interest, the main questions are the following: (1) how does the geothermal gradient vary with depth and laterally over major geological structures (such as passive continental margins)? (2) What are the controlling factors of these variations? (3) How are shallow geothermal gradients related to the lithospheric-scale thermal field?

The goal of this study is to investigate the geothermal gradient as one manifestation of the thermal field that can directly be observed and usually differs significantly according to the specific tectonic settings. Concerning thermal histories, we do not go into much detail as we do not reconstruct thermal histories. The point we want to make is to raise awareness in the context of paleothermal conditions. Our approach follows three principal steps: (1) derive geothermal gradients from two existing and validated 3-D thermal models, both from volcanic passive margins, but with major age differences: the SW African passive margin (130 Ma) and the Norwegian margin (55 Ma); (2) investigate the variability of geothermal gradients with respect to the structural configuration changing from unthinned continental lithosphere onshore, over the stretched margins with great sediment thickness, and finally to the distal oceanic lithosphere; and (3) compare the results of the calculated geothermal gradients for the two different margins. In this context, there are significant variations in the thermal field that need to be considered when sediments, crust, and the lithospheric mantle display pronounced lateral heterogeneities in thickness and composition across the continental margins. In spite of a very similar configuration of the crust, the underlying lithospheric mantle in the two study areas differs. The younger lithospheric mantle beneath the oceanic crustal parts of the North Atlantic is significantly thinner than the older counterpart of the South Atlantic (Scheck-Wenderoth et al., 2007; Scheck-Wenderoth and Maystrenko, 2008; Maystrenko et al., 2013). By comparing the calculated geothermal gradients of these margins, we particularly address the consequences of the lateral heterogeneities for the thermal field and test the hypothesis that

the present-day thermal field is different for the two settings and ultimately determined by the lithospheric mantle characteristics.

4.2. Method

4.2.1. 3-D conductive thermal model

Theoretically, heat is transferred due to a temperature gradient and dependent on the thermal conductivity within the solid media. This statement is known as the law of heat conduction or Fourier's law (Eq. 4.1), where λ stands for the thermal conductivity, and ∇T defines the premier temperature gradient:

$$q = -\lambda \nabla T. \qquad \text{(Eq. 4.1)}$$

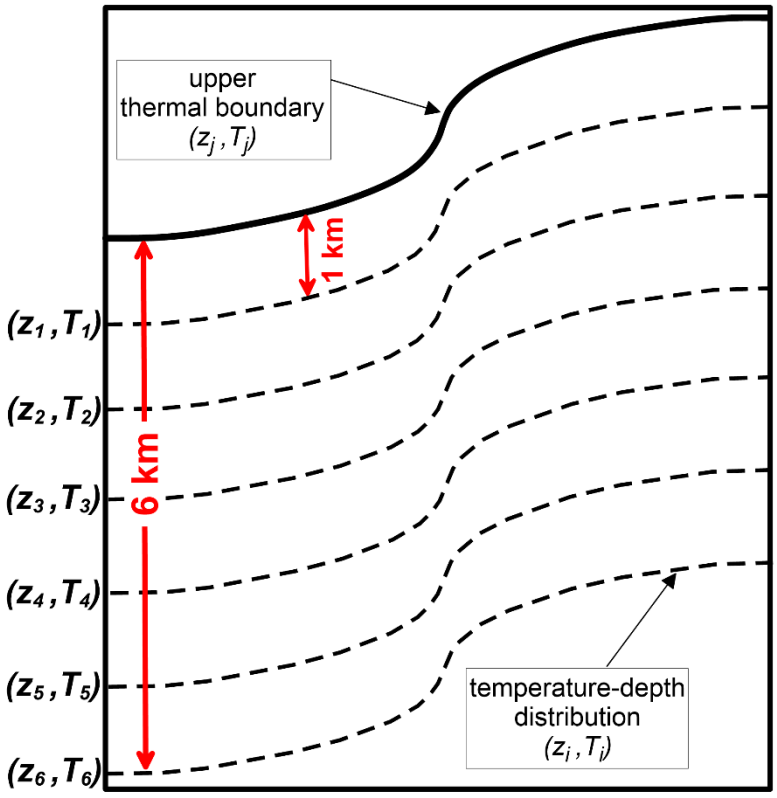

Figure 4.1. The geothermal gradient calculation: schematic of the temperature–depth distributions to calculate the geothermal gradient between the uppermost surface (z_j, T_j) and the corresponding depth levels (z_i, T_i). The temperature–depth distribution maps are presented as Figs. S4.1 and S4.2.

Table 4.1. Oceanic lithosphere age after Müller et al. (2008) and average physical properties of geological units used for thermal modeling after Scheck-Wenderoth and Maystrenko (2008); Maystrenko et al. (2013).

	SW African margin				Norwegian margin			
Geological units	Age	Maximum thickness (km)	Average thermal conductivity (W mK^{-1})	Average heat production (μW m^{-3})	Age	Maximum thickness (km)	Average thermal conductivity (W mK^{-1})	Average heat production (μW m^{-3})
Clastic sediments	Cenozoic	Walvis Basin = 3.6 Lüderitz Basin = 3 Orange Basin = 1.4	1.5	1	Cenozoic	Vøring Basin = 3.2 Møre Basin = 3.6	1.5	1
	Cretaceous	Walvis Basin = 5 Lüderitz Basin = 8 Orange Basin = 15	1.5	1	Cretaceous	Vøring Basin = 3.2 Møre Basin = 3.6	1.5	1
Crystalline crust	–	50	2.8	1.45	–	40	2.7	0.8
High-density crust	–	–	2.7	0.95	–	–	2.6	0.3
High-velocity body	–	–	2.6	0.8	–	–	2.6	0.5
Oceanic crust	130 Ma bp	–	2.75	0.3	55 Ma bp	–	2.1	0.3
Lithospheric mantle	–	135	3.95	0.03	–	110	3.95	0.03

Considering Fourier's law (Eq. 4.1) and assuming conductive heat transport as the main heat transfer mechanism, the heat flow equation can be derived on a lithospheric scale (Eq. 4.2). In these equations T and t represent temperature and time, respectively. The radiogenic heat production is shown by S and Δ is the Laplacian operator. The parameter ρ stands for density, c for the heat capacity, and λ for the thermal conductivity. The two considered 3-D conductive thermal models (Scheck-Wenderoth and Maystrenko, 2008; Maystrenko et al., 2013) were created as a numerical solution to Eq. 4.2 in the steady-state condition ($\frac{\partial T}{\partial t} = 0$) and by considering lithology-dependent thermal properties (Table 4.1). The lower thermal boundary in these models has been fixed at the 1300 °C isotherm signifying the thermal LAB depth, whereas the topography–bathymetry surface with a constant temperature (Norway: 2 °C; SW Africa: 5 °C) has been set as the upper thermal boundary.

$$\rho c \frac{\partial T}{\partial t} = \nabla . (\lambda \nabla T) + S \qquad \text{(Eq. 4.2)}$$

4.2.2. Geothermal gradient

The geothermal gradient is the temperature change with increasing depth (Eq. 4.3). Through the 3-D thermal models, the corresponding temperature to a certain depth is predicted, which simplifies the geothermal gradient calculation. However, since the aim of this study is to compare the variations of the geothermal gradient in different geological settings, a comparable reference frame is required. Therefore, the upper thermal boundary in each thermal model was chosen as the reference surface. We extracted the temperature–depth distributions in 1 km homogeneous depth levels down to 6 km below the upper thermal boundary surface (Fig. 4.1; see also Figs. S4.1 and S4.2 in the Supplement). To calculate the geothermal gradient (Eq. 4.3), we considered T_j and z_j, respectively, as the temperature and the elevation of a surface in the 3-D thermal models for which the upper thermal boundary condition was assigned. In our calculation, z_i was the corresponding depth for i = 1, 2, 3, 4, 5, and 6 km below the upper thermal boundary condition, and T_i was the temperature distributions at the corresponding depth levels of i values (Fig. 4.1, see also Figs. S4.1 and S4.2). The geothermal gradient was then calculated as the temperature difference between the uppermost surface and the corresponding depth levels. Thus, the average geothermal gradient is determined for different levels with increasing depth.

$$\frac{dT}{dz} = \frac{T_i - T_j}{z_i - z_j}, \qquad \text{(Eq. 4.3)}$$

We have chosen this way of illustrating the depth evolution of the geothermal gradient to make our assessment of the average geothermal gradient variation comparable to the observation-derived geothermal gradient variation. In practice geothermal gradients are often calculated from surface heat flow and bottom-hole temperature measurements. As bottom-hole temperatures therefore depend on the absolute depth of the drilled well, the derived average geothermal gradients vary accordingly. Our goal was to show (1) that there is no such thing as one average geothermal gradient and (2) that the latter is subject to variation in response to depth and structural heterogeneity.

4.3. Exploited models

The database for this study consists of regional 3-D lithospheric-scale structural and thermal models for the SW African (Maystrenko et al., 2013) and the Norwegian passive margins (Scheck-Wenderoth et al., 2007; Scheck-Wenderoth and Maystrenko, 2008). These models integrate and are consistent with observed seismic data, gravity data, and measured temperatures and heat flow.

4.3.1. Southwest African passive margin

There are three main sedimentary basins in the study area of the SW African continental margin. From north to south these are the Walvis Basin, the Lüderitz Basin, and the Orange Basin. These basins overlie a thinned continental crust and are filled with Cretaceous and Cenozoic sediments (Fig. 4.2a, Table 4.1). The Orange Basin hosts the thickest sediments compared to the two other basins with a maximum thickness of up to 16 km in the southern part of the basin. Sediment thickness varies in a similar manner in the Lüderitz and Walvis basins and ranges between 5 to 8 km except small parts of the Walvis Basin, where up to 10 km of sediment are present. Onshore, the model also differentiates upper Proterozoic sediments (Owambo and Nama basins; Clauer and Kröner, 1979; Miller, 1997). The continent–ocean boundary (COB; determined from gravity data in combination with reflection seismic and magnetic data; Pawlowski, 2008) runs approximately along the 5 km isopach of the sedimentary fill and parallel to the coastline.

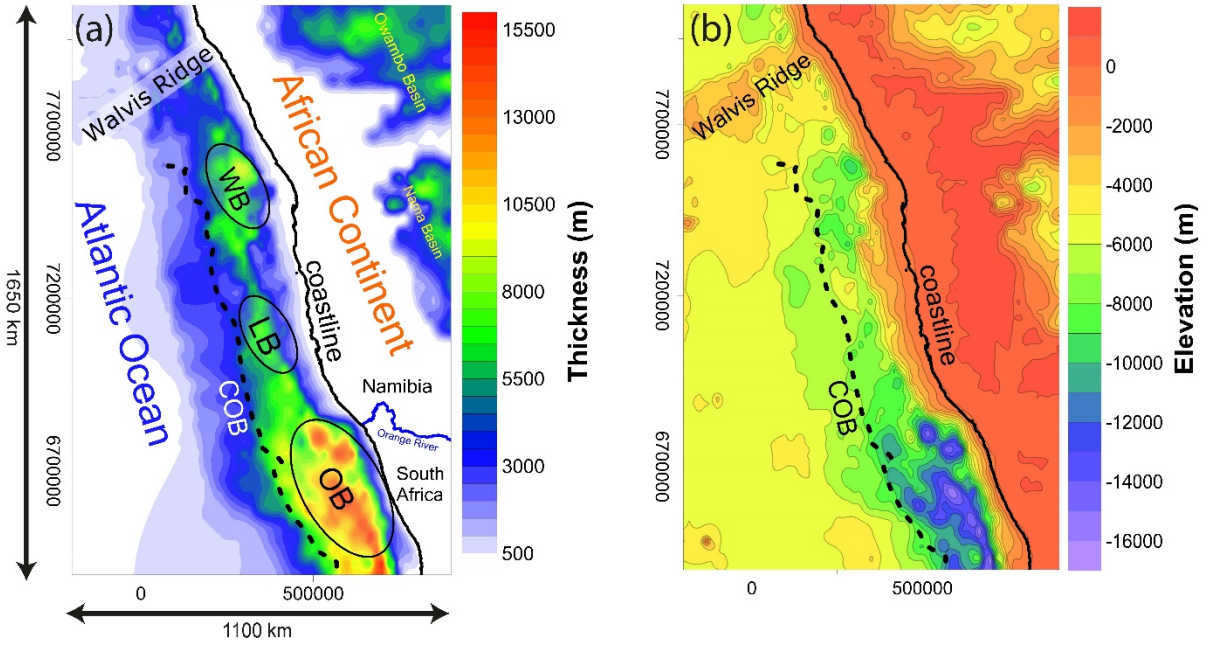

Figure 4.2. 3-D structural model of the SW African passive margin: (a) cumulative thickness map of sediments including offshore Cretaceous–Cenozoic thick sedimentary basins and onshore Proterozoic Owambo and Nama basins; (b) depth to top basement (COB: continent–ocean boundary, WB: Walvis Basin, LB: Lüderitz Basin, OB: Orange Basin, UTM: WGS84, zone 33S).

Below the sedimentary basins, the top crystalline basement descends seaward. Offshore, where the Walvis Ridge intercepts the coast, the shallowest basement is at a depth of 2000 m below sea level (b.s.l.). With 17 km b.s.l., the top basement is deepest in the south–southeast beneath the Orange Basin (Fig. 4.2b). The upper crystalline crustal thickness is largest onshore, with a maximum thickness of more than 45 km. Towards the COB, the thickness of the crystalline crust progressively decreases and attains less than 5 km in the oceanic crustal domain (Fig. 4.3a).

The depth of the Moho varies between 20 and 30 km b.s.l. beneath the continental shelf (Fig. 4.3b), where the lithospheric mantle (the layer between the Moho and the lithosphere–asthenosphere boundary) has the largest and smallest thickness beneath the onshore area at 135 and 75 km, respectively (Fig. 4.3c). Beneath the sedimentary basins, the thickness of the lithospheric mantle is approximately uniform and stays in the range between 80 and 100 km.

In their 3-D thermal model, Maystrenko et al. (2013) considered a temperature of 5 °C as the upper thermal boundary condition at the surface and seafloor. The topography and bathymetry of these surfaces are displayed in Fig. 4.4a. The topography reaches a height of more than 1500 m above sea level (a.s.l.) and decreases seaward. Offshore, the continental shelf is a few hundred meters below sea level; the continental slope descends steeply to the isobath of 3000

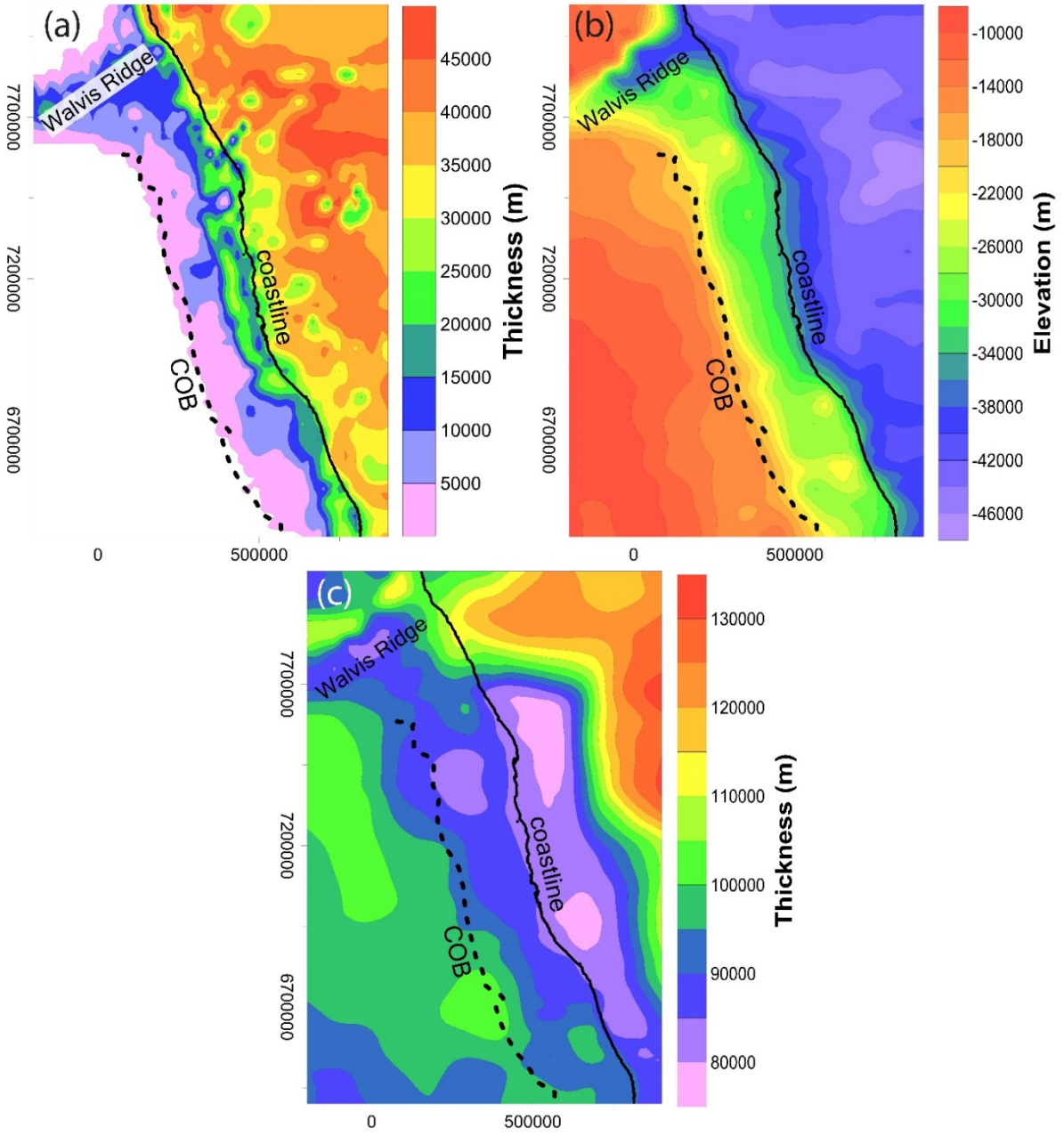

Figure 4.3. 3-D structural model of the SW African passive margin: (a) thickness of the upper crystalline crust; (b) depth to Moho; (c) thickness of the lithospheric mantle.

m b.s.l. at the COB. Further, the seafloor descends with a gentler slope to 5000 m b.s.l. In the investigated area, the deepest part of the ocean is located in the southwestern corner of the model with a depth to 5500 m b.s.l.

Along with the top surface and the seafloor, the lithosphere–asthenosphere boundary (LAB) also constitutes a crucial element in the structural–thermal model as it is the interface to which the lower thermal boundary condition of 1300 °C is assigned. The LAB is deepest (~ -180 km) beneath the onshore areas in the northeast and shallowest (~ -100 km) under the oceanic region (Fig. 4.4b). Beneath the sedimentary basins of the continental margin, the LAB is situated at a depth of 115 to 120 km b.s.l., except for the southern part of the Orange Basin, where the depth of the LAB descends to 130 km b.s.l.

4.3.2. Norwegian passive margin

The Norwegian passive margin includes the Vøring and the Møre basins. We extracted the cumulative thickness of sediment packages from the structural model (Fig. 4.5a). The thickest part of the sediments lies within the Vøring Basin, with a thickness of up to 17 km. Compared to the Vøring Basin, the sediments within the Møre Basin are thinner and rarely thicker than 12 km. The sedimentary thickness is more uniform along the COB and approximately follows the 8 km isopach.

Over the whole area, the depth to the crystalline basement varies between more than 1500 m a.s.l. and 18 km b.s.l. (Fig. 4.5b). The deepest parts of the basement are located beneath the sedimentary basins and parallel to the COB. The depth to the top of the crystalline basement is almost uniform below the oceanic crustal domain and varies between 5 and 6 km b.s.l. The thickness of the upper crystalline crust (Fig. 4.6a) is largest onshore, with more than 35 km beneath the Norwegian Caledonides. Offshore, the thickness decreases seaward to less than 5 km in the oceanic crustal domain.

According to the crustal structure, the Moho is deeper (17 to 37 km b.s.l.) below the continental crust compared to the oceanic crust where the Moho is inferred to be located at a depth of 9 to 20 km b.s.l. (Fig. 4.6b). Below the Moho, the thickness of the lithospheric mantle decreases seaward from 110 km in the continental domain to 45 km in the oceanic crustal domain (Fig. 4.6c).

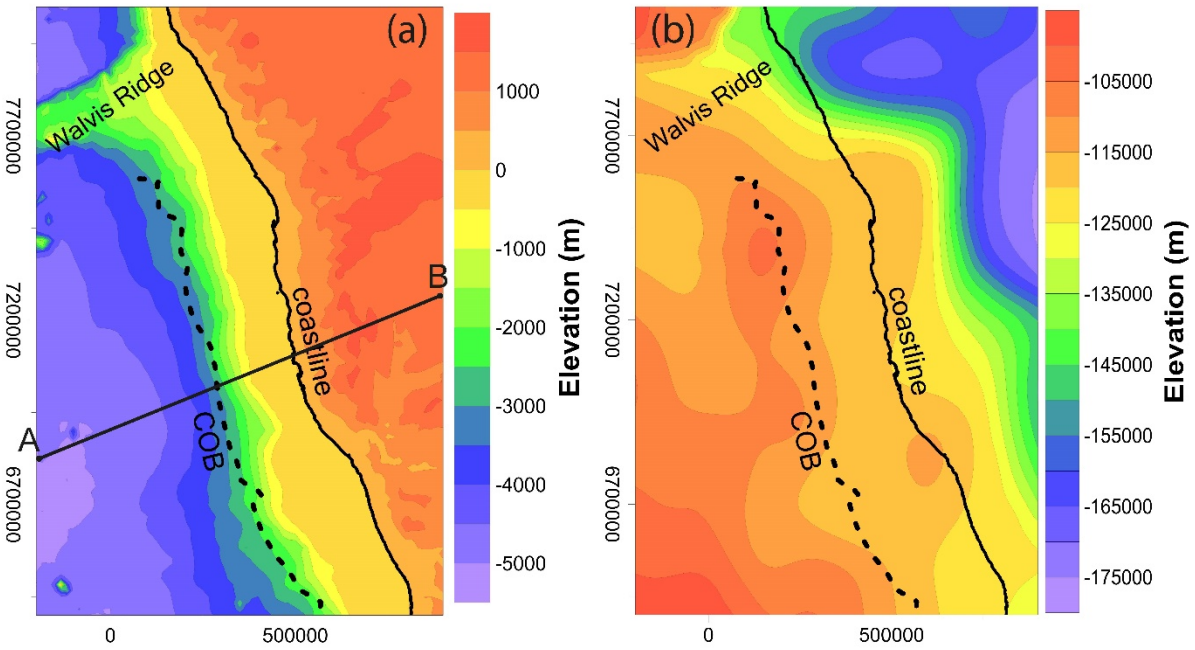

Figure 4.4. Surfaces with a fixed temperature for which the thermal boundary conditions were assigned in the SW African thermal model: (a) topography–bathymetry corresponding to the upper thermal boundary condition (5 °C); (b) depth of the LAB utilized as the lower thermal boundary condition (1300 °C).

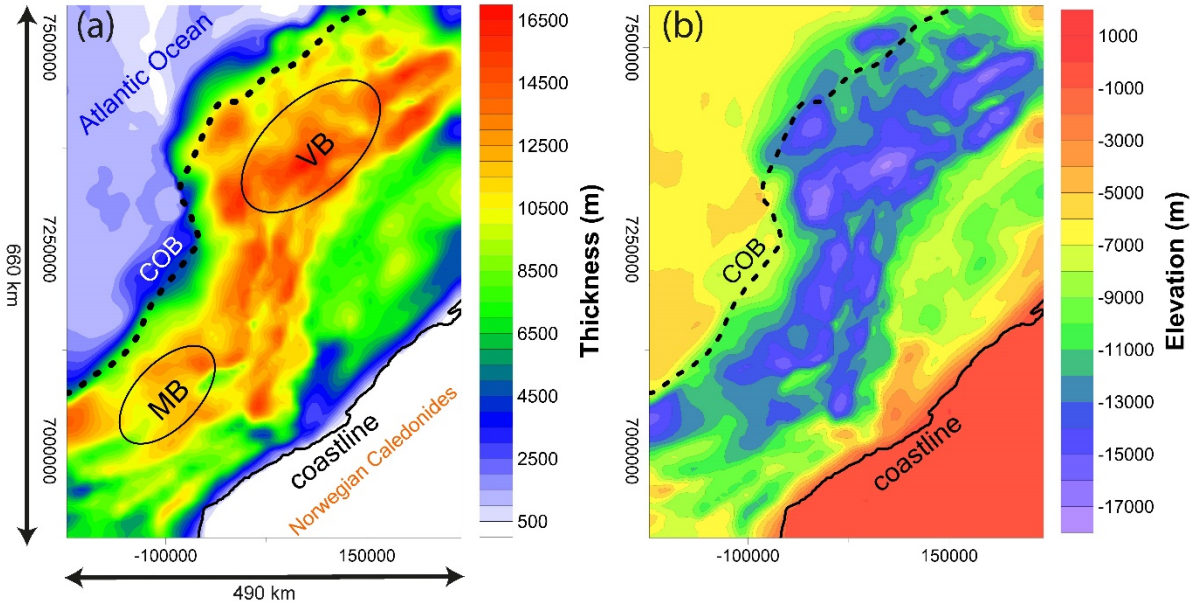

Figure 4.5. 3-D structural model of the Norwegian margin: (a) cumulative sediment thickness; (b) depth to top basement (COB: continent– ocean boundary, VB: Vøring Basin, MB: Møre Basin, UTM: WGS84, zone 33N).

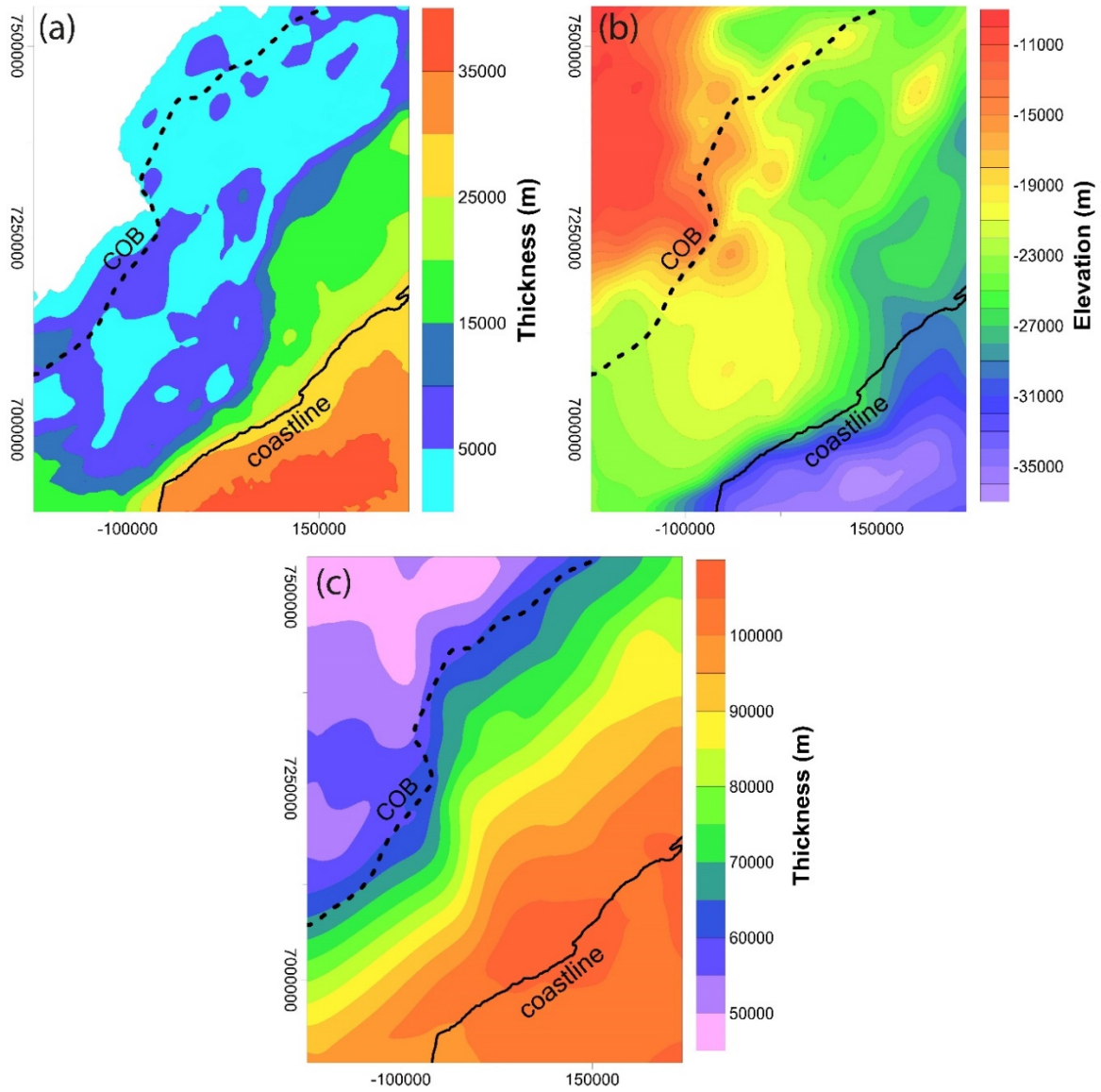

Figure 4.6. 3-D structural model of the Norwegian margin: (a) thickness of the upper crystalline crust; (b) depth to Moho; (c) thickness of the lithospheric mantle at the Norwegian continental margin.

For the thermal model (Scheck-Wenderoth and Maystrenko, 2008), a 2 °C isotherm was assigned as the upper thermal boundary condition at the topography and bathymetry (Fig. 4.7a). Onshore, the topography reaches elevations of close to 2000 m a.s.l. and descends seaward. Offshore, the wide continental shelf is a few hundred meters below sea level. and descends to more than 3500 m b.s.l. in the oceanic crustal domain.

In addition to the upper thermal boundary condition setting and equivalent to the SW African margin, the LAB surface was considered as the lower thermal boundary condition (1300 °C). The depth to the LAB (Fig. 4.7b) changes gradually from 55 km b.s.l. in the oceanic crustal domain to 140 km b.s.l. onshore.

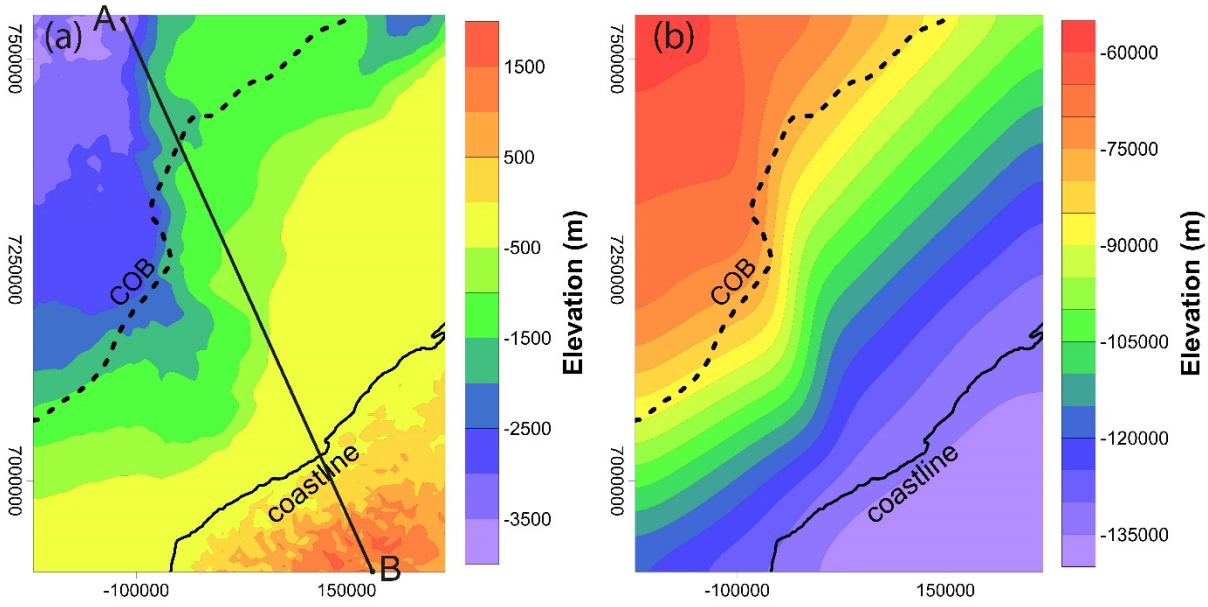

Figure 4.7. Surfaces with a fixed temperature for which the thermal boundary conditions were assigned in the Norwegian thermal model: (a) topography–bathymetry corresponding to the upper thermal boundary condition (2 °C); (b) depth of the LAB utilized as the lower thermal boundary condition (1300 °C).

4.4. Results

Our results show that the geothermal gradient varies laterally across the model area and nonlinearly decreases with depth (Figs. 4.8, 4.9, and 4.10; see also Figs. S4.3 and S4.4). To describe these variations, we classified these results into three different domains considering the geostructural setting: the onshore domain, the continental margin domain (the area between the coastline and the COB), and the oceanic crustal domain.

4.4.1. The onshore domain

In the onshore domain of the SW African model, the geothermal gradient remains in the range of 28–30 °C km^{-1} for all depth levels except for the Precambrian basins (Fig. 4.8). However, there are some local depressions along the coastline. Within the second (Fig. 4.8b) and third (Fig. 4.8c) levels, the geothermal gradient partly decreases to 26–28 °C km^{-1} along the coastline. Within the deepest level (6 km), this range covers the area more uniformly and to a greater extent (Fig. 4.8d, e, f).

Over the onshore domain, the geothermal gradient in the Norwegian model generally stays in the range of 15–17 °C km^{-1} for all depth levels (Fig. 4.9), and this is the lowest value of the geothermal gradient across the entire model domain. Across the coastline, the geothermal gradient increases steeply seaward from 17 to 27 °C km^{-1} within the first depth level (1 km, Fig. 4.9a), which is related to the transition between crystalline crust onshore and sediment fill offshore. The same pattern, but with different ranges, is also recognizable for the deeper levels (Fig. 4.9).

In general, geothermal gradients in the unthinned onshore domain of the SW African margin are greater than in the corresponding domain of the Norwegian margin (Figs. 4.8 and 4.9).

4.4.2. The continental margin domain

In this domain, the geothermal gradient variations also reveal a general trend of reduction with increasing depth. Nevertheless, this general trend displays different lateral variations for each sedimentary basin.

4.4.2.1 The SW African passive margin

In the SW African model, the results display different patterns of variation for the individual depth levels. Within the first depth level (1 km, Fig. 4.8a), the variations are similar in the Walvis and Lüderitz basins. The geothermal gradient increases seaward from the coast and reaches the largest value (48–50 °C km^{-1}) in the central parts of the sedimentary basins where the sediments are thickest (Fig. 4.2a). Oceanward, the gradient declines again towards the distal shelf where the geothermal gradient is in the range of 38–40 °C km^{-1} along the COB. In contrast, the geothermal gradient follows a different pattern within the Orange Basin. It decreases with distance from the coast, reaches the lowest value (34–36 °C km^{-1}) in the central part of the basin and then increases to the COB. The reduced gradient within the first depth

level in the Orange Basin compared to the two other basins correlates with an increased thickness of the uppermost sedimentary unit of the Cenozoic. This unit has the lowest thermal conductivity of the sedimentary units (Table 4.1) and is almost absent in the central part of the Orange Basin (Maystrenko et al., 2013).

The variations in the geothermal gradient within the second, the third, and the fourth depth levels (Fig. 4.8b, c, and d) follow the same trend as in the first depth level. A notable difference between these three depth levels (second, third, and fourth) and the first depth level is the location of the highest geothermal gradient. Within the second, third, and fourth depth levels, these high values occur in the northern part of the Walvis Basin; this contrasts with the first depth level for which the highest value was found in the Lüderitz Basin (Fig. 4.8a). These high values are in the ranges of 44–46, 42–44, and 40–42 °C km^{-1} within the second, the third, and the fourth depth levels, respectively. This difference is explicable by considering the top basement depth (Fig. 4.2b) and the crustal thickness (Fig. 4.3a), which are shallower and thicker beneath the northern part of the Walvis Basin compared to the Lüderitz Basin. Moreover, the youngest sediments (with lower thermal conductivity) are thickest in the Walvis Basin (Table 4.1; Maystrenko et al., 2013), which is an additional reason for these values of high geothermal gradient within the Walvis Basin.

Within the two deepest levels (5 and 6 km), the results show a different pattern of the geothermal gradient variations within the Orange Basin (Fig. 4.8e and f). Unlike the upper depth levels, the geothermal gradient varies in a similar manner to the Walvis and Lüderitz basins. The geothermal gradient increases seaward from the coast, reaches the locally highest value in the central part of the sedimentary basin, and finally declines towards the COB.

Overall, in the SW African model, the highest values of the geothermal gradient for all depth levels occur within the sedimentary basins (Fig. 4.8).

4.4.2.2 The Norwegian margin

The geothermal gradient distribution maps of the Norwegian margin (Fig. 4.9) also reveal lateral and vertical variations across the sedimentary basins.

In the Vøring Basin, the geothermal gradient varies in a similar manner for all depth levels, except the sixth level (Fig. 4.9). Generally, the gradient increases seaward from the coast,

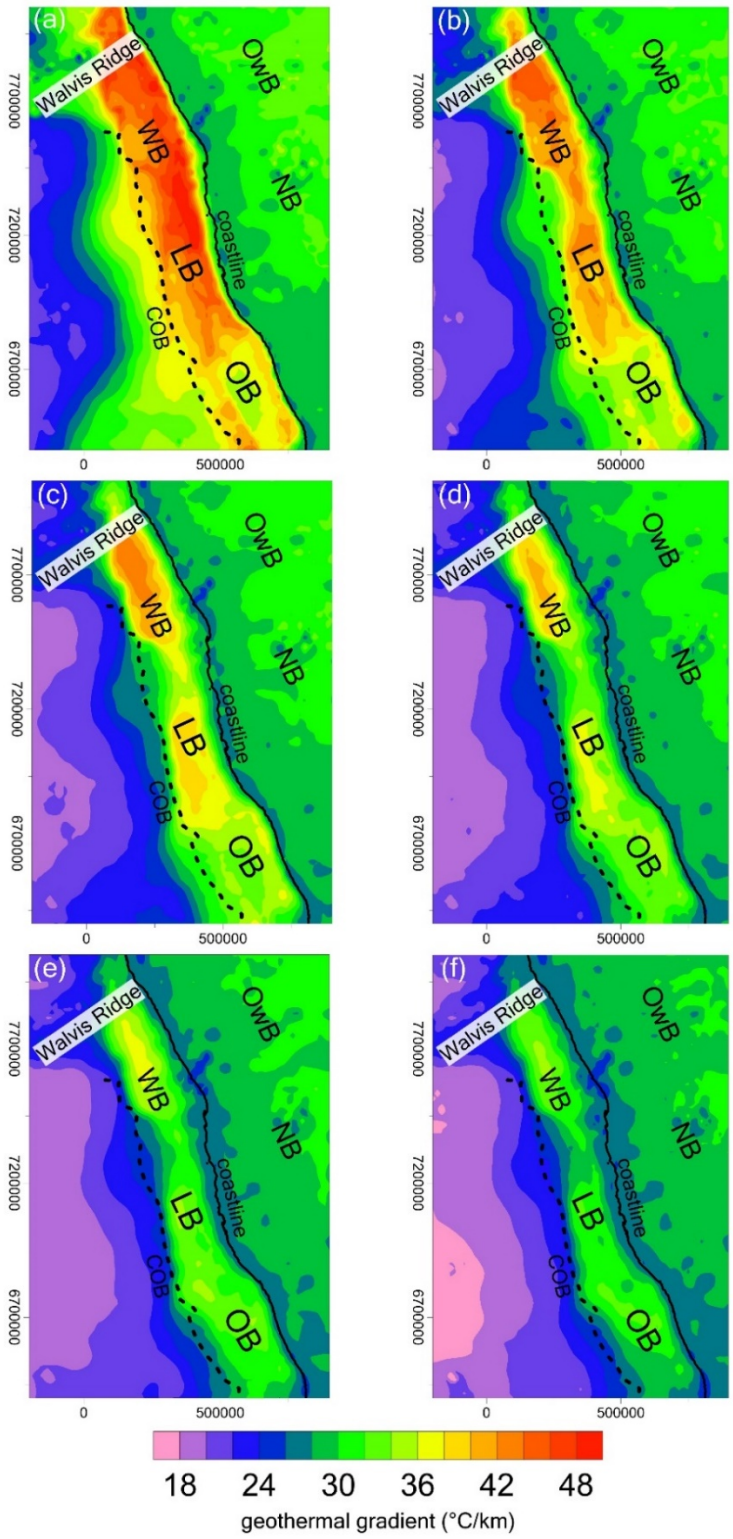

Figure 4.8. Geothermal gradient (°C km^{-1}) at the SW African margin: the gradient calculated as the temperature differences between the uppermost surface (upper thermal boundary) and the corresponding temperature distribution at (a) 1, (b) 2, (c) 3, (d) 4, (e) 5, and (f) 6 km below the uppermost surface (COB: continent–ocean boundary; Cretaceous–Cenozoic basins: WB: Walvis Basin, LB: Lüderitz Basin, OB: Orange Basin; Precambrian basins: OwB: Owambo Basin, NB: Nama Basin; UTM: WGS84, 33S).

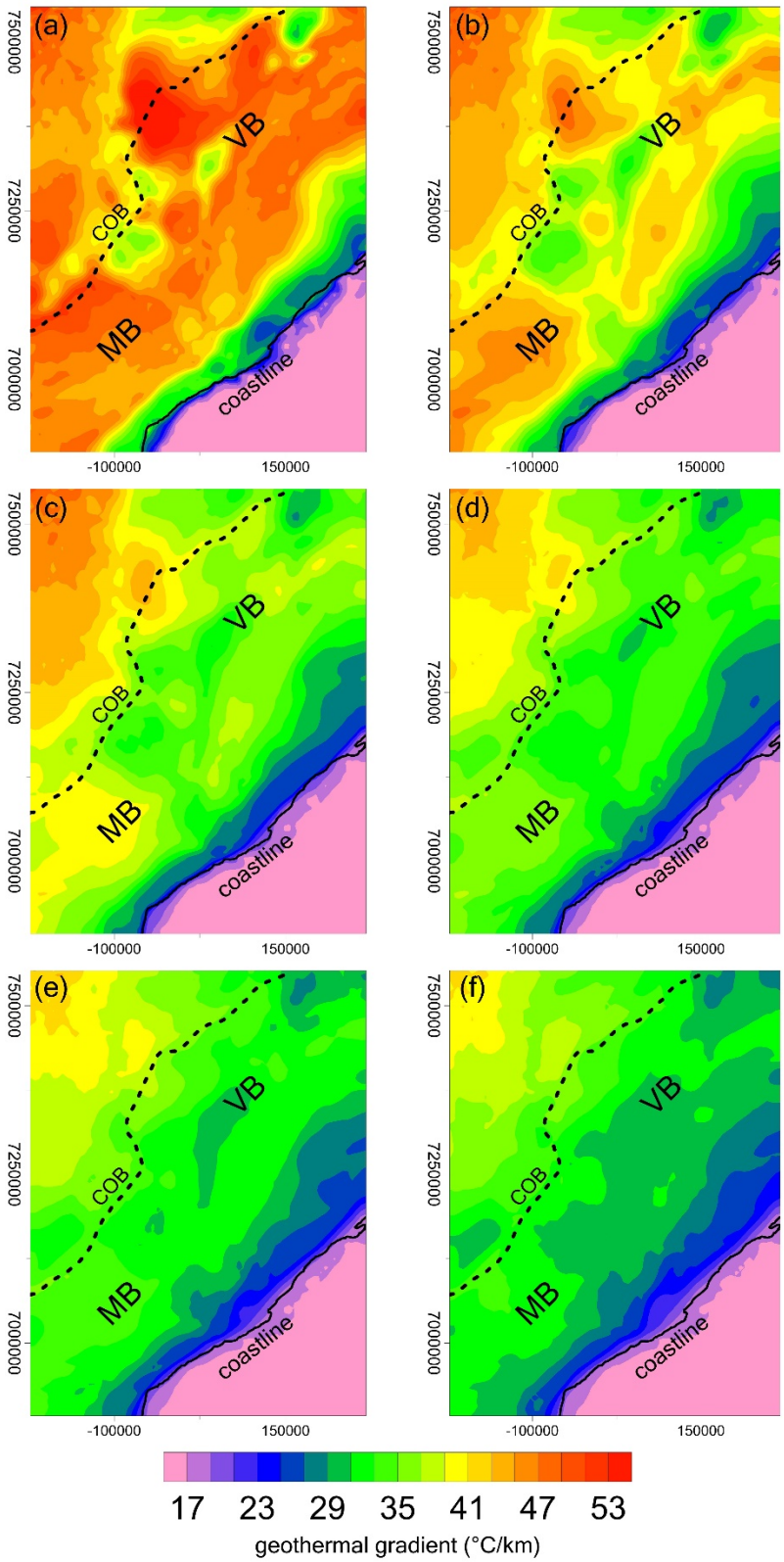

Figure 4.9. Geothermal gradient (°C km^{-1}) at the Norwegian margin: the gradient calculated as the temperature differences between the uppermost surface (upper thermal boundary) and the corresponding temperature distribution at (a) 1, (b) 2, (c) 3, (d) 4, (e) 5, and (f) 6 km below the uppermost surface (COB: continent–ocean boundary; Cretaceous–Cenozoic basins: VB: Vøring Basin, MB: Møre Basin; UTM: WGS84, 33N).

decreases in the central part of the basin, and then increases again toward the COB. Similar to the Orange Basin at the SW African margin, the decrease in the gradient is akin to the central part of the Vøring Basin, where the uppermost Cenozoic sedimentary unit with the lowest thermal conductivity (Table 4.1) is absent (Scheck-Wenderoth et al., 2007). Within the deepest level (Fig. 4.9f), the geothermal gradient increases gradually from the coast towards the COB and no reduction occurs in the central part of the basin. The highest values of the geothermal gradient within the Vøring Basin are found at the distal shelf. These values are in the range of 53–55 °C km^{-1} in the first depth level and attain 35–37 °C km^{-1} within the deepest level.

In contrast to the Vøring Basin, the geothermal gradient within the Møre Basin does not follow a comparable pattern in the first two depth levels. Within the first level, the geothermal gradient increases gradually and continuously from the coast towards the COB (Fig. 4.9a). In the second depth level, the geothermal gradient increases from the coast to the central part of the basin and decreases towards the COB (Fig. 9b). Within the other four depth levels (Fig. 4.9c to f), the general trend of the geothermal gradient variations is similar to the first depth level.

4.4.3. The oceanic crustal domain

The oceanic crustal domain refers to the western side of the COB where the crust is mainly oceanic in composition. Herein, the geothermal gradient variations differ significantly between the SW African and the Norwegian margins.

In the SW African model, the results of the calculated geothermal gradient (Fig. 4.8) for the oceanic crustal domain and within all the depth levels indicate a lateral oceanward decrease. The geothermal gradient gradually decreases oceanward from the COB to reach the minimum at the western model boundary. These lowest values are in the range of 16–18 °C km^{-1} within the deepest level and 18–20 °C km^{-1} within the other five levels, representing the lowest value of the geothermal gradient over the entire model of the SW African Margin (Figs. 4.8 and 4.11c).

In contrast, the results for the Norwegian setting (Fig. 4.9) show that the geothermal gradient increases oceanward in the oceanic crustal domain, where the highest values of the geothermal gradients over the entire margin are found (Figs. 4.9 and 4.11c). From the first depth level (1 km) down to the deepest level (6 km), these high values decrease stepwise from 53–55, 47–49, 45–47, 43–45, 41–43, to 39–41 °C km^{-1}. The 65 Myr year difference in the oceanic crust age (SW Africa: 130 Ma; Norwegian: 55 Ma; see Table 4.1) and the related age-controlled depth

of the thermal LAB (Figs. 4.4b and 4.7b) would be a reasonable explanation for this difference within the oceanic crustal domain of the two differently aged margins. At the older SW African passive margin, the shallowest depth to the LAB is around 100 km b.s.l., below the oceanic crustal domain (Fig. 4.4b), while the LAB depth at the younger Norwegian margin is less than 60 km b.s.l. (Fig. 4.7b).

4.5. Interpretation and discussion

According to our results, the calculated geothermal gradients reveal variations both laterally and with depth for the two different passive margins (Figs. 4.8 and 4.9). In general, the geothermal gradient decreases nonlinearly with depth in both models. However, this occurs in different trends for the two settings. Calculation of the geometric mean value of the geothermal gradient fully shows a nonlinear decrease from the first depth level to the deepest level by 40 to 30 °C km^{-1} in the Norwegian margin and by more than 32 to less than 26 °C km^{-1} in the SW African margin (Fig. 4.10). To address the differences between the present-day thermal field of the SW African passive margin and the Norwegian margin, it is important to compare the geothermal gradient variations with the geological structure, the thermal properties of comparing geological units, and the ages of the oceanic crust (Table 4.1). A structural–thermal cross section (Fig. 4.11a and b) and corresponding profile of average geothermal gradient (Fig. 4.11c) provide supplemental indications for a valid interpretation of shallow thermal field variations across the two differently aged passive margins. We will discuss these issues with regards to the three previously mentioned domains: (1) the onshore domain, (2) the continental margin domain, and (3) the oceanic crustal domain.

Temperature–depth function is simply a linear concept of the geothermal gradient (Eq. 4.3). However, as can be seen from the two models, the geothermal gradient depends on the considered depth level and varies nonlinearly with depth. The solution to the steady-state thermal diffusion equation (Eq. 4.4 derived from Eq. 4.2) is a second-order (nonlinear) temperature function of depth if radiogenic heat production is considered ($S \neq 0$). This fact indicates that the temperature–depth ($T - z$) curvature is highly sensitive to the amount of radiogenic heat production. The interaction of the thermal conductivity of different lithospheric layers and the heat internally produced by the decay of radioactive elements overprint the heat input from larger mantle depth into the lithosphere (Eq. 4.4). For better comprehension and

further comparability, investigating the variability of the geothermal gradient requires representing the same depth levels across the study areas.

$$\frac{\partial^2 T}{\partial z^2} = \frac{S}{\lambda} \tag{4.4}$$

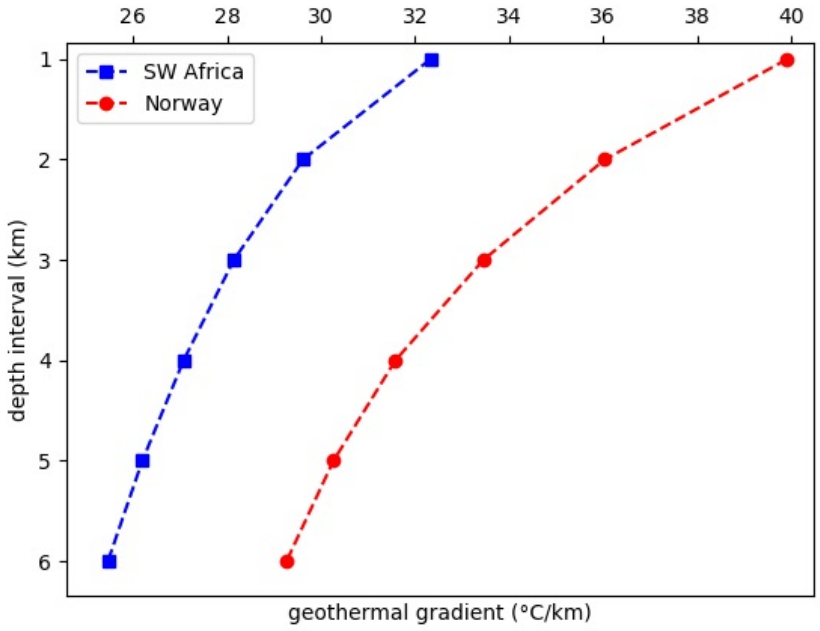

Figure 4.10. The thermal gradient variations with depth: mean values of the geothermal gradient (C km^{-1}) across the model area and for the different depth levels. The temperature–depth distribution maps are presented as Figs. S4.1 and S4.2.

4.5.1. The onshore domain

In the onshore domain, the geothermal gradient is considerably higher (~ 13 °C km^{-1}) at the SW African margin compared to the Norwegian margin. The SW African margin has a thicker crust compared to the Norwegian margin (Figs. 4.3a, 4.6a, 4.11a) and thus relatively more radiogenic heat is contributed by the crust. Additionally, a second reason could be the assigned values of radiogenic heat production in the thermal models (see Eq. 4.4). In the Norwegian model, Scheck-Wenderoth and Maystrenko (2008) considered an average crustal radiogenic heat production of 0.8 µW m^{-3}, which is much lower than the corresponding value (1.45 µW m^{-3}) in the SW African thermal model (Table 4.1). This low value of the geothermal gradient within the onshore domain in the Norwegian model agrees with downhole temperature

measurements in the Scandinavian Caledonides that imply an average geothermal gradient of ~17–20 °C km^{-1} (e.g., Maystrenko et al., 2015; Lorenz et al., 2015; Pascal, 2015).

Another impressive characteristic of the thermal field of these two passive margins is in the vicinity of the coastline. Here, the geothermal gradient decreases by about 2 °C km^{-1} at the SW African margin. This reduction spatially correlates with the crustal thickness decrease (~ 10 km) beneath the coast (Fig. 4.3a). The thinner crust produces less radiogenic heat, which leads to lower temperatures. In contrast, considering the same area at the Norwegian margin, the geothermal gradient increases by approximately 10 °C km^{-1} within the first depth level and gradually decreases within the deeper depth levels. These variations might be explained by the thermal blanketing effect of the up to 1.5 km thick insulating sediments (low thermal conductivity; Table 4.1) along the coast (Fig. 5.5a). While the outcropping crystalline crust onshore efficiently transports heat to the surface in response to its greater thermal conductivity, the heat is stored in the insulating sediments offshore.

4.5.2. The continental margin domain

To interpret the thermal field variations within the sedimentary basins and to compare these differences between the SW African and the Norwegian margins, we need to take a closer look at the geometry of the geological structural units within and beneath the location of the sedimentary basins. These units were presented in Sect. 4.3 and here we will discuss how they affect the thermal field.

Heat is transferred from the oceanic domain to the adjacent distal margin as a natural consequence of the 3-D heat transport. Thereby the local structural configuration and the related variable distribution of thermal rock properties leads to a very specific thermal pattern, be it in the area of “normal” or transfer segments of the margin. Accordingly, our results are consistent with earlier studies analyzing the transition from the oceanic to the continental domain (Nemcoket al., 2012; Henk and Nemcok, 2016).

4.5.2.1. The SW African passive margin

Considering the geothermal gradient variations over the whole study area at the SW African passive margin, the highest values for the geothermal gradient occur within the sedimentary basin areas. Beneath the continental margin, the crystalline crust is thinner (i.e., less radiogenic heat production) in comparison to the onshore domain (Fig. 3.3a). Moreover, the LAB is also deeper beneath the sedimentary basins compared to the LAB depth below the oceanic crustal

domain (Fig. 4.4b). Accordingly, in spite of a lower radiogenic heat production and a larger depth to the thermal LAB, the gradients are highest in the sedimentary part. This indicates that the thermal blanketing effect of the insulating sediments has the strongest control on the shallow thermal field variations within the sedimentary basins, and geothermal gradients widely correlate positively with sediment thickness.

The top basement (Fig. 4.2b) is much deeper below the Orange Basin and the radiogenic crust thinner compared to the Walvis and Lüderitz basins (~ 10 km difference in the center of the sedimentary basins). Accordingly, the thicker sediments within the Orange Basin (Fig. 4.2a) lead to a more pronounced thermal blanketing effect due to the low thermal conductivity of these sediments. Additionally, Cenozoic sediments with lower thermal conductivity are thicker in the Walvis and Lüderitz basins compared with the Orange Basin (Table 4.1; Maystrenko et al., 2013). These differences in the top basement depth and the thickness of younger sediments with low thermal conductivity would explain why the geothermal gradient has the lowest local value in the central part of the Orange Basin in the upper depth levels 1 to 4 km below the upper thermal boundary condition. Within the deeper levels, between 4 and 6 km below the upper thermal boundary condition, all sediments have a Cretaceous age (Table 4.1; Maystrenko et al., 2013). Consequently, the thermal field pattern shows more similarity within all the three sedimentary basins and the geothermal gradient increases toward their central part (Fig. 4.8e and f).

4.5.2.2. The Norwegian margin

In general, the geothermal gradient variations within the sedimentary basins show fewer complexities at the Norwegian margin in comparison to the SW African passive margin. Within the Vøring Basin and for all depth levels, the geothermal gradient generally increases seaward, decreases in the central part of the basins, but increases again toward the distal shelf (Fig. 4.9). While the crystalline crust is thinner (i.e., less radiogenic heat is produced) beneath the sedimentary basins compared to the onshore domain (Fig. 4.6a), the lithospheric mantle (Fig. 4.6c) gradually thins and the LAB (Fig. 4.7b) becomes progressively shallower towards the ocean. In addition, the lack of the post-breakup (uppermost Cenozoic) sedimentary unit in the central part of the Vøring Basin reduces the thermal blanketing effect of insulating sediments (Table 4.1; Scheck-Wenderoth et al., 2007). With increasing depth, the thermal blanketing effect of Cenozoic sediments becomes less relevant for the thermal field variations, while the depth to the LAB plays a more prominent role. As shown in Fig. 4.9f the geothermal gradient

reveals no depression in the central part of the Vøring Basin, but increases seaward due to the shallower LAB and the thinner lithospheric mantle. The same reason would explain the geothermal gradient pattern that characterizes the Møre Basin. Overall, the pattern of the shallow thermal field looks similar for all depth levels in the Møre Basin, increasing gradually from the continental shelf towards the distal shelf. This trend agrees with the oceanward shallowing LAB depth.

The absolute values of the geothermal gradient within the sedimentary basins in the Norwegian model are larger compared to the corresponding values in the SW African model. The highest geothermal gradient at the SW African passive margin occurs within the sedimentary basins (Sect. 4.5.2.1), whereas this is not the case for the Norwegian model. In addition to the quantitative differences, these high values exist within the central part of the sedimentary basins at the SW African margin, while for the Norwegian model the highest local values of the geothermal gradient in the continental margin domain occur closer to the distal shelf. These differences indicate fundamentally different controlling factors for the shallow thermal field at these two differently aged passive margins.

4.5.3. The oceanic crustal domain

The oceanic crustal domain is most important for comparing the shallow thermal field variations for the SW African passive margin and the Norwegian margin. While the SW African model has the lowest values of the geothermal gradient in this domain (Fig. 4.8), the Norwegian model presents the highest value of the geothermal gradient (Fig. 4.9).

The volcanic passive margin of Norway (55 Ma) is significantly younger than the SW African passive margin (130 Ma). This age contrast resulted in an approximate 40 km depth difference of the thermal LAB for these two passive margins (Figs. 4.4b and 4.7b). The consequence of this shallower oceanic LAB is a steeper average geothermal gradient as the 1300 °C difference between the surface and the LAB needs to be accommodated within 60 km. This distance is almost twice as large at the SW African margin where the oceanic LAB is at 110 km of depth. Accordingly, the young Norwegian margin is hotter in comparison to the old SW African margin, which appears to be thermally equilibrated (Maystrenko et al., 2013).

One clear point stands out and that is the first-order difference in the age of breakup at the two margins. Also, the timing of potential interaction in the oceanic opening with a mantle plume is different. For the South Atlantic, recent results (Scheck-Wenderoth et al., 2017) suggest that

the breakup was not initiated by a mantle plume, but some interactions with the Tristan da Cunha hot spot may have influenced the evolution. Both the opening and the potential breakup–plume interactions were terminated at about 130 million years before present. Thus assuming steady-state thermal conditions today is a valid hypothesis as thermal equilibration has been achieved. This is also expressed in the thick oceanic mantle lithosphere derived from seismological and gravity data.

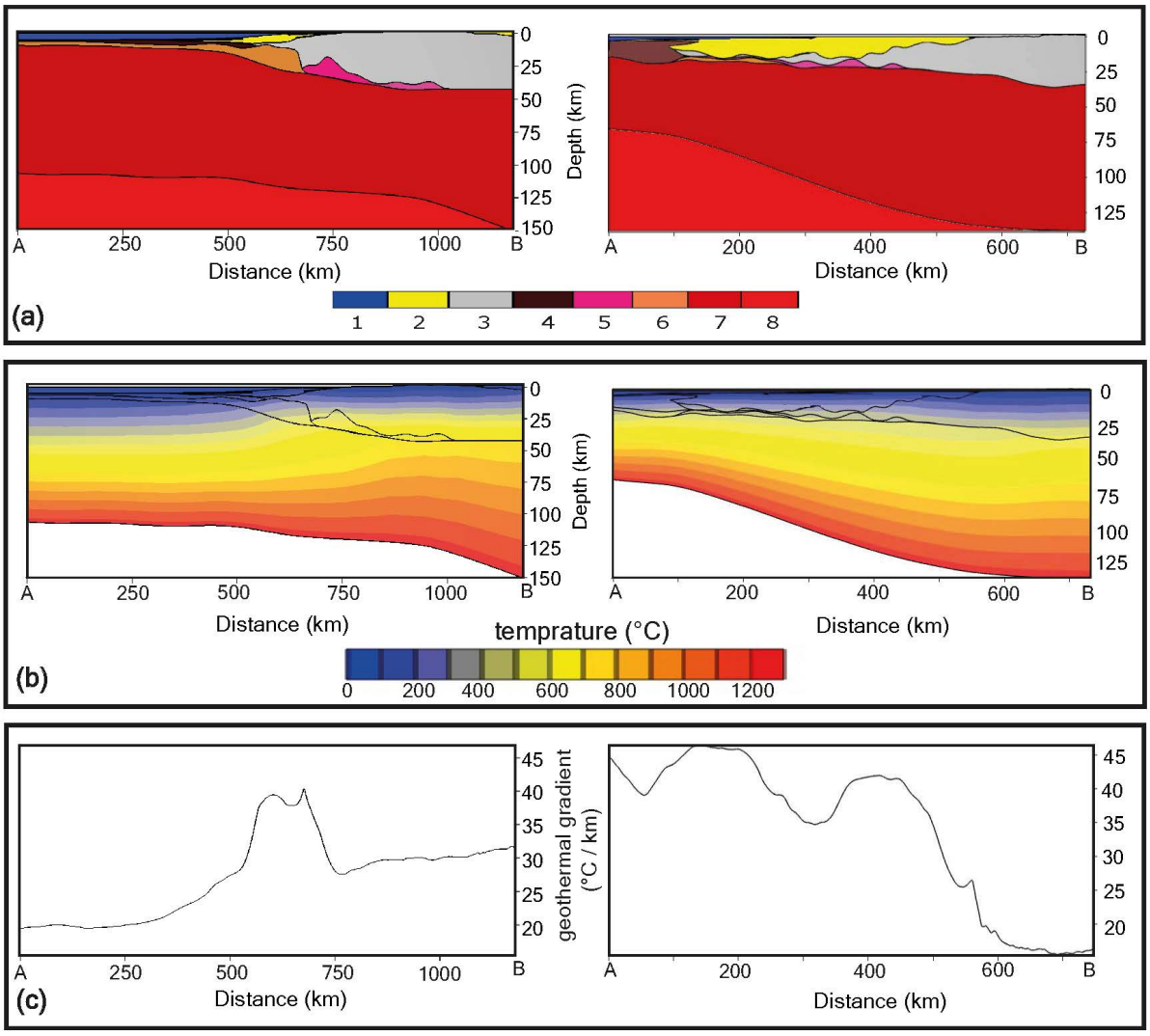

Figure 4.11. Structural–thermal cross section and corresponding average geothermal gradient at the SW African passive margin (left) and Norwegian continental margin (right) after Scheck-Wenderoth et al. (2007); Scheck-Wenderoth and Maystrenko (2008); Maystrenko et al. (2013). (a) Structural crustal cross section along the A–B profile (Figs. 4a and 7a). Numbers near color legend for individual layers: (1) water, (2) sediments, (3) crystalline continental crust, (4) oceanic crust, (5) high-density continental crust, (6) high-velocity high-density lower crustal layer, (7) normal-density mantle, (8) low-density mantle. (b) Temperature distribution within the A–B cross section. (c) Calculated average geothermal gradient along the A–B cross section.

In contrast, the Iceland plume is next door to the Norwegian North Atlantic margin today (Steinberger and Torsvik, 2012) and breakup is significantly younger (55 million years before present). Given the time–thermal constant of the lithosphere, thermal disturbances older than 65 Ma would largely have equilibrated (Turcotte and Schubert, 2014). This implies that the thermal consequences of breakup should have declined after 55 million years and that the system is at least close to thermal equilibrium today. Though this consideration does not account for additional dynamic thermal effects induced by the Iceland plume we use a steady-state thermal model (Scheck-Wenderoth and Maystrenko, 2008) to assess the deep thermal field for two reasons: (1) we aim to base our comparison of the two margins on the same method and (2) both models are consistent with observed temperatures in the upper few kilometers (e.g., Channell et al., 2006) and with surface heat flow (e.g., Ritter et al., 2004). We would additionally like to point out that the potential error related to the steady-state assumption would, in the worst case, cause an underestimation of the mantle heat input, but not the other way round. Reaching the high observed shallow temperatures with a transient simulation, while at the same time respecting the thermal lithosphere base indicated by seismology and gravity, would either require a higher temperature at the base of the lithosphere (if the process is at an early stage) or a late stage in thermal equilibration (close to steady-state).

A further discussion point relates to the nature of the lower crustal body. Depending on which lithology is assumed for the latter, higher (mafic underplate: gabbro) or lower (serpentinized mantle) thermal conductivities and different amounts of radiogenic heat production would result. Autin et al. (2016) have examined the thermal implications of these different compositions for lower crustal bodies at the Argentine magma-rich margin of the South Atlantic. They found that apart from the serpentinite model being colder, the thermal effects of gabbro and eclogites would be similar.

Proximity to the Iceland mantle plume might also be effective in causing high geothermal gradients in the oceanic crustal domain of the Norwegian margin. The North Atlantic breakup was possibly initiated by the abnormally hot mantle of the Iceland plume (White, 1989; Skogseid et al., 1992; Gernigon et al., 2004, 2006; Parkin and White, 2008) activated approximately 5 million years earlier than the continental breakup (Saunders et al., 1997). While some studies have shown that the Iceland plume propagated northward (e.g., Ruedas et al., 2007; Steinberger et al., 2015), seismic tomography (Rickers et al., 2013) suggests lateral movement of plume material in addition to the parallel propagation along the mid-ocean ridge.

Moreover, 3-D thermomechanical models (Koptev et al., 2017) suggest that plume-related thermal perturbations such as hot mantle lateral flows may result in topography at the Norwegian passive margin with long wavelength variations onshore and short wavelength variations offshore. To quantify such effects, future studies need to consider observation-based configurations, but also implement the physics of processes controlling mass and energy transport related to mantle flow dynamics.

With respect to the hypothesis formulated in the introduction that the present-day thermal field at passive continental margins is determined by lithospheric mantle characteristics, our results suggest that considering variations in the crust alone is not sufficient to properly assess the present or past thermal configuration of passive continental margins.

4.5.4. Implications

More recent studies apply complex modeling approaches to simulate thermal histories considering spatial and temporal variations in temperature profiles (e.g., Person and Garven, 1992; Bertotti and Ter Voorde, 1994; Ehlers and Farley, 2003; Ehlers et al., 2003). However, these methods of thermal history reconstruction are mostly based on paleotemperature indicators that experience irreversible structural changes when passing through a certain temperature window (Allen and Allen, 2005; Naeser and McCulloh, 2012), but do not consider observation based on three-dimensional structural settings. The thermal alteration of organic matter, for example, results in specific changes in vitrinite reflectivity, and linear relationships between temperature and vitrinite reflectivity have been established using lab experiments (Dow, 1977; Barker and Pawlewicz, 1986; Burnham and Sweeney, 1989; Corcoran and Clayton, 2001). Likewise, apatite fission track analysis makes use of the specific temperature-dependent behavior of fission track in response to radiogenic decay (Barker, 1996; Gallagher et al., 1998; Stockli et al., 2000; Reiners and Brandon, 2006; Deeken et al., 2006). Such paleotemperature indicators are often translated to amounts of paleo-burial depth assuming a constant paleothermal gradient for a certain study area and the difference between the present-day depth and the paleo-depth is interpreted in terms of vertical movements.

Our results indicate that the thermal gradient may vary significantly both laterally and with time (Fig. 4.11). Accordingly assuming an average paleothermal gradient of 30 °C km^{-1} positions the 70 °C window of an apatite sample at 2 to 3 km of depth, whereas a higher paleo-geothermal gradient of 45 °C km^{-1} would position the same sample at 1.5 km of depth.

Therefore, considering paleo-geothermal gradient variation in response to sedimentation or lithosphere cooling is key if paleotemperatures, paleo-elevations, and vertical movements derived from the latter are deduced. This implies that in addition to the general paleo-tectonic setting, the evolutionary phase and the position in this setting also need to be considered. For passive margin settings this means that it is not only important to take into account the type of passive margin (magma-rich versus magma-poor) but also the location (relative to the continent and to the newly formed oceanic domain) and the time with respect to breakup. A sample from a proximal or distal domain at an early or late stage of evolution has experienced different thermal imprints and the paleo-position should be considered accordingly in thermal history reconstruction.

4.6. Conclusions

The assessment of variations in the geothermal gradient for the two different passive volcanic margins revealed the following.

1. In spite of a similar crustal structure, the geothermal gradient differs laterally across the two passive margins and nonlinearly decreases with depth.

2. The thermal field of the two margins is contrasting. At the Norwegian margin (young) the thermal field is mostly dominated by the thermo-tectonic age and the thermal LAB depth in contrast to the SW African margin (old) where the crustal configuration dominates the pattern of the equilibrated shallow thermal field.

3. Over the onshore domain, the radiogenic heat production is the main heat-controlling factor for both settings. Within the sedimentary basins, the thermal blanketing effect of the insulating sediments has the highest impact on the shallow thermal field at both margins. In the oceanic crustal domain, the thermal field is highly affected by the age of the ocean and the thermal LAB depth. Therefore, the Norwegian model is significantly hotter than the SW African model in the oceanic crustal domain and in the distal margin.

4. While the causative thermal anomaly leading to margin formation in the South Atlantic should be equilibrated, the thermal disturbance in the North Atlantic and the proximity

to the Iceland plume obviously cause thermal effects at the present day. Characteristics of the lithosphere ultimately determine the thermal field for the two settings.

5. The fact that the geothermal gradient is nonlinear and varies across areas has implications for methods of thermal history reconstruction.

Chapter 5

Rheological models of the magma-rich continental rifted passive margins

5.1. Introduction

In the previous chapter, it was shown that in spite of a similar crustal structure of the two magma-rich passive margins in the North and South Atlantic, the present-day thermal field of the two margins is contrasting. In summary, the old SW African passive margin is colder across the oceanic domain while it is hotter over the continental domain (Figs. 4.8 and 4.11). This pattern is totally inverse at the young Norwegian passive margin. There, the oceanic domain is significantly hotter than the continental domain (Figs. 4.9 and 4.11). It was also discussed that these thermal differences between the SW African margin and the Norwegian margin are mainly related to the thermo-tectonic age and depth to the thermal lithosphere-asthenosphere boundary (LAB).

In this chapter, the main objective is to test if and how these thermal differences would affect the present-day lithospheric-scale rheological behavior below the two passive margins. Therefore, a static 3-D lithospheric-scale rheological model is individually introduced for each structural-thermal model of the SW African and Norwegian passive margins. In addition, these results are compared for both structural-thermal models to see how differences in thermo-tectonic age would translate to present-day lithospheric strength. Briefly, the main interest is to assess the rheological responses of these two models of differently aged magma-rich passive margins and to qualitatively compare their modeled rheology.

In this regard, the same equations and methodology as described in Chapter 3 are applied to model the lithospheric strength at the location of the passive margins. Accordingly, structural and thermal models of the Norwegian margin (Scheck-Wenderoth et al., 2007; Scheck-Wenderoth and Maystrenko, 2008) and SW African margin (Maystrenko et al., 2013) are considered as inputs for the rheological modeling. Correspondingly, the assigned mechanical parameters for the structural units (Table 5.1) are chosen based on a comparison between the interpreted lithology of the modeled units (physical properties) and their counterparts in the reference rheological types (laboratory measurements).

5.2. Results

The results of the rheological modeling are illustrated as variations of the calculated integrated lithospheric and crustal strength values across the model areas, as well as the ratio of the crustal strength to the total lithospheric strength (Fig. 5.1 and 5.2). In addition, to analyze the spatial

Table 5.1: Mechanical properties of the modeled geological units based on the interpreted lithology (after Scheck-Wenderoth and Maystrenko, 2008; Maystrenko et al., 2013) and their corresponding compilations of laboratory measurements.

Modeled geological unit	Sediments	Crystalline crust	High-density crust	High-velocity body	Oceanic crust	Mantle (lithospheric)
Average bulk density (ρ) [kg m^{-3}]	varies between 2000 - 2650	2800	3050	3150	2950	3200
Dominate lithology	Clastic sediments	Felsic (granite, gneiss)	Mafic (mafic granulite)	Mafic (mafic granulite)	Intermediate to mafic (basalt, gabbroic rocks)	Peridotite (ultramafic)
Reference rheological type	Brittle sediments	Granite dry [a]	Mafic granulite [b]	Mafic granulite [b]	Diabase dry [a]	Olivine dry [c]
Activation enthalpy (Q) [kJ]	–	186	445	445	276	510
Power-law exponent (n)	–	3.30	4.20	4.20	3.05	3.00
Power-law strain rate (A) [Pa^{-n} s^{-1}]	–	3.16E-26	8.83E-22	8.83E-22	6.31E-20	7.00E-14

[a] Carter and Tsenn (1987), [b] Wilks and Carter (1990), [c] Goetze and Evans (1979).

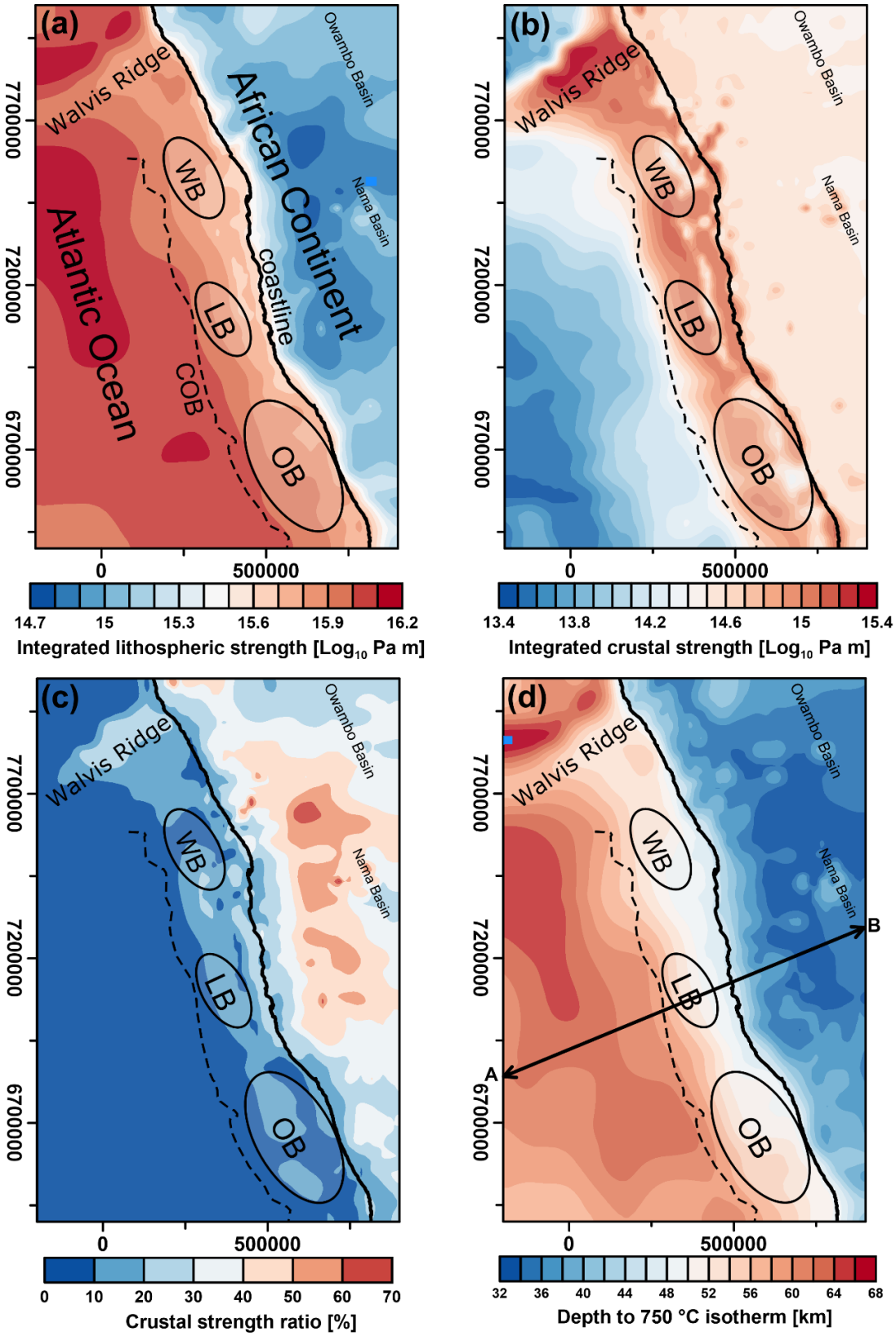

Figure 5.1. Thermal and rheological models of the SW African passive margin. (a) Total integrated lithospheric strength. (b) Integrated crustal strength. (c) The ratio of crustal to total lithospheric strength. (d) Depth to 600 °C isotherm. AB shows the location of the profile in Fig. 3. Abbreviations: continent-ocean boundary (COB), Walvis Basin (WB), Lüderitz Basin (LB), Orange Basin (OB). Maps are in UTM: WGS84, zone 33S.

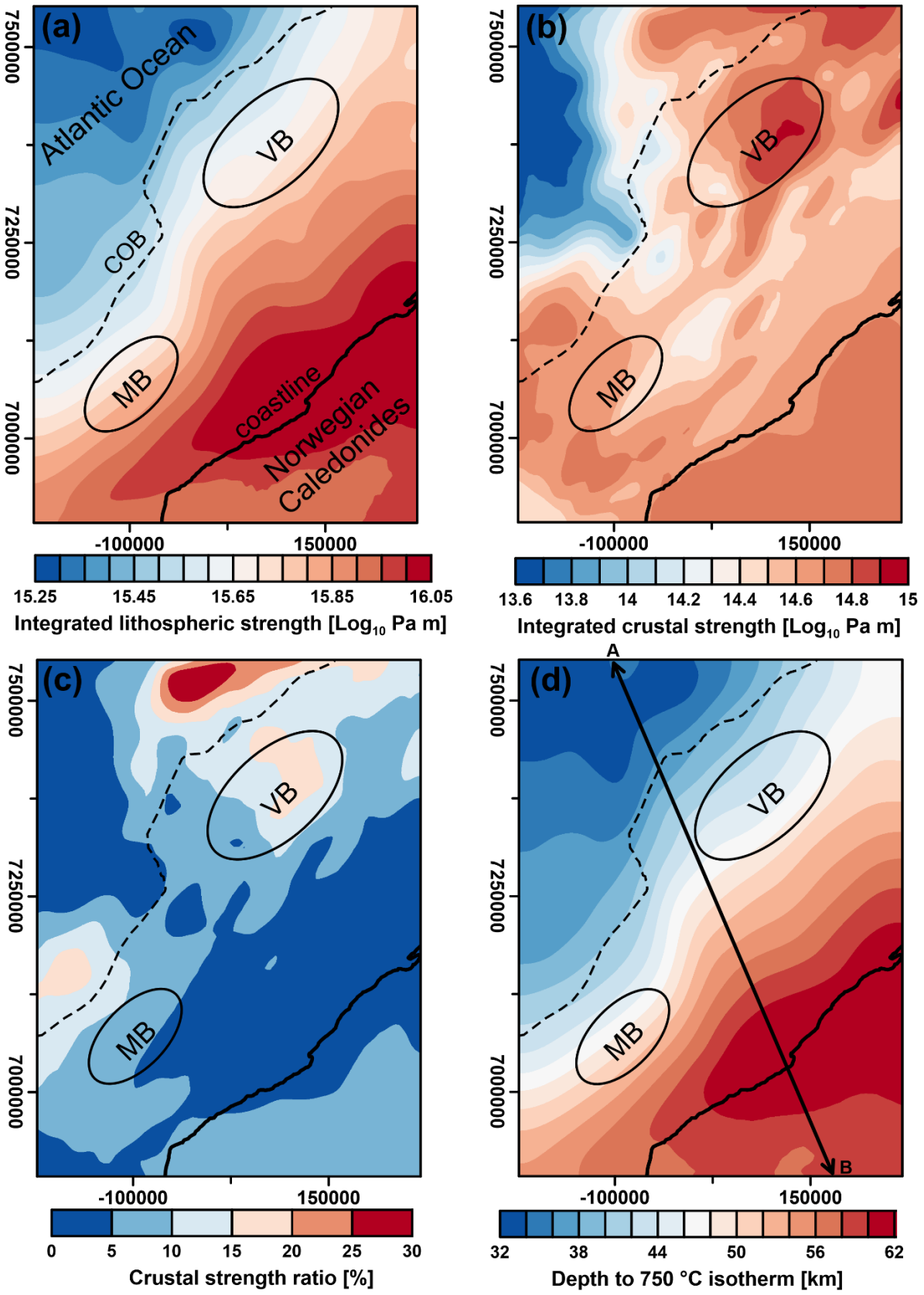

Figure 5.2. Thermal and rheological models of the Norwegian passive margin. (a) Total integrated lithospheric strength. (b) Integrated crustal strength. (c) The ratio of crustal to total lithospheric strength. (d) Depth to 600 °C isotherm. AB shows the location of the profile in Fig. 3. Abbreviations: continent-ocean boundary (COB), Vøring Basin (VB), Møre Basin (MB). Maps are in UTM: WGS84, zone 33N.

correlation between the deep thermal field and the rheological characteristics of each model, the depth to the 750 °C isotherm is also plotted in Figures 5.1 and 5.2.

At the SW African passive margin, the total integrated lithospheric strength values range from 14.7 to 16.2 Log_{10} Pa m (Fig. 5.1a). These values gradually increase from the continental domain towards the oceanic domain that is characterized by the largest modeled lithospheric strength values (Fig. 5.1a). In contrast, the modeled crustal strength (Fig. 5.1b) is smallest (down to 13.4 Log_{10} Pa m) across the oceanic domain, while these values are largest over the margin (up to 15.4 Log_{10} Pa m). Furthermore, the ratio of the integrated crustal strength to the lithospheric strength indicates that the crustal units greatly contribute to the integrated lithospheric strength in the continental domain. However, the crustal contribution is relatively small across the oceanic domain (Fig. 5.1c).

At the Norwegian passive margin, the total integrated lithospheric strength values vary between 15.25 and 16.05 Log_{10} Pa m (Fig. 5.2a). Unlike at the SW African passive margin, the smallest modeled lithospheric strength values are present in the oceanic domain, whereas the largest values are modeled across the marginal and the continental domains. The modeled integrated crustal strength values range from 13.6 to 15 Log_{10} Pa m. The distribution map of these crustal strength values across the Norwegian margin (Fig. 5.2b) indicates the largest values in the continental domain and also in the northern and southern parts of the distal margin. However, as shown by the crustal strength ratio to the integrated lithospheric strength (Fig. 5.2c), the crustal contribution to the total lithospheric strength is generally low. At the highest rate, a ratio of up to 50% is present across the distal margin at the same locations where the highest values of the integrated crustal strength are modeled. These areas spatially correlate with the location of the high-velocity bodies that are interpreted as mechanically strong SDRs mafic rocks (Tables 4.1 and 5.1).

5.3. Discussion

As shown earlier the present-day thermal field is different for these passive margins of the North and South Atlantic. In particular, the ~65 Myr difference in rifting age translates to different lithospheric mantle characteristics, that ultimately control the present-day thermal field beneath these passive margins. As was expected, these two settings are also contrasting in present-day rheological behavior in a similar pattern as the variations in the thermal field.

This illustrates that the thermal history of passive margins may also influence their present-day lithospheric rheological behavior.

At the old SW African passive margin, a strong lithosphere is modeled in the oceanic domain (Fig. 5.1a). Across this area, the lithosphere is considerably colder than its counterparts over the continental domain. For instance, the depth to the 750 °C isotherm is shallower beneath the African continent than below the adjacent Atlantic Ocean (Fig. 5.1d). At the young Norwegian passive margin, however, the oceanic domain represents a weak lithosphere while a strong lithosphere is modeled below the Norwegian Caledonides (Fig. 5.2a). Similar to the SW African model, however, the pattern of the lithospheric strength distribution spatially correlates with the thermal field characteristics across the model area: the lithosphere is weak where it is hot and strong where it is cold. For example, the 750 °C isotherm at the Norwegian margin is relatively deep beneath the coast, while it is shallow below the ocean, representing a cold lithosphere below the continental domain and a hot lithosphere beneath the oceanic domain (Fig. 5.2d). Accordingly, areas with higher values of modeled lithospheric strength at the Norwegian passive margin are obtained for the colder continental domain whereas lower values of modeled lithospheric strength are predicted for the hotter oceanic domain.

Comprehensively, the thermal and rheological models across these two passive margin show that the lithospheric strength is dominantly controlled by the depth to LAB and the thermo-tectonic age. At a young passive margin such as the Norwegian margin, due to the ongoing process of post-break up cooling, the thermal LAB would be relatively shallow beneath the ocean (Fig. 4.7). This consequently leads to a hot and mechanically weak lithosphere (Fig. 5.2). The old SW African passive margin, however, seems to be thermally equilibrated. Consequently, the lithospheric mantle thickness is greater below the ocean (Fig. 4.4). This translates to a colder and accordingly a stronger lithosphere beneath the oceanic domain. As these rheological models suggest, a lithospheric rheological transition (from a weak lithosphere to a stronger lithosphere) also occurs while a passive margin evolves from the rifting and the post-breakup lithospheric cooling phases to the thermal equilibrium state.

For an ultimate comparison between the two models, cross-sections (profiles AB in Fig. 5.1d and 5.2d) are presented in Figures 5.3 and 5.4 for the SW African passive margin and the Norwegian passive margin respectively. On these profiles, in addition to the thermal field illustrated as isotherms along the AB profile, four individual YSEs are also plotted at four specific locations (Fig. 5.3b and 5.4b), that spatially correlate with (c) the oceanic domain, (d)

the domain of thick sediments and the location of high-velocity bodies, (e) of high-density crust, and (f) of thick crystalline crust.

For the oceanic domain (point c), the YSEs represent a rheological model in which a brittle-ductile transition occurs only once and just within the mantle, where the corresponding temperature is ~700 °C and ~750 °C for the SW African and Norwegian models, respectively. These YSEs also illustrate that across the oceanic domain the yield differential stress is about 300 MPa greater at the SW African passive margin compared to the Norwegian passive margin. A comparison of the crustal contribution to the total lithospheric strength indicates that the lithospheric mantle dominates the total lithospheric strength across the oceanic domains of both models (Figs. 5.1c, 5.2c, 5.3c&d, and 5.4c&d), as the oceanic crustal thickness is small compared to the total thickness of the lithosphere. However, at the SW African passive margin, the lithospheric mantle unit is significantly colder below the Atlantic Ocean than at its counterpart at the young Norwegian margin (Fig. 1d, 2d, 3b&e, 4b&e). The contrasting thermal fields of the two settings ultimately differentiate their present-day rheological characteristics as the lithospheric mantle is stronger below the South Atlantic than the lithospheric mantle below the North Atlantic.

At point d and e, YSEs illustrate that high-velocity bodies and high-density crustal units greatly contribute to the crustal strength (Fig. 5.3 and 5.4). These units are mechanically the strongest crustal units (Table 5.1), which may explain the high values of modeled integrated crustal strength across the margin and across the distal margin (Fig. 5.1b and 5.2b).

At point f, the YSEs demonstrate the rheological behavior of the lithosphere over the continental domain. Across the oceanic and marginal domains (c, d, and e), the two settings may differ in the modeled strength values but the rheological variations with depth (integrated behavior) are comparable following a similiar pattern. Across the continental domain, however, the modeled rheological behavior differs significantly comparing the two models. At the SW African passive margin, the plotted YSE at point f (Fig. 5.3b) demonstrates that the mantle is weak and the total lithospheric strength is limited to the crustal contribution (i.e. a “crème brûlée” rheological model: Burov and Watts, 2006; Burov, 2010). At the Norwegian margin, in contrast, the rheological behavior at point f (Fig. 5.4b) displays a mechanical decoupling as corresponding to a jelly sandwich model (Burov and Watts, 2006; Burov, 2010). There, a weak lower crustal zone (the jelly) resides between the strong upper crystalline crust and the strong upper lithospheric mantle (the toasts).

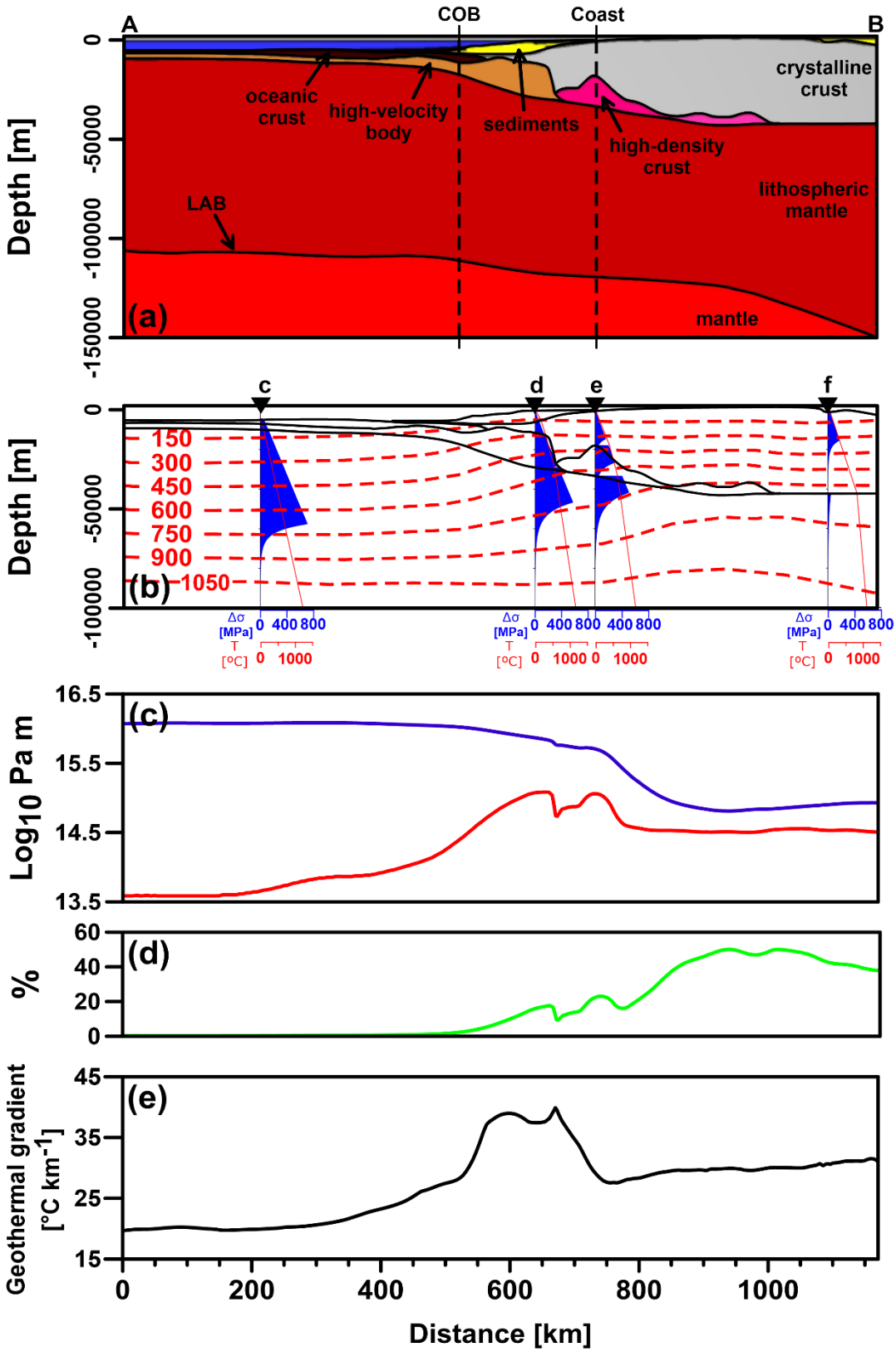

Figure 5.3. SW African passive margin: cross-section along the line of AB in Fig. 1d. (a) Structural model. (b) Yield strength envelopes (YSE) at four different locations of c, d, e, and f. The red dashed lines represent isotherms from 150 °C to 1050 °C in intervals of 150 °C. (c) Integrated lithospheric (blue) and crustal (red) strength along the AB profile. (d) Integrated crustal ratio to the total integrated lithospheric strength (% of red/blue). (e) Corresponding average geothermal gradient.

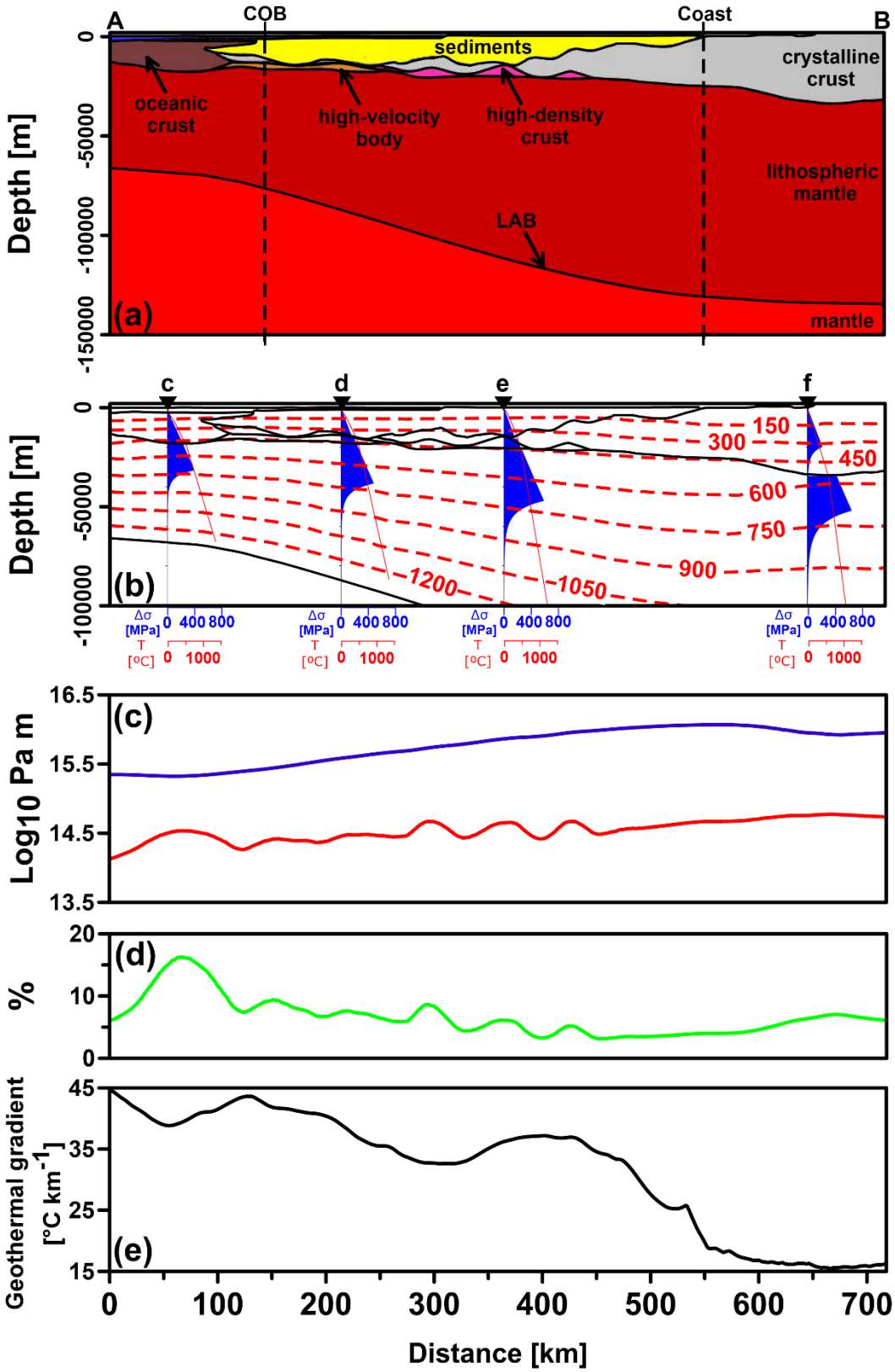

Figure 5.4. Norwegian passive margin: cross-section along the line of AB in Fig. 2d. (a) Structural model. (b) Yield strength envelopes (YSE) at four different locations of c, d, e, and f. The red dashed lines represent isotherms from 150 °C to 1050 °C in intervals of 150 °C. (c) Integrated lithospheric (blue) and crustal (red) strength along the AB profile. (d) Integrated crustal ratio to the total integrated lithospheric strength (% of red/blue). (e) Corresponding average geothermal gradient.

A remarkable question here is why these models differ significantly in rheological behavior across the continental domain, despite the fact that they are almost identical in the lithospheric structure over this domain? A possible reason could be that the average geothermal gradient in the continental domain is considerably higher (~13 °C km^{-1}) at the SW African margin compared to the Norwegian margin (Figs. 5.3e and 5.4e). In addition, the temperature distributions also demonstrate that the lithospheric mantle at the SW African margin is hotter than its counterparts at the Norwegian margin. These thermal differences have been discussed in the previous chapter (Chapter 4, Section 4.5.1). In summary, the SW African margin has a thicker crystalline crust compared to the Norwegian margin (Figs. 4.3a, 4.6a, 5.3a and 5.4a) and consequently more radiogenic heat is contributed by the crust. In addition, the assigned value of radiogenic heat production is much lower (0.8 μW m^{-3}) in the Norwegian thermal model than the corresponding value (1.45 μW m^{-3}) in the SW African thermal model (Table 4.1). Consequently, the smaller contribution of crustal radiogenic heat results in a colder lithospheric mantle in the continental part of the Norwegian margin and causes a "jelly sandwich" configuration. In contrast, the larger contribution of crustal radiogenic heat results in hotter lithospheric mantle of the SW African margin that favors a "crème brûlée" rheological configuration.

In general, these comparisons illustrate that rheological models are highly sensitive to the configuration of the structural models and the related modeled thermal fields. The examples presented here merely represent possible end members for which a certain parametrization was chosen for reasons of limited data availability. Considering the fast progress in numerical modeling methods and computing techniques, future work should address the uncertainties with respect to the structural configuration and the parametrization with physical properties. Such work using data science methods could help to obtain a more detailed assessment of the thermal and mechanical structure.

Finally, a point not at all addressed so far concerns the validity of the mechanical properties assigned to the different geological units. Here we used the same values for average lithologies as currently many authors do, for the simple reason to ensure comparability. It is clear however, that there is a large knowledge gap with respect to the mechanical properties of different rock types, in particular for large pressures and temperatures. Here compositional variations may likewise exert a strong influence on the final rheological behavior of geological systems.

5.4. Conclusions

The calculation of the lithospheric strength for the two different magma-rich passive margins revealed the following:

1. The calculated lithospheric strength values across the two model areas indicate that the lithosphere is generally stronger where it is colder, and vice versa.

2. Beneath the Atlantic Ocean, the present-day lithospheric strength of both South and North Atlantic is ultimately affected by the thermo-tectonic age and the depth to the thermal LAB.

3. Beneath the continental domains of the passive margins, however, the crystalline crust dominantly controls the rheological behavior of the lithosphere.

4. Across the sedimentary basins, the thermal blanketing effect of the insulating thick sediments has the highest impact on the crustal rheological behavior.

5. The modeled thermal field plays a significant role in rheological modeling. Thus, further rheological modeling of passive margins across the Atlantic Ocean requires structural-thermal models at higher resolutions.

6. Mechanical properties needed to parametrize rheological models are heavily under constrained and there is a large demand for better experimental data in this respect.

Chapter 6
Discussion

This chapter discusses how results of the different model areas contribute to the two major questions raised in the introduction (Chapter 1):

1. Which first-order factors determine the thermal field and the strength of the lithosphere?
2. How do these factors translate into the long-term rheological behavior of the lithosphere?

The results of the thermal and rheological models (Chapters 3, 4 and 5) indicate that the thermal field and strength of the lithosphere are dependent on different controlling factors, depending on the nature of the tectonic setting. However, overall, the temperature distribution in the lithosphere is key for the variations of its strength. Consequently, the factors controlling the thermal field also control lithospheric strength and the long-term rheological characteristics of the lithosphere.

6.1. Impact of the lithospheric thermal field on lithospheric strength

A major outcome of this thesis is the notion that the thermal field in response to the structural and tectonic configuration fundamentally determines the thermal properties, and thus the strength of the lithosphere. This is clearly seen by the interaction between the thermal field and the mechanical properties of rocks in all of the individual thermal and rheological models of the three investigated areas. These models thus confirm that the temperature distribution within the lithosphere is the dominant factor that controls the long-term rheological behavior of the lithosphere. Even the same type of rocks with identical mechanical properties may show significant different rheological behavior due to different spatial patterns of the lithospheric thermal field.

6.1.1. The passive Atlantic continental margin setting

The models characterizing the SW African and Norwegian margins are based on identical mechanical properties of the involved rocks (Table 5.1), while the lithospheric thermal thickness differs significantly in the oceanic domain (Figs. 5.3a and 5.4a). Modeled YSEs for the two passive margins (point “c” in Figs. 5.3b and 5.4b) clearly show how this difference in temperature distribution translates into different rheological behavior: colder oceanic lithosphere at the SW African margin is rather stronger than its warmer counterpart at the Norwegian margin. In addition, these YSEs determine the position of the brittle-ductile

transition at a temperature around 700°C, which is consequently shallower at the Norwegian margin compared to the SW African margin.

Across the adjacent continental domain, both models are identical regarding the mechanical properties (Table 5.1) and result in similar values for the lithospheric thermal thickness (Figs. 5.3a and 5.4a). Despite these similarities, however, the modeled YSEs (Figs. 5.3b and 5.4b) do not exhibit a similar rheological behavior in the continental realm. The YSEs suggest a "crème-brûlée" rheological type, with a weak lithospheric mantle at the SW African margin (point "f" in Fig. 5.3b). In contrast, the YSE indicate a "jelly sandwich" rheological behavior, with a strong lithospheric mantle at the Norwegian margin (point "f" in Fig. 5.4b). Here, similar to the oceanic lithosphere, the temperature distribution is the most important determinant that affects lithospheric strength and controls the long-term rheological behavior of the continental lithosphere. The thermal differences between the two models are clearly noticeable when the isotherms (Figs. 5.3b and 5.4b) and the average geothermal gradient are compared (Figs. 5.3e and 5.4e). The modeled thermal field for the two passive Atlantic margins predicts a hotter (i.e. mechanically weaker) continental lithosphere at the SW African margin compared to the Norwegian margin.

6.1.2. The intracontinental transform fault setting in the Sea of Marmara

The results of the rheological modeling of the Sea of Marmara basin (Figs. 3.5 and 3.6) also show that the temperature distribution influences the long-term rheological behavior of the lithosphere. Despite the fact that there are pronounced lateral crustal heterogeneities in this region, which also differ in terms of the mechanical properties between the two models (Table 3.1), the lithospheric mantle exerts the largest influence on the integrated lithospheric strength. Similar to many other areas that have been studied in the past, it is also evident that the general pattern of the lithospheric strength variations is influenced by the temperature distribution: the lithosphere is always stronger, where it is colder. This characteristic becomes prominent when comparing the 750°C isotherm (Figs. 3.5b and 3.6b) and the lithospheric strength profile (Figs. 3.5c and 3.6c). While the mechanical properties of the crustal rocks may have local effects on the lithospheric strength, the general pattern of the lithospheric strength variation is a function of the temperature distribution.

6.2. Factors that control temperature distribution in the lithosphere

Regardless of the type of the tectonic setting, the strength of the lithosphere is ultimately controlled by the lithospheric thermal field. Accordingly, the lithospheric strength is directly affected by those parameters (Eq. 3.1) that control the complex system of the lithosphere thermal field (thermal thickness, internal heat budget, and thermal conductivity).

The thermal field of the continental passive margins was discussed in Chapter 4, and it was demonstrated that the thermal field of the passive margins in the North and South Atlantic is different. Across the oceanic domain, the younger Norwegian margin is warmer than the older SW African passive margin (Figs. 4.10 and 4.11). This thermal difference between the two diachronous passive margins is mainly due to the thermal LAB depth and the lithospheric thermal thickness (Figs. 4.4 and 4.7). Principally, the thermal evolution of the mantle mainly controls the lithospheric thermal field across the oceanic realms.

Beneath the continents, however, the contribution of the crystalline crust to the lithospheric heat budget is the ultimate controlling factor of the temperature distribution, in addition to the thermal lithosphere thickness. Although the thickness of the continental lithosphere is comparable at both margins, the continental lithosphere is stronger at the Norwegian margin compared to the SW African margin, because of the relatively colder conditions in the Norwegian thermal model. As discussed in Chapter 4 (Sec. 4.5.1), the thicker crystalline crust (Figs. 4.3a, 4.6a, 4.11) and the higher rate of radiogenic heat production there (Table 4.1) increase the heat budget of the crystalline crust in the SW African model compared to the Norwegian margin. A caveat has to be mentioned here, in that not all of the assumptions related to the thermal parametrization can be validated; accordingly, the derived conclusions hold just for the chosen parametrization.

Similar to the continental domain of the passive margins, the crustal configuration dominates the pattern of the lithospheric thermal field beneath the continental Sea of Marmara (Chapter 2, Sec. 3.4). There, the modeled temperature distributions within the lithosphere below the basin (Fig. 3.3) indicate that crustal thinning (i.e., lower heat budget of the felsic crystalline crust) causes a colder (i.e., stronger) lithospheric domain.

6.3. Fundamental assumptions, model sensitivities

As in other modeling studies, deriving conclusions based on numerical simulations is sometimes not unambiguous. Therefore, some words of caution are appropriate related to the basic assumptions that were made in the different models. One main assumption is that of a thermally equilibrated system as a steady-state approach is applied to calculate the lithospheric thermal field. Although this was extensively discussed in Sec. 3.6 and Sec. 4.5.3 that a steady-state approach would be a good approximation to calculate the present-day lithospheric thermal field, transient processes could still influence the studied systems. With regards to the passive margins, in particular the Norwegian margin, due to its thermo-tectonic age, has most probably not yet reached thermal equilibrium. However, as temperatures in shallow crustal sectors are consistent with observations, the results of the steady-state thermal modeling may therefore underestimate the temperatures in deeper sectors of the lithosphere.

Likewise, for the continental transform setting of the Marmara Sea basin, the thermal destabilization that was associated with the opening of the Marmara Sea may not have fully propagated through the entire lithosphere. Thus, the modelled temperatures would also underestimate the temperatures in the deeper sectors of lithosphere. In both cases a quantitative assessment of the related uncertainty is difficult and would require stochastic analysis of many different parametrizations that might be achieved in future studies.

Another key assumption in my modeling approach was the introduction of a constant strain rate and a constant value for the coefficient of friction to calculate lithospheric strength. These assumptions and their implications for the rheological modeling were extensively discussed in section 3.6 of Chapter 3 in the context of the models for the Sea of Marmara; similarly, the issues discussed in that section are equally relevant for the models that seek to explain the differences between the two analyzed passive margins.

One major issue regarding the sensitivities of thermal and rheological modeling pertains to the physical properties of rocks, and consequently the model parametrization. This may have an important influence on the thermal and rheological results, specifically regarding the results of the continental settings. As discussed earlier, the structural crustal configuration dominates the variations of the lithospheric thermal field. In addition to the geometric distribution of crustal units, different values of thermal conductivity, radiogenic heat production, and mechanical properties may have an important influence on the results. For instance, the difference in the

values for the radiogenic heat production in the crystalline crust at the North and South Atlantic margins resulted in different rheological models (Chapter 5). Therefore, knowing the properties of deep crustal rocks can lead to interpretations involving different regimes with coupled or decoupled modes of deformation. Additionally, differences in the configuration of the crustal high-density bodies in the Sea of Marmara have implications for the spatial variation of the temperature distribution and lithospheric strength (Chapter 3).

6.3. Outlook

In this study, model parametrization is based on the interpreted lithologies and compilations of corresponding laboratory measurements (Tables 3.1, 4.1 and 5.1). The implementation of different parameters has shown that that future models involving structural, thermal, and rheological parameters should be updated as much as possible if new datasets are available or if computational methods are advanced.

For instance, across the Sea of Marmara, high-resolution geophysical datasets such as marine 3-D reflection seismic data, shipboard gravity measurements, and marine magnetic observations would be very helpful in future endeavors to improve the evaluation and the prediction of the extent of lateral crustal heterogeneities. In addition, deep borehole data such as core and thermal loggings would be very advantageous for the comparison and validation of the numerical models.

Regarding the models of the passive margins in the context of updates in IGMAS+ and novel applications in numerical simulation such as Golem, would be important in renewing structural and thermal models and in the process of optimizing model parameterization. In this context my study has shown that transient thermal and rheological modeling will be an important field of future research.

Chapter 7
Conclusions

Below I briefly summarize the major outcomes of my modeling study:

1. The comparison of the thermal and rheological models of the three analyzed sedimentary basins reveals that variations of the lithospheric strength are fundamentally influenced by the temperature distribution within the lithosphere.

2. The obtained results indicate that the composition of the lithosphere significantly affects the present-day thermal field, and therefore the rheological characteristics of the lithosphere.

3. Similar to oceanic domains, the thermo-tectonic age and the depth to the thermal LAB ultimately affect the thermal configuration of the lithosphere and the thermo-tectonic age clearly controls lithospheric strength.

4. Thermal cooling of the oceanic lithosphere and the transition to continental areas causes variations in the strength distribution of the lithosphere during the evolution of passive margins.

5. In the continents, the crustal configuration ultimately controls the present-day lithospheric thermal field and rheological characteristics due to the effects of radiogenic heat contribution and the spatial distribution of thermal conductivities.

6. Within continental settings, crustal heterogeneities in form of major compositional differences may control the mechanical segmentation along large-scale transform faults such as the NAFZ.

7. The condition of treating the lithosphere as a thermal steady-state system is a valid assumption in studies to elucidate the long-term rheological behavior of the lithosphere.

8. Shallow temperature measurements alone are not sufficient to constrain the deeper rheology of the crust and to predict crustal seismicity, but integrated, multidisciplinary studies using different data sets are required to address the distribution of physical properties in the deeper lithosphere.

References

Akbayram, K., Şengör, A.M.C., Özcan, E., 2017. The evolution of the Intra-Pontide suture: Implications of the discovery of late Cretaceous–early Tertiary mélanges, in: Tectonic Evolution, Collision, and Seismicity of Southwest Asia: In Honor of Manuel Berberian's Forty-Five Years of Research Contributions. Geological Society of America. https://doi.org/10.1130/2016.2525(18)

Akbayram, K., Sorlien, C.C., Okay, A.I., 2016. Evidence for a minimum 52 ± 1 km of total offset along the northern branch of the North Anatolian Fault in northwest Turkey. Tectonophysics 668–669, 35–41. https://doi.org/10.1016/j.tecto.2015.11.026

Aksoy, R., 1996. Mesoscopic Tectonic Features of the Marmara Island and the Kapıdağı Peninsula, NW Turkey. Turkish J. Earth Sci. 5, 187–195.

Aksoy, R., 1995. Stratigraphy of the Marmara Island and Kapıdag Peninsula. Bull. Turkish Pet. Geol. Soc. 7, 33–49.

Amante, C., Eakins, B.W., 2009. ETOPO1 1 Arc-Minute Global Relief Model: Procedures, Data Sources and Analysis. NOAA Tech. Memo. NESDIS NGDC-24 19. https://doi.org/10.1594/PANGAEA.769615

Ambraseys, N., 2002. The seismic activity of the Marmara Sea Region over the last 2000 years. Bull. Seismol. Soc. Am. 92, 1–18. https://doi.org/10.1785/0120000843

Ambraseys, N.N., 1970. Some characteristic features of the Anatolian fault zone. Tectonophysics 9, 143–165. https://doi.org/10.1016/0040-1951(70)90014-4

Anikiev, D., Götze, H.-J., Bott, J., Gómez-García, A. M., Gomez Dacal, M. L., Meeßen, C., Spooner, C., Rodriguez Piceda, C., Plonka, C., Schmidt, S., Scheck-Wenderoth, M., 2021. Interdisciplinary data-constrained 3-D potential field modelling with IGMAS+, EGU General Assembly 2021, online, 19–30 Apr 2021, EGU21-2964. https://doi.org/10.5194/egusphere-egu21-2964

Armijo, R., Meyer, B., Hubert, A., Barka, A., 1999. Westward propagation of the North Anatolian fault into the northern Aegean: Timing and kinematics. Geology 27, 267–270. https://doi.org/10.1130/0091-7613(1999)027<0267:wpotna>2.3.co;2

Armijo, R., Meyer, B., Navarro, S., King, G., Barka, A., 2002. Asymmetric slip partitioning in the sea of Marmara pull-apart: A clue to propagation processes of the North Anatolian Fault? Terra Nov. 14, 80–86. https://doi.org/10.1046/j.1365-3121.2002.00397.x

Armijo, R., Pondard, N., Meyer, B., Ucarkus, G., De Lépinay, B.M., Malavieille, J., Dominguez, S., Gustcher, M.A., Schmidt, S., Beck, C., Cagatay, N., Cakir, Z., Imren, C., Eris, K., Natalin, B., Özalaybey, S., Tolun, L., Lefévre, I., Seeber, L., Gasperini, L., Rangin, C., Emre, O., Sarikavak, K., 2005. Submarine fault scarps in the Sea of Marmara pull-apart (North Anatolian Fault): Implications for seismic hazard in Istanbul. Geochemistry, Geophys. Geosystems 6. https://doi.org/10.1029/2004GC000896

Artemieva, I.M., 2006. Global 1° x 1° thermal model TC1 for the continental lithosphere: Implications for lithosphere secular evolution. Tectonophysics 416, 245–277.

https://doi.org/10.1016/j.tecto.2005.11.022

Artemieva, I.M., Mooney, W.D., 2001. Thermal thickness and evolution of Precambrian lithosphere: A global study. J. Geophys. Res. (Solid Earth) 106, 16,316-387,414. https://doi.org/10.1029/2000JB900439

Ates, A., Bilim, F., Buyuksarac, A., Bektas, Ö., 2008. A tectonic interpretation of the Marmara Sea, NW Turkey from geophysical data. Earth, Planets Sp. 60, 169–177. https://doi.org/10.1186/BF03352780

Ates, A., Kayiran, T., Sincer, I., 2003. Structural interpretation of the Marmara region, NW Turkey, from aeromagnetic, seismic and gravity data. Tectonophysics 367, 41–99. https://doi.org/10.1016/S0040-1951(03)00044-1

Ates, A., Kearey, P., Tufan, S., 1999. New gravity and magnetic anomaly maps of Turkey. Geophys. J. Int. 136, 499–502. https://doi.org/10.1046/j.1365-246X.1999.00732.x

Attanasio, D., Brilli, M., Bruno, M., 2008. The properties and identification of marble from proconnesos (Marmara Island, Turkey): A new database including isotopic, EPR and petrographic data. Archaeometry 50, 747–774. https://doi.org/10.1111/j.1475-4754.2007.00364.x

Autin, J., Scheck-Wenderoth, M., Götze, H.-J., Reichert, C., Marchal, D., 2016. Deep structure of the Argentine margin inferred from 3D gravity and temperature modelling, Colorado Basin. Tectonophysics 676, 198–210. https://doi.org/10.1016/j.tecto.2015.11.023

Barka, A., 1996. Slip distribution along the North Anatolian fault associated with the large earthquakes of the period 1939 to 1967. Bull. Seismol. Soc. Am.

Barka, A., Akyüz, H.S., Altunel, E., Sunal, G., Çakir, Z., Dikbas, A., Yerli, B., Armijo, R., Meyer, B., De Chabalier, J.B., Rockwell, T., Dolan, J.R., Hartleb, R., Dawson, T., Christofferson, S., Tucker, A., Fumal, T., Langridge, R., Stenner, H., Lettis, W., Bachhuber, J., Page, W., 2002. The surface rupture and slip distribution of the 17 August 1999 İzmit earthquake (M 7.4), North Anatolian fault. Bull. Seismol. Soc. Am. 92, 43–60. https://doi.org/10.1785/0120000841

Barka, A., Reilinger, R., 1997. Active tectonics of the Eastern Mediterranean region: deduced from GPS, neotectonic and seismicity data.

Barka, A.A., Hancock, P.L., 1984. Neotectonic deformation patterns in the convex-northwards arc of the North Anatolian fault zone, sp.lyellcollection.org.

Barka, A.A., Kadinsky-Cade, K., 1988. Strike-slip fault geometry in Turkey and its influence on earthquake activity. Tectonics 7, 663–684. https://doi.org/10.1029/TC007i003p00663

Barker, C.E., Pawlewicz, M.J., 1986. The correlation of vitrinite reflectance with maximum temperature in humic organic matter, in: Lecture Notes in Earth Sciences, Berlin Springer Verlag. pp. 79–93. https://doi.org/10.1007/BFb0012103

Barrell, J., 1914. The Strength of the Earth's Crust Part I. Geologic Tests of the Limits of Strength. J. Geol. 22, 28–48. https://doi.org/10.1086/622131

Bayrakci, G., Laigle, M., Bécel, A., Hirn, A., Taymaz, T., Yolsal-C ¸ Evikbilen, S., Team, S., 2013. 3-D sediment-basement tomography of the Northern Marmara trough by a dense OBS network at the nodes of a grid of controlled source profiles along the North Anatolian fault. Geophys. J. Int. Geophys. J. Int 194, 1335–1357. https://doi.org/10.1093/gji/ggt211

Bécel, A., Laigle, M., de Voogd, B., Hirn, A., Taymaz, T., Galvé, A., Shimamura, H., Murai, Y., Lépine, J.C., Sapin, M., Özalaybey, S., 2009. Moho, crustal architecture and deep deformation under the North Marmara Trough, from the SEISMARMARA Leg 1 offshore-onshore reflection-refraction survey. Tectonophysics 467, 1–21. https://doi.org/10.1016/j.tecto.2008.10.022

Bécel, A., Laigle, M., de Voogd, B., Hirn, A., Taymaz, T., Yolsal-Cevikbilen, S., Shimamura, H., 2010. North Marmara Trough architecture of basin infill, basement and faults, from PSDM reflection and OBS refraction seismics. Tectonophysics 490, 1–14. https://doi.org/10.1016/j.tecto.2010.04.004

Blaich, O.A., Faleide, J.I., Tsikalas, F., Franke, D., León, E., 2009. Crustal-scale architecture and segmentation of the Argentine margin and its conjugate off South Africa. Geophys. J. Int. 178, 85–105. https://doi.org/10.1111/j.1365-246X.2009.04171.x

Bohnhoff, M., Bulut, F., Dresen, G., Malin, P.E., Eken, T., Aktar, M., 2013. An earthquake gap south of Istanbul. Nat. Commun. 4, 1–6. https://doi.org/10.1038/ncomms2999

Bohnhoff, M., Dresen, G., Ceken, U., Kadirioglu, F.T., Kartal, R.F., Kilic, T., Nurlu, M., Yanik, K., Acarel, D., Bulut, F., Ito, H., Johnson, W., Malin, P.E., Mencin, D., 2017a. GONAF – the borehole Geophysical Observatory at the North Anatolian Fault in the eastern Sea of Marmara. Sci. Drill. 22, 19–28. https://doi.org/10.5194/sd-22-19-2017

Bohnhoff, M., Ickrath, M., Dresen, G., 2016a. Seismicity distribution in conjunction with spatiotemporal variations of coseismic slip and postseismic creep along the combined 1999 Izmit-Düzce rupture. Tectonophysics 686, 132–145. https://doi.org/10.1016/j.tecto.2016.07.029

Bohnhoff, M., Martínez-Garzón, P., Bulut, F., Stierle, E., Ben-Zion, Y., 2016b. Maximum earthquake magnitudes along different sections of the North Anatolian fault zone. Tectonophysics. https://doi.org/10.1016/j.tecto.2016.02.028

Bohnhoff, M., Wollin, C., Domigall, D., Küperkoch, L., Martínez-Garzón, P., Kwiatek, G., Malin, P.E., 2017b. Repeating Marmara Sea earthquakes: indication for fault creep. Geophys. J. Int. Geophys. J. Int 210, 332–339. https://doi.org/10.1093/gji/ggx169

Boillot, G., Grimaud, S., Mauffret, A., Mougenot, D., Kornprobst, J., Mergoil-Daniel, J., Torrent, G., 1980. Ocean-continent boundary off the Iberian margin: a serpentinite diapir west of the Galicia Bank. Earth and Planetary Science Letters, 48(1), 23–34. https://doi.org/10.1016/0012-821X(80)90166-1

Braun, J., Deschamps, F., Rouby, D., Dauteuil, O., 2013. Flexure of the lithosphere and the geodynamical evolution of non-cylindrical rifted passive margins: Results from a numerical model incorporating variable elastic thickness, surface processes and 3D thermal subsidence. Tectonophysics 604, 72–82. https://doi.org/10.1016/j.tecto.2012.09.033

Brekke, H., 2000. The tectonic evolution of the Norwegian Sea Continental Margin with emphasis on the Voring and More Basins. Geol. Soc. London Spec. Publ. 167, 327–378. https://doi.org/10.1144/GSL.SP.2000.167.01.13

Brocher, T.M., 2005. Empirical relations between elastic wavespeeds and density in the Earth's crust. Bull. Seismol. Soc. Am. 95, 2081–2092. https://doi.org/10.1785/0120050077

Bulut, F., Aktuğ, B., Yaltırak, C., Doğru, A., Özener, H., 2019. Magnitudes of future large earthquakes near Istanbul quantified from 1500 years of historical earthquakes, present-day microseismicity and GPS slip rates. Tectonophysics 764, 77–87. https://doi.org/10.1016/j.tecto.2019.05.005

Bürgmann, R., Dresen, G., 2008. Rheology of the Lower Crust and Upper Mantle: Evidence from Rock Mechanics, Geodesy, and Field Observations. https://doi.org/10.1146/annurev.earth.36.031207.124326

Bürgmann, R., Ergintav, S., Segall, P., Hearn, E.H., McClusky, S., Reilinger, R.E., Woith, H., Zschau, J., 2002. Time-dependent distributed afterslip on and deep below the Izmit earthquake rupture. Bull. Seismol. Soc. Am. 92, 126–137. https://doi.org/10.1785/0120000833

Burnham, A.K., Sweeney, J.J., 1989. A chemical kinetic model of vitrinite maturation and reflectance. Geochim. Cosmochim. Act 53, 2649–2657. https://doi.org/10.1016/0016-7037(89)90136-1

Burov, E.B., 2011. Rheology and strength of the lithosphere. Mar. Pet. Geol. https://doi.org/10.1016/j.marpetgeo.2011.05.008

Burov, E.B., 2010. The equivalent elastic thickness (Te), seismicity and the long-term rheology of continental lithosphere: Time to burn-out "crème brûlée"?. Insights from large-scale geodynamic modeling. Tectonophysics 484, 4–26. https://doi.org/10.1016/j.tecto.2009.06.013

Burov, E.B., Watts, A.B., 2006. the long-term strength of continental lithosphere: "jelly sandwich" or "crème brûlée"? GSa ToDay GSA Today v 16. https://doi.org/10.1130/1052-5173(2006)016<4:tltSOc>2.0.cO;2

Byerlee, J., 1978. Friction of Rocks. pure Appl. Geophys. 116, 615–626. https://doi.org/10.1007/BF00876528

Cacace, M., Jacquey, A.B., 2017. Flexible parallel implicit modelling of coupled thermal–hydraulic–mechanical processes in fractured rocks. Solid Earth 8, 921–941. https://doi.org/10.5194/se-8-921-2017

Cacace, M., Scheck-Wenderoth, M., 2016. Why intracontinental basins subside longer: 3-D feedback effects of lithospheric cooling and sedimentation on the flexural strength of the lithosphere. J. Geophys. Res. Solid Earth 121, 3742–3761. https://doi.org/10.1002/2015JB012682

Carton, H., Singh, S.C., Hirn, A., Bazin, S., de Voogd, B., Vigner, A., Ricolleau, A., Cetin, S., Oçakoğlu, N., Karakoç, F., Sevilgen, V., 2007. Seismic imaging of the three-dimensional architecture of the Çınarcık Basin along the North Anatolian Fault. J. Geophys. Res. Solid

Earth 112. https://doi.org/10.1029/2006JB004548

Cermak, V., Rybach, L., 1982. Thermal conductivity and specific heat of minerals and rocks, in: Angenheister, G. (Ed.), Landolt-Börnstein, New Series, Group V, Geophysics and Space Research. Springer Berlin Heidelberg, pp. 305–343. https://doi.org/10.1007/10201894_62

Chapman, D.S., 1986. Thermal gradients in the continental crust. Geol. Soc. London Spec. Publ. 24, 63–70. https://doi.org/10.1144/GSL.SP.1986.024.01.07

Christensen, N.I., Mooney, W.D., 1995. Seismic velocity structure and composition of the continental crust: a global view. J. Geophys. Res. 100, 9761–9788. https://doi.org/10.1029/95JB00259

Clauer, N., Kröner, A., 1979. Strontium and argon isotopic homogenization of pelitic sediments during low-grade regional metamorphism: The pan-African upper Damara sequence of Northern Namibia (South West Africa). Earth Planet. Sci. Lett. 43, 117–131. https://doi.org/10.1016/0012-821X(79)90161-4

Cochran, J.R., 1980. SOME REMARKS ON ISOSTASY AND THE LONG-TERM BEHAVIOR OF THE CONTINENTAL LITHOSPHERE, Earth and Planetary Science Letters.

Corcoran, D. V., Clayton, G., 2001. Interpretation of vitrinite reflectance profiles in sedimentary basins, onshore and offshore Ireland. Geol. Soc. London Spec. Publ. 188, 61–90. https://doi.org/10.1144/GSL.SP.2001.188.01.04

Corsini, M., Rolland, Y., 2009. Late evolution of the southern European Variscan belt: Exhumation of the lower crust in a context of oblique convergence. Comptes Rendus - Geosci. 341, 214–223. https://doi.org/10.1016/j.crte.2008.12.002

Crosby, A.G., McKenzie, D., 2009. An analysis of young ocean depth, gravity and global residual topography. Geophys. J. Int. 178, 1198–1219. https://doi.org/10.1111/j.1365-246X.2009.04224.x

Crosby, A.G., McKenzie, D., Sclater, J.G., 2006. The relationship between depth, age and gravity in the oceans. Geophys. J. Int. 166, 553–573. https://doi.org/10.1111/j.1365-246X.2006.03015.x

Davies, G.F., 1980. Thermal histories of convective earth models and constraints on radiogenic heat production in the earth. J. Geophys. Res. 85, 2517–2530. https://doi.org/10.1029/JB085iB05p02517

Deeken, A., Sobel, E.R., Coutand, I., Haschke, M., Riller, U., Strecker, M.R., 2006. Development of the southern Eastern Cordillera, NW Argentina, constrained by apatite fission track thermochronology: From early Cretaceous extension to middle Miocene shortening. Tectonics 25, TC6003. https://doi.org/10.1029/2005TC001894

DeLaughter, J., Stein, S., Stein, C.A., 1999. Extraction of a lithospheric cooling signal from oceanwide geoid data. Earth Planet. Sci. Lett. 174, 173–181. https://doi.org/10.1016/S0012-821X(99)00247-2

Dore, A.G., Cartwright, J.A., Stoker, M.S., Turner, J.P., White, N.J., 2002. Exhumation of the North Atlantic margin: introduction and background. Geol. Soc. London Spec. Publ. 196, 1–12. https://doi.org/10.1144/GSL.SP.2002.196.01.01

Ebbing, J., Gernigon, L., Pascal, C., Olesen, O., Osmundsen, P.T., 2009. A discussion of structural and thermal control of magnetic anomalies on the mid-Norwegian margin. Geophys. Prospect. 57, 665–681. https://doi.org/10.1111/j.1365-2478.2009.00800.x

Ehlers, T.A., 2005. Crustal thermal processes and the interpretation of thermochronometer data. Rev. Mineral. Geochemistry. https://doi.org/10.2138/rmg.2005.58.12

Ehlers, T.A., Farley, K.A., 2003. Apatite (U-Th)/He thermochronometry: methods and applications to problems in tectonic and surface processes. Earth Planet. Sci. Lett. 206, 1–14. https://doi.org/10.1016/S0012-821X(02)01069-5

Ehlers, T.A., Willett, S.D., Armstrong, P.A., Chapman, D.S., 2003. Exhumation of the central Wasatch Mountains, Utah: 2. Thermokinematic model of exhumation, erosion, and thermochronometer interpretation. J. Geophys. Res. (Solid Earth) 108, 2173. https://doi.org/10.1029/2001JB001723

Eldholm, O., Gladczenko, T.P., Skogseid, J., Planke, S., 2000. Atlantic volcanic margins: a comparative study. Geol. Soc. London Spec. Publ. 167, 411–428. https://doi.org/10.1144/GSL.SP.2000.167.01.16

Elmas, A., 2003. Late Cenozoic tectonics and stratigraphy and northwestern Anatolia: The effects of the North Anatolian Fault to the region. Int. J. Earth Sci. 92, 380–396. https://doi.org/10.1007/s00531-003-0322-2

Ergintav, S., Reilinger, R.E., Çakmak, R., Floyd, M., Cakir, Z., Doꞌan, U., King, R.W., McClusky, S., Özener, H., 2014. Istanbul's earthquake hot spots: Geodetic constraints on strain accumulation along faults in the Marmara seismic gap. Geophys. Res. Lett. 41, 5783–5788. https://doi.org/10.1002/2014GL060985

Ergün, M., Özel, E., 1995. Structural relationship between the Sea of Marmara Basin and the North Anatolian Fault Zone. Terra Nov. 7, 278–288. https://doi.org/10.1111/j.1365-3121.1995.tb00695.x

Erkan, K., 2015. Geothermal investigations in western Anatolia using equilibrium temperatures from shallow boreholes. Solid Earth 6, 103–113. https://doi.org/10.5194/se-6-103-2015

Faccenna, C., Bellier, O., Martinod, J., Piromallo, C., Regard, V., 2006. Slab detachment beneath eastern Anatolia: A possible cause for the formation of the North Anatolian fault. Earth Planet. Sci. Lett. 242, 85–97. https://doi.org/10.1016/j.epsl.2005.11.046

Fichtner, A., Saygin, E., Taymaz, T., Cupillard, P., Capdeville, Y., Trampert, J., 2013. The deep structure of the North Anatolian Fault Zone. Earth Planet. Sci. Lett. 373, 109–117. https://doi.org/10.1016/j.epsl.2013.04.027

Flerit, F., Armijo, R., King, G., Meyer, B., 2004. The mechanical interaction between the propagating North Anatolian Fault and the back-arc extension in the Aegean. Earth Planet. Sci. Lett. 224, 347–362. https://doi.org/10.1016/j.epsl.2004.05.028

Gallagher, K., Brown, R., Johnson, C., 1998. Fission Track Analysis and Its Applications to Geological Problems. Annu. Rev. Earth Planet. Sci. 26, 519–572. https://doi.org/10.1146/annurev.earth.26.1.519

Géli, L., Henry, P., Grall, C., Tary, J.B., Lomax, A., Batsi, E., Riboulot, V., Cros, E., Gürbüz, C., Işlk, S.E., Sengör, A.M.C., Le Pichon, X., Ruffine, L., Dupré, S., Thomas, Y., Kalafat, D., Bayrakci, G., Coutellier, Q., Regnier, T., Westbrook, G., Saritas, H., Çifçi, G., Çağatay, M.N., Özeren, M.S., Görür, N., Tryon, M., Bohnhoff, M., Gasperini, L., Klingelhoefer, F., Scalabrin, C., Augustin, J.M., Embriaco, D., Marinaro, G., Frugoni, F., Monna, S., Etiope, G., Favali, P., Bécel, A., 2018. Gas and seismicity within the Istanbul seismic gap. Sci. Rep. 8, 1–11. https://doi.org/10.1038/s41598-018-23536-7

Genç, Ş. can, 1998. Evolution of the Bayramic magmatic complex, northwestern Anatolia. J. Volcanol. Geotherm. Res. 85, 233–249. https://doi.org/10.1016/S0377-0273(98)00057-2

GEOFON Data Centre, 1993. GEOFON Seismic Network [WWW Document]. Dtsch. GeoForschungsZentrum GFZ. https://doi.org/10.14470/TR560404

Gernigon, L., Lucazeau, F., Brigaud, F., Ringenbach, J.-C., Planke, S., Le Gall, B., 2006. A moderate melting model for the Vøring margin (Norway) based on structural observations and a thermo-kinematical modelling: Implication for the meaning of the lower crustal bodies. Tectonophysics 412, 255–278. https://doi.org/10.1016/j.tecto.2005.10.038

Gholamrezaie, E., Scheck-Wenderoth, M., Bott, J., Heidbach, O., Strecker, M.R., 2019. 3-D crustal density model of the Sea of Marmara. Solid Earth 10, 785–807. https://doi.org/10.5194/se-10-785-2019

Gholamrezaie, E., Scheck-Wenderoth, M., Bott, J., Heidbach, O., Bohnhoff, M., Strecker, M. R., 2020. 3-D lithospheric-scale rheological model of the Sea of Marmara. EGU General Assembly 2020, Online, EGU2020-4264. https://doi.org/10.5194/egusphere-egu2020-4264

Gholamrezaie, E., Scheck-Wenderoth, M., Sippel, J., Strecker, M.R., 2018. Variability of the geothermal gradient across two differently aged magma-rich continental rifted margins of the Atlantic Ocean: the Southwest African and the Norwegian margins. Solid Earth 9, 139–158. https://doi.org/10.5194/se-9-139-2018

Goetze, C., 1978. The mechanisms of creep in olivine. Philos. Trans. R. Soc. London. Ser. A, Math. Phys. Sci. 288, 99–119. https://doi.org/10.1098/rsta.1978.0008

Goetze, C., Evans, B., 1979. Stress and temperature in the bending lithosphere as constrained by experimental rock mechanics. Geophys. J. Int. 59, 463–478. https://doi.org/10.1111/j.1365-246X.1979.tb02567.x

Götze, H.-J., Alvers, M. R., Barrio-Alvers, L., Lahmeyer, B., Plonka, C. and Schmidt, S., 2015. Advanced interactive 3D potential field modelling. The 17th annual conference of the International Association for Mathematical Geosciences, September 5-13, 2015, Freiberg (Saxony) Germany.

Götze, H. J., Lahmeyer, B., 1988. Application of three-dimensional interactive modeling in gravity and magnetics. Geophysic, 53, 1096–1108. https://doi.org/10.1190/1.1442546

Goodwillie, A.M., Watts, A.B., 1993. An altimetric and bathymetric study of elastic thickness in the central Pacific Ocean. Earth Planet. Sci. Lett. 118, 311–326. https://doi.org/10.1016/0012-821X(93)90175-9

Grevemeyer, I., Villinger, H., 2001. Gas hydrate stability and the assessment of heat flow through continental margins. Geophys. J. Int. 145, 647–660. https://doi.org/10.1046/j.1365-246X.2001.01404.x

Henk, A., Nemčok, M., 2016. Lower-crust ductility patterns associated with transform margins. Geol. Soc. London Spec. Publ. 431, 361–375. https://doi.org/10.1144/SP431.9

Henry, P., Sengör, A.C., Cagatay, M.N., 2007. MARNAUT cruise, RV L'Atalante. https://doi.org/10.17600/7010070

Hergert, T., Heidbach, O., 2011. Geomechanical model of the Marmara Sea region-II. 3-D contemporary background stress field. Geophys. J. Int. 185, 1090–1102. https://doi.org/10.1111/j.1365-246X.2011.04992.x

Hergert, T., Heidbach, O., 2010. Slip-rate variability and distributed deformation in the Marmara Sea fault system. Nat. Geosci. 3, 132–135. https://doi.org/10.1038/ngeo739

Hergert, T., Heidbach, O., Bécel, A., Laigle, M., 2011. Geomechanical model of the Marmara Sea region-I. 3-D contemporary kinematics. Geophys. J. Int. 185, 1073–1089. https://doi.org/10.1111/j.1365-246X.2011.04991.x

HIRN, A., SINGH, S., 2001. SEISMARMARA cruise, RV Le Nadir. https://doi.org/10.17600/1080050

Huismans, R.S., Beaumont, C., 2008. Complex rifted continental margins explained by dynamical models of depth-dependent lithospheric extension. Geology 36, 163–166. https://doi.org/10.1130/G24231A.1

Hussain, E., Wright, T.J., Walters, R.J., Bekaert, D.P.S., Lloyd, R., Hooper, A., 2018. Constant strain accumulation rate between major earthquakes on the North Anatolian Fault. Nat. Commun. 9, 1–9. https://doi.org/10.1038/s41467-018-03739-2

Ince, E.S., Barthelmes, F., Reißland, S., Elger, K., Förste, C., Flechtner, F., Schuh, H., 2019. ICGEM – 15 years of successful collection and distribution of global gravitational models, associated services and future plans. Earth Syst. Sci. Data Discuss. 1–61. https://doi.org/10.5194/essd-2019-17

Jackson, J., 2002. Strength of the continental lithosphere: Time to abandon the jelly sandwich? GSA Today 4–10.

Jacquey, A.B., Cacace, M., 2017. GOLEM, a MOOSE-based application. https://doi.org/10.5281/ZENODO.999401

Janssen, C., Bohnhoff, M., Vapnik, Y., Görgün, E., Bulut, F., Plessen, B., Pohl, D., Aktar, M., Okay, A.I., Dresen, G., 2009. Tectonic evolution of the Ganos segment of the North Anatolian Fault (NW Turkey). J. Struct. Geol. 31, 11–28. https://doi.org/10.1016/j.jsg.2008.09.010

Johnson, H.P., Carlson, R.L., 1992. Variation of sea floor depth with age: A test of models based on drilling results. Geophys. Res. Lett. 19, 1971–1974. https://doi.org/10.1029/92GL01946

Jolivet, L., Beyssac, O., Goffé, B., Avigad, D., Lepvrier, C., Maluski, H., Thang, T.T., 2001. Oligo-Miocene miderustal subhorizontal shear zone in Indochina. Tectonics 20, 46–57. https://doi.org/10.1029/2000TC900021

Jolivet, L., Faccenna, C., Huet, B., Labrousse, L., Le Pourhiet, L., Lacombe, O., Lecomte, E., Burov, E., Denèle, Y., Brun, J.P., Philippon, M., Paul, A., Salaün, G., Karabulut, H., Piromallo, C., Monié, P., Gueydan, F., Okay, A.I., Oberhänsli, R., Pourteau, A., Augier, R., Gadenne, L., Driussi, O., 2013. Aegean tectonics: Strain localisation, slab tearing and trench retreat. Tectonophysics. https://doi.org/10.1016/j.tecto.2012.06.011

Kaminski, E., Jaupart, C., 2000. Lithosphere structure beneath the Phanerozoic intracratonic basins of North America. Earth Planet. Sci. Lett. 178, 139–149. https://doi.org/10.1016/S0012-821X(00)00067-4

Karacik, Z., Yilmaz, Y., Pearce, J.A., Ece, Ö.I., 2008. Petrochemistry of the south Marmara granitoids, northwest Anatolia, Turkey. Int. J. Earth Sci. 97, 1181–1200. https://doi.org/10.1007/s00531-007-0222-y

Karato, S.I., Wu, P., 1993. Rheology of the upper mantle: A synthesis. Science (80-.). 260, 771–778. https://doi.org/10.1126/science.260.5109.771

Kende, J., Henry, P., Bayrakci, G., Özeren, M.S., Grall, C., 2017. Moho depth and crustal thinning in the Marmara Sea region from gravity data inversion. J. Geophys. Res. Solid Earth 122, 1381–1401. https://doi.org/10.1002/2015JB012735

Koptev, A., Cloetingh, S., Burov, E., François, T., Gerya, T., 2017. Long-distance impact of Iceland plume on Norway's rifted margin. Sci. Rep. 7, 10408. https://doi.org/10.1038/s41598-017-07523-y

Kurtuluş, C., Canbay, M.M., 2007. Tracing the middle strand of the North Anatolian Fault Zone through the southern Sea of Marmara based on seismic reflection studies. Geo-Marine Lett. 27, 27–40. https://doi.org/10.1007/s00367-006-0050-2

Labrousse, L., Jolivet, L., Andersen, T.B., Agard, P., Hébert, R., Maluski, H., Schärer, U., 2004. Pressure-temperature-time deformation history of the exhumation of ultra-high pressure rocks in the Western Gneiss Region, Norway. Spec. Pap. Geol. Soc. Am. 380, 155–183. https://doi.org/10.1130/0-8137-2380-9.155

Laigle, M., Becel, A., de Voogd, B., Hirn, A., Taymaz, T., Ozalaybey, S., 2008. A first deep seismic survey in the Sea of Marmara: Deep basins and whole crust architecture and evolution. Earth Planet. Sci. Lett. 270, 168–179. https://doi.org/10.1016/j.epsl.2008.02.031

Lange, D., Kopp, H., Royer, J.Y., Henry, P., Çakir, Z., Petersen, F., Sakic, P., Ballu, V., Bialas, J., Özeren, M.S., Ergintav, S., Géli, L., 2019. Interseismic strain build-up on the submarine North Anatolian Fault offshore Istanbul. Nat. Commun. 10, 1–9. https://doi.org/10.1038/s41467-019-11016-z

Larson, R.L., Ladd, J.W., 1973. Evidence for the Opening of the South Atlantic in the Early Cretaceous. Nature 246, 209–212. https://doi.org/10.1038/246209a0

Lavier, L.L., Manatschal, G., 2006. A mechanism to thin the continental lithosphere at magma-poor margins. Nature 440, 324–328. https://doi.org/10.1038/nature04608

Le Pichon, X., Chamot-Rooke, N., Rangin, C., Sengör, A.M.C., 2003. The North Anatolian fault in the Sea of Marmara. J. Geophys. Res. Solid Earth 108. https://doi.org/10.1029/2002jb001862

Le Pichon, X., Engor, A.M.C., Demirba, E., Rangin, C., Imren, C., Armijo, R., Görür, N., Catay, N., Mercier de Lepinay, B., Meyer, B., Saatclar, R., Tok, B., 2001. The active Main Marmara Fault. Earth Planet. Sci. Lett. 192, 595–616. https://doi.org/10.1016/S0012-821X(01)00449-6

Le Pichon, X., Francheteau, Jean, Bonnin, Jean, Pichon, L., Francheteau, J, Bonnin, J, 1973. Plate tectonics. Elsevier Scientific.

Le Pichon, X., Imren, C., Rangin, C., Şengör, A.M.C., Siyako, M., 2014. The South Marmara Fault. Int. J. Earth Sci. 103, 219–231. https://doi.org/10.1007/s00531-013-0950-0

Le Pichon, X., Şengör, A.M.C., Kende, J., İmren, C., Henry, P., Grall, C., Karabulut, H., 2016. Propagation of a strike-slip plate boundary within an extensional environment: the westward propagation of the North Anatolian Fault. Can. J. Earth Sci. 53, 1416–1439. https://doi.org/10.1139/cjes-2015-0129

Le Pourhiet, L., Huet, B., May, D.A., Labrousse, L., Jolivet, L., 2012. Kinematic interpretation of the 3D shapes of metamorphic core complexes. Geochemistry, Geophys. Geosystems 13. https://doi.org/10.1029/2012GC004271

Le Pourhiet, L., Huet, B., Traoré, N., 2014. Links between long-term and short-term rheology of the lithosphere: Insights from strike-slip fault modelling. Tectonophysics 631, 146–159. https://doi.org/10.1016/j.tecto.2014.06.034

Leloup, P.H., Lacassin, R., Tapponnier, P., Schärer, U., Zhong, D., Liu, X., Zhang, L., Ji, S., Trinh, P.T., 1995. The Ailao Shan-Red River shear zone (Yunnan, China), Tertiary transform boundary of Indochina. Tectonophysics 251. https://doi.org/10.1016/0040-1951(95)00070-4

Lorenz, H., Rosberg, J.-E., Juhlin, C., Bjelm, L., Almqvist, B.S.G., Berthet, T., Conze, R., Gee, D.G., Klonowska, I., Pascal, C., Pedersen, K., Roberts, N.M.W., Tsang, C.-F., 2015. COSC-1 - drilling of a subduction-related allochthon in the Palaeozoic Caledonide orogen of Scandinavia. Sci. Drill. 19, 1–11. https://doi.org/10.5194/sd-19-1-2015

Lorenzo-Martín, F., Roth, F., Wang, R., 2006. Elastic and inelastic triggering of earthquakes in the North Anatolian Fault zone. Tectonophysics 424, 271–289. https://doi.org/10.1016/j.tecto.2006.03.046

Ludwig, W.J., Nafe, J.E., Drake, C.L., 1970. Seismic refraction. Sea 4, 53–84.

Maystrenko, Y.P., Gernigon, L., Nasuti, A., Olesen, O., 2018. Deep structure of the Mid-Norwegian continental margin (the Vøring and Møre basins) according to 3-D density and

magnetic modelling. Geophys. J. Int. 212, 1696–1721. https://doi.org/10.1093/gji/ggx491

Maystrenko, Y.P., Scheck-Wenderoth, M., Hartwig, A., Anka, Z., Watts, A.B., Hirsch, K.K., Fishwick, S., 2013. Structural features of the Southwest African continental margin according to results of lithosphere-scale 3D gravity and thermal modelling. Tectonophysics 604, 104–121. https://doi.org/10.1016/j.tecto.2013.04.014

McKenzie, D., 1972. Active Tectonics of the Mediterranean Region. Geophys. J. Int. 30, 109–185. https://doi.org/10.1111/j.1365-246X.1972.tb02351.x

McKenzie, D., Bickle, M.J., 1988. The volume and composition of melt generated by extension of the lithosphere. J. Petrol. 29, 625–679. https://doi.org/10.1093/petrology/29.3.625

McKenzie, D., Jackson, J., Priestley, K., 2005. Thermal structure of oceanic and continental lithosphere. Earth Planet. Sci. Lett. 233, 337–349. https://doi.org/10.1016/j.epsl.2005.02.005

MediMap Group, 2005. Morpho-bathymetry of the Mediterranean Sea, special publication, Atlases and Maps, two maps at 1⁄2000000, CIESM/Ifremer, Issy-les-Moulineaux, France.

Meeßen, C., 2018. VeloDT: Fast conversion of upper mantle seismic velocities to density and temperature. https://doi.org/10.5281/ZENODO.1172629

Muffler, P., Cataldi, R., 1978. Methods for regional assessment of geothermal resources. Geothermics 7, 53–89.

Müller, R.D., Sdrolias, M., Gaina, C., Roest, W.R., 2008. Age, spreading rates, and spreading asymmetry of the world's ocean crust. Geochemistry, Geophys. Geosystems 9, Q04006. https://doi.org/10.1029/2007GC001743

Murru, M., Akinci, A., Falcone, G., Pucci, S., Console, R., Parsons, T., 2016. M ≥ 7 earthquake rupture forecast and time-dependent probability for the sea of Marmara region, Turkey. J. Geophys. Res. Solid Earth 121, 2679–2707. https://doi.org/10.1002/2015JB012595

Mutter, J.C., Talwani, M., Stoffa, P.L., 1982. Origin of seaward-dipping reflectors in oceanic crust off the Norwegian margin by "subaerial sea-floor spreading." Geology 10, 353. https://doi.org/10.1130/0091-7613(1982)10<353:OOSRIO>2.0.CO;2

Nemcok, M., Henk, A., Allen, R., Sikora, P.J., Stuart, C., 2013. Continental break-up along strike-slip fault zones; observations from the Equatorial Atlantic. Geol. Soc. London Spec. Publ. 369, 537–556. https://doi.org/10.1144/SP369.8

Nirrengarten, M., Gernigon, L., Manatschal, G., 2014. Lower crustal bodies in the Møre volcanic rifted margin: Geophysical determination and geological implications. Tectonophysics 636, 143–157. https://doi.org/10.1016/j.tecto.2014.08.004

Nürnberg, D., Müller, R.D., 1991. The tectonic evolution of the South Atlantic from Late Jurassic to present. Tectonophysics 191, 27–53. https://doi.org/10.1016/0040-1951(91)90231-G

O'Connor, J.M., Duncan, R.A., 1990. Evolution of the Walvis Ridge-Rio Grande Rise Hot Spot System: Implications for African and South American Plate motions over plumes. J.

Geophys. Res. (Solid Earth) 95, 17,417-475,502. https://doi.org/10.1029/JB095iB11p17475

Okay, A.I., Tüysüz, O., 1999. Tethyan sutures of northern Turkey. Geol. Soc. Spec. Publ. 156, 475–515. https://doi.org/10.1144/GSL.SP.1999.156.01.22

Parke, J.R., White, R.S., McKenzie, D., Minshull, T.A., Bull, J.M., Kuşçu, I., Görür, N., Şengör, C., 2002. Interaction between faulting and sedimentation in the Sea of Marmara, western Turkey. J. Geophys. Res. Solid Earth 107, EPM 2-1-EPM 2-20. https://doi.org/10.1029/2001jb000450

Parkin, C.J., White, R.S., 2008. Influence of the Iceland mantle plume on oceanic crust generation in the North Atlantic. Geophys. J. Int. 173, 168–188. https://doi.org/10.1111/j.1365-246X.2007.03689.x

Parsons, B., Sclater, J.G., 1977. An analysis of the variation of ocean floor bathymetry and heat flow with age. J. Geophys. Res. 82, 803–827. https://doi.org/10.1029/JB082i005p00803

Parsons, T., 2004. Recalculated probability of $M \geq 7$ earthquakes beneath the Sea of Marmara, Turkey. J. Geophys. Res. Solid Earth 109. https://doi.org/10.1029/2003JB002667

Pavlis, N.K., Holmes, S.A., Kenyon, S.C., Factor, J.K., 2012. The development and evaluation of the Earth Gravitational Model 2008 (EGM2008). J. Geophys. Res. Solid Earth 117. https://doi.org/10.1029/2011JB008916

Pfister, M., Rybach, L., Simsek, S., 1998. Geothermal reconnaissance of the Marmara Sea region (NW Turkey): surface heat flow density in an area of active continental extension. Tectonophysics 291, 77–89. https://doi.org/10.1016/S0040-1951(98)00032-8

Pollack, H.N., 1986. Cratonization and thermal evolution of the mantle. Earth Planet. Sci. Lett. 80, 175–182. https://doi.org/10.1016/0012-821X(86)90031-2

Priestley, K., McKenzie, D., 2006. The thermal structure of the lithosphere from shear wave velocities. Earth Planet. Sci. Lett. 244, 285–301. https://doi.org/10.1016/j.epsl.2006.01.008

Pucci, S., Palyvos, N., Zabci, C., Pantosti, D., Barchi, M., 2006. Coseismic ruptures and tectonic landforms along the Düzce segment of the North Anatolian Fault Zone (Ms 7.1, November 1999). J. Geophys. Res. Solid Earth 111. https://doi.org/10.1029/2004JB003578

Rabinowitz, P.D., Labrecque, J., 1979. The Mesozoic South Atlantic Ocean and evolution of its continental margins. J. Geophys. Res. (Solid Earth) 84, 5973–6002. https://doi.org/10.1029/JB084iB11p05973

Ranalli, G., 1995. Rheology of the earth, 2nd ed. Chapman & Hall.

Reilinger, R., McClusky, S., Vernant, P., Lawrence, S., Ergintav, S., Cakmak, R., Ozener, H., Kadirov, F., Guliev, I., Stepanyan, R., Nadariya, M., Hahubia, G., Mahmoud, S., Sakr, K., ArRajehi, A., Paradissis, D., Al-Aydrus, A., Prilepin, M., Guseva, T., Evren, E., Dmitrotsa, A., Filikov, S. V., Gomez, F., Al-Ghazzi, R., Karam, G., 2006. GPS constraints on continental deformation in the Africa-Arabia-Eurasia continental collision zone and

implications for the dynamics of plate interactions. J. Geophys. Res. Solid Earth 111, B05411. https://doi.org/10.1029/2005JB004051

Reilinger, R.E., McClusky, S.C., Oral, M.B., King, R.W., Toksoz, M.N., Barka, A.A., Kinik, I., Lenk, O., Sanli, I., 1997. Global Positioning System measurements of present-day crustal movements in the Arabia-Africa-Eurasia plate collision zone. J. Geophys. Res. Solid Earth 102, 9983–9999. https://doi.org/10.1029/96jb03736

Reiners, P.W., Brandon, M.T., 2006. Using Thermochronology to Understand Orogenic Erosion. Annu. Rev. Earth Planet. Sci. 34, 419–466. https://doi.org/10.1146/annurev.earth.34.031405.125202

Rickers, F., Fichtner, A., Trampert, J., 2013. The Iceland-Jan Mayen plume system and its impact on mantle dynamics in the North Atlantic region: Evidence from full-waveform inversion. Earth Planet. Sci. Lett. 367, 39–51. https://doi.org/10.1016/j.epsl.2013.02.022

Robertson, A.H.F., Ustaömer, T., 2004. Tectonic evolution of the Intra-Pontide suture zone in the Armutlu Peninsula, NW Turkey. Tectonophysics 381, 175–209. https://doi.org/10.1016/j.tecto.2002.06.002

Sakic, P., Piété, H., Ballu, V., Royer, J.Y., Kopp, H., Lange, D., Petersen, F., Özeren, M.S., Ergintav, S., Geli, L., Henry, P., Deschamps, A., 2016. No significant steady state surface creep along the North Anatolian Fault offshore Istanbul: Results of 6 months of seafloor acoustic ranging. Geophys. Res. Lett. 43, 6817–6825. https://doi.org/10.1002/2016GL069600

Sandwell, D., Garcia, E., Soofi, K., Wessel, P., Chandler, M., Smith, W.H.F., 2013. Toward 1-mGal accuracy in global marine gravity from CryoSat-2, Envisat, and Jason-1. Lead. Edge 32, 892–899. https://doi.org/10.1190/tle32080892.1

Sandwell, D.T., Müller, R.D., Smith, W.H.F., Garcia, E., Francis, R., 2014. New global marine gravity model from CryoSat-2 and Jason-1 reveals buried tectonic structure. Science (80-.). 346, 65–67. https://doi.org/10.1126/science.1258213

Saunders, A.D., Fitton, J.G., Kerr, A.C., Norry, M.J., Kent, R.W., 1997. The north atlantic igneous province. Washingt. DC Am. Geophys. Union Geophys. Monogr. Ser. 100, 45–93. https://doi.org/10.1029/GM100p0045

Scheck-Wenderoth, M., Lamarche, J., 2005. Crustal memory and basin evolution in the Central European Basin System—new insights from a 3D structural model. Tectonophysics 397, 143–165. https://doi.org/10.1016/j.tecto.2004.10.007

Scheck-Wenderoth, M., Maystrenko, Y., 2008. How warm are passive continental margins? A 3-D lithosphere-scale study from the Norwegian margin. Geology 36, 419–422. https://doi.org/10.1130/G24545A.1

Scheck-Wenderoth, M., Uenzelmann-Neben, G., Trumbull, R., Kukla, P., 2017. Editorial for tectonophysics special issue progress in understanding passive continental margins. Tectonophysics 716, 1–3. https://doi.org/10.1016/j.tecto.2017.04.018

Schmidt, S., Anikiev, D., Götze, H.-J., Gomez Garcia, À., Gomez Dacal, M. L., Meeßen, C., Plonka, C., Rodriguez Piceda, C., Spooner, C., and Scheck-Wenderoth, M., 2020.

IGMAS+ – a tool for interdisciplinary 3D potential field modelling of complex geological structures., EGU General Assembly 2020, Online, 4–8 May 2020, EGU2020-8383. https://doi.org/10.5194/egusphere-egu2020-8383

Schmidt, S., Plonka, C., Götze, H.J., Lahmeyer, B., 2011. Hybrid modelling of gravity, gravity gradients and magnetic fields. Geophys. Prospect. 59, 1046–1051. https://doi.org/10.1111/j.1365-2478.2011.00999.x

Schmittbuhl, J., Karabulut, H., Lengliné, O., Bouchon, M., 2016. Long-lasting seismic repeaters in the Central Basin of the Main Marmara Fault. Geophys. Res. Lett. 43, 9527–9534. https://doi.org/10.1002/2016GL070505

Seipold, U., 1992. Depth dependence of thermal transport properties for typical crustal rocks. Phys. Earth Planet. Inter. 69, 299–303. https://doi.org/10.1016/0031-9201(92)90149-P

Şengör, A.M.., Tüysüz, O., İmren, C., Sakınç, M., Eyidoğan, H., Görür, N., Le Pichon, X., Rangin, C., 2005. THE NORTH ANATOLIAN FAULT: a new look. Annu. Rev. Earth Planet. Sci. 33, 37–112. https://doi.org/10.1146/annurev.earth.32.101802.120415

Şengör, A.M.C., Grall, C., İmren, C., Le Pichon, X., Görür, N., Henry, P., Karabulut, H., Siyako, M., 2014. The geometry of the North Anatolian transform fault in the Sea of Marmara and its temporal evolution: implications for the development of intracontinental transform faults. Can. J. Earth Sci. 51, 222–242. https://doi.org/10.1139/cjes-2013-0160

Séranne, M., Anka, Z., 2005. South Atlantic continental margins of Africa: A comparison of the tectonic vs climate interplay on the evolution of equatorial west Africa and SW Africa margins. J. African Earth Sci. 43, 283–300. https://doi.org/10.1016/j.jafrearsci.2005.07.010

Sibuet, J.C., Mazé, J.P., Amortila, P., Pichon, X.L., 1987. Physiography and structure of the western Iberian continental margin off Galicia from Sea-Beam and seismic data. In: Boillot, G., Winterer, E.L., Meyer, A.W. (Eds.), Proc. Init. Repts (Part. A), vol. 103. ODP, pp. 77–97.

Sippel, J., Scheck-Wenderoth, M., Lewerenz, B., Klitzke, P., 2015. Deep vs. shallow controlling factors of the crustal thermal field - insights from 3D modelling of the Beaufort-Mackenzie Basin (Arctic Canada). Basin Res. 27, 102–123. https://doi.org/10.1111/bre.12075

Skogseid, J., 1994. Dimensions of the Late Cretaceous-Paleocene Northeast Atlantic rift derived from Cenozoic subsidence. Tectonophysics 240, 225–247. https://doi.org/10.1016/0040-1951(94)90274-7

Sobolev, S. V., Petrunin, A., Garfunkel, Z., Babeyko, A.Y., 2005. Thermo-mechanical model of the Dead Sea Transform. Earth Planet. Sci. Lett. 238, 78–95. https://doi.org/10.1016/j.epsl.2005.06.058

Stein, C.A., Stein, S., 1992. A model for the global variation in oceanic depth and heat flow with lithospheric age. Nature 359, 123–129. https://doi.org/10.1038/359123a0

Stein, R.S., Barka, A.A., Dieterich, J.H., 1997. Progressive failure on the North Anatolian fault since 1939 by earthquake stress triggering. Geophys. J. Int. 128, 594–604.

https://doi.org/10.1111/j.1365-246X.1997.tb05321.x

Steinberger, B., Spakman, W., Japsen, P., Torsvik, T.H., 2015. The key role of global solid-Earth processes in preconditioning Greenland's glaciation since the Pliocene. Terra Nov. 27, 1–8. https://doi.org/10.1111/ter.12133

Steinberger, B., Torsvik, T.H., 2012. A geodynamic model of plumes from the margins of Large Low Shear Velocity Provinces. Geochemistry, Geophys. Geosystems 13, Q01W09. https://doi.org/10.1029/2011GC003808

Stewart, J., Watts, A.B., Bagguley, J.G., 2000. Three-dimensional subsidence analysis and gravity modelling of the continental margin offshore Namibia. Geophys. J. Int. 141, 724–746. https://doi.org/10.1046/j.1365-246X.2000.00124.x

Tesauro, M., Kaban, M.K., Cloetingh, S.A.P.L., 2013. Global model for the lithospheric strength and effective elastic thickness. Tectonophysics 602, 78–86. https://doi.org/10.1016/j.tecto.2013.01.006

Turcotte, D.L., Schubert, G., 2014. Geodynamics, Third edit. ed. Cambridge University Press.

Turgut, S., Eseller, G., 2000. Sequence stratigraphy, tectonics and depositional history in eastern Thrace Basin, NW Turkey. Mar. Pet. Geol. 17, 61–100. https://doi.org/10.1016/S0264-8172(99)00015-X

Ünay, E., Emre, Ö., Erkal, T., Keçer, M., 2001. The rodent fauna from the adapazarı pull-apart basin (nw anatolia): Its bearings on the age of the north anatolian fault. Geodin. Acta 14, 169–175. https://doi.org/10.1080/09853111.2001.11432442

Unternehr, P., Curie, D., Olivet, J.L., Goslin, J., Beuzart, P., 1988. South Atlantic fits and intraplate boundaries in Africa and South America. Tectonophysics 155, 169–179. https://doi.org/10.1016/0040-1951(88)90264-8

Ustaömer, P.A., Ustaömer, T., Collins, A.S., Reischpeitsch, J., 2009. Lutetian arc-type magmatism along the southern Eurasian margin: New U-Pb LA-ICPMS and whole-rock geochemical data from Marmara Island, NW Turkey. Mineral. Petrol. 96, 177–196. https://doi.org/10.1007/s00710-009-0051-8

Vilà, M., Fernández, M., Jiménez-Munt, I., 2010. Radiogenic heat production variability of some common lithological groups and its significance to lithospheric thermal modeling. Tectonophysics 490, 152–164. https://doi.org/10.1016/j.tecto.2010.05.003

Watts, A.B., 2001. Isostasy and flexure of the lithosphere. Cambridge University Press.

Watts, A.B., Zhong, S., 2000. Observations of flexure and the rheology of oceanic lithosphere. Geophys. J. Int. 142, 855–875. https://doi.org/10.1046/j.1365-246X.2000.00189.x

Wegener, A., 2003. The origins of continents. In: Dullo WC., Geologische Vereinigung e.V. (eds) Milestones in Geosciences. Springer, Berlin, Heidelberg. https://doi.org/10.1007/978-3-662-08763-3_1

West, D.P., Hubbard, M.S., 1997. Progressive localization of deformation during exhumation of a major strike-slip shear zone: Norumbega fault zone, south-central Maine, USA.

Tectonophysics 273, 185–201. https://doi.org/10.1016/S0040-1951(96)00306-X

White, R., McKenzie, D., 1989. Magmatism at rift zones - The generation of volcanic continental margins and flood basalts. J. Geophys. Res. 94, 7685–7729. https://doi.org/10.1029/JB094iB06p07685

White, R.S., Spence, G.D., Fowler, S.R., McKenzie, D.P., Westbrook, G.K., 1987. Magmatism at rifted continental margins. Nature 330, 439–444. https://doi.org/10.1038/330439a0

Whitmarsh, R.B., Manatschal, G., Minshull, T.A., 2001. Evolution of magma-poor continental margins from rifting to seafloor spreading. Nature 413, 150–154. https://doi.org/10.1038/35093085

Wollin, C., Bohnhoff, M., Martínez-Garzón, P., Küperkoch, L., Raub, C., 2018. A unified earthquake catalogue for the Sea of Marmara Region, Turkey, based on automatized phase picking and travel-time inversion: Seismotectonic implications. Tectonophysics 747–748, 416–444. https://doi.org/10.1016/j.tecto.2018.05.020

Yaltirak, C., 2002. Tectonic evolution of the Marmara Sea and its surroundings. Mar. Geol. 190, 493–529. https://doi.org/10.1016/S0025-3227(02)00360-2

Yaltirak, C., Alpar, B., 2002. Evolution of the middle strand of North Anatolian Fault and shallow seismic investigation of the southeastern Marmara Sea (Gemlik Bay). Mar. Geol. 190, 307–327. https://doi.org/10.1016/S0025-3227(02)00352-3

Yamamoto, R., Kido, M., Ohta, Y., Takahashi, N., Yamamoto, Y., Pinar, A., Kalafat, D., Özener, H., Kaneda, Y., 2019. Seafloor geodesy revealed partial creep of the North Anatolian Fault submerged in the Sea of Marmara. Geophys. Res. Lett. 46, 1268–1275. https://doi.org/10.1029/2018GL080984

Yamamoto, Y., Takahashi, N., Pinar, A., Kalafat, D., Citak, S., Comoglu, M., Polat, R., Kaneda, Y., 2017. Geometry and segmentation of the North Anatolian Fault beneath the Marmara Sea, Turkey, deduced from long-term ocean bottom seismographic observations. J. Geophys. Res. Solid Earth 122, 2069–2084. https://doi.org/10.1002/2016JB013608

Yildirim, C., Melnick, D., Ballato, P., … T.S.-Q.S., 2013, U., 2013. Differential uplift along the northern margin of the Central Anatolian Plateau: inferences from marine terraces. Elsevier.

Yildirim, C., Schildgen, T.F., Echtler, H., Melnick, D., Strecker, M.R., 2011. Late Neogene and active orogenic uplift in the Central Pontides associated with the North Anatolian Fault: Implications for the northern margin of the Central Anatolian Plateau, Turkey. Tectonics 30. https://doi.org/10.1029/2010TC002756

Yildirim, C., Tüysüz, O., 2017. Estimation of the long-term slip, surface uplift and block rotation along the northern strand of the North Anatolian Fault Zone: Inferences from geomorphology of the Almacık Block. Elsevier. https://doi.org/10.1016/j.geomorph.2017.08.038

Supplementary Figures

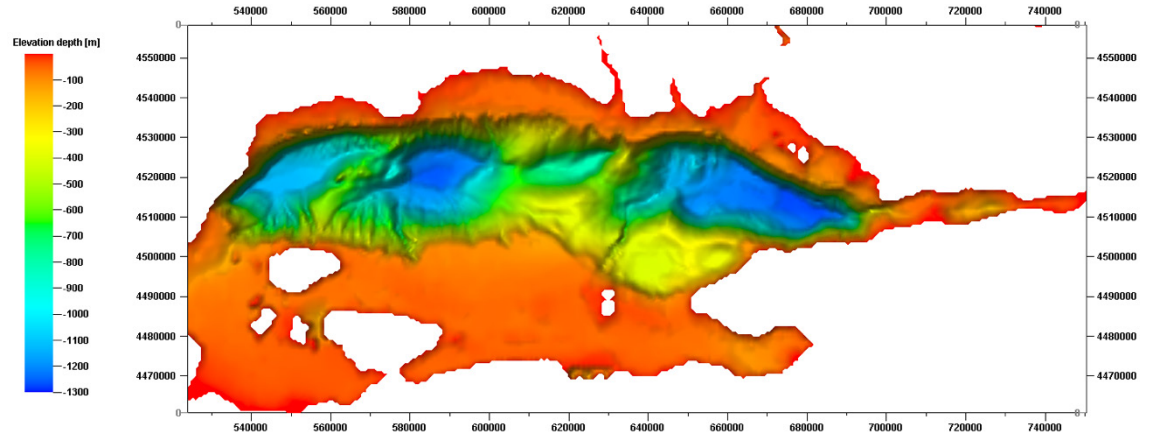

Figure S2.1: High resolution bathymetry within the Marmara Trough (LePichon et al., 2001).

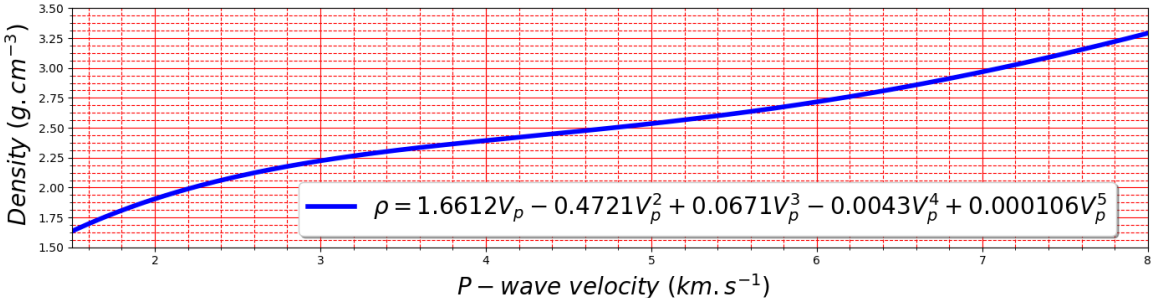

Figure S2.2: Polynomial regression to the Nafe–Drake Curve valid for P-wave velocities between 1.5 to 8.5 km s^{-1} (Brocher, 2005 after Ludwig et al., 1970).

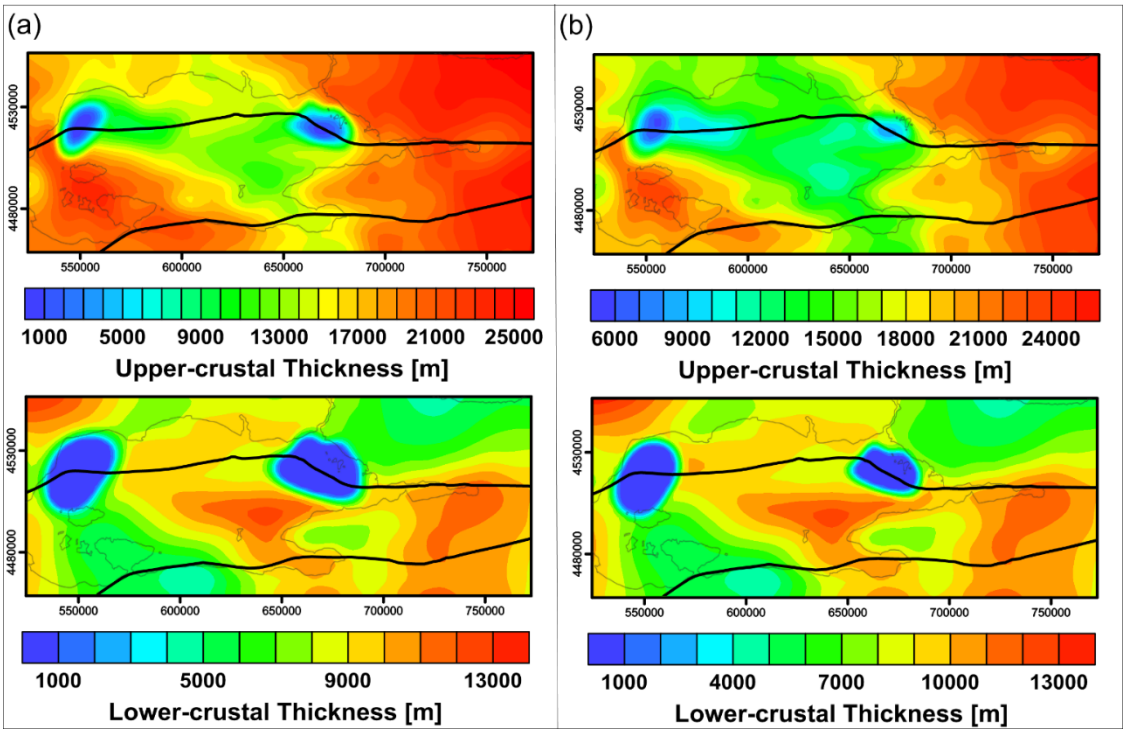

Figure S2.3: Upper and lower crustal thickness based on best-fit gravity models of the Sea of Marmara: (a) Model-I and Model-III; (b) Model-II.

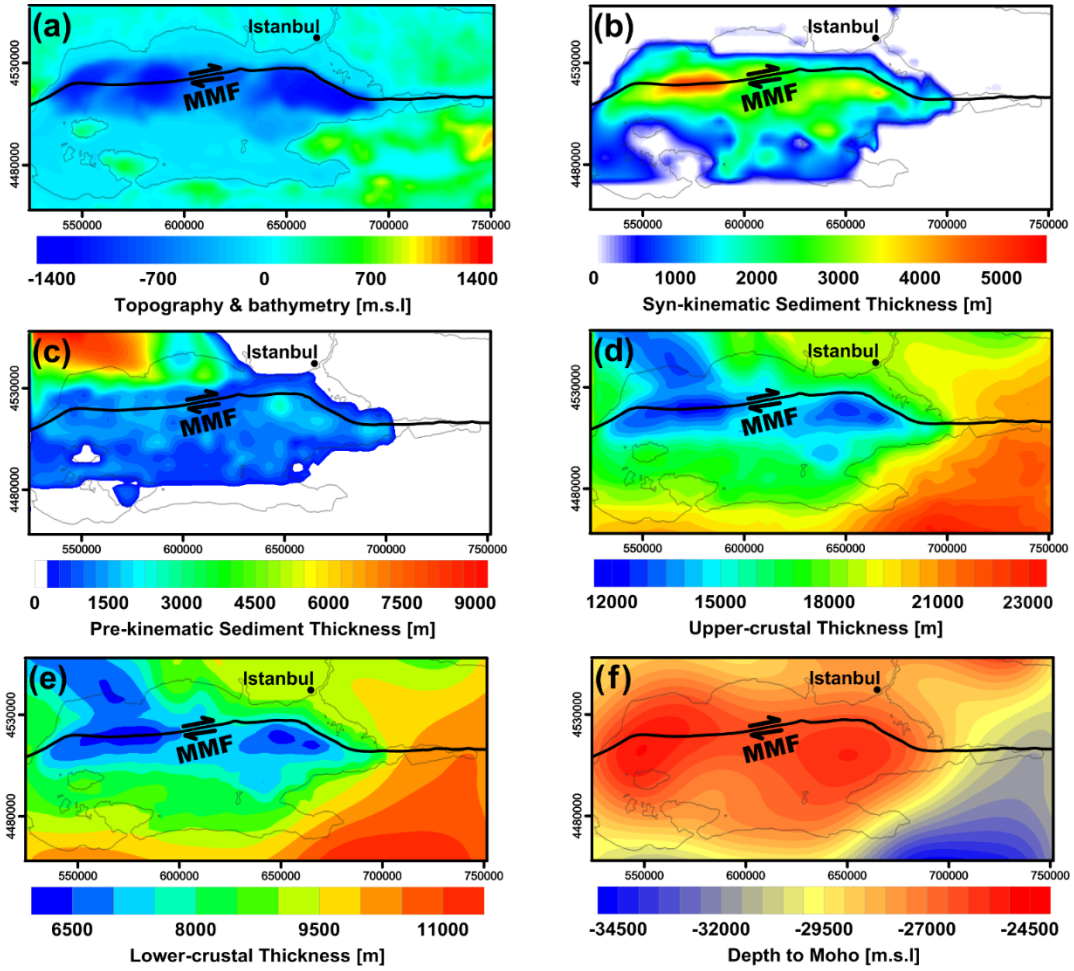

Figure S2.4: Density-structural model of Kende et al. (2017). Syn-kinematic sediments (ρ = 2230 kg m^{-3}), pre-kinematic sediments (ρ = 2590 kg m^{-3}), upper crust (ρ = 2650 kg m^{-3}), lower crust (ρ = 2950 kg m^{-3}), Moho (ρ = 3330 kg m^{-3}).

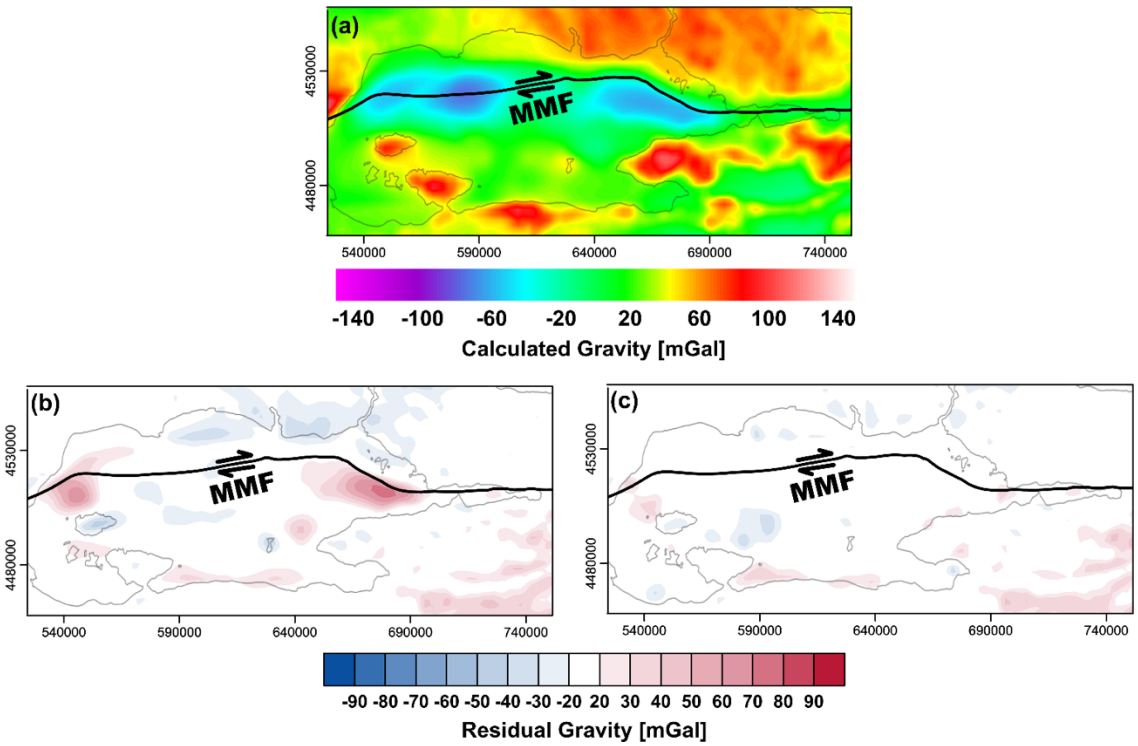

Figure S2.5: Gravity response and corresponding misfit to EIGEN-64C and Improved–TOPEX based on the best-fit model of Kende et al. (2017): (a) Calculated gravity corresponding to the density model in Fig. S3; (b) misfit between the calculated gravity and the gravity anomaly data of EIGEN-6C4; (c) misfit between the calculated and the gravity anomaly data of Improved–TOPEX.

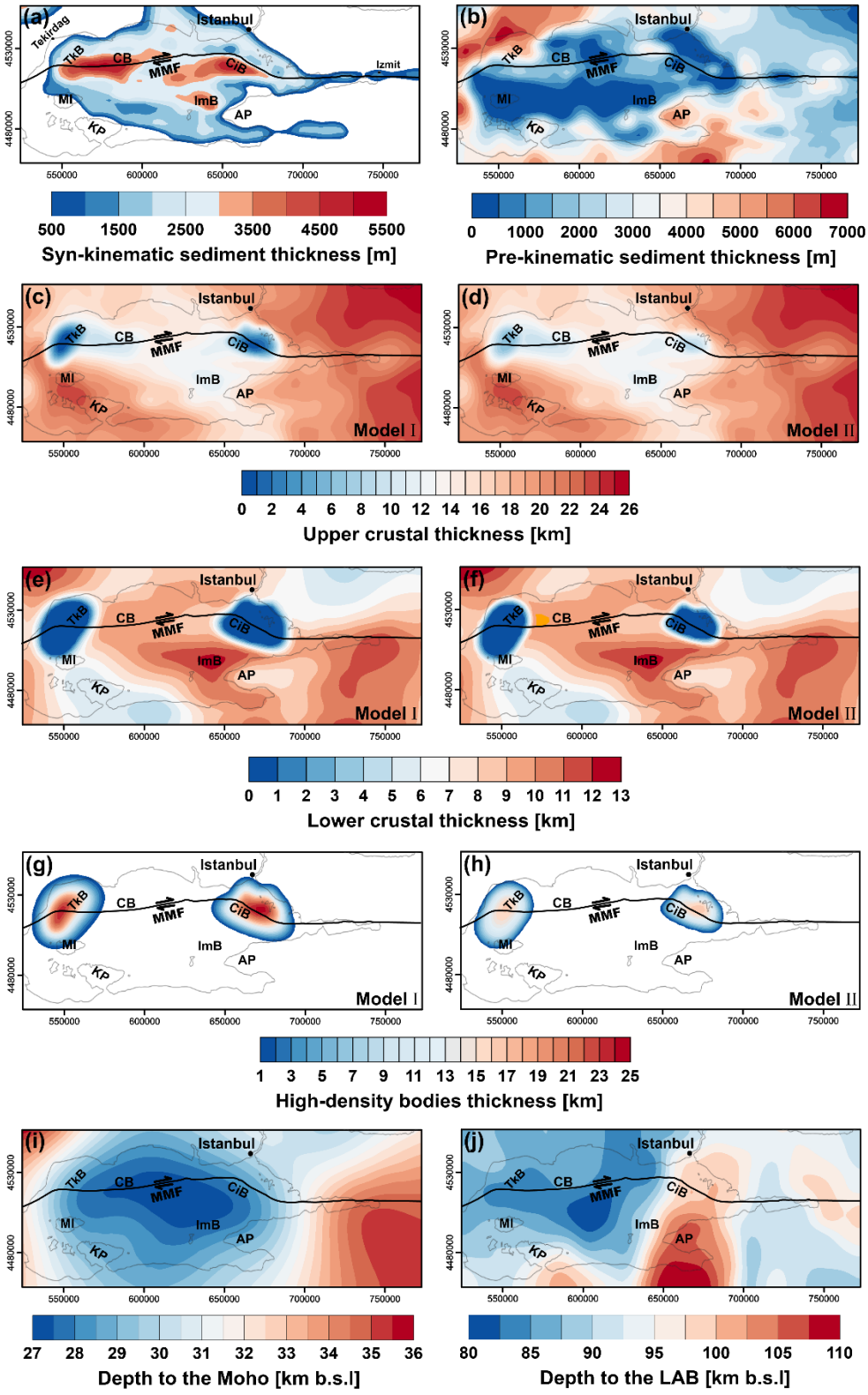

Figure S3.1: 3-D structural input for thermal and rheological modeling. (a) Syn-kinematic sediment thickness. (b) Pre-kinematic sediment thickness. (c) Upper crystalline crustal thickness. (d) Lower crystalline crustal thickness. (e) High-density bodies thickness. (f) Depth to Moho. (g) Depth to thermal LAB (1330°C isotherm). Abbreviations: Main Marmara Fault (MMF), Çınarcık Basin (CiB), Central Basin (CB), Tekirdağ Basin (TkB), Imralı Basin (ImB), Marmara Island (MI), Kapidağ Peninsula (KP), and Armutlu Peninsula (AP).

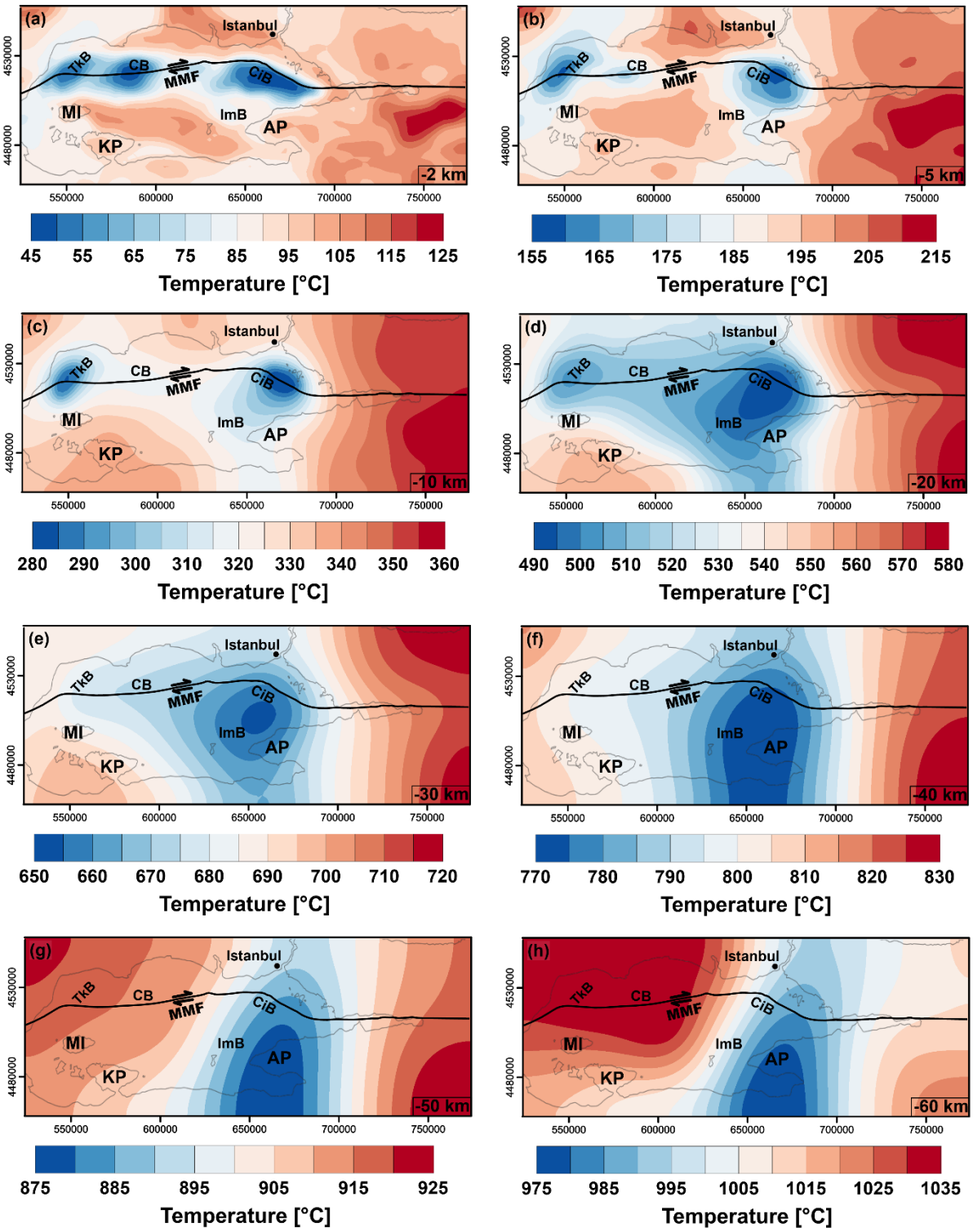

Figure S3.2: 3-D conductive thermal model for Model I. Temperature distribution maps for different depths below the sea-level: (a) 2 km, (b) 5 km, (c) 10 km, (d) 20 km, (e) 30 km, (f) 40 km, (g) 50 km, and (h) 60 km. Abbreviations: Main Marmara Fault (MMF), Çınarcık Basin (CiB), Central Basin (CB), Tekirdağ Basin (TkB), Imralı Basin (ImB), Marmara Island (MI), Kapidağ Peninsula (KP), and Armutlu Peninsula (AP).

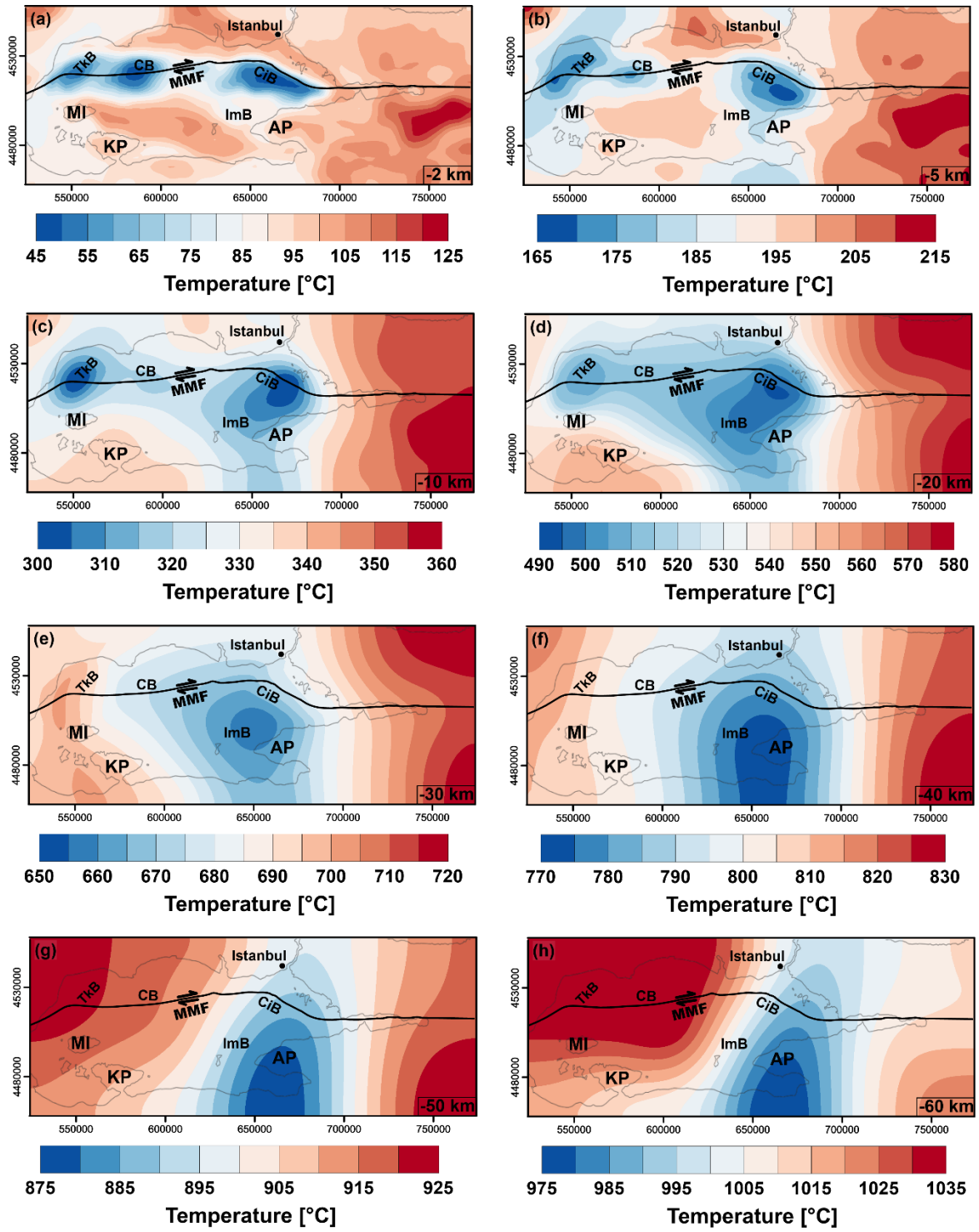

Figure S3.3: 3-D conductive thermal model for Model II. Temperature distribution maps for different depths below the sea-level: (a) 2 km, (b) 5 km, (c) 10 km, (d) 20 km, (e) 30 km, (f) 40 km, (g) 50 km, and (h) 60 km. Abbreviations: Main Marmara Fault (MMF), Çınarcık Basin (CiB), Central Basin (CB), Tekirdağ Basin (TkB), Imralı Basin (ImB), Marmara Island (MI), Kapidağ Peninsula (KP), and Armutlu Peninsula (AP).

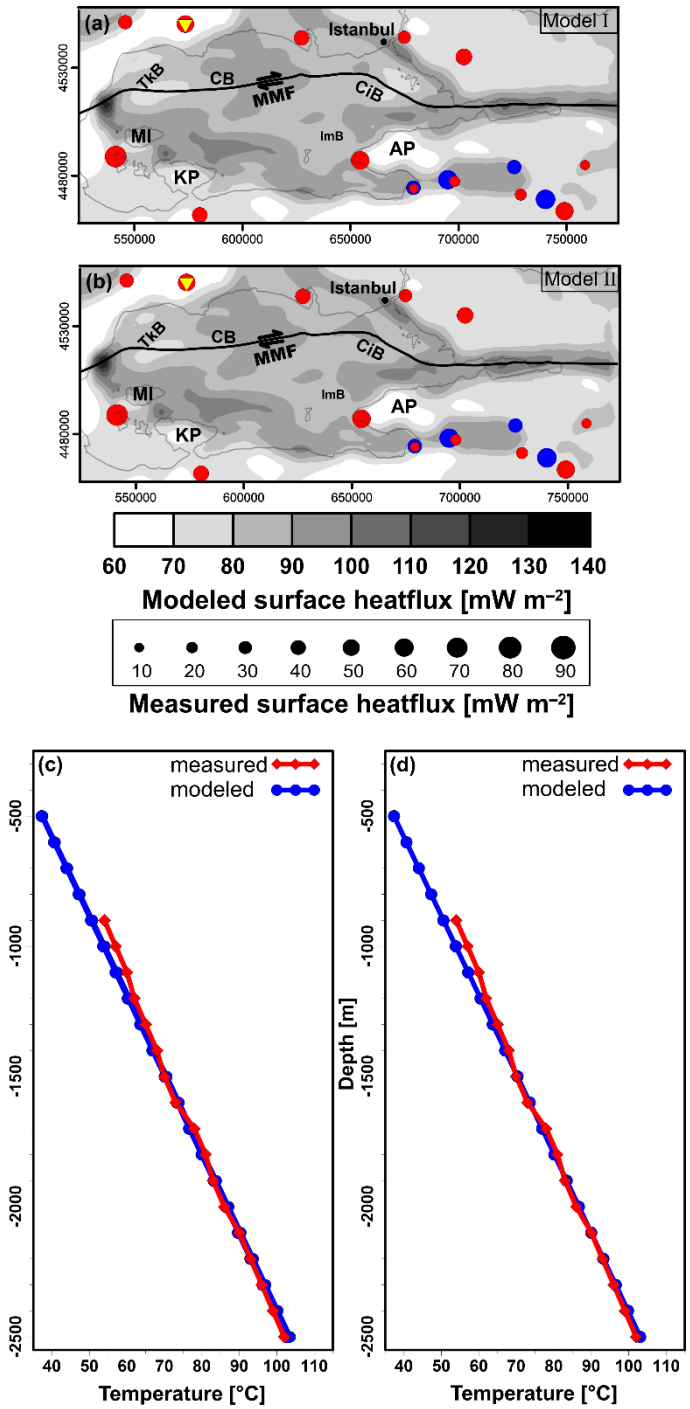

Figure S3.4: Calculated surface heat flow using a constant average value for thermal conductivity (λ = 2 mW m^{-2}). (a) Model I, and (b) Model II. The red (Pfister et al., 1998) and blue (Erkan et al., 2015) circles are measured surface heat flow values. Observed (Pfister et al., 1998) and calculated temperature logs from the 2500 m deep Corlu 1 well: (c) Model I, (c) Model II. The well location is shown as a yellow triangle in (a) and (b). Abbreviations: Main Marmara Fault (MMF), Çınarcık Basin (CiB), Central Basin (CB), Tekirdağ Basin (TkB), Imralı Basin (ImB), Marmara Island (MI), Kapidağ Peninsula (KP), and Armutlu Peninsula (AP).

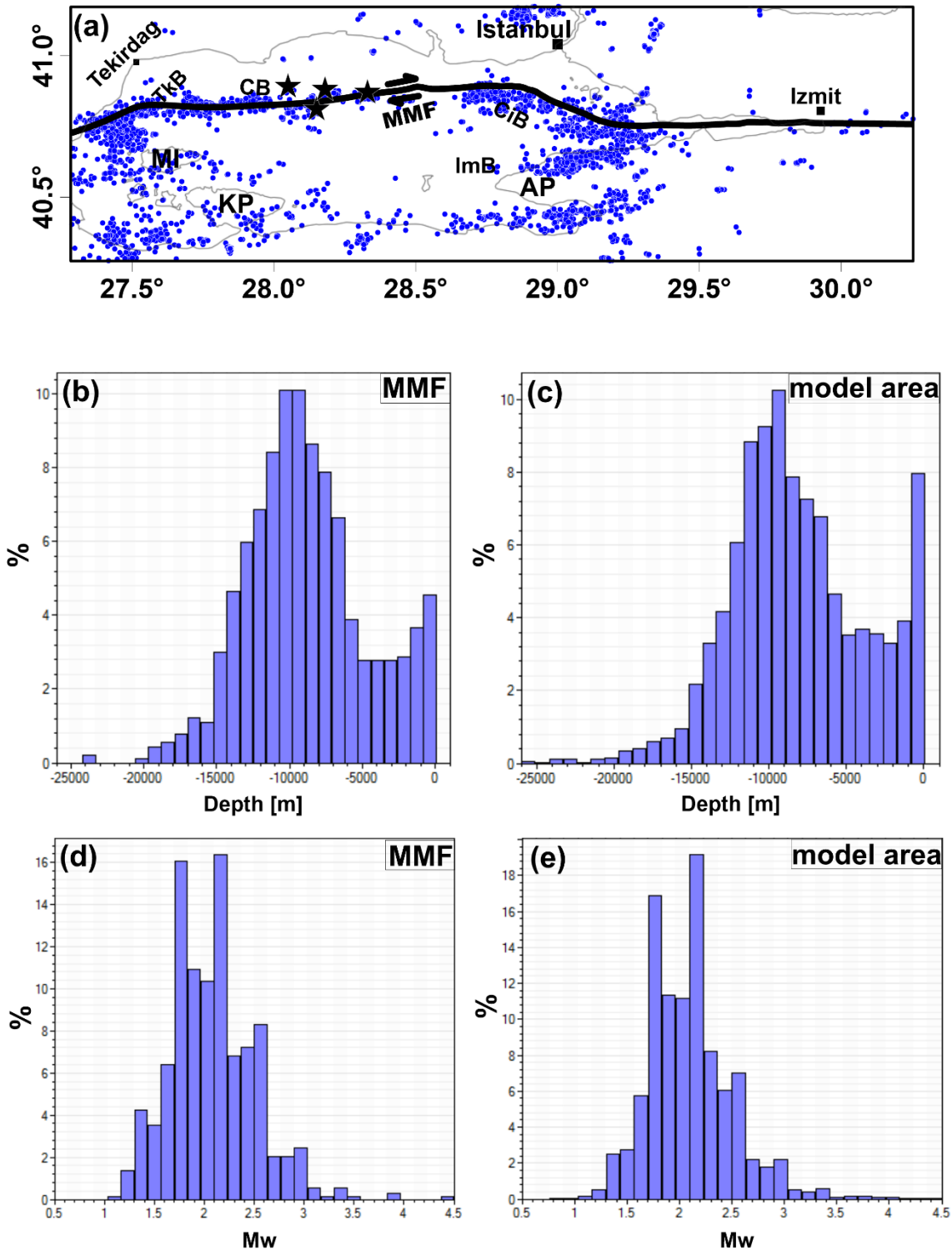

Figure S3.5: Observed seismicity across the modeled area. (a) Distribution of the epicenters over the modeled area. Small gray circles represent observations from 2006 to 2016 (Wollin et al., 2018) and black circles represent recent seismic activity (M>4.1) in September 2019 (data from GEOFON Data Center). (b) Depth distribution of the seismic events37 along the MMF and (c) over the entire modeled area. (d) Magnitude of seismic events37 along the MMF, and (e) over the entire modeled area.

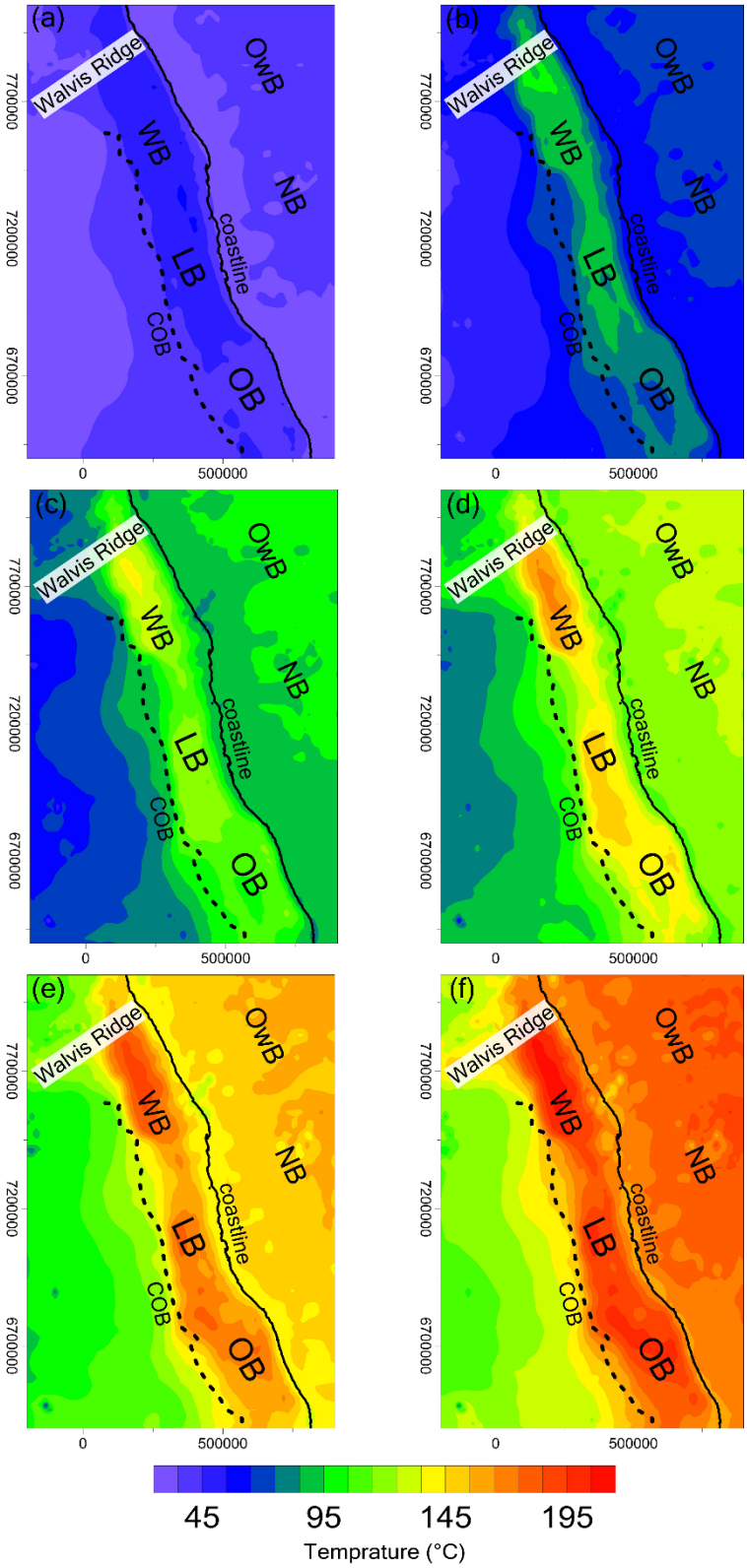

Figure S4.1: SW African margin: Temperature-depth distributions at (a) 1, (b) 2, (c) 3, (d) 4, (e) 5, and (f) 6 km below the upper thermal boundary (COB: Continent-Ocean Boundary; Cretaceous-Cenozoic basins: WB: Walvis Basin, LB: Lüderitz Basin, OB: Orange Basin; Precambrian basins: OwB: Owambo Basin, NB: Nama Basin; UTM: WGS84, 33S).

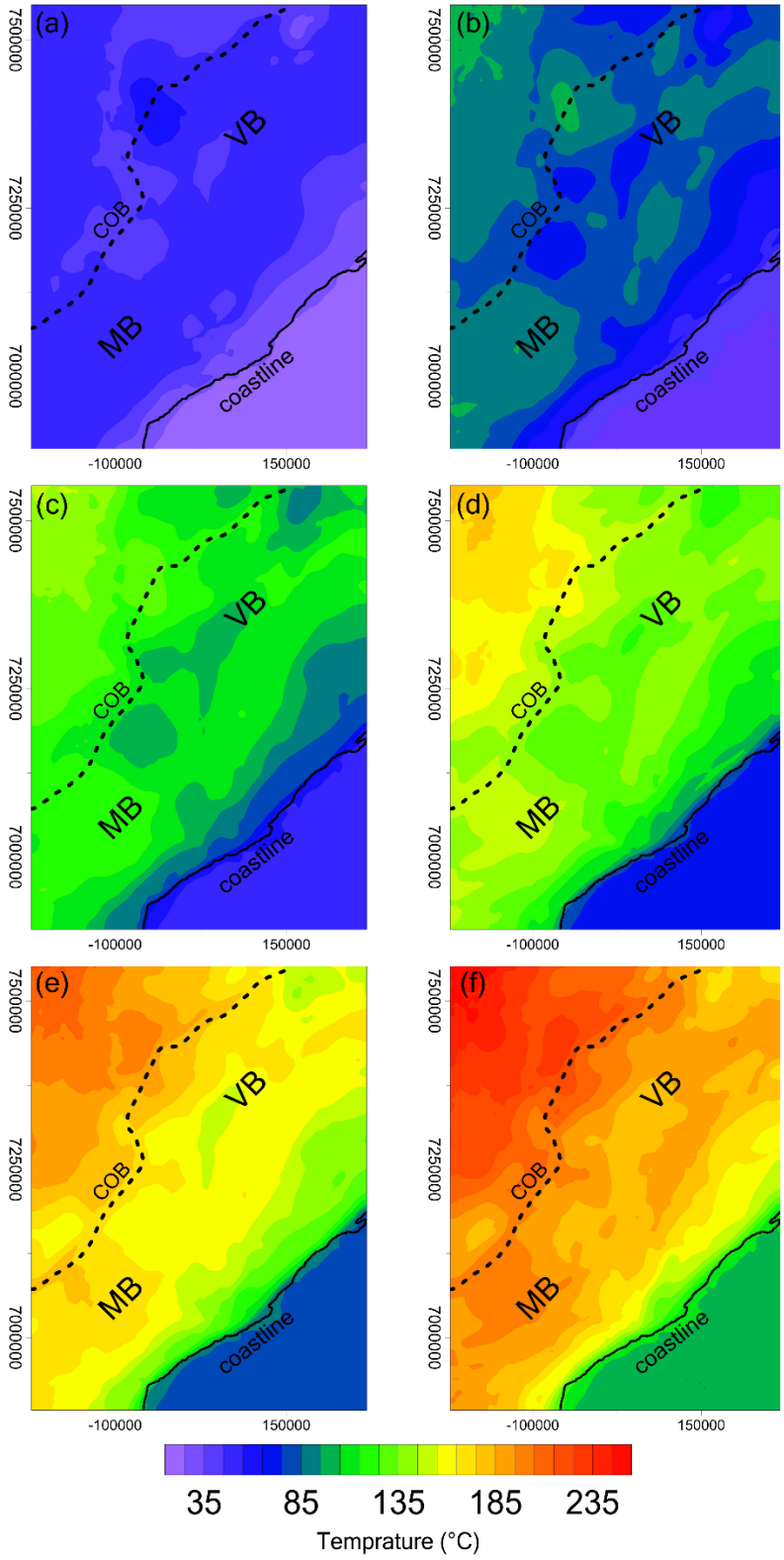

Figure S4.2: Norwegian margin: Temperature-depth distributions at (a) 1, (b) 2, (c) 3, (d) 4, (e) 5, and (f) 6 km below the upper thermal boundary (COB: Continent-Ocean Boundary; Cretaceous-Cenozoic basins: VB: Vøring Basin, MB: Møre Basin; UTM: WGS84, 33N).

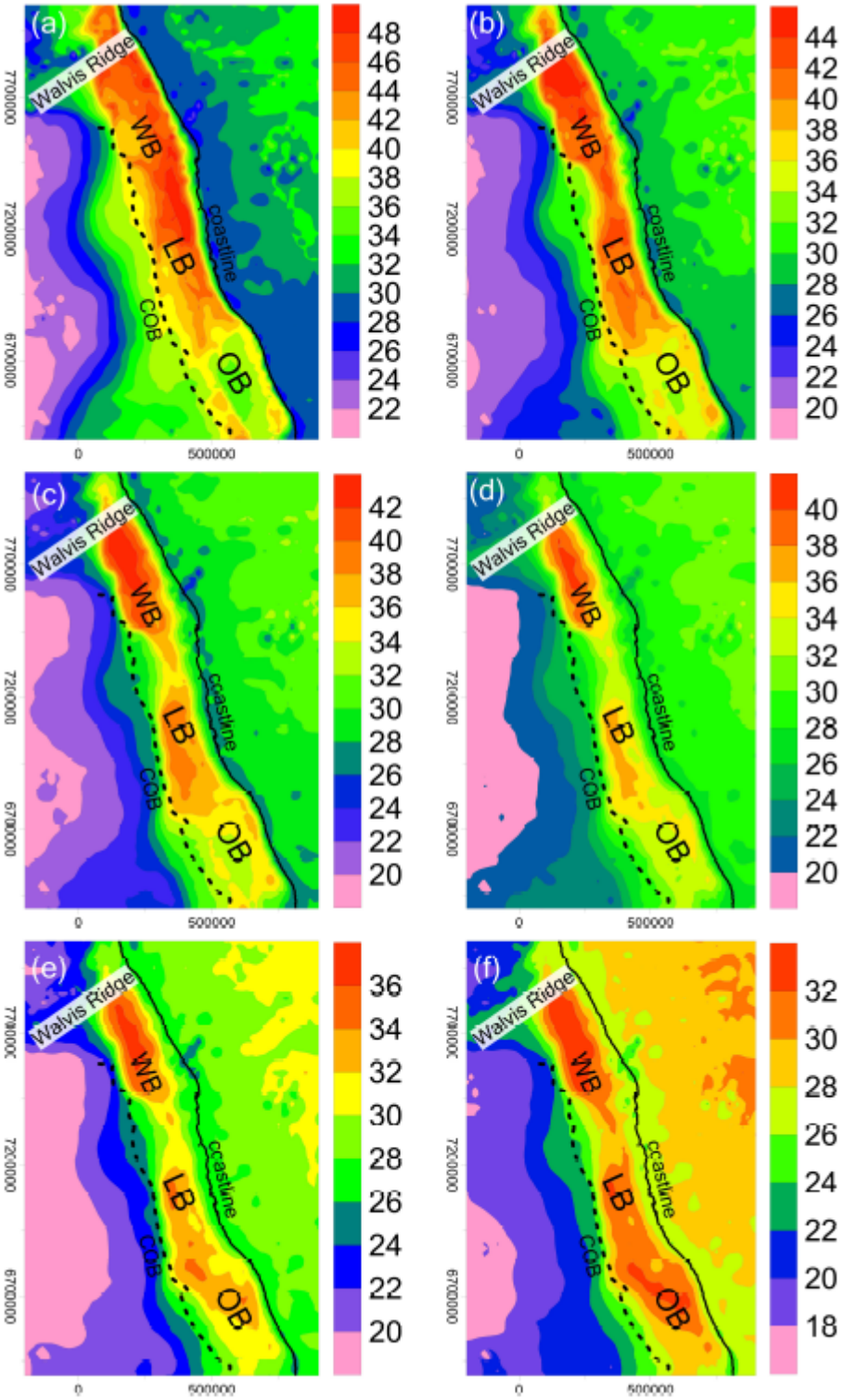

Figure S4.3: Geothermal gradient [◦C/km] at SW African margin: the gradient calculated as the temperature differences between the uppermost surface (upper thermal boundary) and the corresponding temperature distribution at (a) 1, (b) 2, (c) 3, (d) 4, (e) 5, and (f) 6 km below the uppermost surface (COB: Continent-Ocean Boundary; Cretaceous-Cenozoic basins: WB: Walvis Basin, LB: Lüderitz Basin, OB: Orange Basin; UTM: WGS84, 33S).

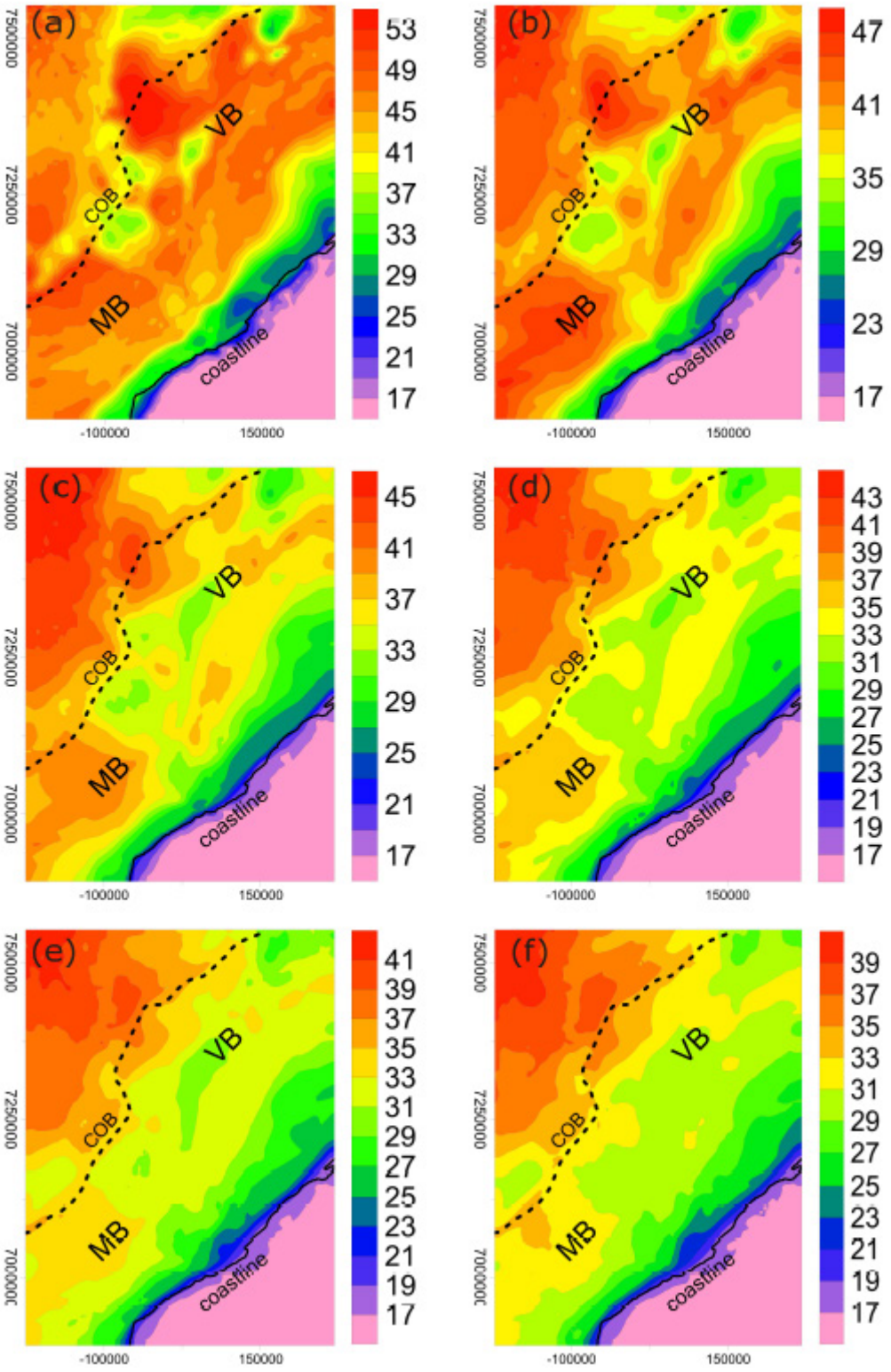

Figure S4.4: Geothermal gradient [◦C/km] at Norwegian margin: the gradient calculated as the temperature differences between the uppermost surface (upper thermal boundary) and the corresponding temperature distribution at (a) 1, (b) 2, (c) 3, (d) 4, (e) 5, and (f) 6 km below the uppermost surface (COB: Continent-Ocean Boundary; Cretaceous-Cenozoic basins: VB: Vøring Basin, MB: Møre Basin; UTM: WGS84, 33N).

Acknowledgments

This study was conducted at the University of Potsdam and the Helmholtz Centre Potsdam - GFZ German Research Centre for Geosciences, under the auspices of the ALErT initiative (Anatolian pLateau climatE and Tectonic hazards), an Initial Training Network (ITN) financed by the European Union's Seventh Framework Programme FP7/2007–2013 under the Marie Skłodowska-Curie Actions (MSCA) REA grant agreement no. 607996. I would therefore like to thank these institutions for their financial supports and for providing a world-leading research environment.

This doctoral study has truly been a journey with many ups and downs. In this path, the support and the encouragement of those surrounding me had an important role to finalize this study. In this regard, I would like to express my sincere gratitude to my supervisors Prof. Dr. Magdalena Scheck-Wenderoth, Prof. Manfred R. Strecker, Ph.D., and Dr. Gerold Zeilinger for their remarkable supports throughout my doctoral study. Dear Leni, many thanks for your boundless patience, for your decisive supports, and for being there for me whenever I was struggling with problems. You grabbed my hands and taught me how to walk as a mother does for her son, and finally enabled me to run freely. It is impossible to put my appreciation for you into words. THANK YOU! Dear Manfred, after our first meeting I was so impressed with the humble quality of your character, and I wished if you were my supervisor. I was so lucky that my wish came true and I had the honor to be a student of yours. Having you by my side throughout this journey was a reassuring feeling that I can always rely on your guidance and supports. Thank you so much for taking care of me! Dear Gerold, I am still thinking about our initial research plan for Bolivia. Many thanks for your unconditional help and supports!

My deepest and special gratitude to Dr. Oliver Heidbach and Prof. Dr. Marco Bohnhoff, with whom I had the honor to work on manuscripts regarding the NAFZ at the Sea of Marmara. I would like also to thank Pierre Henry for his supportive comments and providing me with the Improved-TOPEX gravity dataset and the structural model of Kende at al. (2017) including the high-resolution bathymetry grid of the Sea of Marmara.

The major scientific works of my doctoral research were conducted in Section 4.5: Basin Modelling at GFZ Potsdam. I am indebted to this research group for hosting me during my doctoral study and for providing me with their world-class infrastructures. I would like to thank Dr. Judith Bott and Dr. Mauro Cacace for their thoughtful feedback, their constructive

comments, and their insightful scientific advice. Special thanks to Björn Lewerenz for his help with the software infrastructures. Many thanks to Katharina Mahr and Anna Tihonova for their administrative help and supports. Dr. Jessica Freymark was my first tutor in Section 4.5 to teach me the basis of structural and thermal modeling. Thanks, Jessi! I was so lucky to share the office with Dr. Maximilian Frick and to have tons of fun during our scientific and nonscientific discussions. Thanks, Max! I would like also to express my gratitude to other former and current members of Section 4.5: Adrian, Angela, Anna, Antoine, Cameron, Constanza, Christian, Denis, Federico, Ingo, Katya, Maria Laura, Nasrin, Nora, Peter. You all made Section 4.5 to be my second home. Thanks, modelers!

I would like to thank Prof. Taylor Schildgen, Ph.D., Prof. Dr. Cengiz Yıldırım, Prof. Dr. Robin Lacassin, and Prof. Dr. Rolando Armijo for their informative lectures during the impressive field trips in Turkey and Greece.

I am so grateful to the ALErT administrative team at the University of Potsdam, Dr. Adriana Wipperling, and Dr. Andreas G.N. Bergner. In particular, I am so thankful to Dagmar Fritz for her unconditional help and supports. I would like also to thank the administrative assistants and the technical staff at the Institute of Geosciences at the University of Potsdam, and special thanks to Tanja Klaka-Tauscher, Martina Heidemann, and Ines Münch.

Being a newly arrived person in a new country is always a great challenge. I would like to thank Welcome Center Potsdam for facilitating my stay in Germany through their amazing programs for foreign students and their help with housing and paperwork, and in particular, many thanks to Frauke Stobbe.

Last but not least many thanks to my Family. To my parents, Alireza and Farzaneh, who supported me in every step of my life including my academic career. To Ensi, my amazing sister, who always can make me happy. To my love, Fatemeh, who keeps me motivated and never let me feel that I am alone in my path. Fatemeh, I could not and cannot achieve the seemingly impossible without you. To my son, Arvin, who was born during my doctoral study to be the light of my life and gave me such a motivation to be a Dr. pappa.